2017

Innovative seat suspensions for whole body vibration control of heavy duty vehicles

Donghong Ning
University of Wollongong

INNOVATIVE SEAT SUSPENSIONS FOR WHOLE BODY VIBRATION CONTROL OF HEAVY DUTY VEHICLES

Donghong Ning

School of Electrical, Computer and Telecommunications Engineering

Faculty of Engineering and Information Sciences

University of Wollongong

This Thesis is submitted for the degree of Doctor of Philosophy

August 2017

DECLARATION

I, Donghong Ning, declare that this thesis, submitted in fulfilment of the requirements for the award of Doctor of Philosophy, of the School of Electrical, Computer and Telecommunications Engineering, Faculty of Engineering and Information Sciences, University of Wollongong, is wholly my own work unless otherwise referenced or acknowledged. The document has not been submitted for qualifications at any other academic institution.

Donghong Ning

August, 2017

ABSTRACT

The heavy duty vehicles have played a significant role in the construction, agriculture, mining and even military applications; they have greatly enhanced the work efficiency of human. In the meantime, the ride comfort and health of their operators have been more and more concerned; those operators need to be exposed in severe whole body vibration (WBV) for a long time. In the thesis, the seat suspensions which are regarded as the most direct way to isolate vibration to the driver are developed including the single-degree of freedom (single-DOF) one and the multiple-DOF one; the active vibration control and semi-active vibration control are both investigated.

Three kinds of innovative single-DOF seat suspensions are proposed with the semi-active, active and hybrid control ways, respectively. The active seat suspension applies the rotary motor as actuator, and the scissors structure within a conventional passive seat suspension is applied to transform the rotary torque to a vertical force, thus, no additional transmission mechanism is required; three different control algorithms are designed with acceleration measurement for the active seat suspension. The semi-active seat suspension with MR damper can improve the ride comfort with less power consumption than an active seat suspension; by applying an additional active actuator with small force output, the hybrid seat suspension can greatly improve the performance of the semi-active one. The design concept is intuitive; the MR damper can suppress the high vibration energy in the resonance frequency, and then a small active force can further reduce the vibration magnitude. Different from a traditional semi-active seat suspension with MR or ER damper, an advanced semi-active seat suspension with controllable electromagnetic damper (EMD) system is proposed; two implementation methods for controlling the damping of the EMD are presented and tested.

The multiple-DOF seat suspension for WBV control has been rarely reported; in this thesis, a two-layer multiple-DOF seat suspension is designed and manufactured. The proposed seat suspension can reduce the vibration of driver body in five DOFs except the yaw vibration, which has least effect on human, with only three actuators. Another advantage of a two-layer structure is that, the vertical vibration reduction can be decoupled from reducing the lateral trunk bending and forward flexion of the driver body, according to the fact that the most sensitive frequency contents of the vertical vibration to human are much higher than the frequency content of other DOFs vibrations.

All the proposed seat suspensions are verified with experiments on a 6-DOF vibration platform; the experimental results indicate that all these seat suspension can improve the ride comfort and can be applied for the heavy duty vehicles.

PUBLICATIONS

Journal

Ning, D., Sun, S., Du, H., & Li, W. (2017). Integrated active and semi-active control for seat suspension of a heavy duty vehicle. *Journal of Intelligent Material Systems and Structures*, 1045389X17721032. (Chapter 5)

Ning, D., Sun, S., Zhang, F., Du, H., Li, W., & Zhang, B. (2017). Disturbance observer based Takagi-Sugeno fuzzy control for an active seat suspension. *Mechanical Systems and Signal Processing*, *93*, 515-530. (Chapter 4)

Ning, D., Sun, S., Wei, L., Zhang, B., Du, H., & Li, W. (2017). Vibration reduction of seat suspension using observer based terminal sliding mode control with acceleration data fusion. *Mechatronics*, *44*, 71-83. (Chapter 4)

Ning, D., Sun, S., Li, H., Du, H., & Li, W. (2016). Active control of an innovative seat suspension system with acceleration measurement based friction estimation. *Journal of Sound and Vibration*, *384*, 28-44. (Chapter 4)

Ning, D., Sun, S., Zhang, J., Du, H., Li, W., & Wang, X. (2016). An active seat suspension design for vibration control of heavy-duty vehicles. *Journal of Low Frequency Noise, Vibration and Active Control*, *35*(4), 264-278. (Chapter 4)

Sun, S. S., Ning, D. H., Yang, J., Du, H., Zhang, S. W., Li, W. H., & Nakano, M. (2017). Development of an MR seat suspension with self-powered generation capability. *Smart Material Structures*, *26*(8).

Tang, X., Du, H., Sun, S., Ning, D., Xing, Z., & Li, W. (2017). Takagi–Sugeno Fuzzy Control for Semi-Active Vehicle Suspension With a Magnetorheological Damper and Experimental Validation. *IEEE/ASME Transactions on Mechatronics*, *22*(1), 291-300.

Sun, S. S., Ning, D. H., Yang, J., Du, H., Zhang, S. W., & Li, W. H. (2016). A seat suspension with a rotary magnetorheological damper for heavy duty vehicles. *Smart Materials and Structures*, *25*(10), 105032.

Christie, M. D., Sun, S. S., Ning, D. H., Du, H., Zhang, S. W., & Li, W. H. (2016). A torsional MRE joint for a C-shaped robotic leg. *Smart Materials and Structures*, *26*(1), 015002.

Ning, D., Sun, S., Li, W., Du, H., & Li, W. (2017). An energy saving variable damping seat suspension system with regeneration capability. *IEEE Transaction on Industrial Electronics,* Under review. (Chapter 6)

Ning, D., Sun, S., Du, H., & Li, W. (2017). Vibration control of an energy regenerative seat suspension with variable external resistance. *Mechanical Systems and Signal Processing* , Under review. (Chapter 6)

Ning, D., Sun, S., Du, H., Li, W., & Zhang, B. (2017). An innovative two-layer multiple-DOF seat suspension for vehicle whole body vibration control. *IEEE/ASME Transactions on Mechatronics,* Under review. (Chapter 7)

Ning, D., Sun, S., Li, W., Du, H., & Li, W. (2017). Control of a multiple-DOF vehicle seat suspension with roll and vertical vibration. *Journal of Sound and Vibration* , Under review. (Chapter 7)

Conference

Ning, D., Coyte, J., Huang, H., Du, H., & Li, W. (2015). Experimental Vibration Simulation for Heavy Duty Vehicle Seat Suspension with a Multiple-DOF Motion Platform (No. 2015-01-0613). *SAE Technical Paper*. (Chapter 3)

Ning, D., Zhang, J., Sun, S., Du, H., & Li, W. (2014). Design and test of a multiple-DOF motion platform for vibration analysis of heavy duty vehicle seat suspension. In *8th Australasian Congress on Applied Mechanics*: ACAM 8(p. 14). Engineers Australia. (Chapter 3)

Ning, D., Du, H., & Li, W. (2015). Parameter optimisation design for a six-DOF heavy duty vehicle seat suspension. In *11th World Congress on Structural and Multidisciplinary Optimisation.*

ACKNOWLEDGEMENTS

First and foremost, I would like to express my sincere appreciation to my supervisor, Prof. Haiping Du, who always gives me inspirational guidance and unselfish help during the whole time of my PhD study. I was so confused in the beginning of my research, and I would be lost without the patient guidance from Prof. Haiping Du. He encourages me to try different methods, and quickly gives me responses when I encounter difficulties. He always tries his best to fulfil the requirements for the implementation of my research.

I also would like to thank my co-supervisor, Prof. Weihua Li, who is so thoughtful and always shows consideration to me. Particular thanks are extended to my friend and colleague, Shuaishuai Sun, who is an excellent researcher, and always gives me valuable suggestions. I also want to extend my gratitude to all my good friends and colleagues, Boyuan Li, James Coyte, Jian Yang, Xin Tang, Jiawei Zhang, Dan Yuan, Xianxian Shao, Chao Huang, Wenfei Li, Zhiwei Xing, Tanju Yildirim, Qianbin Zhao, Wenxing Li, for the help and happiness you gave to me. The staffs in the workshop have taught me a lot, and gave me assistance for my research.

Finally, I want to thank my parents and parents-in-law for their love. My wife, Shuang Yu, and my son, Yuhao Ning, who always accompany with me, are the most important person in my life. The particular appreciation to my wife for the contribution she has made for family.

CONTENTS

LIST OF TABLES

LIST OF FIGURES

LIST OF ABBREVIATIONS AND ACRONYMS

ER	Electrorheological
MR	Magnetorheological
TS fuzzy	Takagi-Sugeno fuzzy
AC	Alternating current
DC	Direct current
EMD	Electromagnetic damper
BEM	Back electromagnetic
RMS	Root mean square
PSD	Power spectral density
SEAT	Seat Effective Amplitude Transmissibility
VDV	Vibration dose value
PMSM	Permanent magnet synchronous motor
PWM	Pulse-width modulation
MEMS	Micro-electromechanical systems
IMU	Inertia measurement unit
TSM	Terminal sliding mode

1 INTRODUCTION

1.1 Background and Motivation

Heavy duty vehicles play an important role in the construction, agriculture, mining and even military field; they have greatly enhanced the work efficiency; on the other hand, the vibration transferred from rough road has a significant influence on the operators' discomfort, fatigue and safety[1-3].. In general, the tires, vehicle suspension and seat suspension are capable to reduce the vibration magnitude. The tires can isolate much high frequency vibration, but their parameters cannot be controlled once manufactured. The controlled vehicle suspensions, the semi-active one and active one, can isolate most vibration, however, a reduction of the low frequency vibration will result in an increase of suspension deflection which will affect the vehicle operation; there is an inherent trade-off between ride comfort and suspension deflection. The seat suspension as the second vibration isolation system (the first one is the vehicle suspension) of vehicles is the most direct way to reduce the vibration to the driver body; it can be modified and controlled with much less cost than the vehicle suspension. Thus, the seat suspension has been regarded as an effective way to improve the ride comfort.

The single-DOF seat suspensions for isolating the vertical vibration are widely studied and applied [4-7] ; they can be classified as the passive one, the semi-active one and the active one. For the active seat suspension, it has the best performance among the three kinds of seat suspensions; on the other hand, its cost and the energy consumption are the main issues hindering its practical application. Thus, when designing an active seat suspension, a concise structure should be the priority in order to simplify the manufacture, and a low cost actuator could be used to further reduce costs; in addition, the controller should be developed with feedback variables which can be measured in the practical scenario for its implementation in the field. In terms of the semi-active seat suspension, the smart materials, such as the MR fluid, are always applied; generally, an energized coil is controlled with varying current in order to acquire the variable damping characteristic of a MR fluid damper. In order to improve the semi-active seat suspension, the new semi-active actuators can be designed with less energy required, or even no energy required. Moreover, the traditional semi-active seat suspension can be integrated with low scale actuators which cannot be applied in an active seat suspension independently in order to improve the semi-active seat suspension's performance with less effort.

In the literature about the WBV of heavy duty vehicles, the single-DOF seat suspension cannot successfully reduce multiple-DOF vibration. For heavy duty vehicles, vibration may come from many different sources rather than uneven road surfaces, such as the operation of machine tools for digging, dumping, shovelling, and loading; the frequent rotation of vehicle body when picking and moving objects, etc.; the operators are working in a severe condition. Therefore, the seat suspension for reducing multiple-DOF vibration should be developed [8], which is rarely reported. In the space application, the 6-DOF vibration control platform configured as a Stewart Platform has been studied since 1992; however the space application project obviously has a much higher budget than the vehicle; the high cost 6-DOF vibration

control system is not practical for vehicle application. On the other hand, those researches have inspired the design of a multiple-DOF seat suspension. Firstly, it is necessary to evaluate that whether all the 6 DOFs vibration are worth to be controlled, thus, the complexity of the system structure may be reduced. Then, if the multiple-DOF vibration can be decoupled with the seat suspension structure, the controller design and implementation could be simplified.

On the whole, there are many issues worth to be studied about the seat suspensions for heavy duty vehicles; this thesis is motived to design new structures and control methods for both the single-DOF and multiple-DOF seat suspensions.

1.2 Research Objectives

The overall aim of the research is to improve the drivers' ride comfort and protect their health by developing new seat suspensions and corresponding controllers, and then validating their effectiveness.

The specific objectives of this research are as follows:

1) Developing a multiple-DOF vibration platform for the seat suspension study purpose.
2) Designing a single-DOF active seat suspension which has a concise structure and will not increase much cost from the conventional passive seat suspension. The corresponding control methods should be proposed.
3) Proposing a kind of hybrid seat suspension in order to fill the performance gap between the active seat suspension and the semi-active one (with MR damper).
4) Proposing a new semi-active seat suspension with energy regenerative capability.
5) Developing a multiple-DOF seat suspension to control the WBV.

1.3 Thesis Outline

Chapter 1 introduces the background and motivation of the work, and outlines the research objectives and the thesis structure.

Chapter 2 presents a literature review on the effect of WBV to drivers, the multiple-DOF motion platform, the existing seat suspension designs and control algorithm.

In Chapter 3, a 6-DOF motion platform is built and tested for analysing the performance of seat suspension in laboratory.

In Chapter 4, a single-DOF active seat suspension is designed and manufactured from the modification of a conventional passive seat suspension. Three kinds of controllers with variables, which can be measured in practical application, are developed and validated.

Chapter 5 presents a hybrid seat suspension with a semi-active MR damper and an active actuator.

Chapter 6 proposes an electromagnetic damper for seat suspension; two methods to continuously control its damping are presented and tested.

Chapter 7 focuses on improving the ride comfort by developing a two-layer multiple-DOF seat suspension to control WBV in multiple-DOF.

Chapter 8 concludes the main findings of this thesis and discusses the future research work.

2 LITERATURE REVIEW

2.1 Introduction

This chapter discusses the vehicle vibration which can interfere with the drivers' comfort, activities and health; in particular the operators of heavy duty vehicles suffer from severe WBV. The seat suspension is taken as the most direct way to attenuate vibration suffered by drivers. The single-DOF seat suspensions including passive, semi-active and active seat suspensions are designed and built by many researchers, but there is limited attention on multiple-DOF seat suspension. The chapter also discusses a kind of regenerative damper, which can be applied to vehicle seat as a kind of semi-active seat suspension. Further, the suspension control algorithm is discussed.

2.2 Whole Body Vibration

Drivers of heavy duty vehicles are often exposed to severe vibration transferred from rough road and operation tools, and the vibration magnitude levels for heavy duty vehicles are several times higher than those of passenger vehicles. Agricultural vehicles and industrial vehicles, in particular, need to work in harsh environment for a longer period of time. The exposure of heavy duty vehicle deriver in WBV has drawn widely attention [1-3]. Paddan and Griffin [9] have evaluated the vibration isolation efficiency of seating in 100 work

vehicles, and they concluded that, by improving the seating dynamics, the severity of WBV can be lessened. Kumar [10] studied the vibration in three axes of the seat pan of the heavy haul trucks used in overburden mining, and the vibration at those drivers' third lumbar and seventh cervical vertebral; the appreciable health hazard in drivers was confirmed, and especially, in x and y axes, the WBV exceeded the ISO standards many times. The biodynamic responses to vertical vibration are investigated by Dewangan et al. [11]; they studied the gender and eleven different anthropometric parameters on the seat-to-head vibration transmissibility responses in the vertical and fore-aft directions. Jack et al. [12] quantified the 6-DOF WBV exposure levels of skidders during routine field operating tasks; the high exposure levers of skidder operators have been associated with adverse health outcomes; in this study, it was interesting to note that the operators who reported low back pain and neck pain were not exposed in greatest accelerations, but those with lateral trunk bending and forward flexion for the greatest percentage of time. Cation et al. [13] presented comprehensive 6-DOF field data of forestry vehicle vibration; the skidder seats could amplify the WBV acceleration occurring at the seat/operator interface when compared to chassis. Coyte et al. [14] conducted a review about seated WBV analysis, technologies and modelling. Conrad et al. [15] quantified 6-DOF vibration of 5 commonly used vehicles in the steel making and metal smelting industries; during the daily operating tasks, the comfort predictions based on ISO 2631-1 was ranging from Uncomfortable to Extremely Uncomfortable. Salmoni et al. [16] presented three case studies in WBV assessment in the transportation industry, and the difficulties of the field testing are highlighted, such as limited time to learn about the work environment and poor control over the test setting. All the studies confirmed that the WBV is hazardous to drivers' health; in heavy duty vehicles, the magnitude of the WBV is high, which has not seen much improvement over the past two decades, because there is limited attention on multiple-DOF WBV control. The whole thesis

aims at attenuating vibration to drivers; in particular Chapter 7 proposes a multiple-DOF seat suspension for WBV.

2.3 Vibration Platform for Seat Suspension Development

Tires, chassis suspension and seat suspension are often used to isolate vehicle vibration, but it is generally difficult to modify the parameters of tires and chassis suspension, even many different approaches are suggested to improve upon them. The seat suspension, on the other hand, is practical to modify and optimize. Therefore, it is a simple and effective method to isolate vehicle vibration transmitted to driver body with an appropriate seat suspension. The vibration characteristics of seat suspension are the primary study mission for seat suspension design. Generally, one or two DOFs vibration platform [17] is applied to test seat suspension in translational or vertical direction. However, for heavy duty vehicles, due to their complicated operation environment, vibration may come from many different sources not only uneven road surfaces, such as the operation of machine tools for digging, dumping, shovelling, and loading; the frequent rotation of vehicle body when picking and moving objects, etc. Therefore, a multiple-DOF motion platform is needed to simulate heavy duty vehicle seat suspension vibration in the real working environment.

The multiple-DOF motion platform has been applied widely in many engineering areas [18]. There are many designs about multiple-DOF motion platform, such as Stewart platform which is a classical 6-DOF motion platform, which has a high force-to-weight ratio, high dexterity and a high accuracy of position. Research is also abundant about this platform's kinematics, dynamics, singularity, and control [19-22]. In recent years, there are many applications of 6-DOF platform in vibration related research. A 6-DOF motion platform is applied for studying whole-body vibration in the laboratory setting [23]. A study focusing on selecting seats for industry mobile machines also used a 6-DOF platform, and 6-DOF Seat Effective Amplitude Transmissibility (SEAT) values are used to evaluate the seat

performance in [24]. Frechin et al. [8] applied a 6-DOF platform to test a multiple-DOF seat system.

The single-DOF vibration platform are usually used for seat suspension evaluation, because most works about seat suspension design are concerned more about vertical vibration which has the biggest magnitude among the WBV. The 6-DOF motion platform has been applied in related study to vehicle seats, and it is an ideal vibration platform for seat suspension development, including the multiple-DOF seat suspension. In Chapter 3, a 6-DOF vibration platform is designed and built for the study of seat suspensions.

2.4 Single-DOF Seat Suspension

The single-DOF seat suspensions have been extensively studied in three types, namely, passive, semi-active, and active seat suspensions; all of them have advantages and disadvantages. The single-DOF seat suspension schematics are shown in Figure 2-1 where the passive seat suspension consists of a spring k and a damper c; the semi-active seat suspension includes a variable stiffness Δk and/or a variable damping Δc; the active seat suspension has an active actuator. The controller is required for semi-active and active seat suspension.

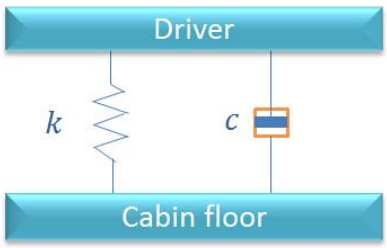

(a)

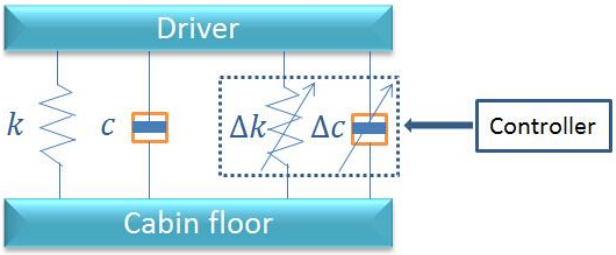

(b)

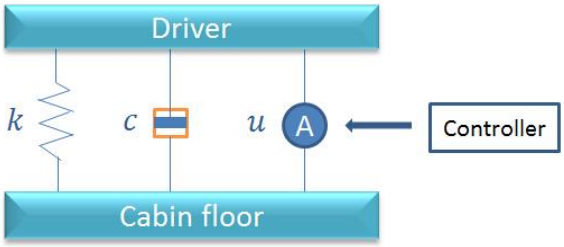

(c)

Figure 2-1. The seat suspension schematic. (a) Passive seat suspension. (b) Semi-active seat suspension. (c) Active seat suspension.

2.4.1 Passive Seat Suspension

The passive seat suspension is a fail-safe system, and is low cost with acceptable performance in certain applications. Optimisations of the spring stiffness and the damping coefficient have been studied for passive seats; but, when it is manufactured, its stiffness and damping cannot be changed. For a passive vehicle suspension, due to its passivity, most of the high frequency vibration will be isolated, and the low frequency vibration (near the resonance frequency of vehicle suspension) will be amplified, even reaching the end-stop limit. The vertical vibration of a heavy duty vehicle seat is highest in the frequency range between 2 and 4 Hz, and heavy vehicle drivers usually experience vibration around 3 Hz which increases fatigue and drowsiness [2]. Many different approaches have been proposed to overcome this problem. Wan and Schimmels [25] applied nonlinear mechanical properties in the design of a seat suspension to improve isolation at the frequency of peak

transmissibility. Le and Ahn [26] designed and fabricated vehicle seat with negative stiffness for improving its vibration isolation effectiveness under low excitation frequencies; the proposed seat suspension used tow symmetric negative stiffness structures in parallel to a positive stiffness structure.

2.4.2 Semi-active Seat Suspension

Semi-active vibration control as a trade-off vibration control strategy between passive and active control, is capable to vary its damping and/or stiffness of a mechanical system in order to address the undesired vibration with less energy consumption than active system; at the same time, it keeps the fail-safe characteristic of the passive system. For a single-DOF system, variations in damping will induce changes in the resonance magnitude; while the changes of stiffness will vary the natural frequencies of the controlled system [27-32]. The MR technology has been widely applied in semi-active actuator development for vehicle suspension [4-7]. In general, the MR fluid damper is controlled by varying the input current to its inside coil; then the magnetic field generated by the energized coil can change the viscosity of the MR fluid. Li et al. [33] designed a MR elastomer isolator for seat vibration control which is also controlled by the magnetic field of a coil with current input. Choi et al. [34] proposed a semi-active seat suspension using ER fluids for commercial vehicle; the built prototype and its sliding mode controller are validated by a hardware-in-the-loop simulation HILS. Then, Choi et al. [17] presented another semi-active seat suspension with a MR fluid damper; this cylindrical MR seat damper is applicable to commercial vehicles; Figure 2-2 shows the seat suspension. Hiemenz et al. [35] developed an MR damper in a semi-active seat suspension for helicopter. The MR elastomer isolator was applied for a semi-active variable stiffness seat suspension by Du et al. [36]; a sub-optimal H_∞ controller was designed for the isolator. An MR elastomer-based isolator is designed for the horizontal vibration reduction of a driver seat [37]. Sun et al. [38] developed a rotary MR damper and installed on

a seat suspension. The performance and energy gaps between the semi-active seat suspension and the active seat one is big; in Chapter 5, a seat suspension integrated semi-active and active control is proposed to address this. Further, in Chapter 6, the electromagnetic seat suspension is designed for semi-active vibration control in order to achieve energy saving control.

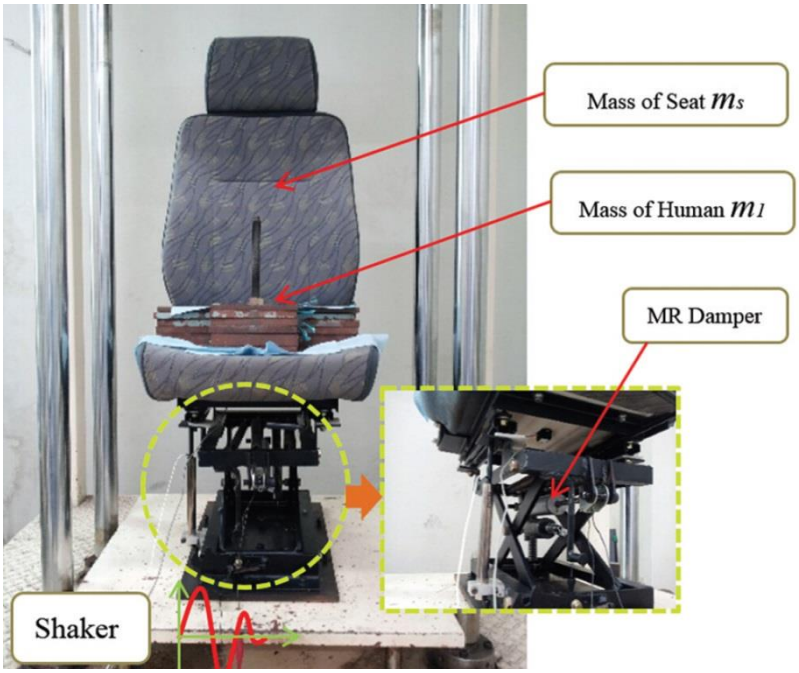

Figure 2-2. MR seat suspension with linear damper [39].

2.4.3 Active seat suspension

The active suspension has attracted more and more attention in recent years because it is widely accepted that the active suspension is the most effective way to improve ride comfort. Gan et al. [40] presented an active seat suspension with two electromagnetic linear actuators (see Figure 2-3) in order to reduce the vibration level transmitted to the occupant under low frequency periodic excitation. Maciejewski et al. [41] proposed an active seat suspension system comprised of a hydraulic absorber and a controlled air-spring; in the 0.5-4 Hz frequency range, the high system robustness of the actively controlled suspension was achieved, and the passive and active seat suspensions showed similar behaviour at higher

frequencies. Kawana and Shimogo [42] used an electric servomotor with a ball screw mechanism as the active seat suspension actuator; this system measured accelerations of the hip point, the seat frame and cab floor, and integrated them to obtain the state variables. Le et al. [43] proposed an active pneumatic vibration isolation system using negative stiffness structures for low excitation frequencies; in order to address the time-varying and nonlinear behaviour of the proposed system, an adaptive intelligent back stepping controller is designed. Perisse and Jezequel [44, 45] developed a seat suspension system with a rotary motor and a rack/pinion device to transform torque into vertical force. In Chapter 4, the torque of a rotary motor is amplified via a gear reducer and exerted directly on the scissor structure center of a seat suspension. This means that a low rated power motor can be used and this will decrease the cost of an active seat suspension greatly. The proposed active seat suspension prototype is also easily fabricated through the use of a commercial passive seat suspension.

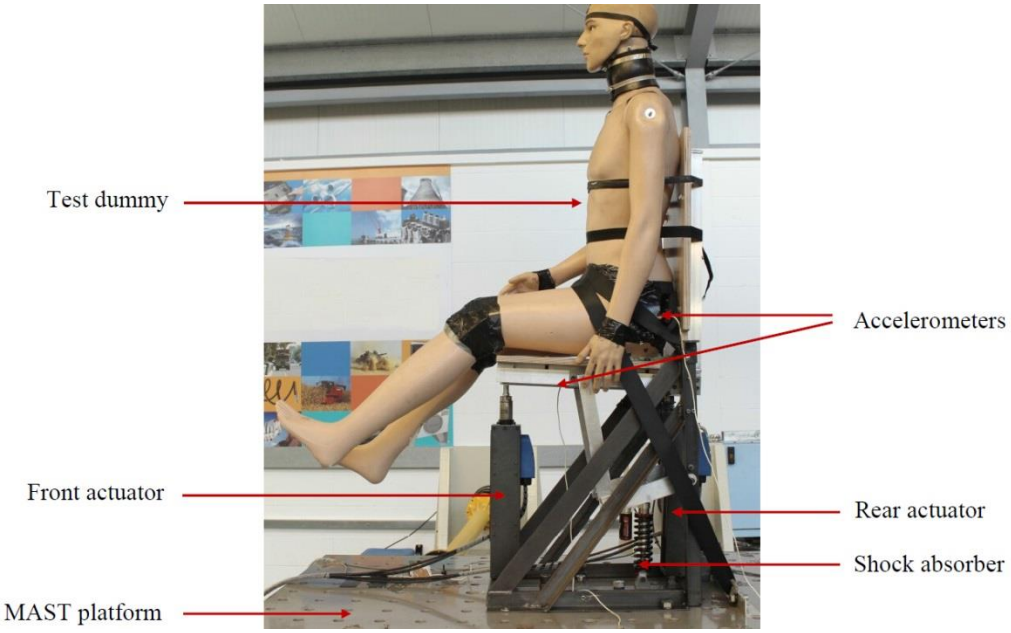

Figure 2-3. Active seat suspension with linear actuators [40].

2.5 Electromagnetic Suspension

The electromagnetic vehicle suspensions, which can harvest energy from the road vibration, are being studied recently [1, 46-49]. The general vehicle suspensions dissipate the vibration energy into heat wastes, while the regenerative suspension will transform the kinetic energy into electricity. Two kinds of motors or generators are applied in this kind of suspensions, namely the rotary one and the linear one. Generally, the regenerative vehicle suspension with rotary motor needs a mechanism, such as rack and pinion, to transfer the linear suspension movement to rotary movement [50, 51]. On the contrary, the linear generator can directly harvest the vibration energy [52-54]; but, with a given space, the rotary generator is capable of generating more power [55]. A regenerative mechatronic damper is proposed for vehicular applications [1]; it applied a three-phase full-bridge boost converter which has been widely applied in motor applications to control the current [56]. Zhang et al. [57] presented an electro-hydraulic semi-active damper (see Figure 2-4) to harvest the suspension kinetic energy; this pumping regenerative damper can transfer the reciprocating suspension vibration into unidirectional rotation of the generator. It is believed that the regeneration suspensions should be combined with the energy harvesting and vibration control for their promising prospect [58]. Though the vibration control of suspension with only regenerative damper is rarely studied, some designs have integrated the regenerative damper with other isolators. Shi et al. [59] proposed a semi-active energy regenerative suspension and studied the ride comfort improvement with experiment; an additional adjustable shock absorber is applied in this work. For providing enough damping force, the magnetorheological (MR) and electrorheological (ER) fluid based regenerative vehicle suspensions are proposed [60, 61]. A self-powered and sensing MR damper based vibration control system is proposed [62]; the control coil of the MR damper was powered directly from the generator. Because the seat suspension requires less damping force than vehicle suspension, with a careful design, the

back electromagnetic (BEM) force will be enough for vibration isolation [63]. The active variable geometry suspension has been extensively studied in [64-66], with electromagnetic actuators. In Chapter 6, two regenerative seat suspension systems are designed and tested; both systems can be semi-active controlled for vibration isolation.

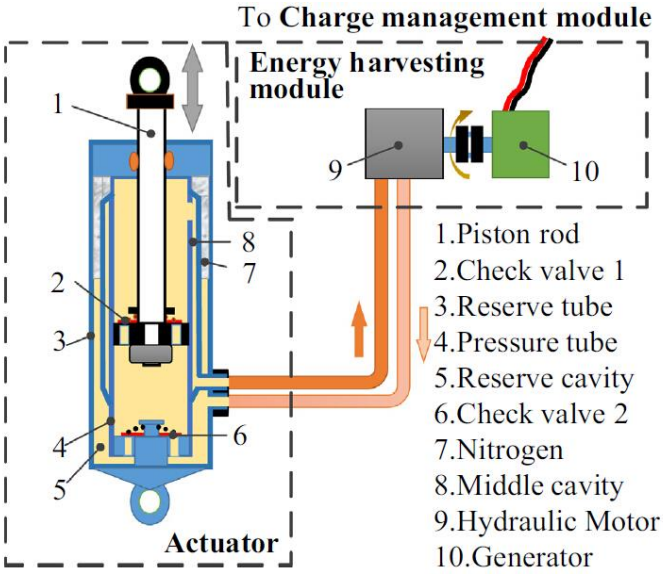

Figure 2-4. The electro-hydraulic semi-active damper [57].

2.6 Multiple-DOF Vibration Control

As can be seen above, the single-DOF seat suspension has been widely studied to improve drivers' ride comfort and protect their health; while the multiple-DOF vibration control has been rarely studied.

2.6.1 Non-seat Suspension

In space application, for telescopes, imaging cameras and other sensitive optical instruments, the 6-DOF active vibration isolation technology has been developed. Parallel manipulator has been applied in M-DOF vibration isolation since 1992 [67, 68] for space application. Geng et al. [67] proposed and built an multiple-DOF vibration system with magnetostrictive material Terfonol-D. The peak to peak strokes of its actuators were 0.01 inches (0.254 mm). Total 18 input signals were used, namely, 6 top accelerometers, 6 bottom accelerometers and 6 force

transducers. They proposed a cubic configuration of parallel manipulator which was applied by most following researchers. The cubic configuration had the advantages of uniformity in control and stiffness in all directions, simple kinematics and dynamic analysis, and simple mechanical design. Spanos et al. [69] presented an M-DOF vibration isolation system with electromagnetic voice coil actuator in parallel with a soft spring. The actuator stroke is 0.254 mm, and it was improved to 1.27 mm later [70]. This work also used 18 sensors and cubic configuration. Following the two great work, several works presented. Zhang et al. [71] built an M-DOF vibration isolation system which used giant magnetostrictive actuators with TbDyFe rods. Although the actuator stroke was only 0.1 mm, its output force can be up to 1500 N. Haugen and Campbell [72] presented their work in which six voice coil actuators were applied; this system named HT/UW had large actuator stroke (± 5 mm for precision pointing) and a number of sensors (each of the six struts has a three-axis load cell, a base and a payload geophone and a LVDT). Preumonta et al. [73] reported a six-axis vibration isolator for space applications which used six voice coil actuators with ± 0.7 mm stroke and 2.7 N force output. Chi et at. [74] presented the design and experimental study of a voice coil motor (VCM)-based Stewart platform used for active vibration isolation. Except from the researches for space application, there are some other M-DOF vibration isolation studies. Cui et al. [75] proposed a large stroke vibration isolation hexapod platform with hydraulic actuator for vehicular optical equipment. This isolator was equipped with 6 hydraulic cylinder, six LVDT displacement sensors, and 12 accelerometers. The high cost prevents it from being used for vehicle seat. Zhu et al. [76] presented a novel 6-DOF maglev isolation system which applies quasi-zero stiffness levitation principle to get low resonance frequency. In Table 2-1, the main organisations who have presented work about 6-DOF vibration control are shown with their applied technology. The voice coil actuator is the most popular one used for vibration control. In the existing 6-DOF vibration control systems, most of them are

designed for space application which obviously has much higher budget than vehicle application. Thus, the innovative structure should be proposed for multiple-DOF seat suspension, which should be uncomplicated, and controllability of 6 DOFs may not be necessary for seat vibration considering that the vibration in certain DOFs may have small magnitude or have few influence on human bodies.

Table 2-1. Multiple-DOF vibration control research.

	Magnetostrictive material	Voice coil actuator	Hydraulic actuator	Magnetic suspension
1992	Intelligent Automation, Inc. (NASA) [67, 68]			
1995		Jet Propulsion Laboratory. (NASA) [69]		
1998		Jet Propulsion Laboratory. (NASA) [70]		
2004	Beijing University of Aeronautics and Astronautics [71]	University of Washington [72]		
2007		ULB, Belgium [73]		
2011			Beijing University of Aeronautics and Astronautics [75]	
2015		Harbin Institute of Technology [74]		Saitama University, Japan [76]

2.6.2 Seat Suspension

Though the WBV has drawn researchers' attention, the multiple-DOF vibration control of seat suspension has been rarely studied. A six-DOF active seat suspension with six actuators

designed as Stewart Platform has been applied for a patent [77], which is a similar design with the 6-DOF vibration control platform used in space application; its practicality needs to be validated. Kieneke et al. [12] presented an active seat suspension with two-DOFs for military vehicles in order to control the vertical and lateral vibration; the effectiveness of the proposed seat suspension has been validated in the experiments. A lateral seat suspension for off-road vehicles is designed and tested in [13]; the investigations in laboratory and field testing have been implemented in order to demonstrate the potential in improving ride. Frechin et al. [8] developed a four-DOF seat (see Figure 2-5) which actually isolates from vertical vibrations and compensates the rest of the inclinations and translational accelerations generated during vehicle motion. This seat was based on a four-DOF motion system and the seat DOF's were: roll, pitch, yaw, and heave. Klooster [78] designed a multiple-DOF seat suspension with 3 parallel hydraulic actuators for the independent control of the vertical, horizontal and pitch angle directions; the proposed seat suspension was evaluated in each DOF to understand the potential of the seat to isolate harmful vibration. Actually, the sensitiveness of human body to the six DOFs of vibration is different, and with certain DOF vibration, it contains many frequencies within which some have limited effect on operators' health and ride comfort. Thus, in Chapter 7, a two layers multiple-DOF seat suspension is designed by analysing the practical application.

Figure 2-5. Seat suspension with 4-DOF spherical motion system [8].

2.7 Control Algorithm

There are many reputable control strategies for suspensions, e.g., H_∞ control [66, 79-84], linear quadratic Gaussian (LQG) [85, 86], adaptive control [87] and fuzzy control [88, 89]. A two-step methodology is proposed to design the static output-feedback controllers for vehicle suspensions in [80]. The finite frequency H_∞ controller for active suspensions has been proposed in [81, 82]. Li et al. [83] present a work about output-feedback-based control strategy for vehicle suspension control with control delay. An adaptive sliding mode control algorithm for nonlinear suspension is proposed in [87]. Du et al. [90] propose an observer based H_∞ controller with a TS fuzzy model to solve the non-linear problem of a semi-active seat. Maciejewski [91] proposes an active vibration control strategy based on a primary controller and actuator's reverse dynamics. Bououden et al. [92] propose a robust predictive control design for nonlinear active suspension systems via TS fuzzy approach. However, most of the previous researches for vehicle or seat suspension control system do not include the acceleration feedback into controller. Although high frequency noises will be introduced when acceleration signal is measured, with appropriate algorithms, a controller could be

designed to be more effective to suppress vibration with acceleration measurement. It is also noted that TS fuzzy approach has been applied in the suspension control; however, very few works consider the friction issue, which is unavoidable in all the practical engineering applications, especially, in the seat suspension, because the friction can greatly affect the seat suspension dynamics.

Disturbance observer has been extensively studied and proven to be able to improve the controller's performance effectively. Deshpande et al. [93] propose a novel nonlinear disturbance compensator for active suspension system. The disturbance observer for sliding mode control has been studied in many papers [94, 95]. Kim et al. present a disturbance observer for estimating higher order disturbances [96]. Pan et al. propose tracking control method for nonlinear suspension system with disturbance compensation [97]. Saturation is another important issue in practical applications that needs to be paid attention [98]. In the literature, several methods have been proposed to handle the effects of saturation [99]. Among them, the anti-windup approach is proven to be an effective way to deal with actuator saturation [100], and it is extensively studied in [101, 102].

Sliding mode control is an effective way to handle nonlinear uncertainties within a system and has been applied in suspension control [103]. Choi and Han [104] proposed a sliding mode controller in which a state observer is designed for semi-active seat suspension. Li et al. [87] proposed a TS fuzzy approach based adaptive sliding mode control for a nonlinear active suspension. Disturbance observer design with sliding mode control to improve the controller's performance has been applied in much research [105, 106]. The terminal sliding mode (TSM) control offers some superior properties, such as, fast finite time convergence when compared with conventional sliding mode control [107]. Non-singular TSM control has also been proposed [108]. Generally speaking, the active seat suspension control is not a typical tracking problem, because the seat acceleration and suspension deflection do not need

to be zero due to the low levels of vibration which will not affect the ride comfort and can help the driver stay awake. The practical application of sliding mode control in active seat control is an area which requires further study.

2.8 Conclusions

This literature review showed that the operators of heavy duty vehicles, such as construction, forestry, agricultural and mining vehicles, are exposed to high levels of WBV which will pose health risks to them and deteriorate their ride comfort. Efforts have been done by many researchers to develop high performance vehicle seat suspensions to improve ride condition. Single-DOF seat suspensions with semi-active or active control have been extensively studied; while the multiple-DOF seat suspension for WBV control is rarely investigated. In addition, for improving the development of single-DOF seat suspension, the cost and energy consumption are principal issues in the active seat suspension design; the higher performance and lower energy consumption should be the aims of the semi-active seat suspension study.

This chapter also discussed the electromagnetic damper which has been applied in vehicle suspension. This kind of regenerative suspension has the potential in semi-active vibration control with low energy cost, and it can be extended to the study of semi-active seat suspension.

The literature on suspension control revealed that most of the vibration control algorithms for vehicle suspension have ignored the effect of suspension friction; while due to much less weight on seat suspension than vehicle suspension, the friction plays an important role in seat suspension's dynamic. Thus, in the algorithm development of seat suspension, the friction should be considered.

3 6-DOF VIBRATION PLATFORM

3.1 Introduction

It is important to validate the effectiveness of a seat suspension and its controller, when a new seat suspension or a controller is proposed. Generally, the field test is the most convincing way; however, it will take a long time to prepare for the test, and it is difficult to control the test condition in the field. Thus, the vibration platform has been widely applied in the laboratory to evaluate the seat suspension prototype. Moreover, for evaluating the WBV of a seat suspension, the 6-DOF motion is required to simulate the real working environment.

In this chapter, the processes of developing a 6-DOF vibration platform for the seat suspension design are presented; the vibration platform is tested with different vibrations, and it is measured with a laser displacement sensor and an IMU sensor for evaluating its performance.

3.2 6-DOF Vibration Platform System

The 6-DOF vibration platform has been applied in the laboratory; generally, the hydraulic actuators or electrical cylinders are used. With the same actuator volume, the hydraulic one can generate a higher magnitude of force, but its system is complicated and hard to maintain; thus, it is usually applied for the airplane simulator or the vehicle simulator which needs to

excite heavy loads. For the research regarding seat suspension, the maximum load is less than 200 Kg (including the seat and driver), so the electrical cylinder which is easy to control and maintain is selected in this work as the actuator.

The 6-DOF motion platform consists of a fixed base platform, a movable top platform and six extendable legs. The legs consists of six 750 W electrical cylinders; their strokes are 150 mm, and the maximum force output of one electrical cylinder is 2600 N with a maximum velocity 200 mm/s. The motion of the electrical cylinder can be accurately controlled by their drives. According to the dimension of the electrical cylinder, the motion platform is designed with the PTC Creo (a design software) as shown in Figure 3-1. Square steel tubes are used to fabricate the top and base platforms which are regular hexagons with the lengths of sides 350mm and 500mm, respectively; then the cubic configuration can be achieved to make the platform has a good motion capability in 6-DOF [67]. The six electrical cylinders connect the top and base platform with spherical joints.

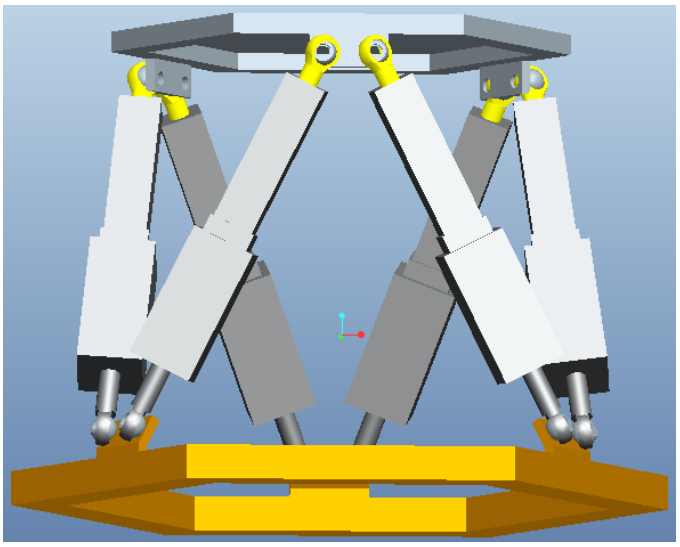

Figure 3-1. The 6-DOF vibration platform designed with PTC Creo.

The 6-DOF motion platform system is shown in Figure 3-2. A computer is applied to interact with users who can import the desired multiple-DOF vibration profile; in the computer,

according to the vibration profile, the desired motion of each electrical cylinder is calculated by the platform's inverse kinematic model which will be introduced in the next section. Then, the desired motions are sent to an NI CompactRio 9074 which is a high performance real-time controller; two digital output modules NI 9401 are mounted on the controller in order to send the desired motion of each electrical cylinder to the corresponding servo motor drives. Then, the servo motor drives can accurately control the electrical cylinders moving according to the command from the controller.

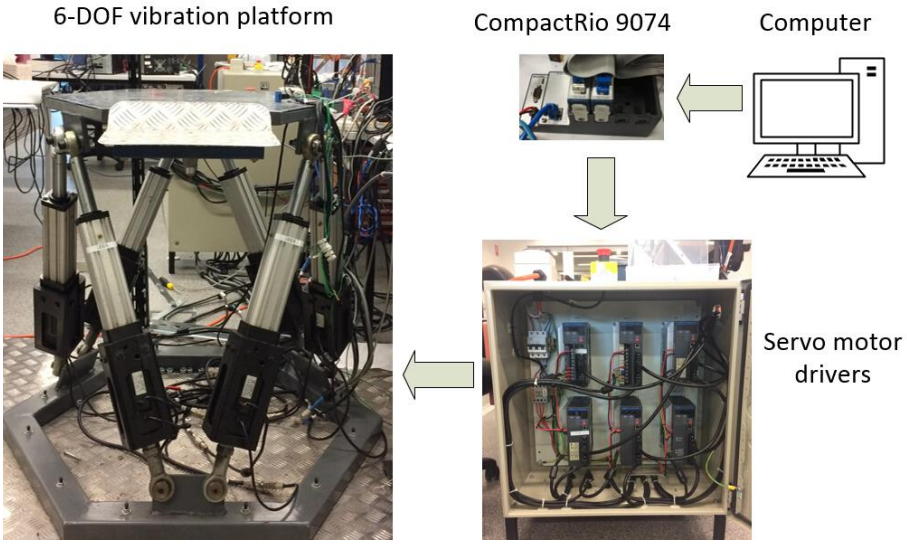

Figure 3-2. The 6-DOF vibration platform system.

3.3 Inverse Kinematic

The performance of the motion platform, which is designed for the simulation of vehicle seat suspension vibration, is determined by the accuracy of the motion of electrical cylinders. The inverse kinematics model is applied to solve this, that is, using the given position and orientation of the top platform to get the desired lengths of six legs which can be achieved by controlling electrical cylinders with extending or contracting movement.

The single leg schematic view is shown in Figure 3-3. The inertial frame O is fixed at the centre of the base platform with a vertical z-axis. Another coordinate system P, which is a

movable platform frame, is fixed on the centre of upper surface of the top platform with a z-axis perpendicular to the surface of top platform. The movement of frame P simulates the motion of heavy duty vehicle cab floor where seat suspension is attached. The pose of moving platform frame P can be defined as:

$$\mathbf{q} = [\mathrm{x}, \quad \mathrm{y}, \quad \mathrm{z}, \quad \alpha, \quad \beta, \quad \gamma]^{\mathrm{T}} \tag{3-1}$$

where $\mathbf{t} = [\mathrm{x} \quad \mathrm{y} \quad \mathrm{z}]^{\mathrm{T}}$ is a vector of frame O to frame P which means the translation of top platform, and α, β, γ are the Euler angles around the $\mathrm{x}, \mathrm{y}, \mathrm{z}$ axes which represents the platform rotation. The rotation matrix can be described as:

$$\mathbf{R} = \begin{bmatrix} \cos\beta\cos\gamma & -\cos\beta\sin\gamma & \sin\beta \\ \cos\gamma\sin\beta\sin\alpha + \cos\alpha\sin\gamma & \cos\alpha\cos\gamma - \sin\alpha\sin\beta\sin\gamma & -\sin\alpha\cos\beta \\ \sin\alpha\sin\gamma - \cos\alpha\cos\gamma\sin\beta & \cos\gamma\sin\alpha + \cos\alpha\sin\beta\sin\gamma & \cos\alpha\cos\beta \end{bmatrix} \tag{3-2}$$

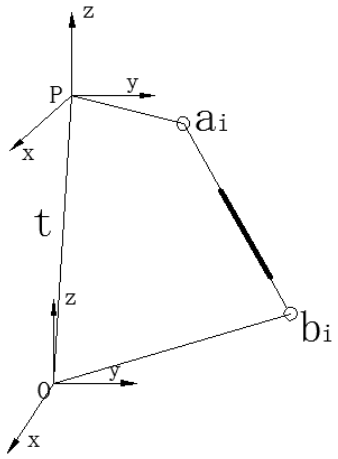

Figure 3-3. Single leg schematic.

According to the rotation matrix **R**, the *i*th leg vector $\mathbf{l_i}$ in terms of frame O is given by:

$$\mathbf{l_i} = \mathbf{t} + \mathbf{R}\mathbf{a_i^p} - \mathbf{b_i} \qquad \mathrm{i} = 1, 2, \ldots, 6 \tag{3-3}$$

where $\mathbf{a_i^p}$ is the position vector of the ith connecting joint of the top platform and the electrical cylinder in the movable frame P, and $\mathbf{b_i}$ is the position vector of the ith connecting joint of the base platform and the electrical cylinder in the fixed reference frame O. So the ith leg length is given by:

$$L_i = \sqrt{(t + Ra_i^p - b_i)^T (t + Ra_i^p - b_i)} \quad (3\text{-}4)$$

L_i is the ith leg length which can make the top platform reach the expected pose **q**. The displacement that each electrical cylinder should extend is described as:

$$D_i = L_i - L_o \quad (3\text{-}5)$$

Where L_o is the leg length when the electrical cylinders are in the initial position.

3.4 Test

The performance of the platform has been evaluated. As shown in Figure 3-4, a laser displacement sensor (Micro Epsilon ILD1302-100) is set under the top platform in order to measure the real displacement of the top platform along z axis of the fixed frame O; a 6-DOF IMU (XSENS) which can output the three estimated Euler angles is mounted on the top platform.

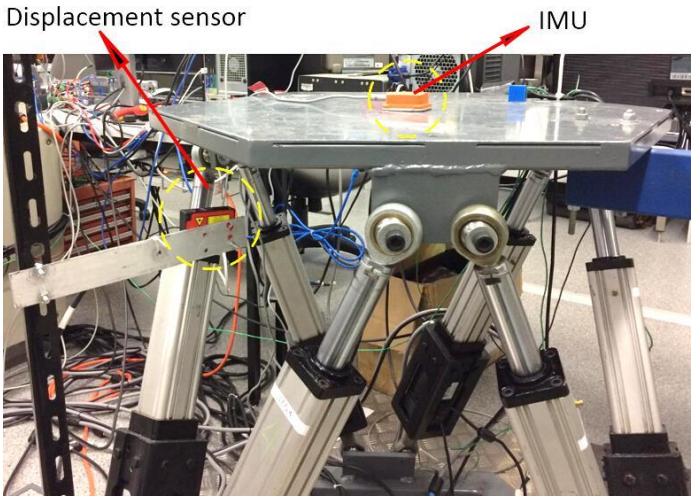

Figure 3-4. Platform test.

The motion accuracy along z axis of frame O has been tested firstly. Figure 3-5 shows the displacement of the top platform when it simulates a bump excitation, and in Figure 3-6, a random vertical vibration has been implemented; both the results show that the desired

displacement and measured displacement are matched very well, which indicates that the accuracy of the motion platform is high.

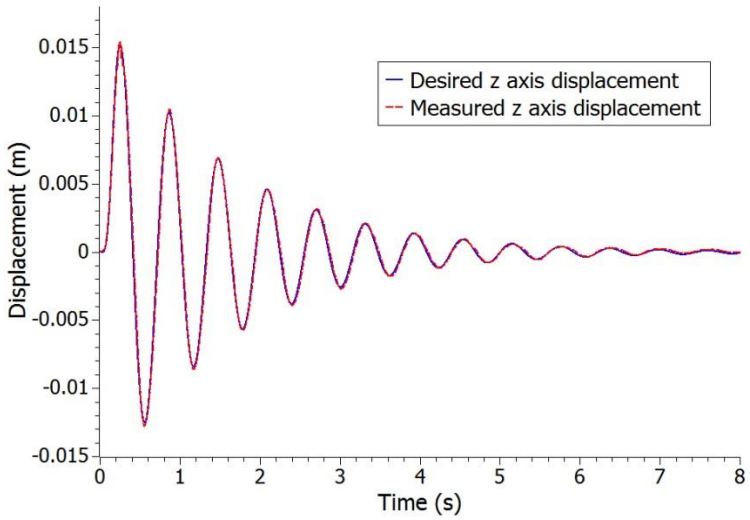

Figure 3-5. Bump excitation along z axis.

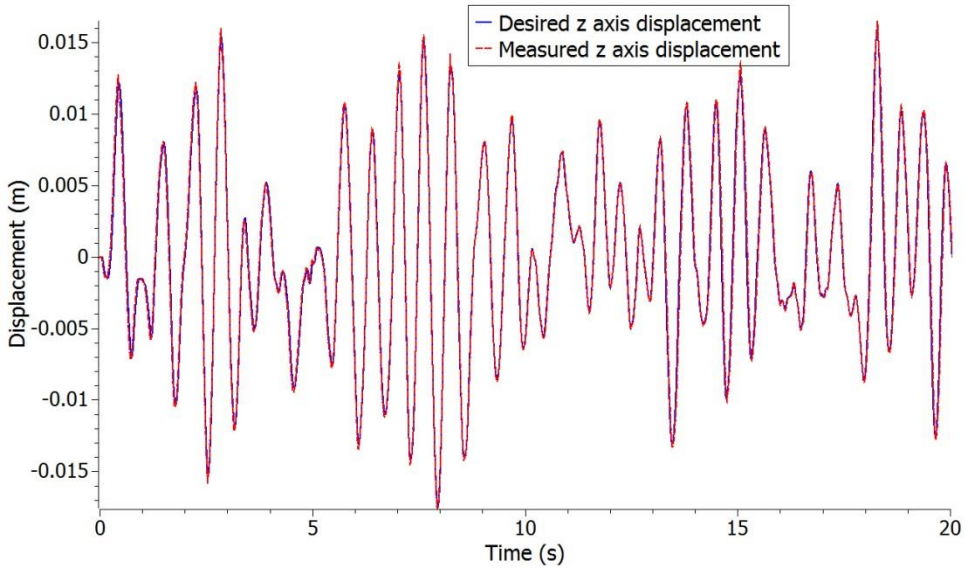

Figure 3-6. Random vibration along z axis.

Then, with the 4° amplitude and 0.1 Hz frequency, both sinusoidal roll and pitch rotations are implemented, respectively. The output data from IMU can match the desired angle (see Figure 3-7 and 3-8); the results illustrate that the 6-DOF platform can accurately simulate multiple-DOF rotational vibration.

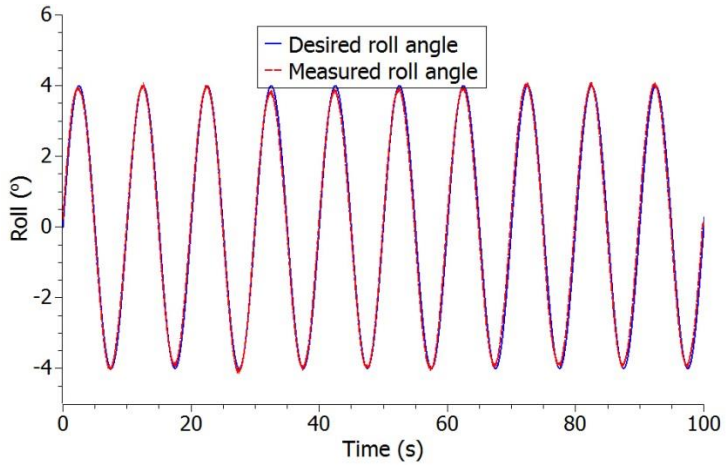

Figure 3-7. Roll test.

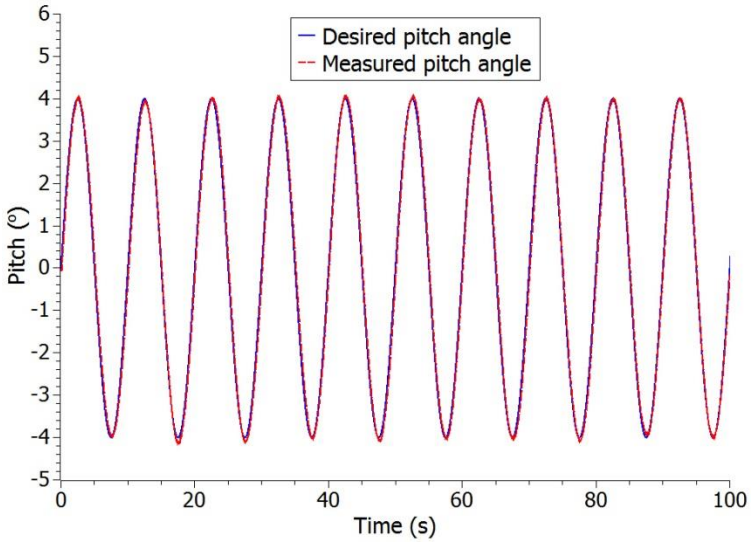

Figure 3-8. Pitch test.

3.5 Conclusions

The vibration platform is a fundamental setup in vehicle seat suspension study. This chapter has presented the development of a 6-DOF vibration platform. Benefitting from the accurate motion control of electrical cylinders with servo drives, the complicated tracking control has been done; we just need to get the desired motion of each leg, then the expected multiple-DOF motion can be generated. The application of the inverse kinematic model instead of the dynamic model has greatly simplified the control of a 6-DOF vibration platform. The test

results illustrated that the 6-DOF vibration platform can generate desired multiple-DOF vibration for seat suspension analysis in the following works.

4 SINGLE-DOF ACTIVE SEAT SUSPENSION

4.1 Introduction

This chapter presents the design, fabrication and test of an innovative active seat suspension system for heavy duty vehicles. Rather than using conventional linear actuators, such as hydraulic cylinders or linear motors, which need to be well maintained and are always expensive when high force outputs are required, the proposed seat suspension system directly applies a rotary motor in order to provide the required active actuation, without changing the basic structure of the existing off-the-shelf seat suspension; the rotary actuator is installed in the centre of the seat's scissors structure, thus, no additional mechanism is required to transform the rotary motion to a linear one. A gear reducer is also applied to amplify the output torque of the rotary motor so that a high output torque can be achieved using a low rated power motor.

The contributions of this chapter also include proposing a H_∞ controller with friction compensation for this seat suspension where the friction is estimated and compensated based on the seat acceleration measurement. The controller applies the practically measurable variables as feedback, which is suitable for application. Further, a TS fuzzy control method is

applied to enhance the controller's performance by considering the variation of the driver's weight. A disturbance observer and state observer based terminal sliding mode controller with acceleration data fusion is proposed; in practical applications, the driver's body and the friction forces are difficult to be accurately described with a mathematical model; for this reason, the proposed controller is designed based on a simplified model from a 6-DOF seat-driver model with nonlinear friction. The proposed controllers are validated with experiments which shows their effectiveness.

4.2 Active Seat Suspension System

In this section, the design of a low cost single-DOF seat suspension has been presented, and it friction model is identified.

4.2.1 Seat suspension design

The active seat suspension is designed with a low cost actuator and a concise structure (see Figure 4-1). The high cost of active actuators is one of the reasons why active suspension has not been widely used in industrial application. The rotary motor has a lower price than other linear actuators, such as the linear motor, the electrical cylinder and the hydraulic actuator, with the same rated power; it is also easier to install and control. In addition, a rotary motor's price is proportional to its rated power; the rated rotary speed of a motor is much higher than the maximum actuator's rotary speed of a seat suspension, thus, an applied rotary motor's price is also proportional to its maximum torque output. In order to reduce costs further, the gear reducer is applied to amplify the motor's torque output; it means that a lower price motor can be utilised for active vibration control. The scissors structures with rolling wheels are widely applied in seat suspension design. In this active seat suspension, the actuator module consists of one rotary motor and one gear reducer that is installed in the scissors structure's rotary centre to drive the suspension's vertical movement. A cam mechanism with

the spring is applied in the suspension; when the suspension is loaded, the cam, which is fixed with one of the scissor bars, can push the follower to move along its guide, and then the spring is extended to support the external load. The passive spring force and active motor torque are exerted on the seat in parallel.

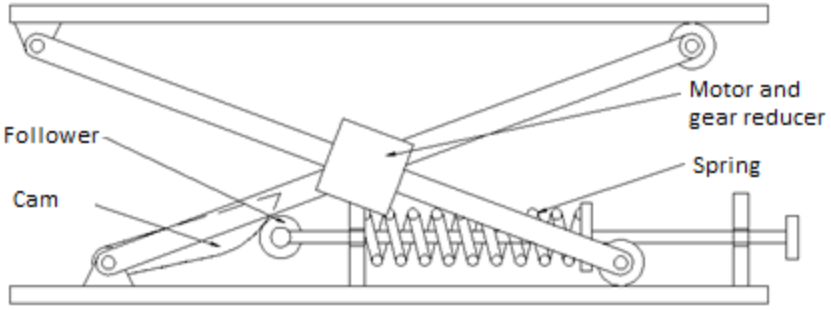

Figure 4-1. Schematic of active seat suspension

This active seat suspension prototype is a modification of a normal commercial vehicle seat (GARPEN GSSC7). Figure 4-2 shows the active seat suspension prototype. To balance the suspension system, two sets of actuator modules are installed on the seat's two sides. Two 400 W Panasonic servo motors (MSMJ042G1U) are used; their torque outputs can be controlled by sending analogue signals to their servo motor drives (MBDKT2510CA1). The motors' rated torque outputs are 1.3 Nm and the torques are amplified by two gear reducers with a ratio of 20:1, and its backlash is less than 0.1°. For each actuator module, the maximum torque output can reach 26 Nm.

Most seat suspension systems have passive dampers in order to suppress the resonance vibration, but this active seat suspension has good passive performance without a damper. The use of the two gear reducers makes this active suspension's internal friction force larger than that in normal seat suspensions and this enables the vibration energy to dissipate. At the same time, the spring stiffness is carefully chosen to ensure that its resonance frequency is

around 2 Hz. Then the seat suspension can have a good passive performance from 4-8 Hz which is the most sensitive vibration frequency of the human body.

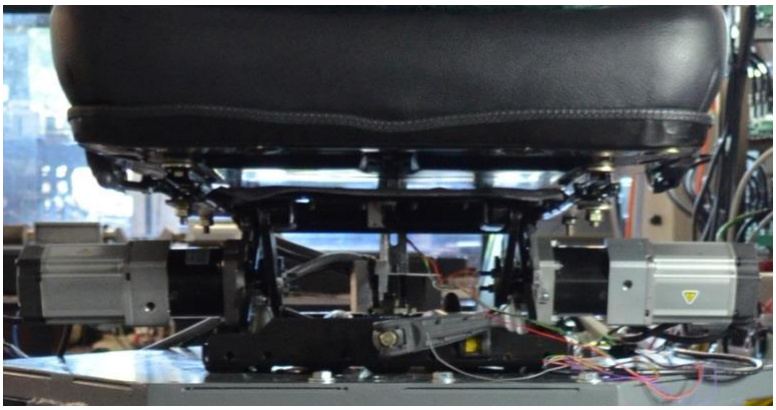

Figure 4-2. Front view of active seat suspension prototype.

4.2.2 Transformation of force and torque

This active seat suspension is designed to control vertical vibration, thus, an active controller is developed which can output the desired vertical force. As only the rotary motors' torque outputs can be controlled, the designed vertical force needs to be equivalent to a torque based on the seat's geometric structure. Figure 4-3 shows the equivalent relationship between the torque exerted on the scissors structure and the force to the seat. For one bar of the scissors structure, the torque can be defined as:

$$T = \frac{F}{2}W = \frac{F}{2}\sqrt{L^2 - H^2} \tag{4-1}$$

where L is the length of the scissors structure bar, H is the height of the suspension. L is a constant 0.287 m, and H can be measured in real-time.

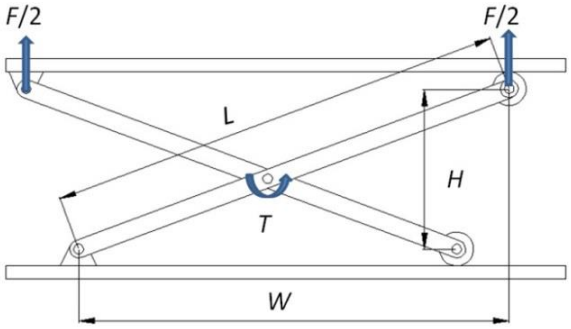

Figure 4-3. Transformation of force and torque.

4.2.3 Friction model identification

In order to reduce the requirement of motors, the gear reducers which can amplify the output torque of motors are applied in the active seat suspension prototype. At the same time, the additional friction is introduced into the active seat suspension system; the two gear reducers can work as friction dampers to dissipate vibration energy. For implementing the control algorithm in simulations, the friction model parameters are identified in this section. The MTS (a company provides test and measurement solutions) test system with measured force and displacement output was utilised to test the active seat suspension prototype in the laboratory as shown in Figure 4-4. The non-energised active seat suspension was exerted with movement of 5 mm and 10 mm at frequency of 0.5 Hz, respectively. When the spring force is removed from the measured force, the inner friction is obtained as shown in Figure 4-5 which shows that the friction direction will change based on the variation of suspension relative deflection rate, and it will saturate around 80 N.

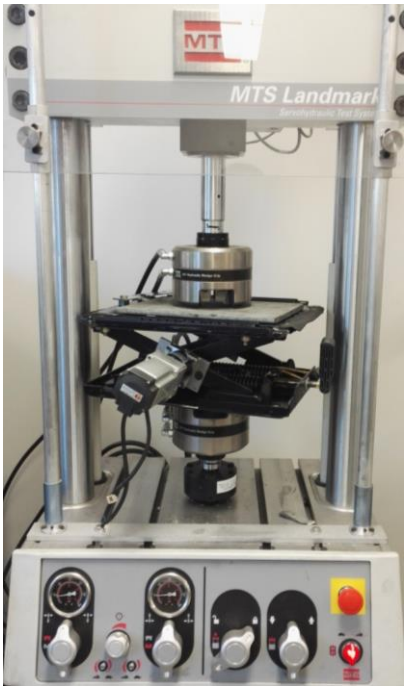

Figure 4-4. MTS test.

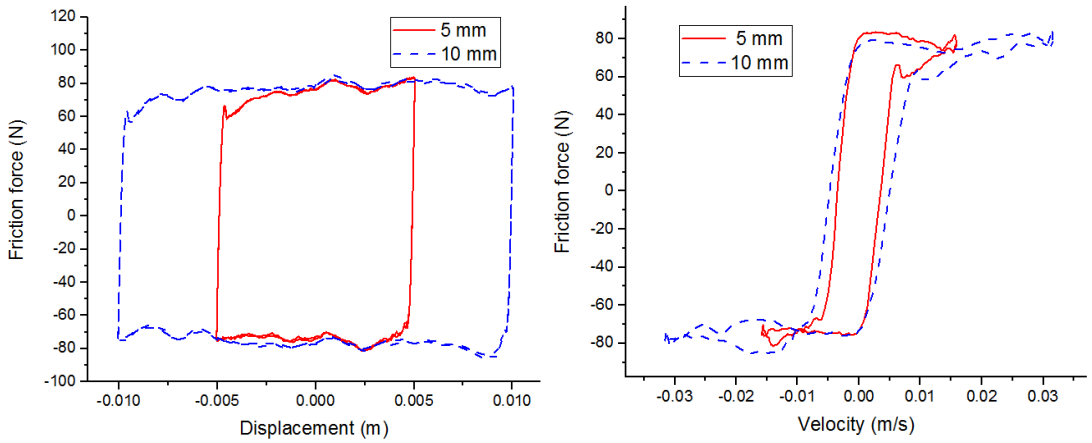

Figure 4-5. Displacement-force and velocity-force plot of friction.

To date, many models have been proposed to describe the friction. A phenomenological model based on Bouc-Wen hysteresis model is applied in the simulation to validate the proposed control algorithm. The friction can be defined as:

$$f_r = \alpha z_d \tag{4-2}$$

$$\dot{z_d} = -\gamma_d |v| z_d |z_d| - \beta_d v |z_d|^2 + A_d v \tag{4-3}$$

where v is the suspension deflection rate. The friction model parameters are identified as $\alpha = 3.0983 \times 10^5$ N/m, $\gamma_d = 2.1617 \times 10^8$ m^{-2}, $\beta_d = -9.8889 \times 10^7$ m^{-2} and $A_d = 6.9321$. The simulated friction is compared with measured friction in Figure 4-6 which shows the applied friction model can describe the actual friction in active seat suspension.

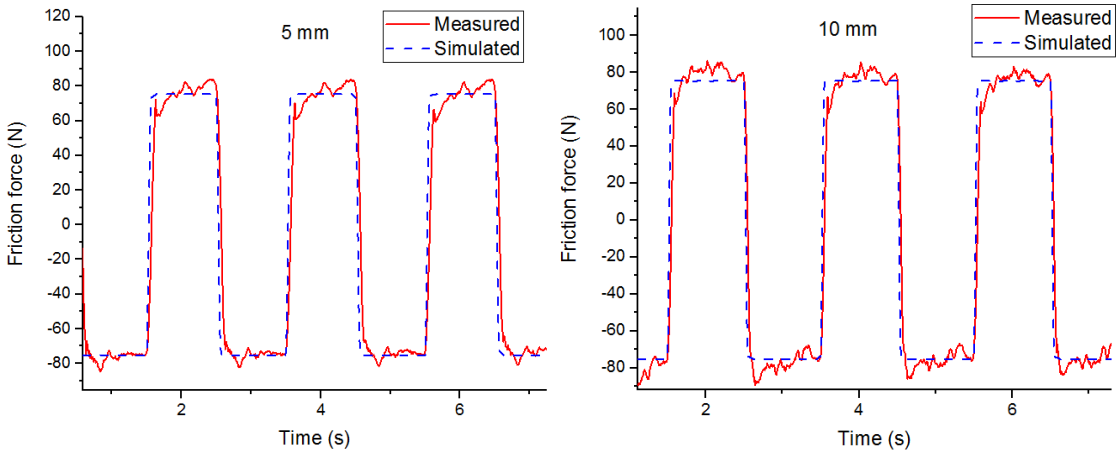

Figure 4-6. Friction model identification.

4.3 Experimental System for Vibration Control

The schematic diagram of the experimental setup is shown in Figure 4-7. The 6-DOF vibration platform is applied to generate the vertical vibration excitation. The displacement sensor 1 (Keyence LB-11) is used to measure the seat's absolute displacement; the displacement sensor 2 (Micro Epsilon ILD1302-100) is installed on the base of seat suspension to measure the suspension relative displacement; the accelerometer 1 (ADXL203EB) is used to measure seat acceleration; and accelerometer 2 (ADXL203EB) is used to measure vibration excitation acceleration. Those sensors are used as the controller feedback or to evaluate the performance of the active seat suspension system. One NI CompactRio 9074 with one NI 9205 and one NI 9264 module are applied as the active seat suspension controller. The measurement and control frequency is set as 500 Hz. The measurement data from four sensors are acquired by this controller and then the desired motor torque output signals are sent out to two actuator motors' drives. PC 1 is applied to log

experimental data. Figure 4-8 and 4-9 show the installation of the displacement sensors and the. Figure 4-10 shows the real experimental setup with the active seat suspension and the 6-DOF vibration platform.

Three different types of experiments were carried out. The uncontrolled experiment applies the active seat suspension without a controller; the active experiment is done using the proposed active seat suspension and control algorithms. A conventional passive seat suspension (GARPEN GSSC7), from which the proposed active seat suspension prototype was developed, was also tested for comparison in what we have called a conventional passive experiment.

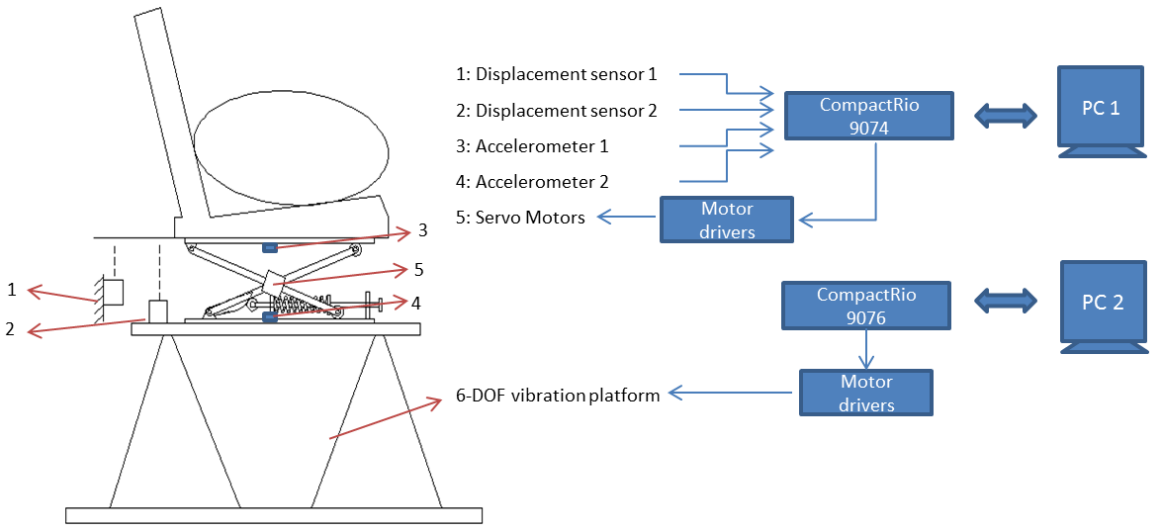

Figure 4-7. Schematic diagram of the experimental setup.

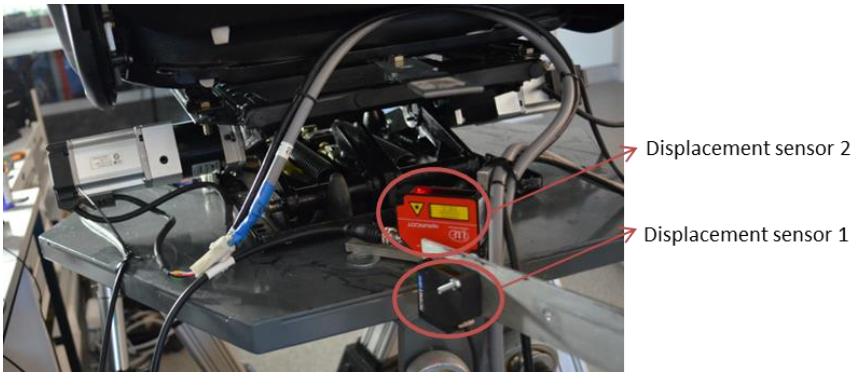

Figure 4-8. Displacement sensors installation.

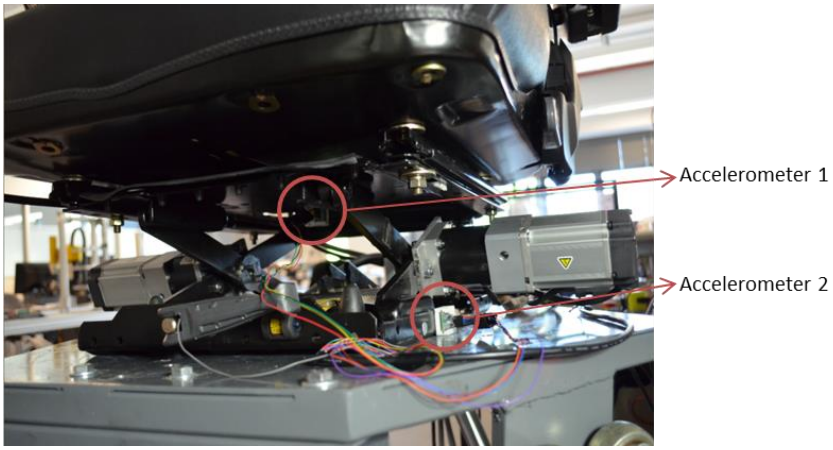

Figure 4-9. Accelerometers installation.

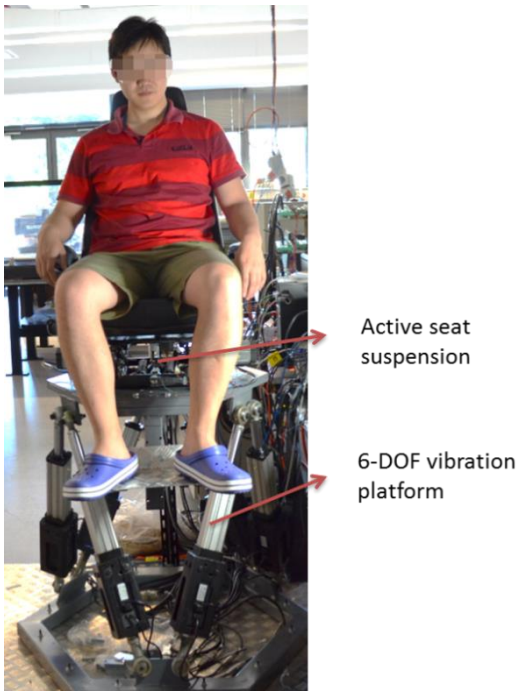

Figure 4-10. Experimental setup.

4.4 Acceleration Measurement Based Friction Estimation

In this section, an active vibration control algorithm with acceleration measurement based friction estimation is proposed and validated with simulations and experiments.

4.4.1 Control algorithm

4.4.1.1 Seat suspension model with single DOF

Figure 4-11 shows a simplified active seat suspension model with stiffness k, damping coefficient c, friction force f_r and actuator A. The suspension upper and base displacements are z_s and z_v, respectively. The governing equation of motion for the active seat suspension is:

$$m\ddot{z_s} + k(z_s - z_v) + c(\dot{z_s} - \dot{z_v}) + f_r = u \tag{4-4}$$

where m is the total mass of a driver's body, the seat suspension top platform and the cushion, et al.; u stands for the desired active force of the actuator.

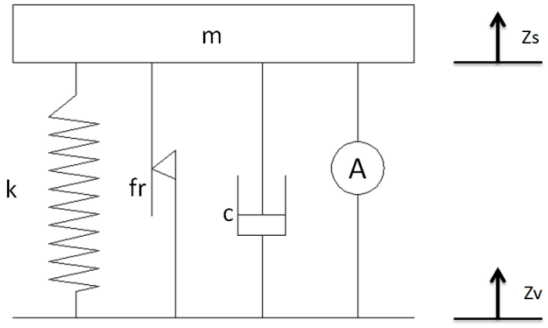

Figure 4-11. Simplified seat suspension model

In the practical application, the relative displacement of seat suspension and seat acceleration can be easily measured; the suspension relative velocity can be obtained from the differential of suspension relative displacement. Because the measurement noise of the displacement signal will be amplified if we obtain velocity from the differential of displacement signals directly, a first-order point by point low pass filter has been applied to process those signals. In this thesis, the state variables are chosen as$\mathbf{X} = [z_s - z_v \quad \dot{z_s} - \dot{z_v}]^{\mathrm{T}}$, disturbance is $d = \ddot{z_v}$, and the measurement variables are $\mathbf{Y_1} = [z_s - z_v \quad \dot{z_s} - \dot{z_v}]^{\mathrm{T}}$ and $Y_2 = \ddot{z_s}$. Thus the system model can be rearranged as:

$$\dot{\mathbf{X}} = \mathbf{A}\mathbf{X} + \mathbf{B_1}(u - f_r) + \mathbf{B_2}d \tag{4-5}$$

$$\mathbf{Y_1} = \mathbf{C_1 X} \tag{4-6}$$

$$Y_2 = \mathbf{C_2 X} + D_2(u - f_r) \tag{4-7}$$

where $\mathbf{A} = \begin{bmatrix} 0 & 1 \\ -\frac{k}{m} & -\frac{c}{m} \end{bmatrix}$, $\mathbf{B_1} = \begin{bmatrix} 0 \\ \frac{1}{m} \end{bmatrix}$, $\mathbf{B_2} = \begin{bmatrix} 0 \\ -1 \end{bmatrix}$, $\mathbf{C_1} = \begin{bmatrix} 1 & 0 \\ 0 & 1 \end{bmatrix}$, $\mathbf{C_2} = \begin{bmatrix} -\frac{k}{m} & -\frac{c}{m} \end{bmatrix}$, $D_2 = \frac{1}{m}$.

In terms of the vehicle seat suspension design, the driver comfort and vehicle handling are two main performance criteria. Driver comfort, which can usually be quantified by the seat acceleration, is the main control objective that needs to be optimized in the controller design process. The vehicle's operation devices, such as steering wheel and gear shift lever, are always fixed on the vehicle cab floor. This means that the suspension deflection, $z_s - z_v$, needs to be reduced in order to make sure the driver can easily handle those devices. The structural features of the seat suspension also constrain the amount of suspension deflection; this not only results in rapid deterioration in ride comfort, but also increases the wear on the suspension when the suspension hits the deflection limit. In order to satisfy the above-mentioned performance requirements, the controlled output is defined as: $\mathbf{Z} = [\ddot{z}_s \quad z_s - z_v]^T$ for the active seat suspension model. Therefore, the controlled output is defined as:

$$\boldsymbol{\alpha}\mathbf{Z} = \mathbf{C_3 X} + \mathbf{D_3}(u - f_r) \tag{4-8}$$

where $\mathbf{C_3} = \begin{bmatrix} -\frac{k}{m} & -\frac{c}{m} \\ 1 & 0 \end{bmatrix}$, $\mathbf{D_3} = \begin{bmatrix} \frac{1}{m} \\ 0 \end{bmatrix}$, $\boldsymbol{\alpha} = \begin{bmatrix} \alpha_1 & 0 \\ 0 & \alpha_2 \end{bmatrix}$ is a weighting matrix for the controlled output.

4.4.1.2 Friction observer

In the existing observers, such as the disturbance observer and the state observer, the state equations are always applied to estimate the state variables. In this system, the friction and disturbance are in the same channel as the state equations, so if a traditional observer is applied, the existence of disturbance will greatly deteriorate the friction observer's

performance. To effectively estimate the friction by using the easily measured acceleration signal, the friction estimation error can be defined based on the acceleration measurement as:

$$e_f = f_r - \widehat{f_r} = Y_2 - \widehat{Y_2} \tag{4-9}$$

So, the friction observer can be designed as:

$$\dot{\widehat{f_r}} = L\left(Y_2 - \widehat{Y_2}\right) = L[Y_2 - (\mathbf{C_2X} + \mathbf{D_2}(u - \widehat{\mathbf{f_r}}))] \tag{4-10}$$

where L is the friction observer gain to be designed.

Because the friction varies slowly relative to the observer dynamics, it is reasonable to assume that $\dot{f}_r = 0$. The dynamic equation of the friction estimation error can be defined as:

$$\dot{e_f} = \dot{f}_r - \dot{\widehat{f_r}} = L\mathbf{D_2}e_f \tag{4-11}$$

4.4.1.3 H_∞ Controller with friction compensation

The state feedback controller is constructed as:

$$u = \mathbf{KX} + \widehat{f_r} \tag{4-12}$$

where $\mathbf{K}$ is the state feedback gain to be designed, $\widehat{f_r}$ is the estimated friction by friction observer.

Substitute (4-12) and (4-11) into (4-5), then:

$$\dot{\mathbf{X}} = (\mathbf{A} + \mathbf{B_1K})\mathbf{X} - \mathbf{B_1}e_f + \mathbf{B_2}d \tag{4-13}$$

Combining the state equation of friction estimation error (4-11) with (4-8) and (4-13) yield:

$$\dot{\overline{\mathbf{X}}} = \overline{\mathbf{A}}\overline{\mathbf{X}} + \overline{\mathbf{B}}d \tag{4-14}$$

$$\boldsymbol{\alpha}\mathbf{Z} = \overline{\mathbf{C}}\overline{\mathbf{X}} \tag{4-15}$$

where $\overline{\mathbf{X}} = \begin{bmatrix}\mathbf{X}\\ e_f\end{bmatrix}$, $\overline{\mathbf{A}} = \begin{bmatrix}\mathbf{A} + \mathbf{B_1K} & -\mathbf{B_1}\\ 0 & LD_2\end{bmatrix}$, $\overline{\mathbf{B}} = \begin{bmatrix}\mathbf{B_2}\\ 0\end{bmatrix}$, $\overline{\mathbf{C}} = [\mathbf{C_3} + \mathbf{D_3K} \quad -\mathbf{D_3}]$.

The H_∞ norm is chosen as the control performance measure. The L_2 gain of the system (4-14) and (4-15) is defined as:

$$\|T_{Zd}\|_\infty = \sup \frac{\|Z\|_2}{\|d\|_2} \tag{4-16}$$

where $\|Z\|_2 = \int_0^\infty \mathbf{Z}^{\mathrm{T}}(t)\mathbf{Z}(t)\mathrm{d}t$ and $\|d\|_2 = \int_0^\infty d^{\mathrm{T}}(t)d(t)\mathrm{d}t$.

The Lyapunov function for the system (4-14) is defined as:

$$V = \bar{\mathbf{X}}^{\mathbf{T}}\mathbf{P}\bar{\mathbf{X}} \tag{4-17}$$

where $\mathbf{P} = \begin{bmatrix} \mathbf{P_1} & * \\ 0 & \mathbf{P_2} \end{bmatrix}$ is a positive definite matrix with $\mathbf{P}=\mathbf{P}^{\mathbf{T}}$, $\mathbf{P_1}$ and $\mathbf{P_2}$ are both positive definite matrices.

When (4-17) is differentiated, the following equation is derived:

$$\dot{V} = \dot{\bar{\mathbf{X}}}^{\mathbf{T}}\mathbf{P}\bar{\mathbf{X}} + \bar{\mathbf{X}}^{\mathbf{T}}\mathbf{P}\dot{\bar{\mathbf{X}}} = \begin{bmatrix} \bar{\mathbf{X}} \\ d \end{bmatrix}^{\mathbf{T}} \begin{bmatrix} \bar{\mathbf{A}}^{\mathbf{T}}\mathbf{P} + \mathbf{P}\bar{\mathbf{A}} & * \\ \bar{\mathbf{B}}^{\mathbf{T}}\mathbf{P} & 0 \end{bmatrix} \begin{bmatrix} \bar{\mathbf{X}} \\ d \end{bmatrix} \tag{4-18}$$

Adding $[\boldsymbol{\alpha}\mathbf{Z}]^{\mathbf{T}}[\boldsymbol{\alpha}\mathbf{Z}] - \lambda^2 d^{\mathrm{T}}d$ to the two sides of (4-18), we obtain:

$$\dot{V} + [\boldsymbol{\alpha}\mathbf{Z}]^{\mathbf{T}}[\boldsymbol{\alpha}\mathbf{Z}] - \lambda^2 d^{\mathrm{T}}d = \begin{bmatrix} \bar{\mathbf{X}} \\ d \end{bmatrix}^{\mathrm{T}} \begin{bmatrix} \bar{\mathbf{A}}^{\mathbf{T}}\mathbf{P} + \mathbf{P}\bar{\mathbf{A}} + \bar{\mathbf{C}}^{\mathbf{T}}\boldsymbol{\alpha}^{\mathbf{T}}\boldsymbol{\alpha}\bar{\mathbf{C}} & * \\ \bar{\mathbf{B}}^{\mathbf{T}}\mathbf{P} & -\lambda^2 \end{bmatrix} \begin{bmatrix} \bar{\mathbf{X}} \\ d \end{bmatrix} \tag{4-19}$$

If we consider that:

$$\exists = \begin{bmatrix} \bar{\mathbf{A}}^{\mathbf{T}}\mathbf{P} + \mathbf{P}\bar{\mathbf{A}} + \bar{\mathbf{C}}^{\mathbf{T}}\boldsymbol{\alpha}^{\mathbf{T}}\boldsymbol{\alpha}\bar{\mathbf{C}} & * \\ \bar{\mathbf{B}}^{\mathbf{T}}\mathbf{P} & -\lambda^2 \end{bmatrix} < 0 \tag{4-20}$$

then $\dot{V}(x) + [\boldsymbol{\alpha}\mathbf{Z}]^{\mathbf{T}}[\boldsymbol{\alpha}\mathbf{Z}] - \lambda^2 d^{\mathrm{T}}d < 0$, and the L_2 gain defined in (4-16) is less than $\lambda > 0$ with the initial condition $x(0) = 0$.

By Schur complement, $\exists < 0$ is equivalent to:

$$\in = \begin{bmatrix} \bar{\mathbf{A}}^{\mathbf{T}}\mathbf{P} + \mathbf{P}\bar{\mathbf{A}} & * & * \\ \bar{\mathbf{B}}^{\mathbf{T}}\mathbf{P} & -\lambda^2 & * \\ \boldsymbol{\alpha}\bar{\mathbf{C}} & 0 & -\mathbf{I} \end{bmatrix}$$

$$= \begin{bmatrix} (\mathbf{A}+\mathbf{B_1K})^{\mathbf{T}}\mathbf{P_1}+\mathbf{P_1}(\mathbf{A}+\mathbf{B_1K}) & * & * & * \\ -\mathbf{B_1}^{\mathbf{T}}\mathbf{P_1} & \mathbf{D_2}^{\mathbf{T}}L^{\mathrm{T}}\mathbf{P_2}+\mathbf{P_2}L\mathbf{D_2} & * & * \\ \mathbf{B_2}^{\mathbf{T}}\mathbf{P_1} & 0 & -\lambda^2 & * \\ \boldsymbol{\alpha}(\mathbf{C_3}+\mathbf{D_3K}) & -\boldsymbol{\alpha}\mathbf{D_3} & 0 & -\mathbf{I} \end{bmatrix} < 0 \quad (4\text{-}21)$$

Equation (4-21) is pre- and post-multiplied by diag($\mathbf{P_1}^{-1}, \mathbf{I}, \mathbf{I}, \mathbf{I}$) and its transposition, respectively, define $\mathbf{Q} = \mathbf{P_1}^{-1}$, $\mathbf{KQ} = \mathbf{R}$, $\mathbf{P_2}L = \mathbf{G}$, and $\mathbf{P_2}$ is set as a constant matrix, the H_∞ controller with friction compensation can then be obtained by solving the following linear matrix inequality (LMI):

$$\begin{bmatrix} \mathbf{AQ}+\mathbf{B_1R}+(\mathbf{AQ}+\mathbf{B_1R})^{\mathbf{T}} & * & * & * \\ -\mathbf{B_1}^{\mathbf{T}} & (\mathbf{GD_2})^{\mathbf{T}}+\mathbf{GD_2} & * & * \\ \mathbf{B_2}^{\mathbf{T}} & 0 & -\lambda^2 & * \\ \boldsymbol{\alpha}\mathbf{C_3Q}+\boldsymbol{\alpha}\mathbf{D_3R} & -\boldsymbol{\alpha}\mathbf{D_3} & 0 & -\mathbf{I} \end{bmatrix} < 0 \quad (4\text{-}22)$$

where $\mathbf{Q} = \mathbf{Q}^{\mathbf{T}}, \mathbf{Q} > 0$, λ is a given performance index. After solving (4-22) for matrices $\mathbf{Q}$, $\mathbf{R}$ and $\boldsymbol{G}$, the controller gain is obtained as $\mathbf{K} = \mathbf{RQ}^{-1}$, and the observer gain is $L = \mathbf{P_2}^{-1}\mathbf{G}$.

Table 4-1 shows the parameters used for the suspension model. Although there is no damper in the system, a small damping is chosen for controller design. After choosing $\lambda = 7.5$, the weighting matrix $\boldsymbol{\alpha} = \begin{bmatrix} 1.3 & * \\ 0 & 0.8 \end{bmatrix}$ and $\mathbf{P_2} = 10$, based on the Matlab LMI Toolbox, the control gain is obtained as $\mathbf{K} = [4500 \quad -123]$, and the friction observer gain is $L = -3282$.

Table 4-1. Parameter values used for the seat suspension.

Parameter	m (kg)	stiffness (N/m)	damping (Ns/m)
Value	80	4600	50

4.4.2 Experimental Results

In order to evaluate the active seat suspension performance with respect to ride comfort and vehicle handling, the evaluation of the suspension is based on the examination of seat acceleration and suspension deflection using different levels of cab floor vibration.

4.4.2.1 Sinusoidal vibration

Sinusoidal excitations were used to test this active seat suspension. Table 4-2 shows the signal details.

Table 4-2. Sinusoidal excitation signals.

Frequency (Hz)	1	1.25	1.5	1.75	2	2.25	2.5	2.75	3	3.25	3.5	3.75	4	4.25	4.5
Amplitude (mm)	6	6	6	6	5	5	5	4	3	3	3	2.5	2	2	2

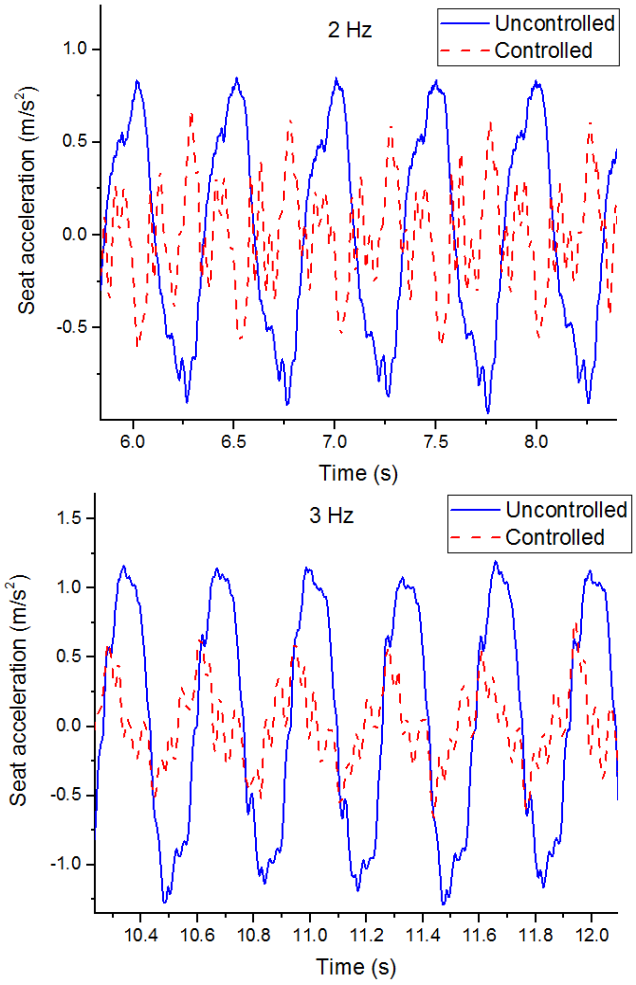

Figure 4-12. Seat acceleration.

Figure 4-12 shows the accelerations of the seat vibration in the time domain without control and with control when the frequencies of the excitation vibrations are given as 2 Hz and 3 Hz, respectively. The peak accelerations of the seat can be reduced which indicates that the high level acceleration has been filtered out. The reduction of seat acceleration means the ride comfort has been improved. Figure 4-13 indicates that the active controller tries to keep the seat in its balanced position; the less the absolute displacement of the seat, the greater its stability.

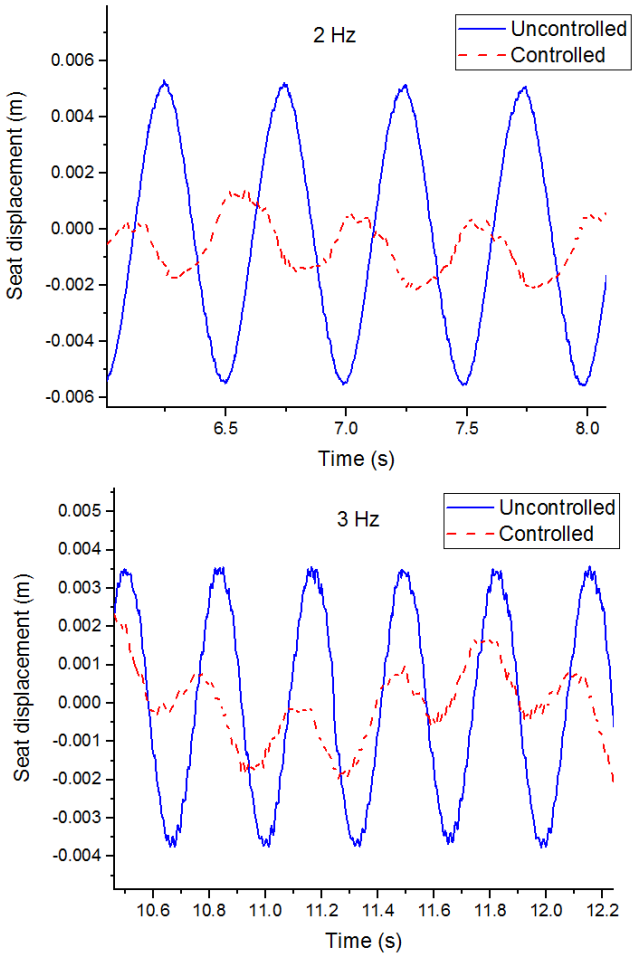

Figure 4-13. Seat displacement.

The friction observer's performance is shown in Figure 4-14. We can see that the estimated friction can track the change of the Coulomb friction. The Coulomb friction is the simplest way to model the friction. When the motion reverses, the actual friction will not reverse

immediately as the Coulomb friction does, but gradually reverses over a certain period of displacement. In Figure 4-14, the friction change in the pre-sliding regime can be estimated by the observer. When the Coulomb friction reverses, the estimated friction reverses gradually. The estimated friction models the real situation more accurately than the Coulomb friction model does. The assumption that $\dot{f}_r = 0$ in the observer design indicates that the observer can be more accurate at lower frequencies, because the friction reverses less frequently.

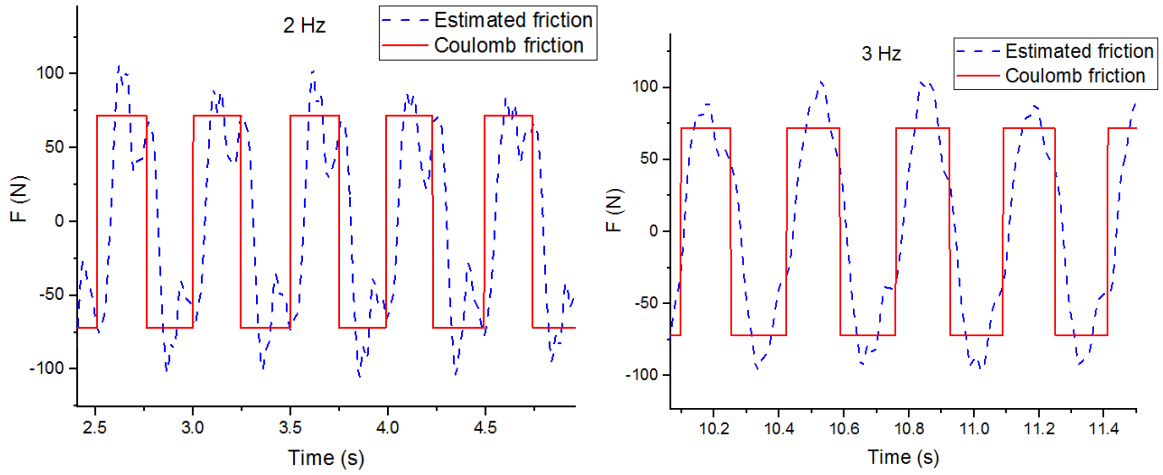

Figure 4-14. Estimated friction (a) 2 Hz, (b) 3 Hz.

The RMS value is applied to evaluate the measured accelerations for further analysis of the active seat suspension performance. The RMS is defined as:

$$RMS(a) = \sqrt{\frac{1}{N}\sum_{i=1}^{N} {a_i}^2} \tag{4-23}$$

where N is the number of recorded accelerations, and a_i is the value of acceleration.

The RMS of seat vibration acceleration in uncontrolled suspension experiments, controlled suspension experiments, and conventional passive suspension experiments are defined as a_{un}, a_c and a_p, respectively. The RMS of excitation vibration acceleration is defined as a_v.

The uncontrolled, controlled and conventional passive suspension acceleration transmissibility at the tested frequency can be defined as:

$$\mathrm{T}_{un} = a_{un}/a_v \tag{4-24}$$

$$\mathrm{T}_{\mathrm{c}} = a_c/a_v \tag{4-25}$$

$$\mathrm{T}_{\mathrm{p}} = a_p/a_v \tag{4-26}$$

Figure 4-15 indicates the comparison of suspension acceleration transmissibility. The proposed active seat suspension's passive performance is almost the same as the conventional seat. The active seat suspension performs much better than the passive suspension does in the tested frequency range. The active seat performs best at 2.25 Hz and successfully suppresses the resonance vibration. At a low frequency, about 1.5 Hz, the passive suspension's relative displacement and velocity are very small and the acceleration transmissibility is large as the damping force or friction prevents the seat suspension from isolating the vibration. The seat acceleration of the active seat suspension can perceive the influence of the low frequency excitation; the estimated friction by acceleration is applied to reduce vibration transfer to the driver's body.

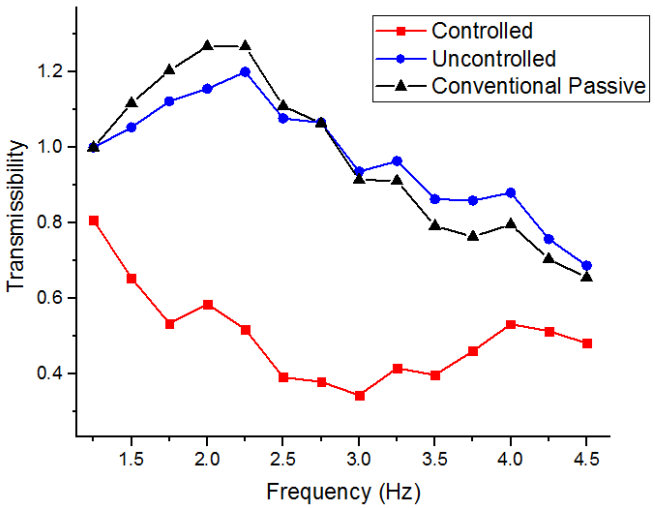

Figure 4-15. Acceleration transmissibility.

4.4.2.2 Bump and random vibration

The bump and random road profiles which are often used to evaluate vehicle suspension performance in the time domain are applied to generate excitation vibration for the active seat suspension with a quarter-car suspension model. In this thesis, the corresponding ground displacements of bump and random vibration are generated firstly. The road profiles are then put into the quarter-car suspension model with parameter values in [90]. This thesis focuses on heavy duty vehicles in which the sprung mass is much heavier than the seat suspension, and the influence of the seat mass to the response of sprung mass is small, thus the sprung mass displacement is treated as the cab floor vibration and sent to the 6-DOF vibration platform controller to generate excitation vibration.

An isolated bump road surface is given by:

$$z_r(t) = \begin{cases} \frac{a}{2}\left(1 - \cos\left(\frac{2\pi v_0}{l}t\right)\right), & 0 \le t \le \frac{l}{v_0} \\ 0, & t > \frac{l}{v_0} \end{cases} \tag{4-27}$$

where a and l are the height and length of the bump [109], and $a = 0.07$ m, $l = 0.8$ m are chosen. The vehicle forward velocity is set as $v_0 = 2.77$ m/s.

The road displacement of the random ground surface [109] is defined as:

$$\dot{z_r}(t) + \rho V z_r(t) = V W_n \tag{4-28}$$

where ρ is the road roughness parameter, V is the vehicle speed, and W_n is white noise with intensity $2\delta^2\rho V$ in which δ^2 is the covariance of road irregularity. When generating the random ground profile, $\rho = 0.45\ \mathrm{m}^{-1}$, $\delta^2 = 300\ \mathrm{mm}^2$, and $V = 20$ m/s are chosen.

It should be emphasised that the active seat suspension is mainly applied to heavy duty vehicles which often have vehicle (chassis) suspension systems that isolate the vibration transferred from the uneven road. Generally, a well-tuned vehicle suspension can eliminate most of the high frequency vibration but the low frequency vibration isolation capacity is

limited by vehicle suspension spring stiffness. In practice, the vertical vibration of a heavy duty vehicle seat is highest in the frequency range 2 to 4 Hz, and heavy vehicle drivers usually experience vibration around 3 Hz which increases fatigue and drowsiness [2]. This is the reason why the applied random vibration excitation generated from a quarter-car suspension model with random road profile is larger at low frequencies.

The seat performance during the bump test can indicate the controller's capacity to respond to excitation. Figure 4-16 shows the seat acceleration under bumpy road conditions. The peak acceleration magnitude drops from 1.13 m/s^2 to 0.716 m/s^2. Figure 4-17 further indicates its good transient response performance with a reduction of about 50% of absolute seat displacement.

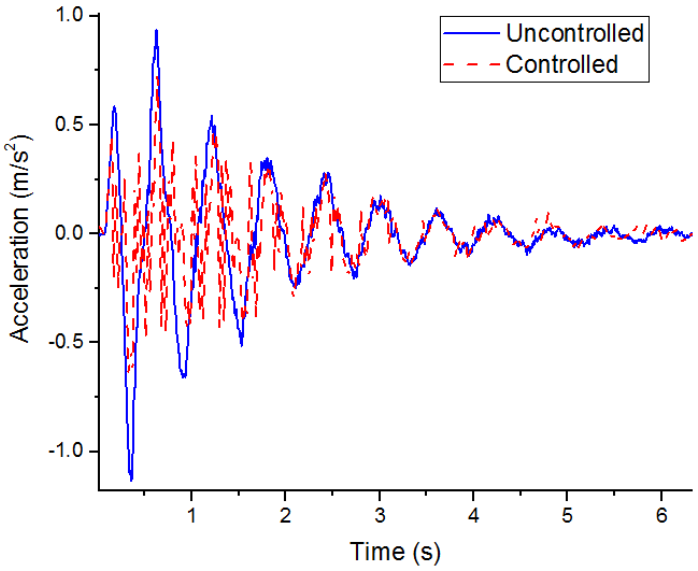

Figure 4-16. Seat acceleration with bumpy road.

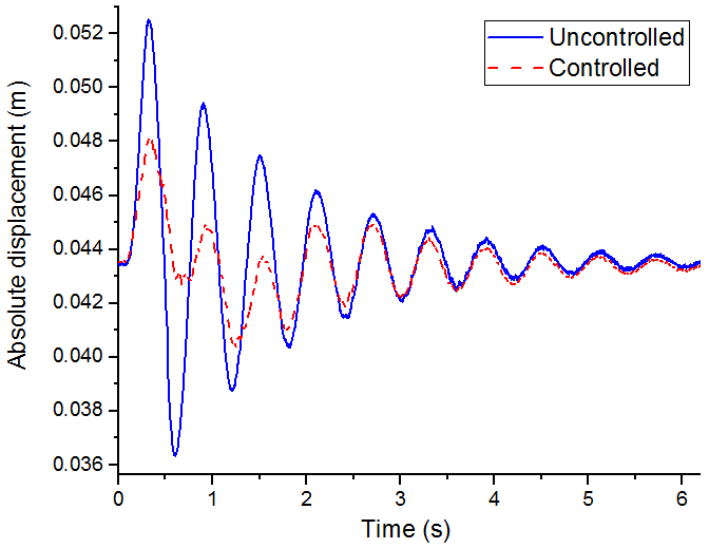

Figure 4-17. Seat displacement with bumpy road.

Figure 4-18 shows the seat acceleration under random vibration. The power spectral density (PSD) of acceleration is compared in Figure 4-19 which indicates that the uncontrolled active seat and the conventional passive seat have a peak value of around 1.7 Hz. The active seat suspension can control the acceleration PSD value to a very low magnitude for all the frequencies considered. It is common for some low magnitude and high frequency noises to be introduced with active controls. To further investigate whether those low magnitude vibrations will affect driver comfort, ISO 2631-1 [110] (which is an international standard for evaluating human exposure to whole body vibration) is applied to evaluate the three kinds of seat suspensions. The seat effective amplitude transmissibility (SEAT) and fourth power vibration dose value (VDV) ratio are obtained as follows:

$$a_w = \left[\frac{1}{T}\int_0^T \{a_w(t)^2 \mathrm{d}t\}\right]^{1/2}$$

$$VDV = \left[\int_0^T \{a_w(t)^4 \mathrm{d}t\}\right]^{1/4}$$

$$SEAT = \frac{a_{w,driver}}{a_{w,vibration}}$$

$$VDV\ ratio = \frac{VDV_{driver}}{VDV_{vibration}} \tag{4-29}$$

where a_w is the frequency-weighted RMS (FW-RMS) acceleration which is obtained based on the ISO 2631-1 recommended frequency-weighting curve, and VDV is another evaluation method which is more sensitive to peaks than the frequency-weighted RMS method.

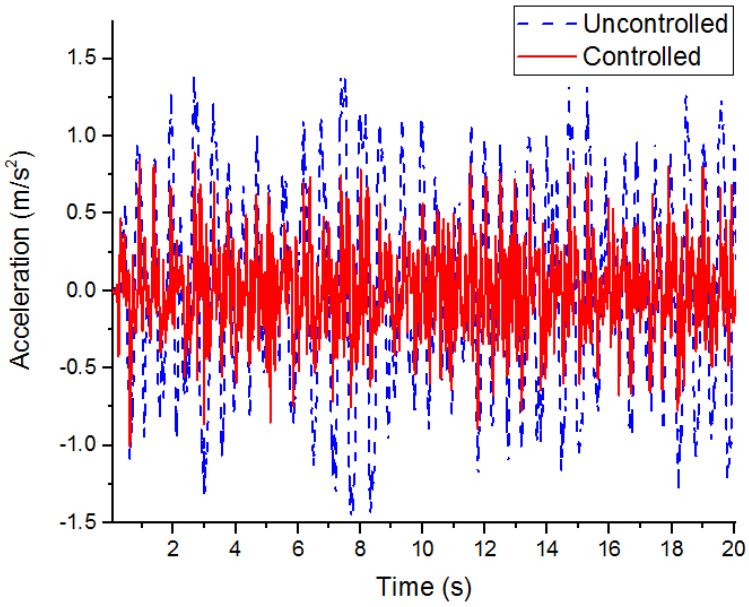

Figure 4-18. Seat acceleration with random road.

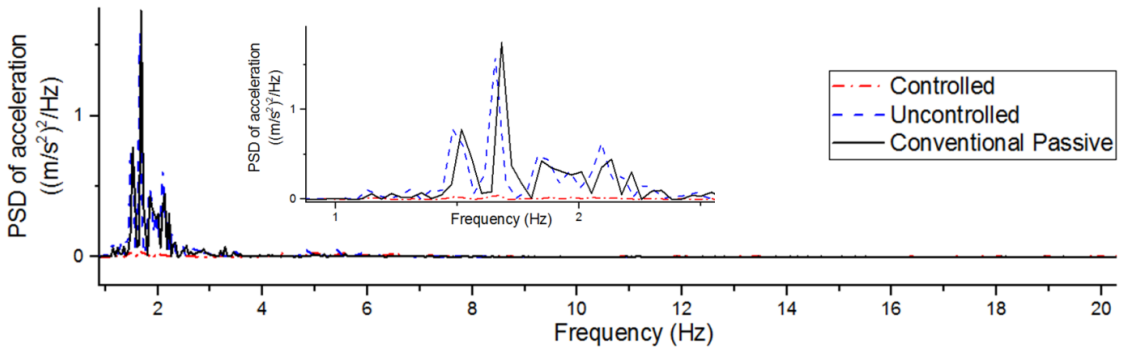

Figure 4-19. Seat vibration magnitude with random vibration.

Table 4-3 shows the acceleration analysis of the well-tuned conventional passive seat suspension, and uncontrolled and controlled active seat suspensions. There is a 35.5 % reduction in the FW-RMS value when the active seat suspension is controlled. This means

the driver's ride experience is greatly improved because the frequency-weighting curve is related to health, comfort and perception.

Table 4-4 gives ISO 2631-1 recommended values of the likely reactions to various magnitudes. If the normal RMS acceleration method is applied, the conventional passive seat suspension acceleration is within the 'fairly uncomfortable' range but if the FW-RMS method is applied it is within the 'a little uncomfortable' range. The active seat suspension is in the 'not uncomfortable' range with both evaluation methods. The results also indicate that the introduced low magnitude and high frequency noise may not affect the driver's comfort.

Table 4-3. Evaluation of seat acceleration.

	Passive	Uncontrolled	Controlled	Comparison of controlled and passive
RMS (m/s^2)	0.6082	0.6267	0.2615	-57%
FW-RMS (m/s^2)	0.4045	0.4295	0.2608	-35.5%
VDV $(m/s^{1.75})$	1.089	1.064	0.7121	-34.6%
SEAT	0.752	0.798	0.484	-35.6%
VDV ratio	0.622	0.608	0.407	-34.6%

Table 4-4. ISO 2631-1 comfort evaluation.

Less than 0.315 $\mathbf{m/s^2}$	Not uncomfortable
0.315 m/s^2 to 0.63 m/s^2	A little uncomfortable
0.5 m/s^2 to 1 m/s^2	Fairly uncomfortable
0.8 m/s^2 to 1.6 m/s^2	Uncomfortable
1.25 m/s^2 to 2.5 m/s^2	Very uncomfortable
Greater than 2 m/s^2	Extremely uncomfortable

The high energy consumption is one of the main limitations of the active seat suspension's application. The theoretical power of this active seat suspension is defined as $P(t) = F(t)V(t)$, where $F(t)$ is the force output of the controller and $V(t)$ is the suspension deflection velocity. Figure 4-1 shows the suspension's power with random vibration (the maximum power is 21.71 W). The suspension has an RMS power of 3.82 W which means low energy consumption.

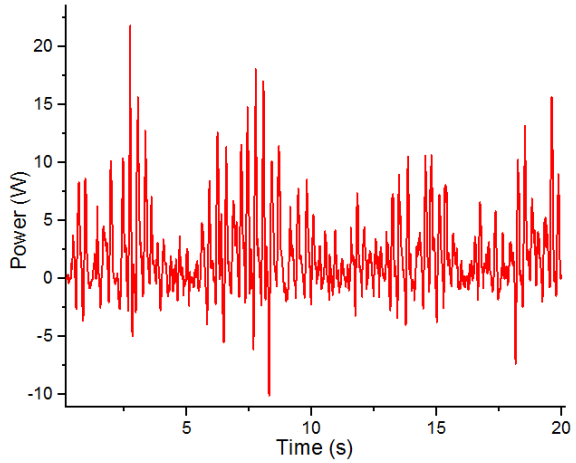

Figure 4-20. The power of active seat suspension in random vibration test.

4.5 Disturbance Observer Based Takagi-Sugeno Fuzzy Control

In this section, the control algorithm in last section is improved by involving a TS-fuzzy model.

4.5.1 Control algorithm

4.5.1.1 Seat suspension model with disturbance

A two DOFs model is applied in this section which can more accurately describe the seat suspension system. The seat suspension model is shown in Figure 4-21 where m_b is the human body mass; m_s is the seat frame mass; k_c and c_c are the stiffness and damping between human body and seat frame; k_f is the stiffness of the seat suspension; f_r is the seat suspension friction force; $\bar{u}$ is the saturated active force generated by actuator; z_b and z_s are

the displacements of the corresponding masses, respectively, and z_v is the displacement of cabin floor. Compared with Figure 4-11, the new model has included the mass of driver and the saturation of output force. The dynamic model of the system can be described as:

$$m_s\ddot{z}_s = -k_f(z_s - z_v) + k_c(z_b - z_s) + c_c(\dot{z}_b - \dot{z}_s) - f_r + \bar{u} \tag{4-30}$$

$$m_b\ddot{z}_b = -k_c(z_c - z_s) - c_c(\dot{z}_c - \dot{z}_s) \tag{4-31}$$

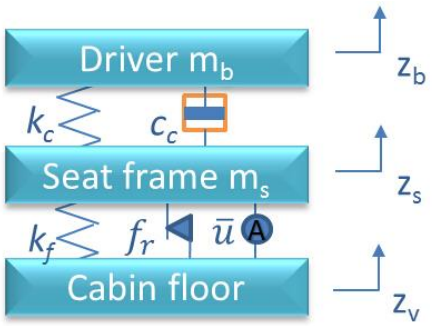

Figure 4-21. Seat suspension model.

Control algorithms based on the model states measurement or estimation have been extensively explored [39, 111]. However, in practice, the measurable variables are very limited, e.g. accelerations of masses and the relative displacement between seat frame and cabin floor. The complicated multi-states estimation algorithms which always include matrix multiplications and integral of variables require a high calculation speed which will increase the hardware cost. In addition, the active actuator output saturation exists in almost all the real applications [98, 99, 112]. Considering the possible actuator output saturation and other dynamic disturbances, a simple but accurate single degree of freedom (SDOF) seat model is defined as:

$$M\ddot{z}_s = -k_f(z_s - z_v) - F_d + u \tag{4-32}$$

$$M = m_b + m_s \tag{4-33}$$

$$F_d = f_r + f_{\Delta m} + \Delta u \tag{4-34}$$

$$\bar{u} = \mathrm{sat}(u) = \begin{cases} -u_{lim}, & \text{if } u < -u_{lim} \\ u, & \text{if } -u_{lim} < u < u_{lim} \\ u_{lim}, & \text{if } u > u_{lim} \end{cases} \quad (4\text{-}35)$$

where M is the total mass of driver body and seat frame, F_d is the unmeasurable disturbance that includes friction force f_r, model simplification caused disturbance $f_{\Delta m} = m_b(\ddot{z}_b - \ddot{z}_s)$ and control output error $\Delta u = u - \bar{u}$ (caused by actuator output saturation), u is the desired control input, $\bar{u} = \mathrm{sat}(u)$is the saturated control input defined in (4-35), u_{lim} is the control input limit. Because a soft spring is always applied for seat suspension to make the seat comfortable (k_c is always much higher than k_f), in this model, m_b and m_s are taken as a solid mass to simplify the model; the caused $f_{\Delta m}$ is small in low frequency vibration and will correspondingly increase with vibration frequency. Considering that most of the high frequency vibration has been isolated by vehicle suspension and the low frequency vibration magnitude is hard to be decreased for the stiffness limitation of a passive vehicle suspension, model (4-32) is practical to be applied for an active seat suspension control.

The seat acceleration and seat suspension deflection are measured, and suspension deflection rate is calculated out from seat suspension deflection. Although noise will be introduced when directly differentiating the suspension deflection to obtain its deflection rate, the noise can be easy to deal with by applying a point by point low pass filter. The state variables are chosen as $\mathbf{X} = [z_s - z_v \quad \dot{z}_s - \dot{z}_v]^{\mathrm{T}}$, the vibration disturbance is $d = \ddot{z}_v$, and the measurement variables are $\mathbf{Y_1} = [z_s - z_v \quad \dot{z}_s - \dot{z}_v]^{\mathrm{T}}$ and $Y_2 = \ddot{z}_s$. Thus, combing with (4-32) the system model is defined as:

$$\dot{\mathbf{X}} = \mathbf{A}\mathbf{X} + \mathbf{B_1}(u - F_d) + \mathbf{B_2}d \quad (4\text{-}36)$$

$$\mathbf{Y_1} = \mathbf{C_1}\mathbf{X} \quad (4\text{-}37)$$

$$Y_2 = \mathrm{C}_2\mathrm{X} + D_2(u - F_d) \quad (4\text{-}38)$$

where $\mathbf{A} = \begin{bmatrix} 0 & 1 \\ -\frac{k_f}{M} & 0 \end{bmatrix}$, $\mathbf{B_1} = \begin{bmatrix} 0 \\ \frac{1}{M} \end{bmatrix}$, $\mathbf{B_2} = \begin{bmatrix} 0 \\ -1 \end{bmatrix}$, $\mathbf{C_1} = \begin{bmatrix} 1 & 0 \\ 0 & 1 \end{bmatrix}$, $\mathbf{C_2} = \begin{bmatrix} -\frac{k_f}{M} & 0 \end{bmatrix}$, $D_2 = \frac{1}{M}$.

Driver's comfort can be quantified by the seat acceleration, which is the main optimization objective in the controller design process. Therefore, the controlled output is defined as:

$$Z_1 = \mathbf{C_3 X} + D_3(u - F_d) \tag{4-39}$$

where $\mathbf{C_3} = \alpha \mathbf{C_2}$, $D_3 = \alpha D_2$, α is a constant.

4.5.1.2 TS fuzzy model

The weight of driver body will change when different drivers are driving. To make the seat suspension have similar performance, the driver's mass variation has been considered into the controller design. The mass variation range is assumed as $[m_{bmin} \quad m_{bmax}]$, where m_{bmin} and m_{bmax} are the possible minimum and maximum driver's masses, respectively. Therefore, the simplified model mass can be expressed as:

$$\frac{1}{M} = h_1 \frac{1}{m_{bmin}+m_s} + h_2 \frac{1}{m_{bmax}+m_s} = h_1 \frac{1}{M_{min}} + h_2 \frac{1}{M_{max}} \tag{4-40}$$

where M_{min} and M_{max} are the possible minimum and maximum total masses of the driver and seat suspension; h_1 and h_2 are defined as:

$$h_1 = \frac{1/M - 1/M_{max}}{1/Mmin - 1/M_{max}}, \; h_2 = \frac{1/Mmin - 1/M}{1/Mmin - 1/M_{max}} \tag{4-41}$$

where $h_i \geq 0$, $i = 1, 2$, and $\sum_{i=1}^{2} h_i = 1$. The suspension model in (4-36) with a variable driver's weight can be expressed as:

$$\dot{\mathbf{X}} = \sum_{i=1}^{2} h_i \, \mathbf{A}_i \mathbf{X} + \sum_{i=1}^{2} h_i \, \mathbf{B}_{1i}(u - F_d) + \mathbf{B}_2 d \tag{4-42}$$

where matrix $\mathbf{A}_i$ and $\mathbf{B_{1i}}$, $i = 1, 2$, are obtained by replacing M with M_{min} and M_{max}.

Similarly, the measurement variable (4-38) and the control output (4-39) can be expressed as

$$Y_2 = \sum_{i=1}^{2} h_i \, \mathbf{C}_{2i} \mathbf{X} + \sum_{i=1}^{2} h_i \, D_{2i}(u - F_d) \tag{4-43}$$

$$Z_1 = \sum_{i=1}^{2} h_i \, \mathbf{C}_{3i}\mathbf{X} + \sum_{i=1}^{2} h_i \, D_{3i}(u - F_d) \tag{4-44}$$

For description simplicity, we define $\mathbf{A}_h = \sum_{i=1}^{2} h_i \, \mathbf{A}_i$, and the same simplification method is applied to other model matrices.

4.5.1.3 TS fuzzy disturbance observer

Equation (4-32) shows that three forces are exerted on the suspended mass, namely spring force, disturbance force and active force. The friction force f_r is an important component of disturbance force F_d. The active seat suspension prototype applied in this thesis has a peak friction of about 80 N which is shown in Appendix. It indicates that F_d has a great influence on the system dynamic, thus F_d needs to be estimated to improve controller's performance. Equation (4-32) can be written as:

$$F_d = -M\ddot{z}_s - k_f(z_s - z_v) + u \tag{4-45}$$

Modifying the estimation by the difference between the estimated value and the actual value is the main idea to design an observer. Thus, a disturbance observer is defined as:

$$\dot{\widehat{F_d}} = -l(F_d - \widehat{F_d}) \tag{4-46}$$

Combing (4-38) and (4-45), it is rearranged as:

$$\dot{\widehat{F_d}} = l\left(M\ddot{z}_s - \left(-k_f(z_s - z_v) - \widehat{F_d} + u\right)\right) = L[Y_2 - (\mathbf{C_2}\mathbf{X} + D_2(u - \widehat{F_d}))] \tag{4-47}$$

where $L = lM$.

The observer error is defined as:

$$e_f = F_d - \widehat{F_d} \tag{4-48}$$

Since, generally, there is no prior information about the derivative of the disturbance F_d, and disturbance varies slowly relative to the observer dynamics, $\dot{F}_d = 0$ is a reasonable assumption. Combining (4-38) with (4-47) yields:

$$\dot{e_f} = \dot{F_d} - \dot{\widehat{F_d}} = LD_2 e_f \tag{4-49}$$

With time t, we can obtain that $e_f(t) = \mathrm{e}^{LD_2(t-t_0)} e_f(t_0)$. Thus, if $\Gamma = LD_2 < 0$, the observer error will be exponentially converged.

The disturbance observer in (4-47) is an acceleration measurement based observer. The acceleration is introduced into control algorithm by estimating the differential of the disturbance. The sensitivity of acceleration to vibration can improve algorithm's dynamic response.

Considering the TS fuzzy model (4-43), the TS fuzzy disturbance observer can be defined as:

$$\dot{\widehat{F_d}} = L_h[Y_2 - (\mathbf{C}_{2h}\mathbf{X} + D_{2h}(u - \widehat{F_d}))] \tag{4-50}$$

The differential of estimation error is:

$$\dot{e_f} = L_h D_{2h} e_f \tag{4-51}$$

In order to get the same convergence rate for different driver weights, the TS fuzzy observer gains are obtained

$$L_i = \frac{D_{2i}}{\Gamma}, \qquad i = 1,2 \tag{4-52}$$

where $\Gamma < 0$ is a constant. The convergence rate is inversely proportional to $|\Gamma|$. A smaller $|\Gamma|$ will lead to a more accurate estimation of the disturbance; on the other hand, the chattering problem may be introduced by compensating a fast varying disturbance value. Thus, $|\Gamma|$ needs to be selected according to the practical application.

4.5.1.4 TS fuzzy H∞ controller design with disturbance compensation

Since the disturbance is estimated, a state feedback controller with disturbance compensation is constructed as:

$$u = \mathbf{K}_h\mathbf{X} + \widehat{F_d} \tag{4-53}$$

where $\mathbf{K}_h$ is the state feedback gain to be designed.

Substitute (4-53) into (4-42), then

$$\dot{\mathbf{X}} = (\mathbf{A}_h + \mathbf{B}_{1h}\mathbf{K}_h)\mathbf{X} - \mathbf{B}_{1h}e_f + \mathbf{B_2}d \tag{4-54}$$

Combining the disturbance force estimation, a new state space equation is obtained:

$$\dot{\overline{\mathbf{X}}} = \overline{\mathbf{A}}_h\overline{\mathbf{X}} + \overline{\mathbf{B}}d \tag{4-55}$$

where $\overline{\mathbf{X}} = \begin{bmatrix}\mathbf{X}\\ e_f\end{bmatrix}$, , $\overline{\mathbf{A}}_h = \begin{bmatrix}\mathbf{A}_h + \mathbf{B}_{1h}\mathbf{K}_h & -\mathbf{B}_{1h}\\ 0 & L_hD_{2h}\end{bmatrix}$, $\overline{\mathbf{B}} = \begin{bmatrix}\mathbf{B_2}\\ 0\end{bmatrix}$,

To achieve good ride comfort and reduce the effect of disturbance's estimation error, the objective output is defined as

$$\mathbf{Z} = \bar{\mathbf{C}}_h\overline{\mathbf{X}} \tag{4-56}$$

where $\bar{\mathbf{C}}_h = \begin{bmatrix}\mathbf{C}_{3h} + D_{3h}\mathbf{K}_h & -D_{3h}\\ 0 & c_0\end{bmatrix}$, c_0 is a constant.

The $\mathcal{L}_2$ gain of the system (4-55) and (4-56) is defined as:

$$\|T_{Zd}\|_\infty = \sup\frac{\|\mathbf{Z}\|_2}{\|d\|_2} \quad (d \neq 0) \tag{4-57}$$

where $\|\mathbf{Z}\|_2 = \int_0^\infty \mathbf{Z}^{\mathrm{T}}(t)\mathbf{Z}(t)\mathrm{d}t$ and $\|d\|_2 = \int_0^\infty d^{\mathrm{T}}(t)d(t)\mathrm{d}t$.

It is easy to conclude that if there is a positive definite matrix $\mathbf{P} = \begin{bmatrix}\mathbf{P_1} & *\\ 0 & \mathbf{P_2}\end{bmatrix}$, $\mathbf{P_1} = \mathbf{P_1}^{\mathbf{T}} > \mathbf{0}$, $\mathbf{P_2} = \mathbf{P_2}^{\mathbf{T}} > \mathbf{0}$, such that the following LMI is satisfied [113]:

$$\in = \begin{bmatrix}\overline{\boldsymbol{A}}_h{}^T\boldsymbol{P} + \boldsymbol{P}\overline{\boldsymbol{A}}_h & * & *\\ \overline{\mathbf{B}}^{\mathbf{T}}\mathbf{P} & -\lambda^2\mathbf{I} & *\\ \overline{\boldsymbol{C}}_h & 0 & -\mathbf{I}\end{bmatrix}$$

$$= \begin{bmatrix}(\mathbf{A}_h + \mathbf{B}_{1h}\mathbf{K}_h)^{\mathbf{T}}\mathbf{P_1} + \mathbf{P_1}(\mathbf{A}_h + \mathbf{B}_{1h}\mathbf{K}_h) & * & * & * & *\\ -\mathbf{B}_{1h}{}^{\mathbf{T}}\mathbf{P_1} & D_{2h}{}^{\mathbf{T}}L_h{}^{\mathrm{T}}\mathbf{P_2} + \mathbf{P_2}L_hD_{2h} & * & * & *\\ \mathbf{B_2}{}^{\mathbf{T}}\mathbf{P_1} & 0 & -\lambda^2\mathbf{I} & * & *\\ \boldsymbol{C}_{3h} + D_{3h}\boldsymbol{K}_h & -D_{3h} & 0 & -\mathbf{I} & *\\ 0 & c_0 & 0 & 0 & -\mathbf{I}\end{bmatrix} < 0 \tag{4-58}$$

then the system (4-55) is stable with H_∞ performance index $\lambda > 0$.

Pre- and post-multiply (4-58) by diag($\mathbf{P_1}^{-1}, \mathbf{I}, \mathbf{I}, \mathbf{I}, \mathbf{I}$) and its transpose, respectively. Defining $\mathbf{Q} = \mathbf{P_1}^{-1}$, $\mathbf{K}_h\mathbf{Q} = \mathbf{R}_h$, and $\mathbf{P_2}$ is set as a constant matrix. The condition $\in < 0$ is equivalent to

$$\sum_{i,j=1}^{2} h_i h_j \ni_{ij} < 0 \tag{4-59}$$

where

$$\ni_{ij} = \begin{bmatrix} \mathbf{A}_i\mathbf{Q} + \mathbf{B}_{1i}\mathbf{R}_j + (\mathbf{A}_i\mathbf{Q} + \mathbf{B}_{1i}\mathbf{R}_j)^{\mathrm{T}} & * & * & * & * \\ -\mathbf{B}_{1i}{}^{\mathrm{T}} & (\mathbf{P_2}L_jD_{2i})^{\mathrm{T}} + \mathbf{P_2}L_jD_{2i} & * & * & * \\ \mathbf{B}_2{}^{\mathrm{T}} & 0 & -\lambda^2\mathbf{I} & * & * \\ C_{3i}\mathbf{Q} + \mathbf{D}_{3i}\mathbf{R}_j & -\mathbf{D}_{3i} & 0 & -\mathbf{I} & * \\ 0 & c_0 & 0 & 0 & -\mathbf{I} \end{bmatrix} < 0 \tag{4-60}$$

Based on parameterized linear matrix inequality (PLMI) techniques [113], the relaxation result can be written as:

$$\ni_{ii} \leq 0, \qquad i = 1,2 \tag{4-61}$$

$$\ni_{ii} + \frac{1}{2}\left(\ni_{ij} + \ni_{ji}\right) < 0, \qquad 1 \leq i \neq j \leq 2 \tag{4-62}$$

After solving (4-61) and (4-62) by linear matrix inequality (LMI) toolbox in Matlab, the controller gain is obtained as $\mathbf{K_i} = \mathbf{R_i}\mathbf{Q}^{-1}$.

The controller implementation procedure is shown in Figure 4-22. As the applied disturbance compensation strategy considers all the possible disturbances, uncertainties, modelling errors, actuator saturation, etc., the robustness of the proposed method is enhanced.

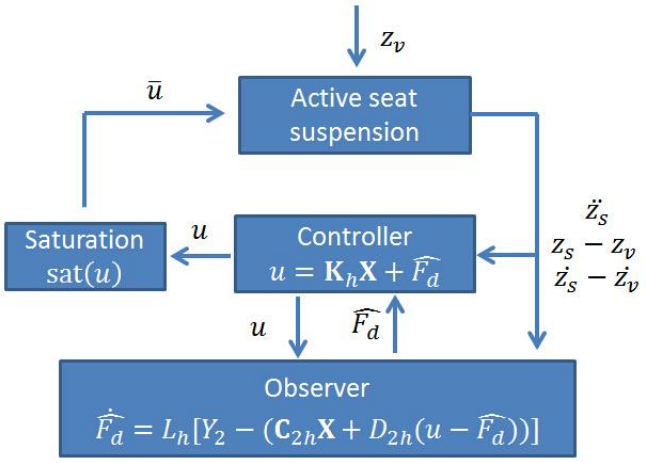

Figure 4-22. Controller implementation.

Remark 1. To evaluate a new method, it is common to compare it with other available existing methods in dealing with the same problem. We noticed that many references have proposed different control methods for vehicle suspensions [82, 111], but they cannot be directly compared with our proposed method because there are different aspects between seat suspension control and vehicle suspension control. Even though some papers studied about seat suspensions but most of them only considered road input disturbance but did not consider the practical friction issue. On the other hand, from implementation point of view, some control strategies, such as the proposed output feedback control by Li et.al [83], are complicated when compared to the state feedback control using available measurements. Thus to make a fair evaluation for the proposed method, we only compare it with the uncontrolled case in the simulations and passive and uncontrolled cases in the experiments to validate its effectiveness.

4.5.2 Simulation Results

In order to evaluate the performance of proposed observer and controller, the simulation is implemented on the 2-DOF system model (4-30) and (4-31). The friction model in Section 4.2.3 is applied with the identified parameters. Table 4-5 shows the parameters in simulation.

The TS fuzzy controller gains are obtained as $K_1 = [4573 \quad -90]$ and $K_2 = [4560 \quad -134]$. Two sets of observer parameters are selected, where Γ_1 is chosen for Observer 1 and the disturbance observer gains are $L_{11} = -4566$ and $L_{12} = -3086$; Γ_2 is chosen for Observer 2 and the disturbance observer gains are $L_{21} = -13699$ and $L_{22} = -9259$.

A bump road surface is applied to the simulation model as:

$$z_v(t) = \begin{cases} \frac{a}{2}\left(1 - \cos\left(\frac{2\pi v_0}{l}t\right)\right), & 0 \le t \le \frac{l}{v_0} \\ 0, & t > \frac{l}{v_0} \end{cases} \tag{4-63}$$

where $a = 0.07$ m and $l = 0.8$ m are the height and length of the bump. The vehicle velocity is set as $v_0 = 1\,\mathrm{m/s}$.

Table 4-5. Parameters used in the simulation.

$\boldsymbol{m_b}$	55 Kg	$\boldsymbol{\alpha}$	0.02
m_s	28 Kg	P_2	400
k_c	90000 N/m	λ	1.2
c_c	2500 Ns/m	Γ_1	$-3e^{-6}$
k_f	4600 N/m	Γ_2	$-1e^{-6}$
u_{lim}	250 N	m_{bmin}	45 Kg
m_{bmax}	120 Kg		

The driver body acceleration is shown in Figure 4-23 where there is big peak acceleration about 4 $\mathrm{m/s^2}$ with uncontrolled seat suspension, and the driver body accelerations are both decreased when the controller is implemented with either Observer 1 or Observer 2. Although the acceleration magnitudes are very close with the two observers, with Observer 2, the acceleration goes to zero faster. Figure 4-24 shows the observers performance. The Observer

2 can track the disturbance better than Observer 1, but it has a bigger peak disturbance because of actuator saturation. The saturated control force is shown in Figure 4-25. It needs to be explained here that the friction model is included in the simulation, so when the seat suspension is stable, the static friction may not be zero. The simulation with bump surface indicates that, with a smaller $|\Gamma|$, the controller and observer will have better performance when the actuator output is not saturated; but when the actuator output is saturated, a bigger disturbance value is appeared and this will affect the controller's performance.

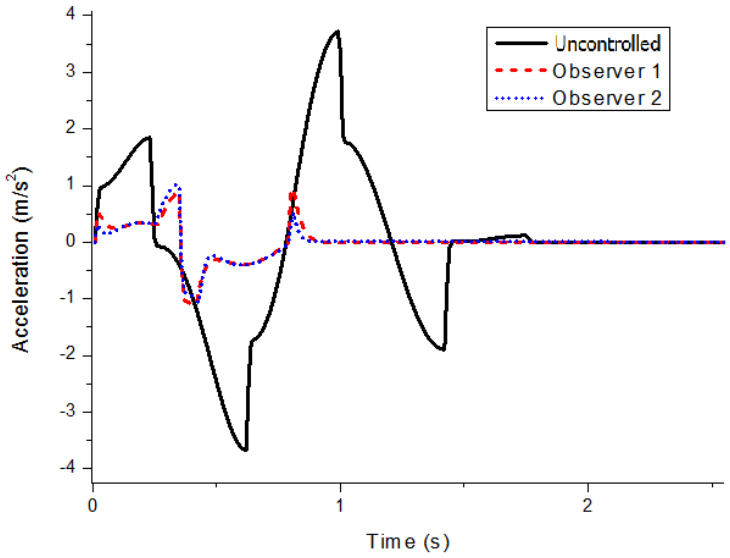

Figure 4-23. Acceleration of driver body.

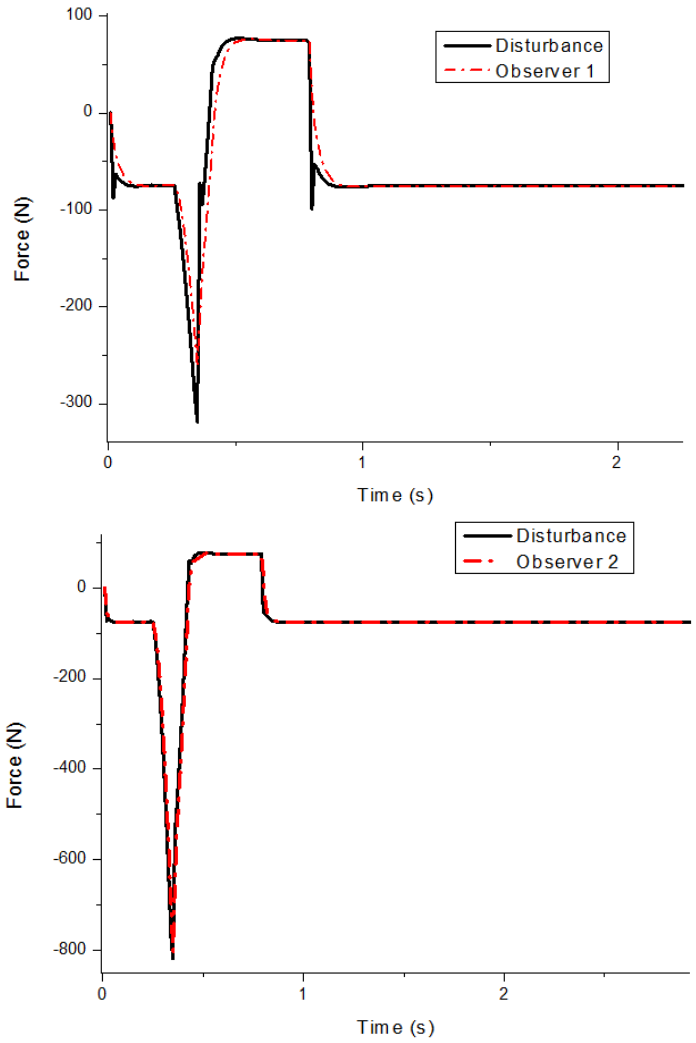

Figure 4-24. Observer performance.

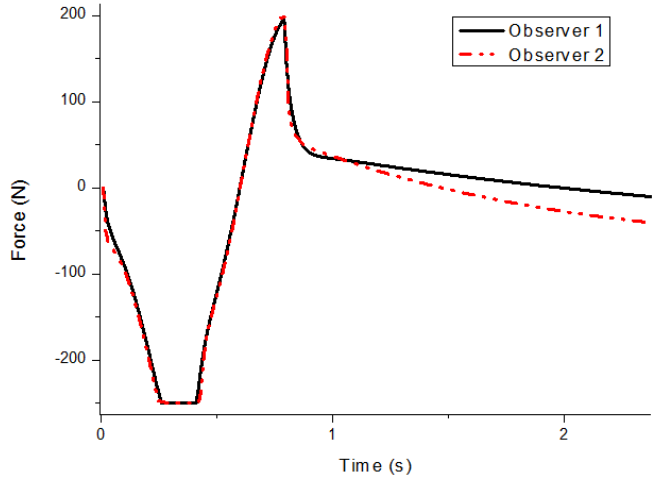

Figure 4-25. Saturated control force.

Figure 4-26 shows the vibration transmissibility of the uncontrolled and controlled active seat suspension with Observer 1. In the low frequency range, the acceleration transmissibility is kept in low magnitude (around 0.4), which means the highest magnitude vibration of heavy duty vehicles can be controlled. Considering that this thesis focuses on implementing the algorithm in practical application, more experimental results and analysis are presented in the following sections.

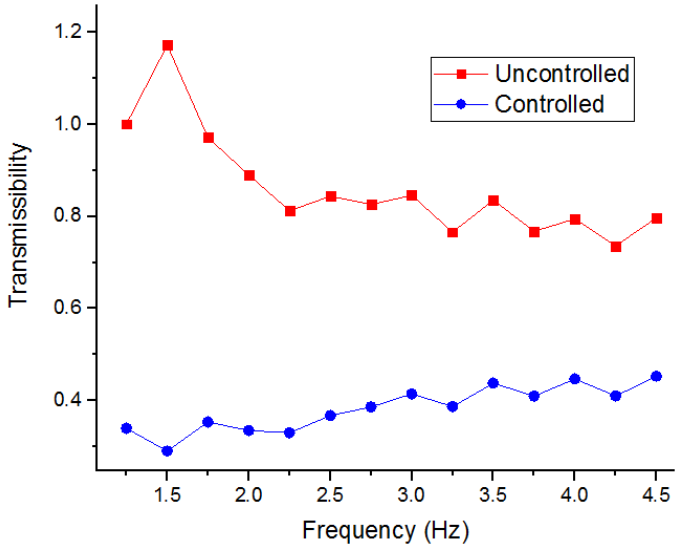

Figure 4-26. Simulation acceleration transmissibility of seat suspension.

4.5.3 Experimental Results

Sinusoidal excitations were applied to the seat suspensions with 55 Kg load. Figure 4-27 shows the acceleration transmissibility of three kinds of seat suspensions. The uncontrolled active seat suspension has a better performance in suppressing resonance vibration than the well-tuned passive seat suspension because of its inner friction. When the excitation frequency is increased, both acceleration transmissibility of uncontrolled active seat suspension and passive suspension decreased. In the frequency range 2.5 to 4.5 Hz, this well-tuned passive seat suspension has a better performance than the uncontrolled active seat suspension, but their transmissibility curves are very close. The controlled active seat

suspension can successfully isolate the low frequency vibration, which proves the proposed controller's effectiveness. It should be emphasised that when vibration frequency is higher than 4 Hz, the passive seat suspension and uncontrolled active seat suspension have low acceleration transmissibility which indicates that seat suspensions can perform good with their passivity in high frequency vibration. On the other hand, the vertical vibration of heavy duty vehicle seat is highest in the frequency range 2 to 4 Hz, because the vehicle (chassis) suspension system has already isolated most of high frequency vibration from uneven road. This test result proves that it is reasonable to focus on low frequency vibration control for heavy duty vehicle seat suspension.

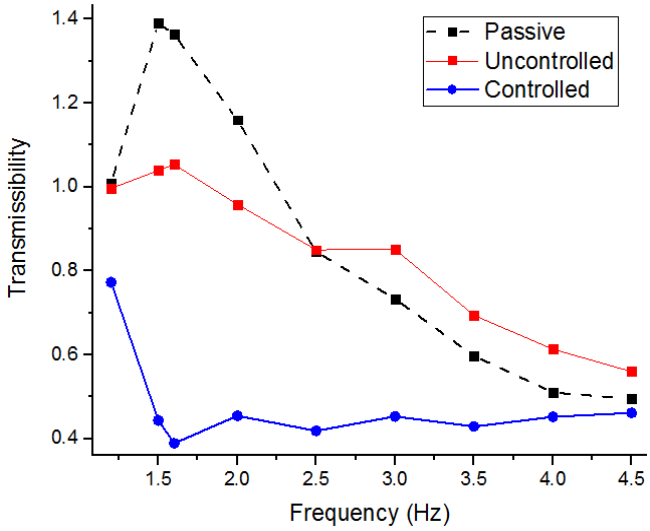

Figure 4-27. Experimental acceleration transmissibility to seat.

The bump excitation can test the controller's transient response performance. Figure 4-28 and Figure 4-29 show the seat acceleration comparison of the passive seat suspension and controlled active seat suspension with different loads. When 55 Kg mass is loaded on the seat, the peak acceleration magnitude is reduced from 2.02 m/s^2 to 1.32 m/s^2. When 70 Kg mass is loaded, the peak acceleration magnitude is reduced from 2.33 m/s^2 to 1.03 m/s^2. The results indicated the TS fuzzy controller with disturbance observer can fast response to bump excitation and reduce the vibration peak magnitude with different loads.

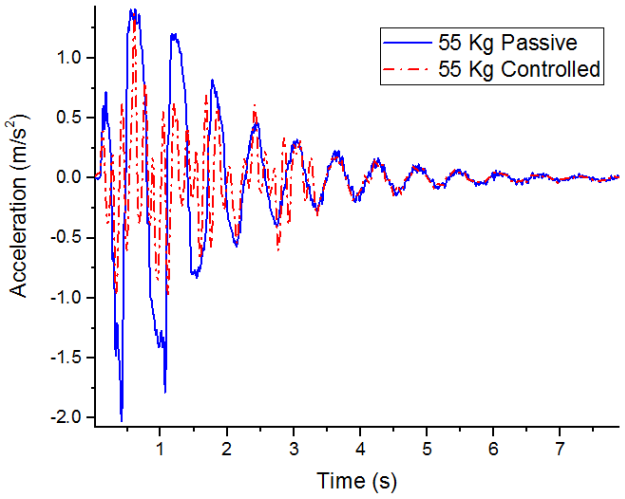

Figure 4-28. Bump excitation with 55 Kg load.

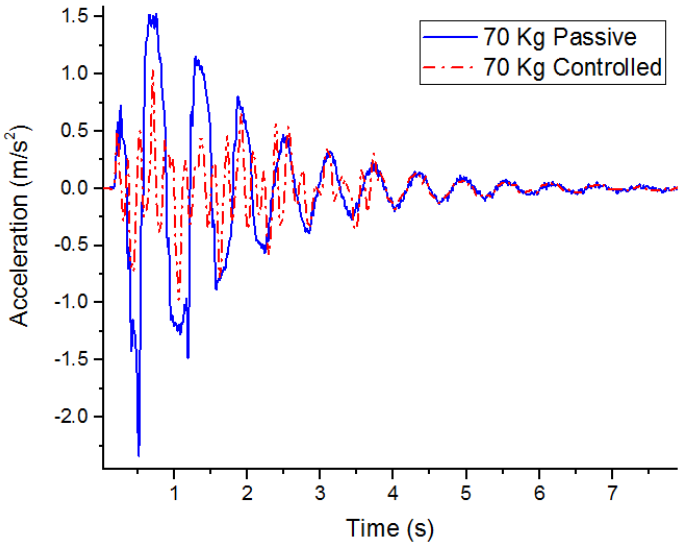

Figure 4-29. Bump excitation with 70 Kg load

Random excitation is always applied to evaluate seat suspension's performance in time domain. Figure 4-30 and Figure 4-31 show seats' acceleration with different loads. It can be seen that, for the uncontrolled active seat suspension, it has a big peak vibration magnitude about 6 m/s^2, this is because the inner friction cannot suppress the big magnitude vibration around resonance frequency; the suspension is unstable. The passive seat suspension can suppress this vibration, but has bigger vibration magnitude in other parts. The controlled seat suspension can keep the seat acceleration at low magnitude all the time. Table 4-6 shows

comparison of the Root Mean Square (RMS) acceleration, there are 45.5% and 49.5% reductions between controlled active seat suspension and passive seat suspension with 55 Kg load and 70 Kg load, respectively.

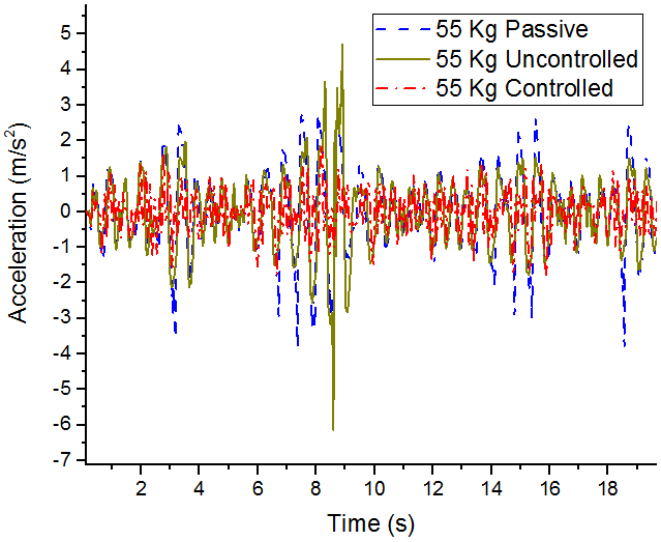

Figure 4-30. Random excitation with 50 Kg load.

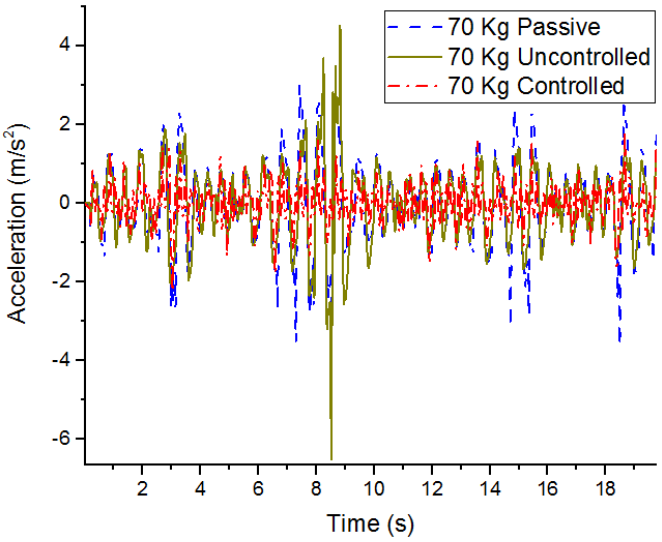

Figure 4-31. Random excitation with 70 Kg load.

Table 4-6. RMS acceleration

	Passive	Uncontrolled (m/s^2)	Controlled	Reduction (%)

	(m/s^2)		(m/s^2)	
55 Kg	1.061	1.067	0.578	45.5
70 Kg	1.005	1.020	0.508	49.5

For further analysing the random excitation performance, Power Spectral Density (PSD) is shown in Figure 4-32 and Figure 4-33. Both passive seat suspension and uncontrolled active seat suspension have a big PSD value around 2 Hz, and have very low value in higher frequency. The controlled active seat suspension can control the vibration in low magnitude at the whole presented frequency range.

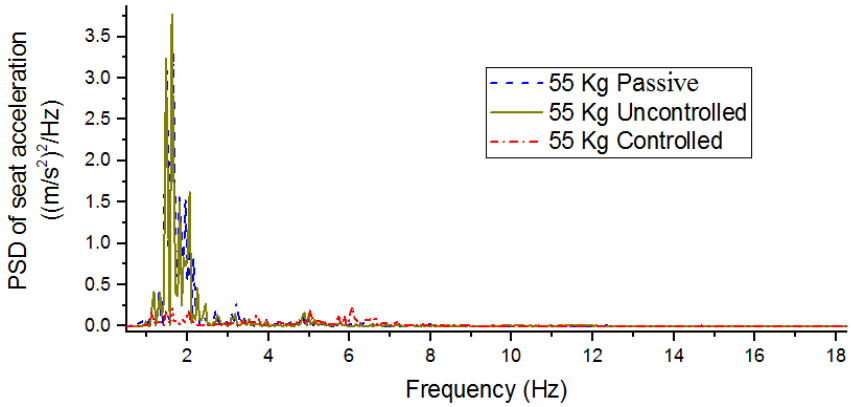

Figure 4-32. PSD of vibration with 55 Kg load.

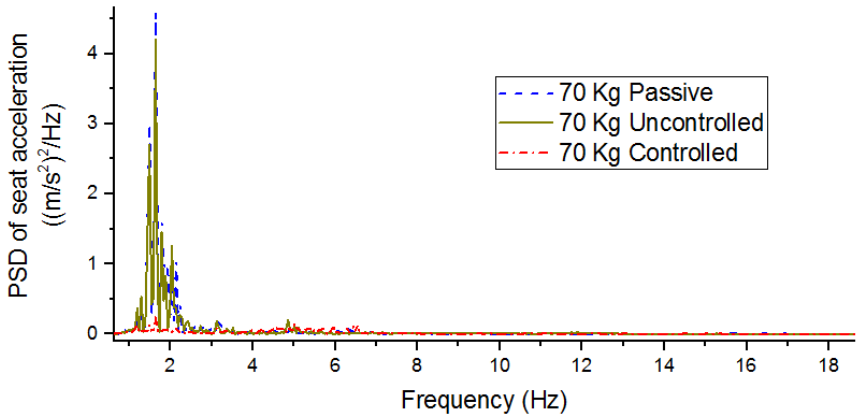

Figure 4-33. PSD of vibration with 70 Kg load.

4.6 Observer Based Terminal Sliding Mode Control

The sliding mode controller is applied in this section. Different from the previous two controllers, the absolute velocity of the seat is estimated and applied in this algorithm.

4.6.1 Control algorithm

4.6.1.1 Active seat suspension with driver body model

An active seat suspension is shown in Figure 4-34, where m_s is the seat frame mass; m_c is the seat cushion mass; the driver body mass is composed of thighs m_1, lower torso m_2, upper torso m_3 and head m_4. z_s, z_c and $z_{1\sim4}$ are the displacements of the corresponding masses, respectively, and z_v is the cabin floor displacement. k_f and f_r are the seat suspension stiffness and inner friction, respectively. u is the actuator output. k_c, c_c, $k_{1\sim4}$ and $c_{1\sim4}$ are defined in Table 4-7. Different from the applied models in the previous sections, this model has considered a 4-DOF driver body model.

The dynamic motion equations for the seat-driver model are defined as:

$$m_s\ddot{z}_s = -k_f(z_s - z_v) - f_r + u + k_c(z_c - z_s) + c_c(\dot{z}_c - \dot{z}_s) \tag{4-64}$$

$$m_c\ddot{z}_c = -k_c(z_c - z_s) - c_c(\dot{z}_c - \dot{z}_s) + k_1(z_1 - z_c) + c_1(\dot{z}_1 - \dot{z}_c) \tag{4-65}$$

$$m_1\ddot{z}_1 = -k_1(z_1 - z_c) - c_1(\dot{z}_1 - \dot{z}_c) + k_2(z_2 - z_1) + c_2(\dot{z}_2 - \dot{z}_1) \tag{4-66}$$

$$m_2\ddot{z}_2 = -k_2(z_2 - z_1) - c_2(\dot{z}_2 - \dot{z}_1) + k_3(z_3 - z_2) + c_3(\dot{z}_3 - \dot{z}_2) \tag{4-67}$$

$$m_3\ddot{z}_3 = -k_3(z_3 - z_2) - c_3(\dot{z}_3 - \dot{z}_2) + k_4(z_4 - z_3) + c_4(\dot{z}_4 - \dot{z}_3) \tag{4-68}$$

$$m_4\ddot{z}_4 = -k_4(z_4 - z_3) - c_4(\dot{z}_4 - \dot{z}_3) \tag{4-69}$$

The inner friction f_r can be modelled by several ways [114]. The Coulomb friction model is applied in this research, and is implemented as following way:

$$f_r = \begin{cases} F_0 \mathrm{sgn}(\dot{z}_s - \dot{z}_v) & |\dot{z}_s - \dot{z}_v \geq \mu \\ F_0 \frac{\dot{z}_s - \dot{z}_v}{\mu} & |\dot{z}_s - \dot{z}_v| < \mu \end{cases} \tag{4-70}$$

where F_0 is the coulomb friction constant, μ is a positive constant for setting the bound of friction direction reversion.

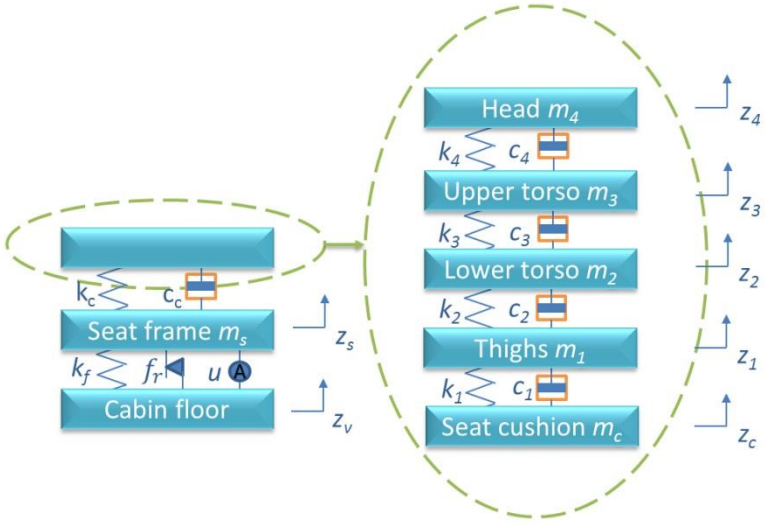

Figure 4-34. Active seat suspension with driver body model.

Table 4-7. Parameters of the seat-driver model.

$\boldsymbol{k_c}$	Stiffness of seat cushion	$\boldsymbol{c_c}$	Damping of seat cushion
k_1	Stiffness of buttocks and thighs	c_1	Damping of buttocks and thighs
k_2	Stiffness of lumber spine	c_2	Damping of lumber spine
k_3	Stiffness of thoracic spine	c_3	Damping of thoracic spine
k_4	Stiffness of cervical spine	c_4	Damping of cervical spine

4.6.1.2 Model simplification

Although previous research has included driver body model into the controller design, in reality, the driver body model is nonlinear, and its parameters will change when the driver changes position; the driver body states are difficult to measure in practical application and the estimation of driver body states will make the controller complicated, thus it is difficult to implement. If the model is simplified to a single DOF model, the controller design procedure

and implementation will be easier. On the other hand, some disturbances due to model simplification will occur. It will be a challenge to use a simplified model to design a robust controller for a multiple DOF model. In this thesis, the simplified model for controller design is defined as:

$$M\ddot{z}_s = -k_f(z_s - z_v) - F_d + u \tag{4-71}$$

$$M = m_s + m_c + m_1 + m_2 + m_3 + m_4 \tag{4-72}$$

$$F_d = f_r + f_{\Delta m} \tag{4-73}$$

where $f_{\Delta m} = m_c(\ddot{z}_c - \ddot{z}_s) + m_1(\ddot{z}_1 - \ddot{z}_s) + m_2(\ddot{z}_2 - \ddot{z}_s) + m_3(\ddot{z}_3 - \ddot{z}_s) + m_4(\ddot{z}_4 - \ddot{z}_s)$ is the disturbance generated from the model simplification; F_d is the bounded total system disturbance satisfying $\left|\frac{F_d}{M}\right| \leq l_g$ where $l_g > 0$.

In the practical scenario, the relative displacement of seat suspension and the seat acceleration are measurable. In this thesis, the state variables are chosen as $x_1 = z_s - z_v$, $x_2 = \dot{z}_s$; and the measurement variables are $Y_1 = z_s - z_v$, $Y_2 = \ddot{z}_s$. Thus the system model (4-71) can be rearranged as:

$$\dot{\mathbf{X}} = \mathbf{A}\mathbf{X} + \mathbf{B_1}(u - F_d) + \mathbf{B_2}d \tag{4-74}$$

$$Y_1 = \mathbf{C_1}\mathbf{X} \tag{4-75}$$

$$Y_2 = \mathbf{C_2}\mathbf{X} + \mathbf{D_2}(u - F_d) \tag{4-76}$$

where $\mathbf{A} = \begin{bmatrix} 0 & 1 \\ -\frac{k_f}{M} & 0 \end{bmatrix}$, $\mathbf{B_1} = \begin{bmatrix} 0 \\ \frac{1}{M} \end{bmatrix}$, $\mathbf{B_2} = \begin{bmatrix} -1 \\ 0 \end{bmatrix}$, $d = \dot{z}_v$, $\mathbf{C_1} = [1\ 0]$, $\mathbf{C_2} = [-\frac{k_f}{M}\ 0]$, and $\mathbf{D_2} = \frac{1}{M}$.

4.6.1.3 Conventional TSM control

The conventional TSM control for models (4-71) is described by the following first–order terminal sliding variable:

$$s = x_2 + \beta x_1^{q/p} \tag{4-77}$$

where q and p are odd integers, $p > q > 0$, $0 < q/p < 1$, $\beta > 0$ is a constant to be designed.

A commonly used state feedback control design is:

$$u = k_f x_1 - M\beta \frac{q}{p} x_1^{q/p-1} \dot{x_1} - M(l_g + \eta)\text{sgn}(s) \tag{4-78}$$

where $\eta > 0$.

Analysis of the stability:

$$\begin{aligned} \dot{s} &= \dot{x_2} + \beta \frac{q}{p} x_1^{q/p-1} \dot{x_1} \\ &= -\frac{k_f}{M} x_1 + \frac{1}{M}(u - F_d) + \beta \frac{q}{p} x_1^{q/p-1} \dot{x_1} \\ &= -\big(l_g + \eta\big)\text{sgn}(s) - \frac{F_d}{M} \end{aligned} \tag{4-79}$$

$$s\dot{s} = -\big(l_g + \eta\big)|s| - \frac{F_d}{M} s \leq -\eta|s| \tag{4-80}$$

It can be difficult to use a conventional TSM controller (4-78) in practical seat suspension control, because it has a number of problems:

The upper seat suspension absolute velocity cannot be directly measured in engineering application, so the terminal sliding variable cannot be obtained.

Based on the previous literature [115], gear reducers or similar mechanical systems are applied in the active seat suspension to amplify the actuator's force output. Thus, the friction magnitude is large and cannot be neglected. Because $\left|\frac{F_d}{M}\right| < (l_g + \eta)$, the term related to the sliding variable in the controller needs a big switching parameter and this may cause chattering.

For the case of $x_2 \neq 0$ when $x_1 = 0$ before the system states reach to the sliding surface $s = 0$, the singularity will occur.

To deal with above problems, in this thesis, a modified TSM controller with a disturbance observer and a state observer is proposed. The non-singular TSM controller has been proposed in [108] for state feedback control. When it is applied in the output feedback control, the singularity still exists in the controller which could be solved with a saturated function [103]. In addition, based on ISO 2631-1 [110], when the vibration magnitude of passenger is less than 0.315 m/s^2, it can be evaluated as "not uncomfortable", which indicates that the state variables and the sliding surface are not necessary to converge to zero, but to an ultimate bound. Thus, to simplify the controller implementation, the indirect non-singular TSM control is applied with a saturated function that can guarantee the convergence of the sliding dynamics to the ultimate bound in finite time.

4.6.1.4 Disturbance observer and state observer design

From model (4-74), there are one mismatched disturbance d and one matched disturbance F_d. Combining the analysis in (4-79), the switching parameter of the controller's sliding variable is required to be larger than the bound of the matched disturbance $\frac{F_d}{M}$. Thus, if F_d can be estimated and directly compensated in the controller, a small switching parameter could be chosen and the risk of chattering could be reduced.

The disturbance estimation error can be defined as:

$$\widetilde{F_d} = F_d - \widehat{F_d} = -\frac{1}{\mathbf{D_2}}(Y_2 - \widehat{Y_2}) \tag{4-81}$$

where $\widehat{Y_2} = \mathbf{C_2}\mathbf{X} + \mathbf{D_2}(u - \widehat{F_d})$, because only x_1 is required in the calculation of $\widehat{Y_2}$, $\widehat{\mathbf{X}} = \mathbf{X}$ in this equation.

The basic design concept of the observer is to amend the estimation value by the difference between the estimated value and the real one. Thus, the disturbance observer based on acceleration measurement can be designed as:

$$\dot{\widehat{F_d}} = L_1\left(Y_2 - \widehat{Y_2}\right) = -L_1\mathbf{D_2}\widetilde{F_d} \tag{4-82}$$

Though it is known that F_d is composed of un-modelled dynamics and friction force, there is no information about the derivative of it. In addition, the disturbance F_d may have high frequency components which have been shown in the simulation. If the actual F_d is totally compensated by the controller, the actuator needs to output a fast time-varying force which is not practical and may introduce additional disturbance to the system. Moreover, the dynamics of the disturbance observer is much higher than the disturbance with interested frequency components. Thus, it is reasonable to assume that $\dot{F_d} = 0$ [116-118]. The dynamics equation of the disturbance estimation error can be defined as:

$$\dot{\widetilde{F_d}} = \dot{F_d} - \dot{\widehat{F_d}} = L_1\mathbf{D_2}\widetilde{F_d} \tag{4-83}$$

Furthermore, the state observer can be designed as:

$$\dot{\widehat{\mathbf{X}}} = \mathbf{A}\widehat{\mathbf{X}} + \mathbf{B_1}(u - \widehat{F_d}) + \mathbf{L_2}(Y_1 - \widehat{Y_1}) \tag{4-84}$$

where $\widehat{Y_1} = \mathbf{C_1}\widehat{\mathbf{X}}$.

The estimation error of states is defined as $\widetilde{\mathbf{X}} = \mathbf{X} - \widehat{\mathbf{X}}$, thus, the dynamics of the state observer is:

$$\dot{\widetilde{\mathbf{X}}} = \dot{\mathbf{X}} - \dot{\widehat{\mathbf{X}}} = (\mathbf{A} - \mathbf{L_2C_1})\widetilde{\mathbf{X}} - \mathbf{B_1}\widetilde{F_d} + \mathbf{B_2}d \tag{4-85}$$

Combining (4-83) and (4-85), the dynamics of the two observers' estimation errors can be written as:

$$\dot{\mathbf{e}} = \bar{\mathbf{A}}\mathbf{e} + \bar{\mathbf{B}}d \tag{4-86}$$

where $\mathbf{e} = \begin{bmatrix} \widetilde{\mathbf{X}} \\ \widetilde{F_d} \end{bmatrix}$ $\bar{\mathbf{A}} = \begin{bmatrix} \mathbf{A} - \mathbf{L_2 C_1} & -\mathbf{B_1} \\ 0 & L_1 \mathbf{D_2} \end{bmatrix}$, $\bar{\mathbf{B}} = \begin{bmatrix} \mathbf{B_2} \\ 0 \end{bmatrix}$.

To design the observer gain, the controlled estimation errors are defined as:

$$\mathbf{z} = \mathbf{C_3 e} \tag{4-87}$$

where $\mathbf{C_3} = \begin{bmatrix} 1 & * & * \\ 0 & 1 & * \\ 0 & 0 & 1 \end{bmatrix}$. For convenience of following analysis, $\mathbf{C_3}$ is separated into two matrices, $\mathbf{C_{31}} = \begin{bmatrix} 1 & 0 \\ 0 & 1 \\ 0 & 0 \end{bmatrix}$, $\mathbf{C_{32}} = \begin{bmatrix} 0 \\ 0 \\ 1 \end{bmatrix}$.

Define the Lyapunov function as:

$$V = \mathbf{e}^{\mathrm{T}} \mathbf{P e} \tag{4-88}$$

where $\mathbf{P} = \begin{bmatrix} \mathbf{P_1} & * \\ 0 & \mathrm{P}_2 \end{bmatrix}$ is a positive symmetric matrix.

From (4-86) and (4-88), we have

$$\dot{V} + \mathbf{z}^{\mathrm{T}} \mathbf{z} - \lambda^2 d^{\mathrm{T}} d = \begin{bmatrix} \mathbf{e} \\ d \end{bmatrix}^{\mathrm{T}} \begin{bmatrix} \mathbf{P}\bar{\mathbf{A}} + (\mathbf{P}\bar{\mathbf{A}})^{\mathrm{T}} + \mathbf{C_3}^{\mathrm{T}} \mathbf{C_3} & * \\ \mathbf{B_2}^{\mathrm{T}} \mathbf{P} & -\lambda^2 \mathbf{I} \end{bmatrix} \begin{bmatrix} \mathbf{e} \\ d \end{bmatrix} \tag{4-89}$$

where $\lambda > 0$ is said to be the H_∞ norm bound for the whole observer.

For guaranteeing the convergence of the two observers, we define [119]

$$\Omega = \begin{bmatrix} \mathbf{P}\bar{\mathbf{A}} + (\mathbf{P}\bar{\mathbf{A}})^{\mathrm{T}} + \mathbf{C_3}^{\mathrm{T}} \mathbf{C_3} & * \\ \mathbf{B_2}^{\mathrm{T}} \mathbf{P} & -\lambda^2 \mathbf{I} \end{bmatrix} + \mathrm{diag}[\boldsymbol{\alpha}\mathbf{P} \quad 0] < 0 \tag{4-90}$$

where $\boldsymbol{\alpha} = \begin{bmatrix} \alpha_1 \boldsymbol{I} & * \\ 0 & \alpha_2 \end{bmatrix}$, $\alpha_1 > 0$ and $\alpha_1 > 0$.

Thus, when $d = 0$, we have

$$\dot{V}|_{d=0} \leq -\boldsymbol{\alpha} \mathbf{e}^{\mathrm{T}} \mathbf{P e} = -\boldsymbol{\alpha} V \tag{4-91}$$

This implies,

$$V(t)|_{d=0} \le e^{-\boldsymbol{\alpha}_{min}(t-t_0)}V(t_0), \quad t \ge t_0 \ge 0 \tag{4-92}$$

Hence, actually, the observer (4-83) and (4-85) with $d = 0$ are global exponentially stable with convergence rates α_2 and α_1, respectively.

With $d \neq 0$, we have

$$\|\mathbf{e}\|_2^2 \le \lambda^2 \|d\|_2^2 \tag{4-93}$$

which shows that the system (4-86) has the disturbance attenuation λ.

For solving the LMI (4-90), we define $\mathbf{G_1} = \mathbf{P_1 L_2}$, $\mathbf{G_2} = \mathrm{P_2 L_1}$. the LMI (4-90) is equivalent to

$$\bar{\Omega} = \begin{bmatrix} \mathbf{P_1 A} - \mathbf{G_1 C_1} + (\mathbf{P_1 A} - \mathbf{G_1 C_1})^{\mathbf{T}} + \alpha_1 \mathbf{P_1} & * & * & * \\ -\boldsymbol{B_1}^{\mathbf{T}} \mathbf{P_1} & \mathbf{G_2 D_2} + (\mathbf{G_2 D_2})^{\mathbf{T}} + \alpha_2 \mathbf{P_2} & * & * \\ \boldsymbol{B_2}^{\mathbf{T}} \mathbf{P_1} & \mathbf{0} & -\lambda^2 \boldsymbol{I} & * \\ \mathbf{C_{31}} & \mathbf{C_{32}} & \mathbf{0} & -\boldsymbol{I} \end{bmatrix} < 0 \tag{4-94}$$

By defining the exponentially convergence rate $\boldsymbol{\alpha}$, disturbance attenuation λ, the above LMI can be solved with Matlab LMI toolbox. Thus, the two observer gains are obtained $L_1 = \mathbf{P_2}^{-\mathbf{1}}\mathbf{G_2}$, $\mathbf{L_2} = \mathbf{P_1}^{-\mathbf{1}}\mathbf{G_1}$.

4.6.1.5 Proposed controller

As mentioned above, with the disturbance estimation, the switching parameters of the sliding term can be decreased. A modified TSM controller with disturbance compensation is proposed as:

$$u = k_f x_1 - M\beta \frac{q}{p} \varphi \dot{x_1} - M(\xi + \eta)\mathrm{sgn}(\hat{s}) + \widehat{F_d} \tag{4-95}$$

$$\varphi = \begin{cases} x_1^{q/p-1}, & |x_1| > \epsilon \\ \epsilon^{q/p-1}, & otherwise \end{cases} \tag{4-96}$$

where $\left|\frac{\widetilde{F_d}}{M}\right| \le \xi$, $\hat{s} = \widehat{x_2} + \beta x_1^{q/p}$, the states x_1 and x_2 will converge to an ultimate bound in finite time. $\epsilon > 0$ is a small bound of x_1. This is an indirect way used to deal with the

singularity problem in conventional TSM control [103, 107, 108]. For the seat suspension control, this strategy has practical meaning as mentioned in Section 4.6.1.3. Based on the definition of sliding surface, the estimation error of sliding surface is

$$\tilde{s} = s - \hat{s} = \widetilde{x_2} \tag{4-97}$$

The derivative of the sliding variable is:

$$\begin{aligned}
\dot{s} &= \dot{x_2} + \beta \frac{\mathrm{d}}{\mathrm{d}t} x_1^{q/p} \\
&= -\frac{k_f}{M} x_1 + \frac{1}{M}(u - F_d) + \beta \frac{\mathrm{d}}{\mathrm{d}t} x_1^{q/p} \\
&= -\frac{\tilde{F}_d}{M} - (\xi + \eta)\mathrm{sgn}(\hat{s})
\end{aligned} \tag{4-98}$$

Considering the Lyapunov function as:

$$V_0 = \frac{1}{2} s^2 \tag{4-99}$$

So, its derivative is:

$$\begin{aligned}
\dot{V}_0 &= s\dot{s} \\
&= s\left(-\frac{\tilde{F}_d}{M} - (\xi + \eta)\mathrm{sgn}(\hat{s})\right) \\
&= (s - \hat{s} + \hat{s})\left(-\frac{\tilde{F}_d}{M} - (\xi + \eta)\mathrm{sgn}(\hat{s})\right) \\
&= -(\xi + \eta)|\hat{s}| - \widetilde{x_2}(\xi + \eta)\mathrm{sgn}(\hat{s}) - \hat{s}\frac{\tilde{F}_d}{M} - \widetilde{x_2}\frac{\tilde{F}_d}{M} \\
&\leq -(\xi + \eta)|\hat{s}| + \widetilde{x_2}(\xi + \eta) + \hat{s}\xi + \widetilde{x_2}\xi \\
&= -\eta|\hat{s}| + |\widetilde{x_2}|(\eta + 2\xi)
\end{aligned} \tag{4-100}$$

When $d = 0$, $\widetilde{x_2}$ is globally exponentially stable with convergence rate α_1. If the selected α_1 is big enough to make sure the convergence of the state observer is faster than the sliding surface, we can obtain:

$$\dot{V}_0(t) = s\dot{s} \leq -\eta|\hat{s}| \tag{4-101}$$

Assuming that if $s(0) \neq 0$, the system will reach the sliding mode $s = 0$ within the finite time t_r, i.e., $s(t_r) = 0$, and

$$\dot{s} = -\frac{\eta|\hat{s}|}{s} = \pm\eta \tag{4-102}$$

$$\int_{s=s(0)}^{s=s(t_r)} \mathrm{d}s = \int_0^{t_r} \pm\eta \mathrm{d}t \tag{4-103}$$

i.e.:

$$s(t_r) - s(0) = \pm\eta t_r \tag{4-104}$$

$$t_r = \frac{|s(0)|}{\eta} \tag{4-105}$$

after time t_r, $s(t_r) = 0$ and $d = 0$, in time $t_r + t_s$, $x_1 = 0$, then:

$$x_2 + \beta x_1^{q/p} = 0 \tag{4-106}$$

$$\dot{x_1} = -\beta x_1^{q/p} \tag{4-107}$$

$$\int_{x_1(t_r)}^{0} x_1^{-\frac{q}{p}} \mathrm{d}x_1 = \int_{t_r}^{t_r+t_s} -\beta \, \mathrm{dt} \tag{4-108}$$

Then,

$$-\frac{p}{p-q} x_1^{1-\frac{q}{p}}(t_r) = -\beta t_s \tag{4-109}$$

$$t_s = \frac{p}{\beta(p-q)} x_1^{1-\frac{q}{p}}(t_r) \tag{4-110}$$

Because q and p are positive odd numbers, $p - q$ is even, $x_1^{1-\frac{q}{p}}(t_r) \geq 0$. In finite time t_s, the first system variable will travel from $x_1(t_r) \neq 0$ to $x_1(t_r + t_s) = 0$; in this period of time, $d = 0$, so the second system variable will also travel to 0.

When $d \neq 0$, the observer error has disturbance attenuation λ. In practical scenario, d is bounded, thus $\widetilde{x_2}$ is also bounded. Within the bound $|\hat{s}| > \frac{|\widetilde{x_2}|(\eta+2\xi)}{\eta}$, $\dot{V}_0 < 0$. Thus, it can guarantee that the sliding variable s can enter a bound $|s| < \zeta_1$ in a finite time. Then, the sliding variable ultimately leaves this bound because of the dynamics of the sliding surface. In the end, the sliding variable will stay in a larger domain $|s| < \zeta_2$, where $\zeta_2 > \zeta_1$ resulting in a practical sliding mode.

4.6.1.6 Acceleration data fusion with complementary filter

In order to improve the accuracy of the estimation of x_2, the acceleration data is fused in the algorithm. In theory, $x_2 = \int \dot{x}_2 \mathrm{d}t$, where $\dot{x}_2$ is the upper seat suspension acceleration which can be measured and can accurately indicate the variation rate of velocity. In practical application, the direct integration of acceleration will produce data drift due to the measurement noise and discrete integral. Complementary filter has been widely applied and developed in attitude estimation with IMU where the estimations based on acceleration and rotary rate are fused together [120]. In this thesis, the complementary filter is applied to fuse the integral result and state observer result; then, the convergence characteristic of the extended state observer is combined with the accuracy of the acceleration based estimation. The estimation of x_2 is implemented in discrete-time as:

$$\widehat{x_2}(k+1) = \varepsilon\widehat{x_{2ob}}(k) + (1-\varepsilon)(\widehat{x_2}(k) + y_2\Delta t) \tag{4-111}$$

where $\widehat{x_{2ob}}$ is the estimation from sate observer, Δt is the sample time, k the sample time number, $0 < \varepsilon < 1$ is a weighting parameter needing to be carefully select to keep the convergence of the observer, and at the same time, make the full use of the acceleration.

4.6.2 Simulation Results

In this section, numerical simulations are conducted to show the effectiveness of the proposed controller. The parameters used in the simulation are listed in Table 4-8. $\mu = 0.004$ m/s and $F_0 = 65$ N are chosen for the friction model.

Table 4-8. Model parameter values.

Mass (kg)		Stiffness(N/m)		Damping (Ns/m)	
m_4	5.31	k_4	310000	c_4	400
m_3	28.49	k_3	183000	c_3	4750
m_2	8.62	k_2	162800	c_2	4585
m_1	12.78	k_1	90000	c_1	2064
m_c	1	k_c	18000	c_c	200
m_s	20	k_f	5100		

Firstly, the two observers are designed with the disturbance attenuation $\lambda = 1.2$ and the exponential convergence rate $\boldsymbol{\alpha} = \begin{bmatrix} 1 & 0 \\ 0 & 100 \end{bmatrix}$. By solving Eq. (4-94), $L_1 = -3847$ and $L_2 = [25.8 \;\; 67.5]$ are obtained. The complementary filter parameter $\varepsilon = 0.4$ is applied. Then, in the sliding variable, q and p are odd integers, $p > q > 0$, $0 < q/p < 1$, $\beta > 0$ is a constant to be designed. Thus, $p = 5$, $q = 3$ and $\beta = 0.1$ are chosen in this thesis. Finally, the parameters for TSM controller are designed. Considering $\left|\frac{\widetilde{F_d}}{M}\right| \leq \xi$ and $\eta > 0$, $\xi + \eta = 0.2$ is chosen, and $\epsilon = 0.003$ m is adopted to deal with the singularity problem.

The controller in (4-78), called TSMC with state feedback, is applied for comparison with the assumption that x_2 is measurable. Because $\left|\frac{F_d}{M}\right| \leq l_g$ should be satisfied for this state feedback controller, $l_g + \eta = 0.9$ is chosen.

For validating the proposed controller, the bump excitation is given by:

$$z_r(t) = \begin{cases} \frac{a}{2}\left(1 - \cos\left(\frac{2\pi v}{l}t\right)\right), & 0 \le t \le \frac{l}{v_0} \\ 0, & t > \frac{l}{v_0} \end{cases} \tag{4-112}$$

where $a = 0.05$ m and $l = 0.5$ m are the height and length of the bump [109]. The vehicle forward velocities are set as $v = 5$ m/s and $v = 10$ m/s.

The head acceleration response is shown in Figure 4-35, and the control force of the two controllers is shown in Figure 4-36. Both the two controllers present good performance in controlling the peak acceleration when compared with the uncontrolled seat suspension. Though the control force of the two controllers is very close, the proposed TSMC with observers has the smallest peak acceleration. On the other hand, the head acceleration using TSMC with state feedback converges to zero faster than the one using the proposed controller. As mentioned above, based on ISO 2631-1, the small magnitude of vibration will not affect the driver's comfort. Thus, we can conclude that, the proposed controller has a better performance in improving ride comfort. The control force of the proposed control is smoother, because it applied a smaller sliding parameter. The result also illustrates that, with the higher forward velocity (10 m/s), the peak head acceleration is lower than the case of 5 m/s in the uncontrolled case; this verifies that the passivity of the seat suspension can indeed help to isolate high frequency vibration.

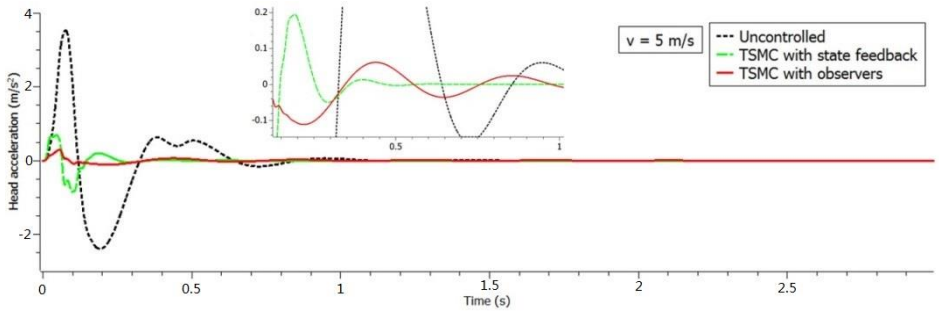

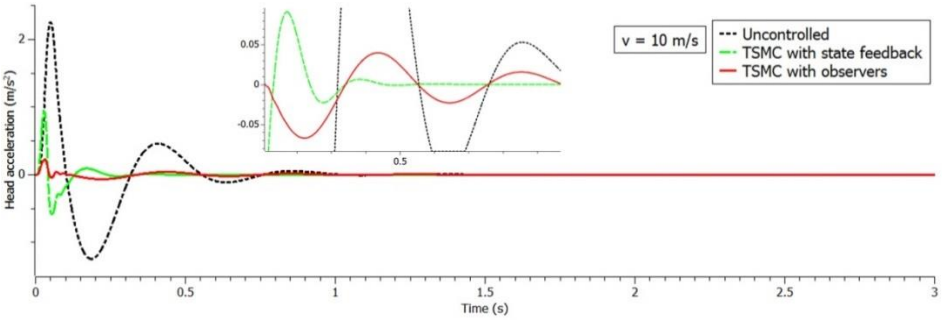

Figure 4-35. Head acceleration.

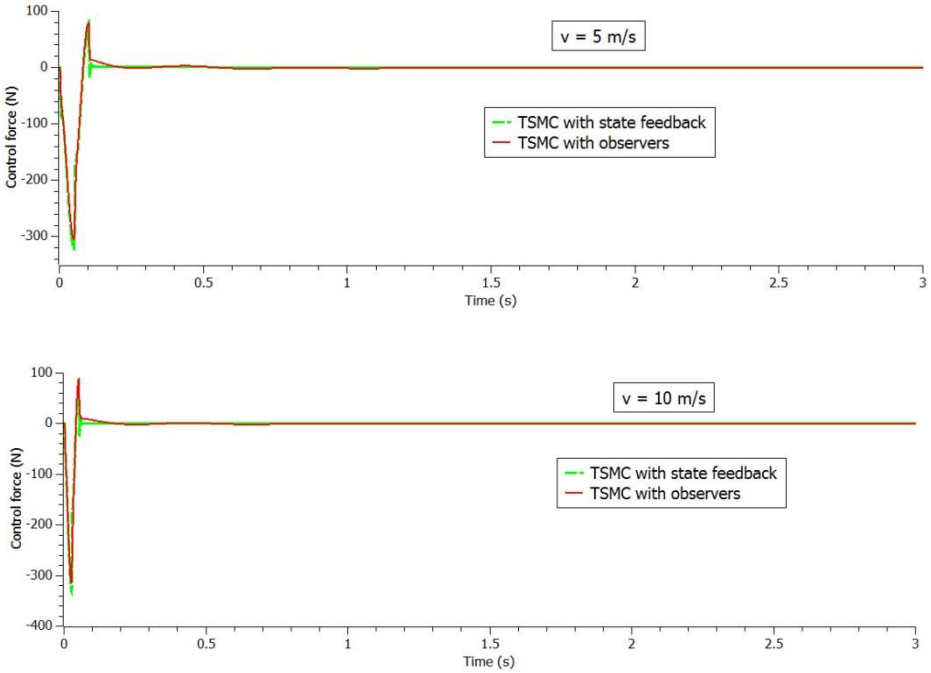

Figure 4-36. Control force.

The disturbance observer performance is shown in Figure 4-37 where the disturbance can be successfully estimated except the high frequency components in both velocities. Figure 4-38 and 4-39 show the comparison of system states where the TSMC with state feedback presents a faster convergence of x_2. In Figure 4-40, the sliding surface of the proposed controller goes to zero slower than the TSMC with state feedback.

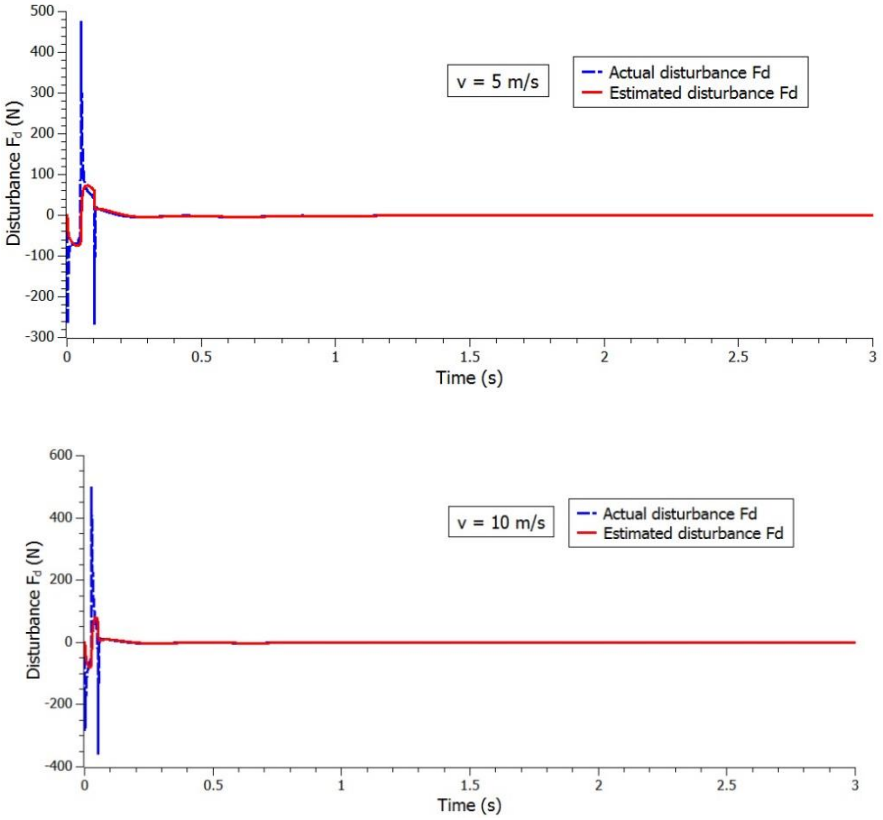

Figure 4-37. Disturbance estimation.

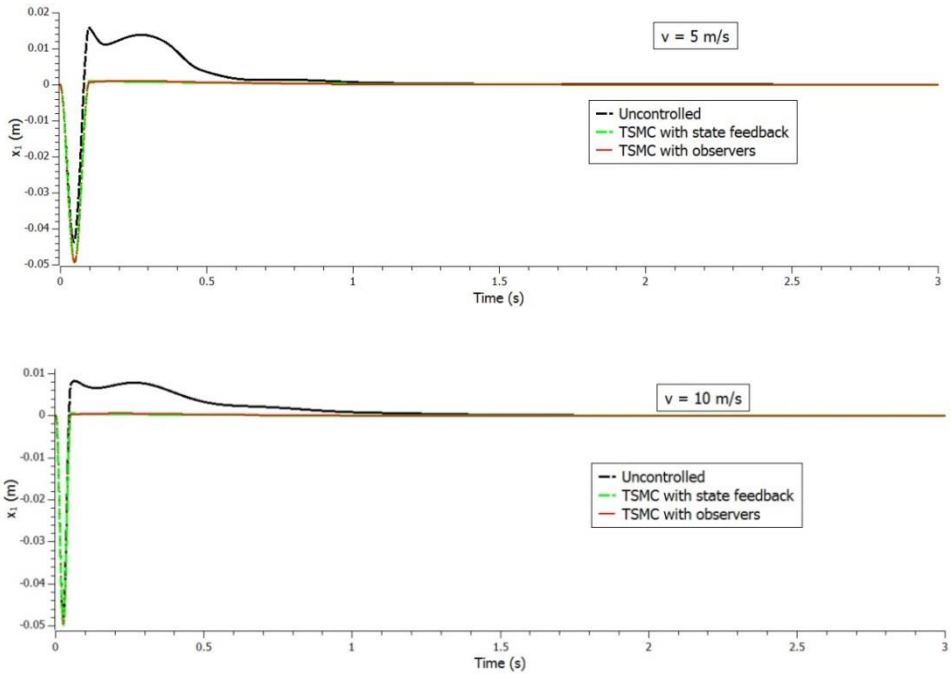

Figure 4-38. Comparison of x_1.

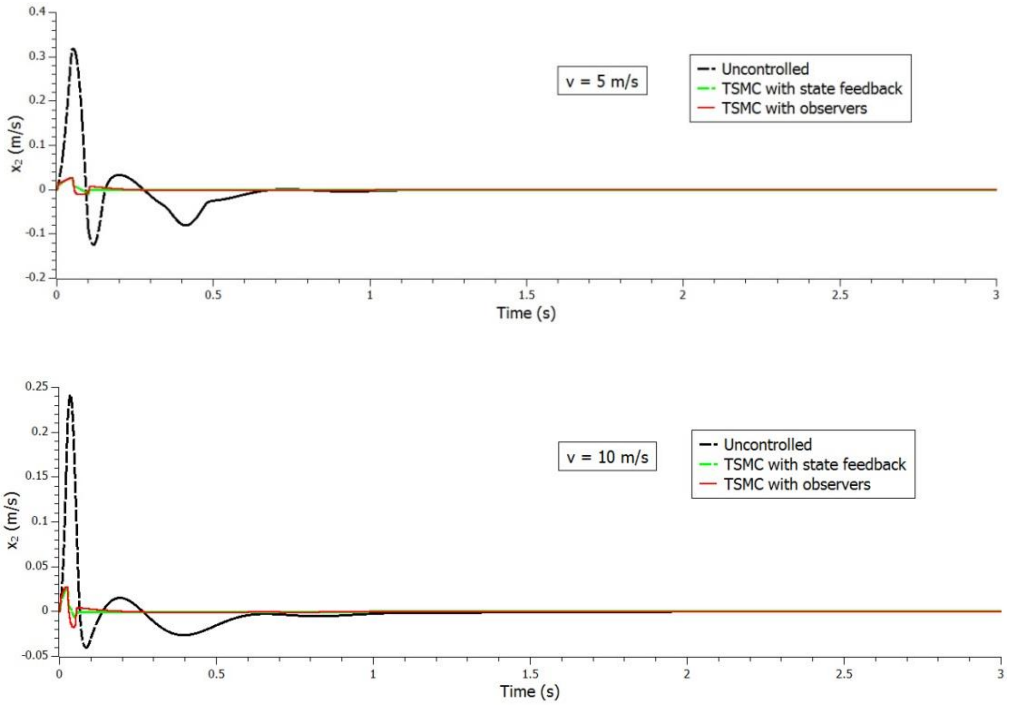

Figure 4-39. Comparison of x_2.

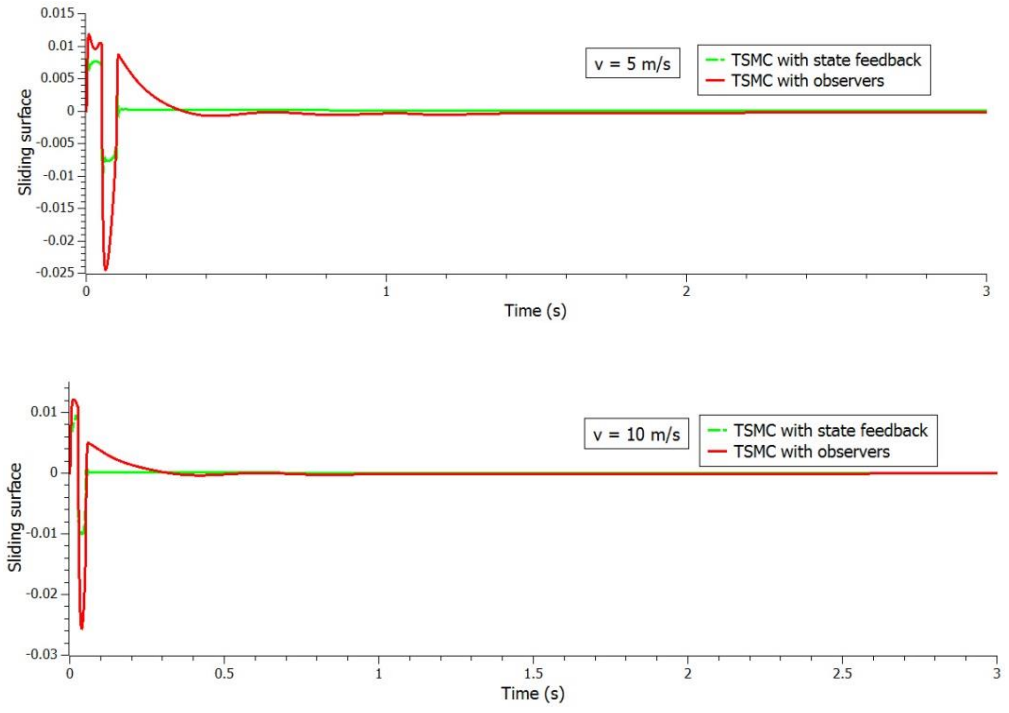

Figure 4-40. Sliding surface.

In the simulation, it is easy to see that, with the state feedback, the sliding surface and system states of the TSMC can have a faster convergence rate; while in the practical application, we

have to observe the system states due to their unavailability. When the disturbance is observed and compensated in the proposed controller, the ride comfort can be further improved.

In addition, the effect of un-modelled dynamics $f_{\Delta m}$ on the displacement of seat z_s is shown in Figure 4-41 where the simplified model without un-modelled dynamics can just roughly describe the whole model. The result indicates the necessity of considering the un-modelled dynamics into controller design.

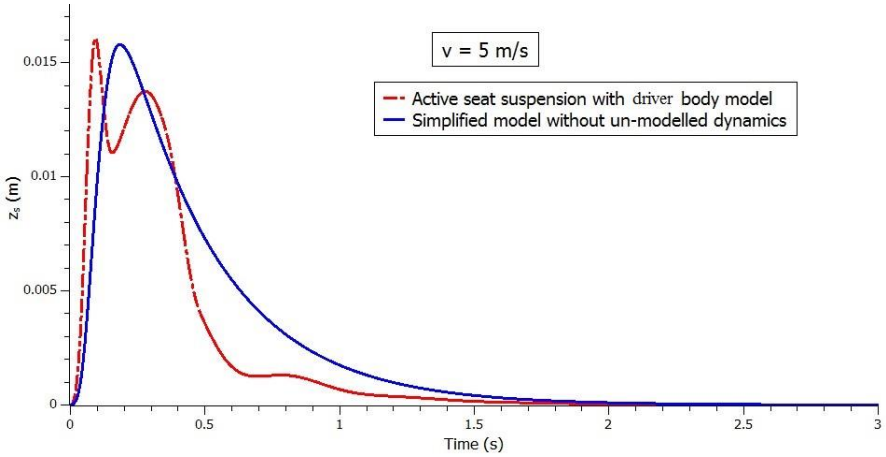

Figure 4-41. The effect of un-modelled dynamics.

4.6.3 Experimental Results

The sinusoidal excitations were used to test the seat suspensions to examine their performance in the frequency domain. The loaded mass on the seat suspension is about 70 kg. It should be emphasised that the active seat suspension and the passive seat suspension are both with nonlinear parameters; with different amplitude sinusoidal vibration, the vibration transmissibility may change a little. Figure 4-42 shows the vibration transmissibility from vibration platform to upper seat suspension. The results show some of the seat suspensions' characteristics. The resonance frequency of the seat suspension is about 1.5 Hz. The passive seat suspension is relatively stiffer than the uncontrolled active seat suspension and the controlled active seat suspension has best performance among the tested frequencies.

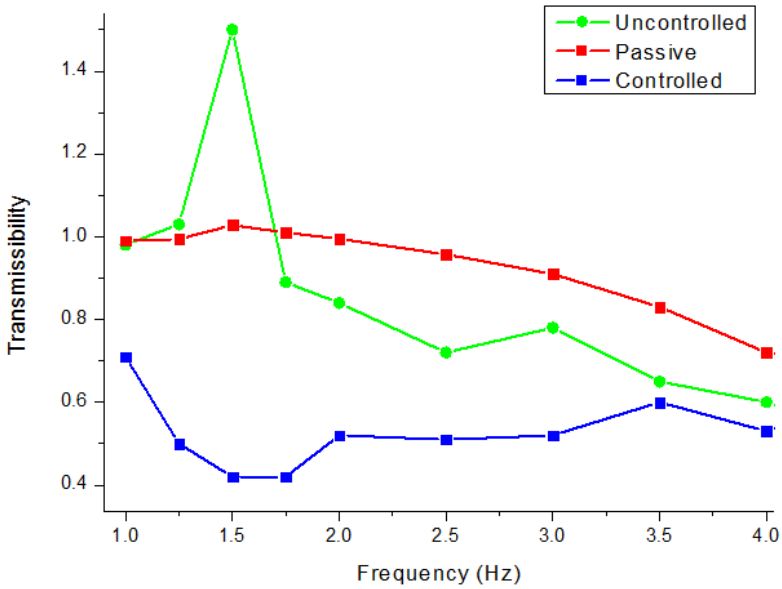

Figure 4-42. Vibration transmissibility.

The seat acceleration with bump excitation is shown in Figure 4-43 where the peak acceleration of the passive seat suspension can be reduced from 1.74 m/s^2 to 1.12 m/s^2, when the active seat suspension is controlled. The 35.6% reduction of the peak acceleration indicates the good transient response of the active control algorithm.

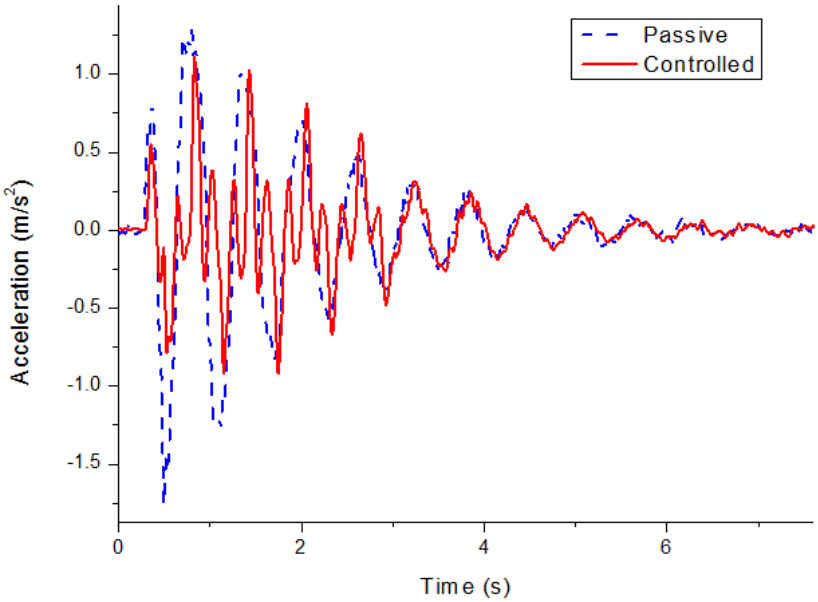

Figure 4-43. Seat acceleration with bump excitation.

The random vibration test result in time domain is shown in Figure 4-44, and the output force is shown in Figure 4-45. After about 8.5 s, the uncontrolled active seat suspension has resonance, and the passive seat suspension also has big acceleration amplitude; the controlled seat suspension has small acceleration magnitude in all the test time.

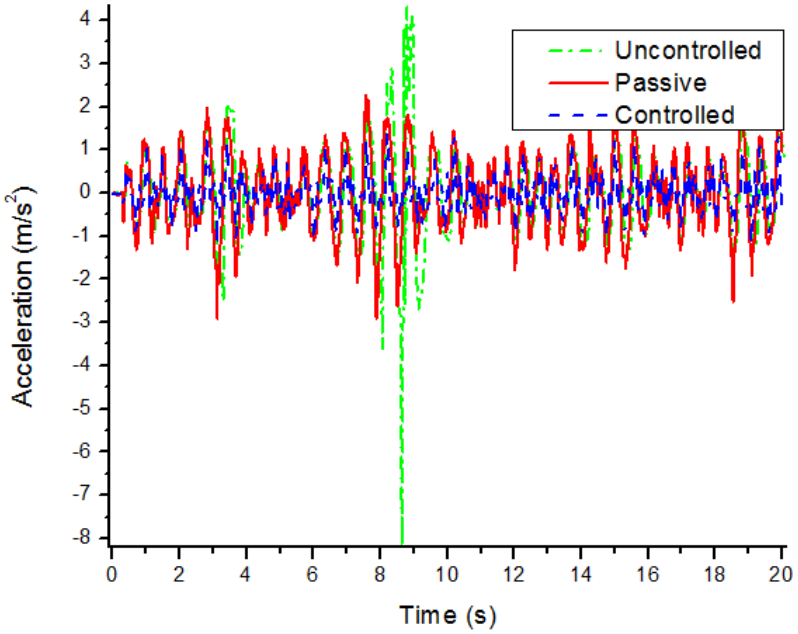

(a)

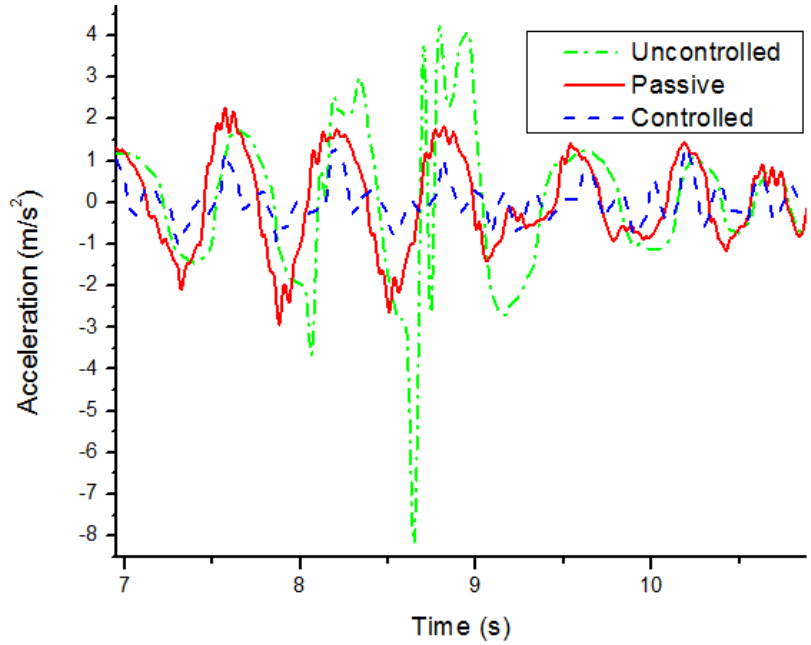

(b)

Figure 4-44. (a) Seat acceleration with random excitation. (b) Zoom in.

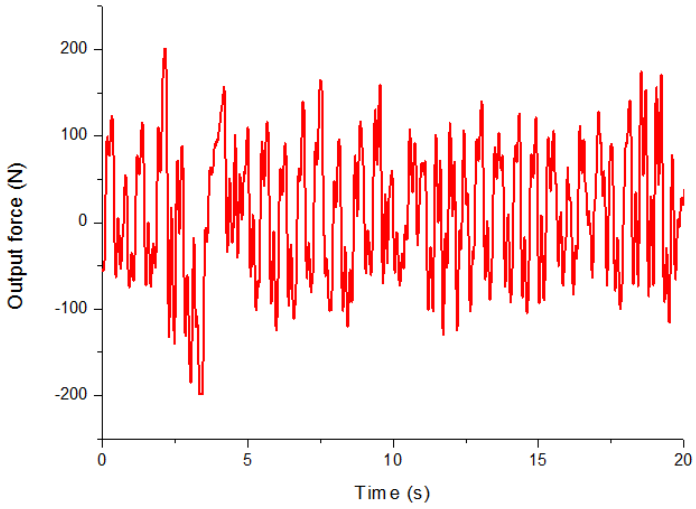

Figure 4-45. Output force.

The Figure 4-46 shows the PSD comparison of the seat acceleration. The uncontrolled active seat suspension and passive seat suspension have big values around resonance frequency, and the controlled active seat suspension has small value in all the presented frequencies. The seat acceleration evaluation based on ISO 2631-1 is shown in Table 4-9 where the column of "Reduction" shows the reduction percentage of the parameters with controlled active seat suspension when compared with passive seat suspension. The passive seat suspension has better performance than uncontrolled active seat suspension both in frequency-weighted RMS and VDV values. The controlled active seat suspension has 34.1% and 32.6 % reduction of frequency-weighted RMS and VDV, respectively. The experimental results indicate that the controlled active seat suspension can greatly reduce the acceleration magnitude and improve the ride comfort.

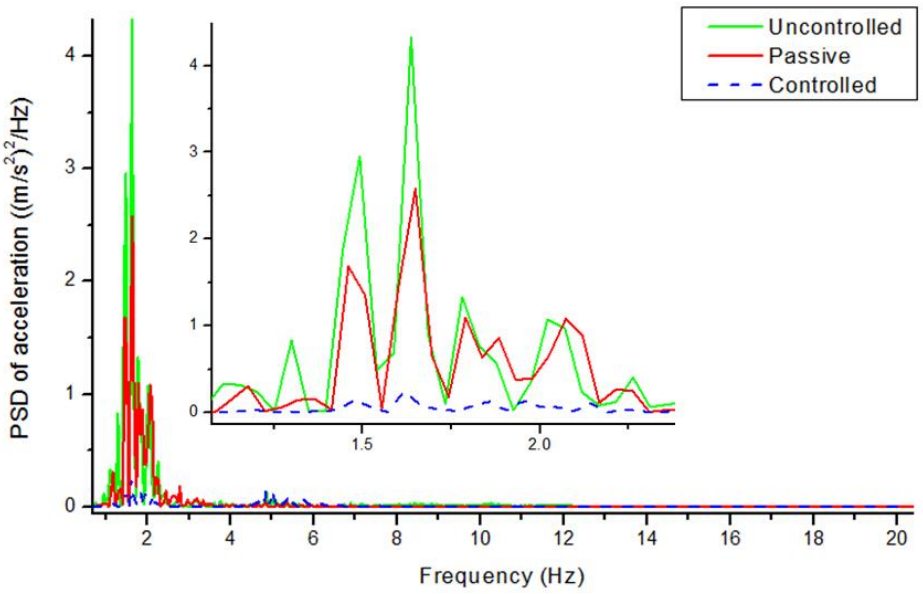

Figure 4-46. PSD of seat acceleration.

Table 4-9. Evaluation of seat acceleration.

	Passive	Uncontrolled	Controlled	Reduction
RMS	0.928	1.066	0.421	54.6%
FW-RMS	0.577	0.692	0.38	34.1%
VDV	1.554	3.036	1.047	32.6%
SEAT	0.767	0.919	0.505	34.1%
VDV ratio	0.659	1.287	0.443	32.6%

4.7 Conclusions

In order to improve the ride comfort for drivers of heavy duty vehicles, an innovative single-DOF active suspension system has been proposed with low cost and concise structure in this chapter. A rotary motor has been applied as the actuator and its output torque is amplified by a gear reducer, thus, a low rated power motor can be used for this active suspension and this can reduce the cost of the suspension set-up. The rotary actuator is installed in the scissors

structure center of a passive suspension. The proposed active seat suspension can be easily modified from a conventional passive suspension. The suspension parameters have been identified by force-displacement response tests, where the friction force is found to have a high magnitude.

A friction observer has been developed based on acceleration measurement which made the control system more sensitive to the vibration. The measurable variables, such as the relative displacement, the relative velocity and the acceleration have been applied as feedback in this controller. 1 to 4.5 Hz sinusoidal excitations have been applied to test the active seat suspension's uncontrolled and controlled performance and a well-tuned passive heavy duty vehicle seat suspension. The bump test shows the active seat suspension has good transient response performance. The random vibration experiment results are analysed with PSD method and ISO 2631-1 standard. The FW-RMS acceleration shows that this active seat suspension can improve ride comfort of a well-tuned passive seat suspension from 'a little uncomfortable' level to 'not uncomfortable' level.

Further, a TS fuzzy controller with a disturbance observer has been designed and validated on the active seat suspension; the variation of driver's weight has been considered in this controller. The designed algorithm introduced seat acceleration into a disturbance observer which can estimate the system disturbance force which includes the friction force, the disturbance caused by model simplification and the output error. The simulation result shows that the acceleration transmissibility can be greatly reduced in the low frequency vibration. Then, the experiments have been implemented; a well-tuned passive seat suspension has been applied to evaluate the performance of the active seat suspension system. Loads of 55 Kg and 70 Kg have been applied to test the TS fuzzy controller. The active seat suspension performs much better than the well-tuned passive seat suspension both in the time domain and the frequency domain. There are a 45.5% and a 49.5% reduction of the RMS acceleration with 55

Kg and 70 Kg loads, respectively. The low frequency vibration can be controlled to a very low magnitude by the active seat suspension.

An observer-based TSM controller with acceleration data fusion has been proposed for the control of an active seat suspension. The control algorithm has been developed considering the practical scenario where only the suspension acceleration and relative displacement can be measured, and the accurate friction model and driver body model are unknown. In order to reduce chattering in the controller, a disturbance observer with acceleration measurement has been designed to reduce the switching gain of the controller. The state observer has been applied to estimate the unmeasurable absolute seat velocity, and a complementary filter has been designed to fuse velocity estimation based on acceleration and the state observer estimation. In the controller design, the output saturation has been considered and analysed. The numerical simulation has been implemented with different bump excitations, and a state feedback TSM controller has been implemented for comparison. The simulation results show that, with the proposed controller, the ride comfort can be further improved when compared with the state feedback TSM controller. Though it has a slower convergence rate to zero, it has a faster convergence rate when the states are outside of a small bound. The control algorithm has been implemented on the active seat suspension prototype, and a well-tuned commercial seat suspension was applied in this experiment to evaluate the performance of the active seat suspension.

Based on the experimental results, the controller in Section 4.4 has best performance in vibration reduction when the random vibration is exerted on the seat suspension; the TS fuzzy control in Section 4.5 has good performance with different drivers; the control method in Section 4.6 is able to suppress the high magnitude random vibration due to the great transient response of a TSM controller. The above three control algorithms and the designed active

seat suspension can improve driver's ride comfort and reduce fatigue, and they are very practical for the practical application.

5 HYBRID ACTIVE AND SEMI-ACTIVE SEAT SUSPENSION

5.1 Introduction

In this chapter, an hybrid active and semi-active seat suspension for heavy duty vehicles is proposed, and its prototype is built; an hybrid control algorithm that used measurable variables (suspension relative displacement and seat acceleration) is designed for the proposed seat prototype. Generally, the semi-active MR seat suspension can reduce the high vibration magnitude in resonance with less energy consumption where a high maximum force output (about 200 N) is required for an active seat suspension. In this seat prototype, an active actuator with a low maximum force output (70 N), which is insufficient for an active seat suspension to control the resonance vibration, is applied together with a semi-active MR damper. The MR damper can suppress the high vibration energy in resonance frequency, and then a small active force can further reduce the vibration magnitude; thus, the performance of a MR seat suspension can be greatly improved.

5.2 Hybrid Active and Semi-active Seat Suspension Prototype

An hybrid active and semi-active seat suspension prototype is designed and built (see Figure 5-1). This prototype is a modification of a normal commercial vehicle seat (GARPEN GSSC7) where the original damper has been removed. An active rotary motor (Panasonic MSMJ042G1U) and a semi-active rotary MR damper are installed on the scissors structures centre of the suspension's two sides, respectively. The rated torque output of the motor is 1.3 Nm; gear reducers, with ratio 20:1 and 8:1, are applied to amplify torque output of the active motor and the semi-active MR damper. The active rotary motor with its gear reducer is working as an active actuator; similarly, the rotary MR damper with its gear reducer is the semi-active actuator.

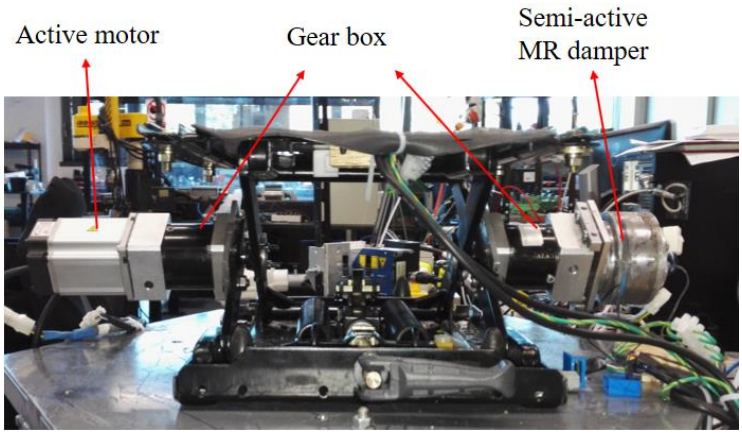

Figure 5-1. The hybrid active and semi-active seat prototype.

Figure 5-2 shows the structural design of the applied rotary MR damper. This rotary MR damper mainly consists of a cylinder, a coil, a shaft, a rotor and the enclosed reservoir that is filled with MRF. Unlike a linear MR damper, there is no spring or gas chamber to provide the initial pressure in the rotary MR damper. For the consideration of magnetic circuit design, the rotor is made of low-carbon steel and the shaft is made of aluminium. When the coil, which is composed by winding the copper wire around the rotor, is energized, the magnetic circuit is

formed as shown in Figure 5-2. This design can guarantee that the magnetic flux passes through the MRF.

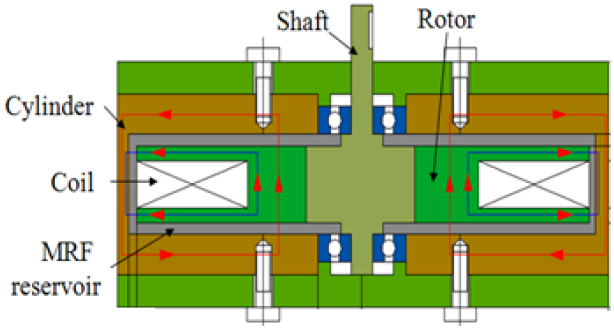

Figure 5-2. Rotary MR damper schematic.

5.3 The Prototype Test and Model Identification

5.3.1 Testing system

The dynamic properties of the seat suspension system were tested and evaluated with a MTS machine (Load Frame Model: 370.02, MST Systems Corporation) as shown in Figure 5-3 which has been introduced in Section 4.2.3.

Figure 5-3. Test system.

5.3.2 Test results

The field, amplitude, and frequency-dependent performance of the seat suspension are evaluated with above described test setup. For field-dependent test, different currents were chosen to energize the magnetic field with same sinusoidal movement routine (with 10 mm amplitude and 1 Hz frequency). Figure 5-4 shows the force-displacement relationships of the seat suspension with different currents. As the area of the enclosed force-displacement loops can indicate the system damping, it can be seen that the damping of this seat suspension can be controlled by the applied current.

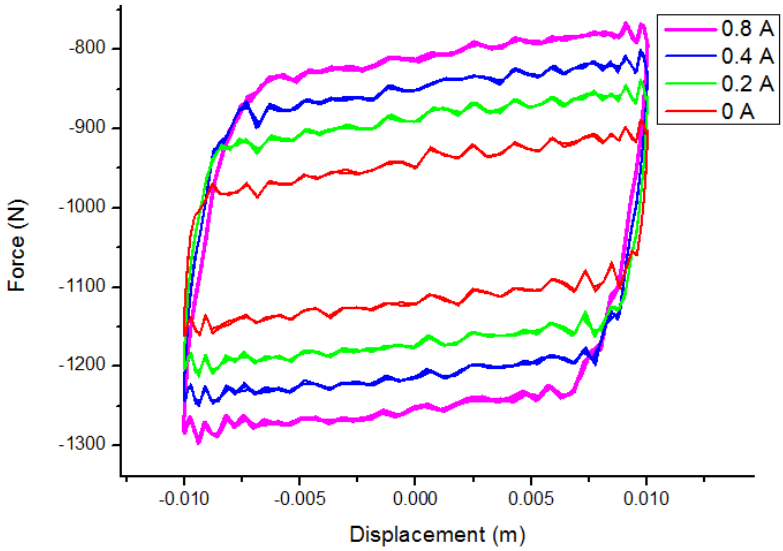

Figure 5-4. Test results with different currents.

The amplitude-dependant performance of the seat suspension is shown in Figure 5-5, when the seat suspension was loaded with sinusoidal signals with different amplitudes (3 mm, 5 mm and 10 mm) at a constant frequency (1 Hz) and current (0.5 A). The response forces of seat suspension are nearly equal in its initial balance position where its relative movement velocities are different and the spring forces are equal. It indicates that with the same current, the saturation force of the MR damper is equal in different velocity. Similarly, the effects of changing frequencies are presented in Figure 5-6 where the amplitude and current are

constants with 10 mm and 0.5 A, respectively. It can be seen that the maximum force has slight variations with different frequencies.

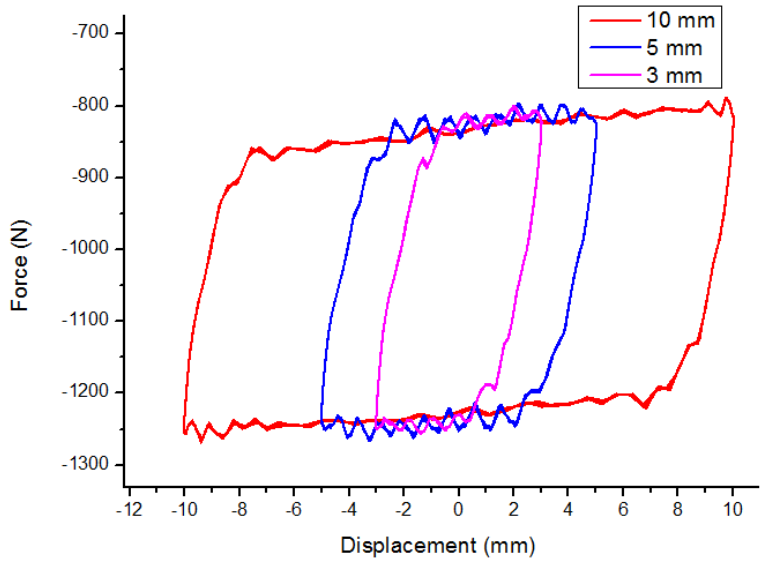

Figure 5-5. Test results with different amplitudes.

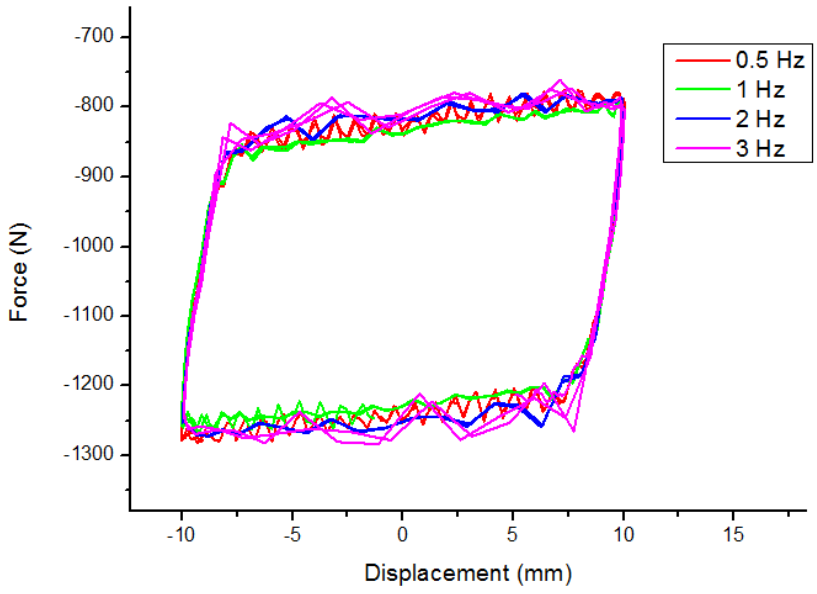

Figure 5-6. Test results with different frequencies.

The above experiments show that the semi-active actuator of the hybrid seat suspension is controllable and has stable properties in different velocities. In addition, the torque output of the active actuator can be accurately controlled by the motor drive. As the transformation of

active actuator from torque output to vertical force output can be easily implemented (Section 4.2.2), the whole seat suspension system is controllable.

5.3.3 Model identification

As two gear reducers are applied in the system, the friction force in the system cannot be ignored. The seat suspension model is shown in Figure 5-7 where z_s and z_v are the displacement of upper and lower platform of the seat suspension, k_s is the spring stiffness, f_r is the inner friction. The Bouc-Wen model is applied to describe the MR damper. Considering that the friction has similar hysteresis phenomenon as MR damper, the inner friction is modelled into MR damper force together.

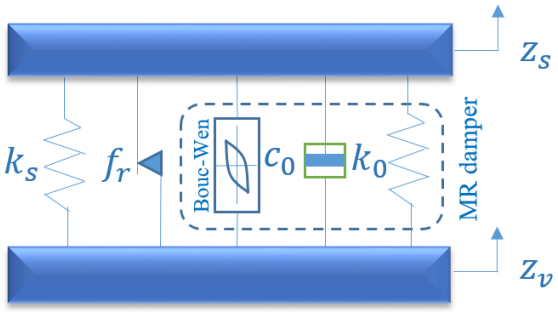

Figure 5-7. Seat suspension model.

The seat suspension model is defined as:

$$x_d = z_s - z_v \tag{5-1}$$

$$F_t = k_s x_d + f_r + F_{mr} \tag{5-2}$$

$$F_d = f_r + F_{mr} = c_1 \dot{y}_d \tag{5-3}$$

$$\dot{y}_d = \frac{1}{c_0 + c_1}[\alpha z_d + c_0 \dot{x}_d + k_0 (x_d - y_d)] \tag{5-4}$$

$$\dot{z}_d = -\gamma_d |\dot{x}_d - \dot{y}_d| z_d |z_d|^{n-1} - \beta_d (\dot{x}_d - \dot{y}_d) |z_d|^n + A_d (\dot{x}_d - \dot{y}_d) \tag{5-5}$$

$$\alpha = \alpha_1 + \alpha_2 I + \alpha_3 I^2 \tag{5-6}$$

$$c_0 = c_{01} + c_{02}I + c_{03}I^2 \tag{5-7}$$

$$c_1 = c_{11} + c_{12}I + c_{13}I^2 \tag{5-8}$$

where I is the current applied to the MR damper. The parameters γ_d, β_d, A_d, n, k_0, α_1, α_2, α_3, c_{01}, c_{02}, c_{03}, c_{11}, c_{12} and c_{13} are used to characterize the MR damper [90, 121]. The optimized values of those parameters are determined by fitting the model with experimental data using MATLAB parameter estimation toolbox. Table 5-1 shows the identified model parameters. The fitting result in Figure 5-8 shows the simulation data matches the experimental data very well.

Table 5-1. The identified model parameters.

$\boldsymbol{\gamma_d}$	7.263e+05		$\boldsymbol{\alpha_3}$	-1.005e+05
β_d	7.359e+05		c_{01}	95.873
A_d	1.860		c_{02}	9.428e+02
n	2		c_{03}	-5.249e+02
k_s	4600		c_{11}	1.338e+04
k_0	3.519e+02		c_{12}	-5.981e+04
α_1	7.553e+04		c_{13}	3.078e+05
α_2	1.972e+05			

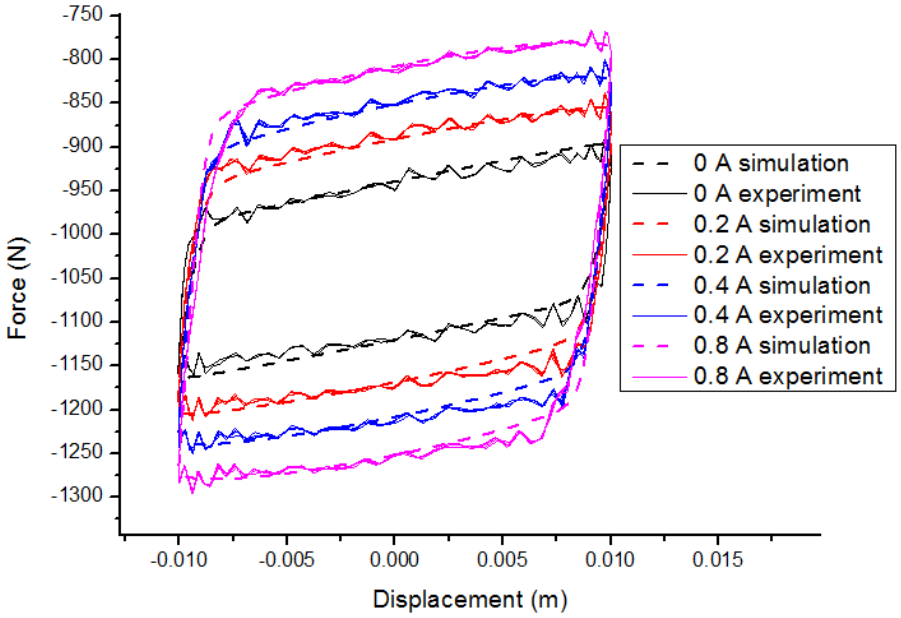

Figure 5-8. The fitting result of model.

5.4 Control Algorithm

This section proposes a control algorithm for the hybrid active and semi-active seat suspension. This algorithm is based on a modified semi-active on-off control method with the compensation of small active force when the MR damper is off. The relative displacement and seat acceleration, which can be easily obtained in practical application, are used as control feedback.

5.4.1 Hybrid seat suspension model

The hybrid seat model is shown in Figure 5-9 where m is the mass loaded on the suspension, F_d includes inner friction and variable damping force, and u is the output of active force. The dynamic model of the system can be described as:

$$m\ddot{z}_s = -k_s(z_s - z_v) - F_d + u \tag{5-9}$$

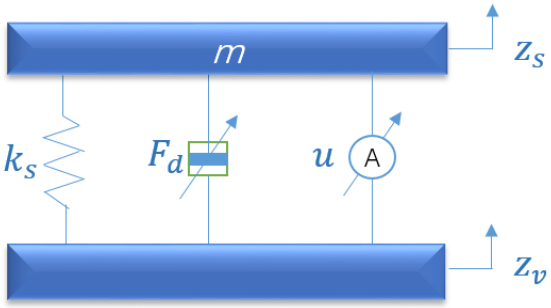

Figure 5-9. Hybrid active and semi-active seat model.

In the practical application, the suspension relative displacement and seat acceleration can be measured; the suspension relative velocity can be obtained from the differential of relative displacement. Therefore, the state variables are chosen as $\mathbf{X} = [z_s - z_v \quad \dot{z}_s - \dot{z}_v]^{\mathrm{T}}$, the vibration disturbance is $d = \ddot{z}_v$, and the measurement variables are $\mathbf{Y_1} = [z_s - z_v \quad \dot{z}_s - \dot{z}_v]^{\mathrm{T}}$ and $Y_2 = \ddot{z}_s$. Thus, combing with (5-9), the system model is defined as:

$$\dot{\mathrm{X}} = \mathrm{AX} + \mathrm{B}_1(u - F_d) + \mathrm{B}_2 d \tag{5-10}$$

$$\mathbf{Y_1} = \mathbf{C_1 X} \tag{5-11}$$

$$Y_2 = \mathbf{C_2 X} + D_2(u - F_d) \tag{5-12}$$

where $\mathbf{A} = \begin{bmatrix} 0 & 1 \\ -\frac{k_s}{m} & 0 \end{bmatrix}$, $\mathbf{B_1} = \begin{bmatrix} 0 \\ \frac{1}{m} \end{bmatrix}$, $\mathbf{B_2} = \begin{bmatrix} 0 \\ -1 \end{bmatrix}$, $\mathbf{C_1} = \begin{bmatrix} 1 & 0 \\ 0 & 1 \end{bmatrix}$, $\mathbf{C_2} = \begin{bmatrix} -\frac{k_s}{m} & 0 \end{bmatrix}$, $D_2 = \frac{1}{m}$.

The seat acceleration is the main optimization objective in the controller design. Therefore, the controlled output is defined as:

$$Z_1 = \mathrm{C}_3\mathrm{X} + D_3(u - F_d) \tag{5-13}$$

where $\mathbf{C_3} = \alpha \mathbf{C_2}$, $D_3 = \alpha D_2$, α is a constant.

5.4.2 Controller design

Firstly, the controllers for the two actuators are designed, respectively.

Controller 1:

The modified on-off control method is a very efficient way for the semi-active actuator; it is designed as $u_I = \text{sat}(I)$, where $\text{sat}(I)$ is a saturation function defined as:

$$I = k_i \ddot{z}_s (\dot{z}_s - \dot{z}_v) \tag{5-14}$$

$$\text{sat}(I) = \begin{cases} I_{max}, & I > I_{max} \\ I & I_{max} > I > 0 \\ 0, & Others \end{cases} \tag{5-15}$$

where k_i is positive constant, I_{max} is the maximum input current for MR damper. This controller is very intuitive. When the direction of the generated force of the MR damper is opposite to the inertia force $M\ddot{z}_s$, it can impede the increase of the acceleration, thus a large damping is expected by loading current into the MR damper; otherwise the damper will be kept in its smallest state (smallest damping). For instant, if the direction of $\ddot{z}_s$ and $\dot{z}_s - \dot{z}_v$ are both positive, thus the force of the MR damper is opposite with the inertia force. In this case, the acceleration can be reduced when the force of the MR damper is increased by loading current. On the contrary, when $\ddot{z}_s$ and $\dot{z}_s - \dot{z}_v$ have different directions, there should have no current input applied to the MR damper to keep the MR damper to be soft.

In the practical application, the measurement noise of sensors is inevitable. This modified on-off controller with saturation can attenuate the frequent variation between the maximum current and no current in the MR damper.

Controller 2:

The inner friction cannot be measured; and the force output of MR damper, which varies based on suspension relative velocity and the output of Controller 1, is also unmeasured. A disturbance observer is applied to estimate the unmeasurable force F_d.

$$\dot{\widehat{F_d}} = L[Y_2 - (\mathbf{C_2 X} + D_2(u - \widehat{F_d}))] \tag{5-16}$$

where the observer gain L is a constant to be designed.

A H_∞ controller with disturbance compensation is constructed as:

$$u = \mathbf{KX} + \widehat{F_d} \tag{5-17}$$

where **K** is the state feedback gain to be designed.

The disturbance observer gain L and H_∞ controller gain **K** can be obtained by solving the following linear matrix inequality (LMI) with Matlab LMI toolbox:

$$\begin{bmatrix} \mathbf{AQ} + \mathbf{B_1 R} + (\mathbf{AQ} + \mathbf{B_1 R})^{\mathrm{T}} & * & * & * \\ -\mathbf{B_1}^{\mathbf{T}} & (\mathbf{G}D_2)^{\mathbf{T}} + \mathbf{G}D_2 & * & * \\ \mathbf{B_2}^{\mathbf{T}} & 0 & -\lambda^2 & * \\ \mathbf{C_3 Q} + \mathbf{D_3 R} & -D_3 & 0 & -\mathbf{I} \end{bmatrix} < 0 \tag{5-18}$$

where $\mathbf{Q} = \mathbf{Q^T}, \mathbf{Q} > 0$, and λ is a given performance index. After solving Eq. (5-18) for matrices **Q**, **R** and $\boldsymbol{G}$, the controller gain is obtained as $\mathbf{K} = \mathbf{RQ^{-1}}$, and the observer gain is $L = \mathbf{P_2}^{-1}\mathbf{G}$. The computation procedure is similar as that used in Section 4.4 and omitted here for brevity. In this study, L is chosen as -2000; **K** is chosen as $[3000 \quad -20]$.

Secondly, the two controllers are hybrid together. The MR damper can only do negative work which means the direction of the force generated by the MR damper should be opposite to the direction of suspension relative movement. When the negative work can dissipate the vibration energy and thus suppress the seat vibration, the output of Controller 1 is not equal to zero. On the contrary, when the seat suspension needs positive work to reduce seat vibration, the MR damper should keep its softest state in order to do least negative work due to its semi-active control characteristic. In the proposed hybrid seat suspension, when the MR damper keeps its softest state, the output of Controller 1 is equal to zero, but the motor will do positive work to reduce seat acceleration. Figure 5-10 shows the control strategy. The Controller 1 is the main controller which controls the current for rotary MR damper. The Controller 2's output will send to the active actuator when Controller 1's output is equal to zero. This control strategy can save the active actuator's energy consumption.

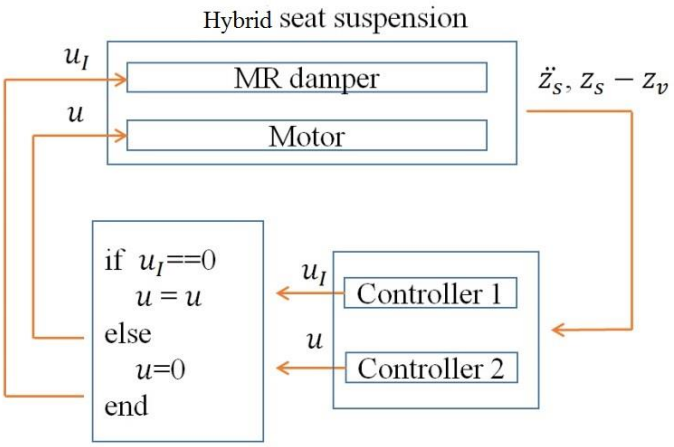

Figure 5-10. Hybrid controller.

5.5 Evaluation

5.5.1 Numerical simulation

In this test, the performance of the hybrid active and semi-active controller applied to the seat suspension model is evaluated. The cushion model is included in the simulation with a stiffness 90000 N/m and a damping 2000 Ns/m. The suspension and driver body mass are 28 Kg and 70 Kg, respectively. The saturated active force is chosen as 70 N which is insufficient to control the resonance vibration independently. The saturated semi-active control current is chosen as 0.7 A, and $k_i = 100$ is applied.

The harmonic excitation test, which was a sweep frequency signal from 1 Hz to 3 Hz in 20 seconds with 30 mm amplitude, was firstly implemented. Figure 11 shows the seat absolute displacements of semi-active control compared with seat suspension with different current (0 A, 0.1 A and 0.7 A). The soft suspension (0 A current) has resonance around the 5 second and performs best in higher frequency. When 0.1 A current is loaded, the resonance amplitude has been greatly suppressed. Although the hard suspension (0.7 A current) has best performance around resonance frequency, it works worst in high frequency. The semi-active control suspension can successfully suppress the resonance vibration. At the same time, it

performs close to a soft suspension (0 A current) at high frequency. This result indicates that the semi-active control can improve the seat suspension performance. Figure 5-12 shows the result comparison of semi-active and hybrid control. The seat displacement of the hybrid control is further reduced in the whole test time range. Especially around the resonance frequency, the MR damper can suppress the resonance vibration, and then a small active force can further isolate the vibration.

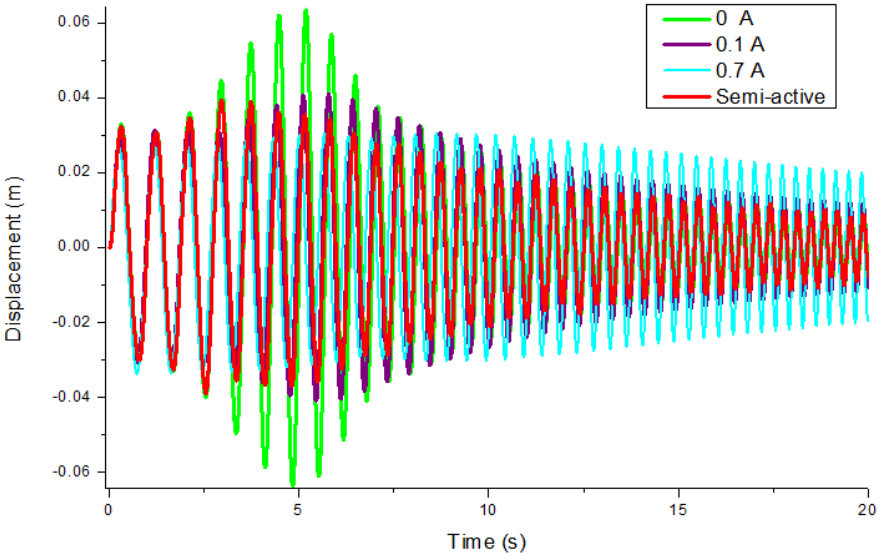

Figure 5-11. Semi-active control result comparison.

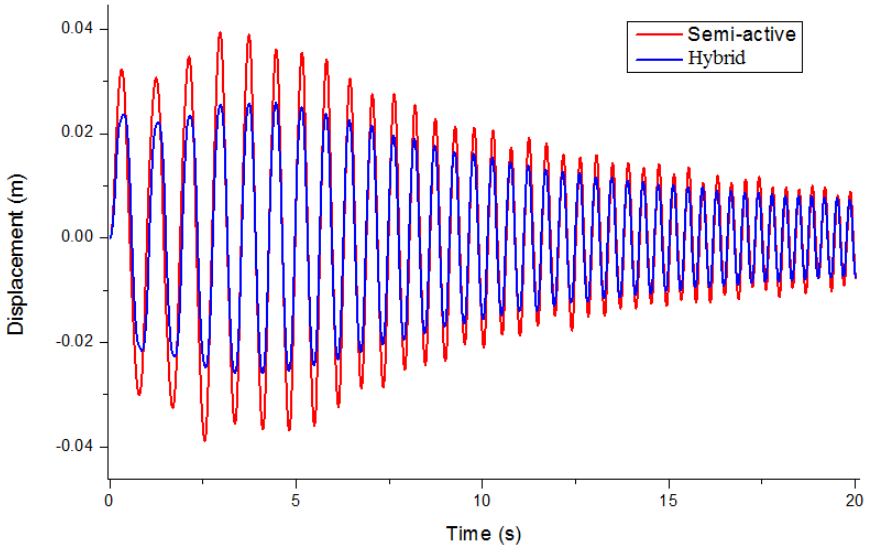

Figure 5-12. Hybrid control result comparison.

The random vibration test was implemented. Table 5-2 shows the RMS acceleration comparison, where the hybrid control has the lowest value, and has a 15.5% reduction compared with semi-active control. The time domain and frequency domain acceleration in Figure 5-13 further validates the control algorithm. The hybrid control has lowest PDS value around resonance frequency, and has low value in higher frequencies vibration.

Table 5-2. RMS acceleration of random vibration (m/s^2)

Hybrid	Semi-active	Power on	Power off
1.09	1.29	1.40	1.46

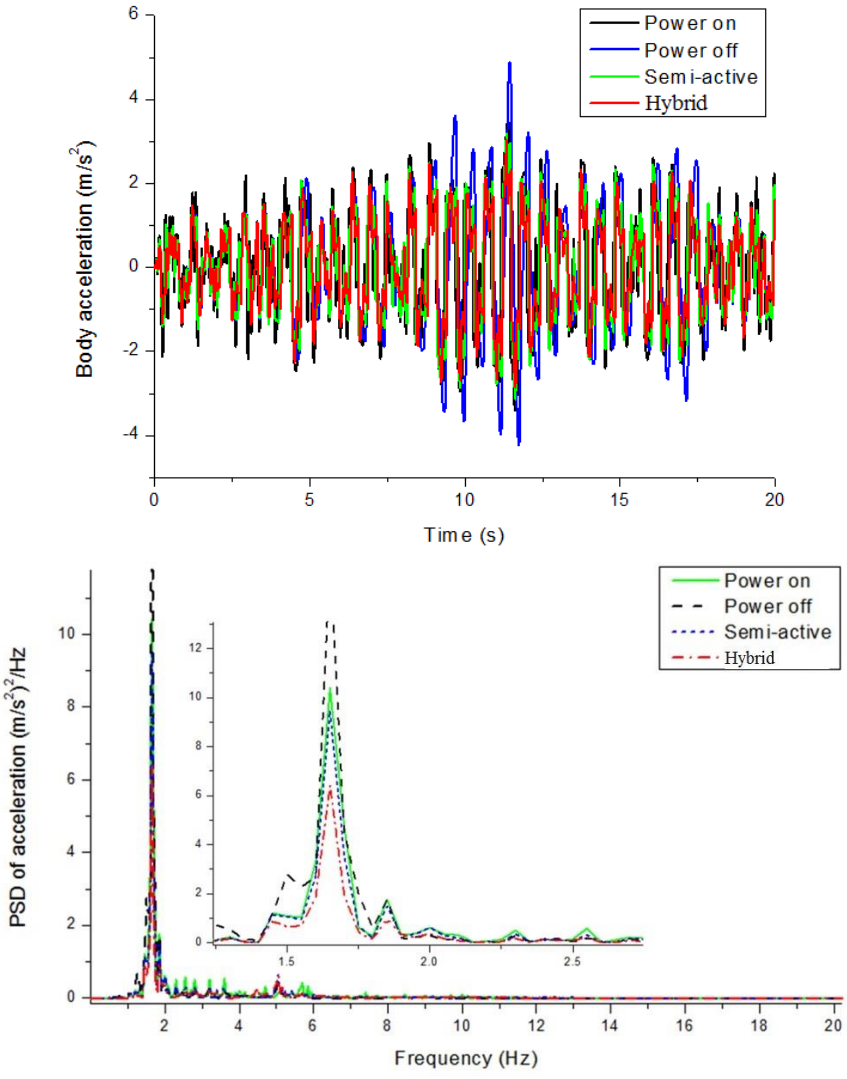

Figure 5-13. Acceleration with random vibration.

5.5.2 Experimental setup

The experimental setup is shown in Figure 5-14. The seat suspension was fixed on the upper platform of the 6-DOF vibration platform. A NI CompactRio 9074 was applied to acquire data and implement designed controller; the control frequency is 500 Hz. Two accelerometers (ADXL203EB) were used to measure the vertical seat acceleration and excitation acceleration, respectively. The suspension relative displacement was measured by a laser displacement sensor (Micro Epsilon ILD1302-100). The desired current signal is amplified by a power amplifier and then used to control the rotary MR damper. The active actuator applied in this prototype can output a maximum force of 150 N. To verify the proposed controller, the active force was limited as ± 70 N.

There are three kinds of experiments. The passive experiment tests the seat suspension's passive response when the MR damper is loaded with different current (0 A, 0.1 A and 0.7 A). In the semi-active control experiment, the semi-active controller is applied. In the hybrid control experiment, the proposed hybrid controller is implemented. It should be emphasised that the active actuator only works when the MR damper is in off state (0 A current). Disturbance may be introduced because the active actuator is turned on and off suddenly. For example, when MR damper turns off, and a 50 N active force is required, the motor output needs to change from 0 N to 50 N. So, a one-order low pass point by point filter module in Libview (a software for developing program in NI CompactRio 9074) was applied to the active control output to avoid its sudden change.

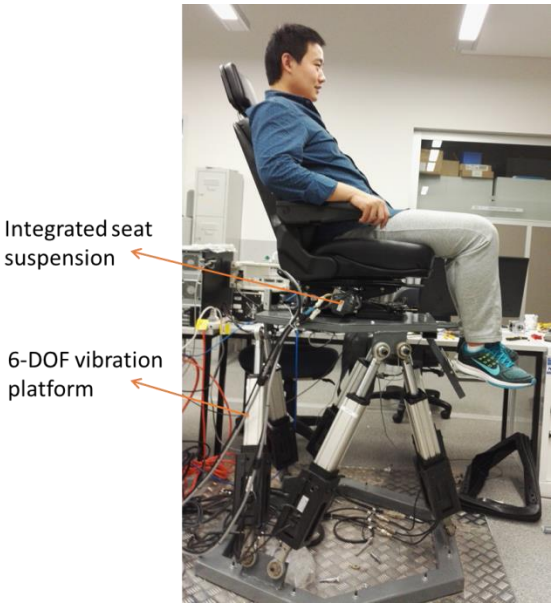

Figure 5-14. Experimental setup.

5.5.3 Experimental results

The sinusoidal excitations were applied to the seat suspensions with 75 Kg load. Figure 15 shows the seat acceleration comparison in both time and frequency domain with resonance frequency (1.6 Hz). When the MR damper is powered off (0 A), the seat has maximum peak acceleration. The hybrid control has the best performance. When the vibration frequency is higher than resonance frequency range, a soft seat suspension should perform better than a hard suspension. Figure 5-16 shows the seat acceleration with 2.4 Hz vibration when the soft seat suspension (0 A) can successfully isolate vibration. When the MR damper is loaded with 0.1 A current, the peak acceleration will greatly increase. The performance of semi-active control is between when the MR damper has 0 A and 0.1 A current. The hybrid control can greatly reduce the acceleration; its acceleration is even lower than the 0 A current case.

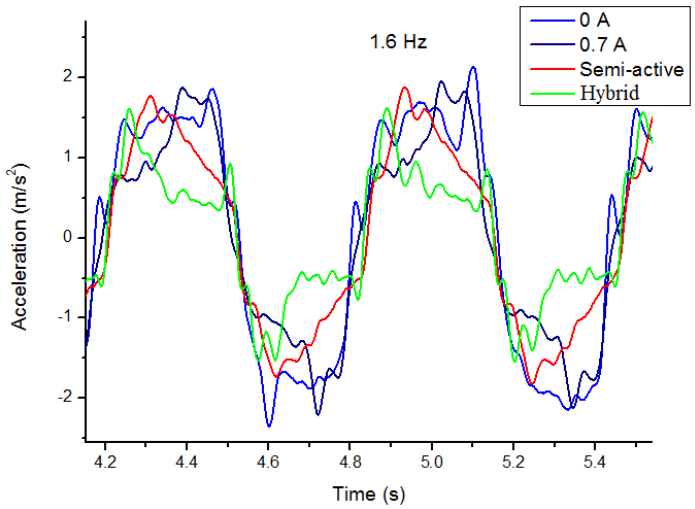

(a)

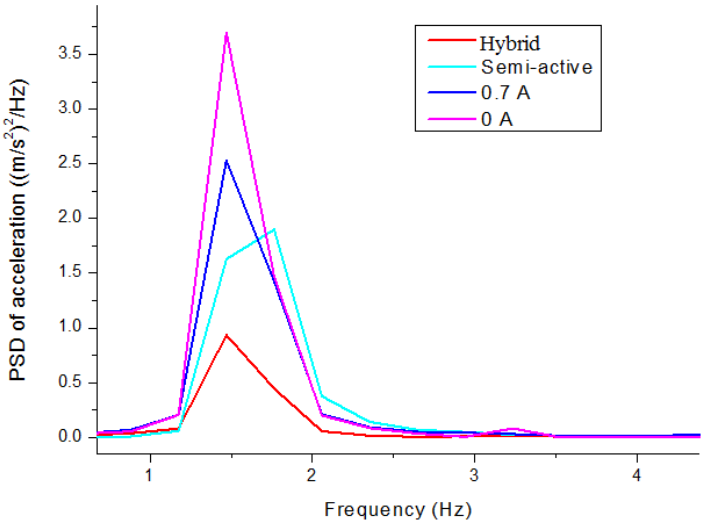

(b)

Figure 5-15. Seat acceleration at 1.6 Hz vibration. (a) Time domain; (b) Frequency domain.

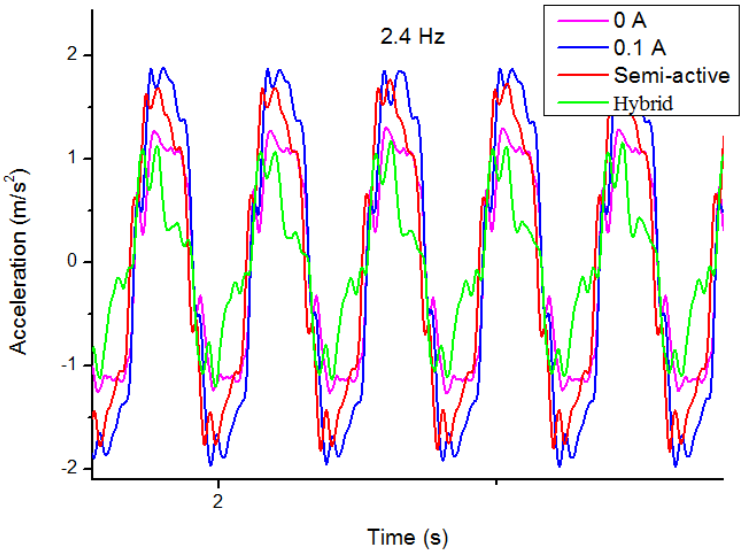

(a)

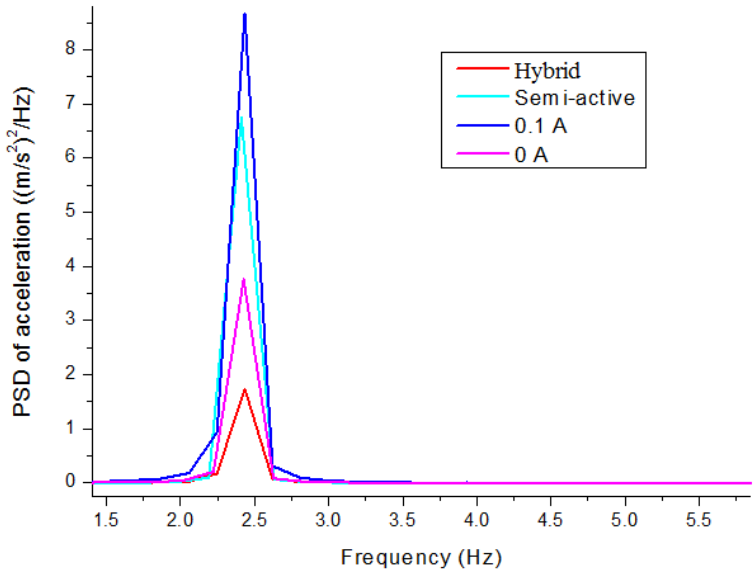

(b)

Figure 5-16. Seat acceleration at 2.4 Hz vibration. (a) Time domain; (b) Frequency domain.

The transmissibility of the seat suspension is shown in Figure 5-17. When the MR damper is powered with 0.7 A current, the vibration transmissibility is around 1.05 in the whole testing frequency range. On the contrary, when the MR damper is power off (0 A), the vibration transmissibility is highest ay 1.6 Hz, and then going down. In other words, the soft seat suspension has the resonance around 1.6 Hz, and starts to isolate vibration when the vibration

frequency is above resonance frequency. The semi-active control seat suspension can suppress the resonance vibration and even performs better than a hard (0.7 A) suspension in 1.6 Hz. The hybrid control has lowest transmissibility in 1.6 Hz, and performs better than the soft seat suspension (0 A) in higher frequency. The experiments result verified the seat suspension's design idea and validated the proposed control algorithm. When the vibration is around resonance frequency, the semi-active control MR damper can dissipate much vibration energy, and then a small active force, which is insufficient to control vibration independently, can successfully further isolate the vibration to a low magnitude. In the higher frequency vibration, the required active force is relative small, so the applied active force can reduce the vibration transmissibility to values lower than a soft seat suspension (0 A). Generally, the semi-active control is hard to perform as good as a passive soft seat suspension with high frequency vibration in practical application.

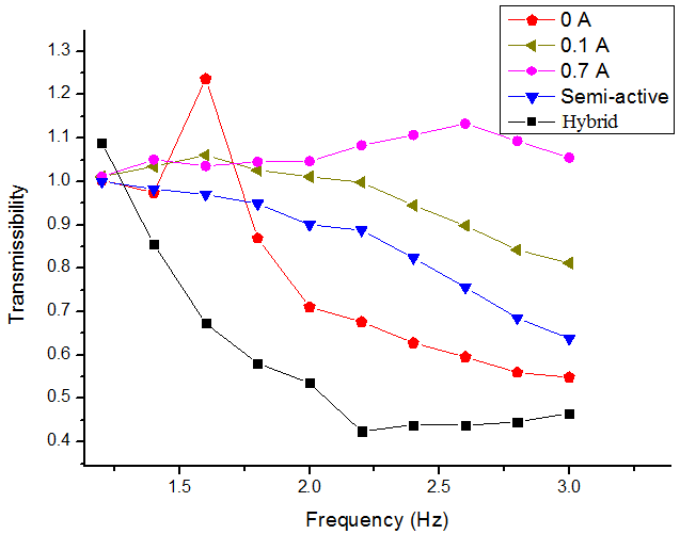

Figure 5-17. Transmissibility.

The random vibration is often used to evaluate seat suspension performance in the time domain. Figure 5-18 shows the seat acceleration with random vibration. When the MR damper is power off (0 A), there is resonance around the 8 second. On the other hand, when the MR damper is power on (0.7 A), its acceleration is obviously larger than other cases

except in the resonance range. Table 5-3 shows the RMS acceleration comparison. The acceleration of hybrid control seat suspension has 47.7% and 33.1% reductions when compared with power on and power off seat suspension. Furthermore, there is 26.5% reduction of RMS acceleration when compared with semi-active control seat suspension. Figure 5-19 shows the PSD value of acceleration, which further indicates that the hybrid seat suspension with a small active force can improve the performance of a semi-active control seat suspension greatly.

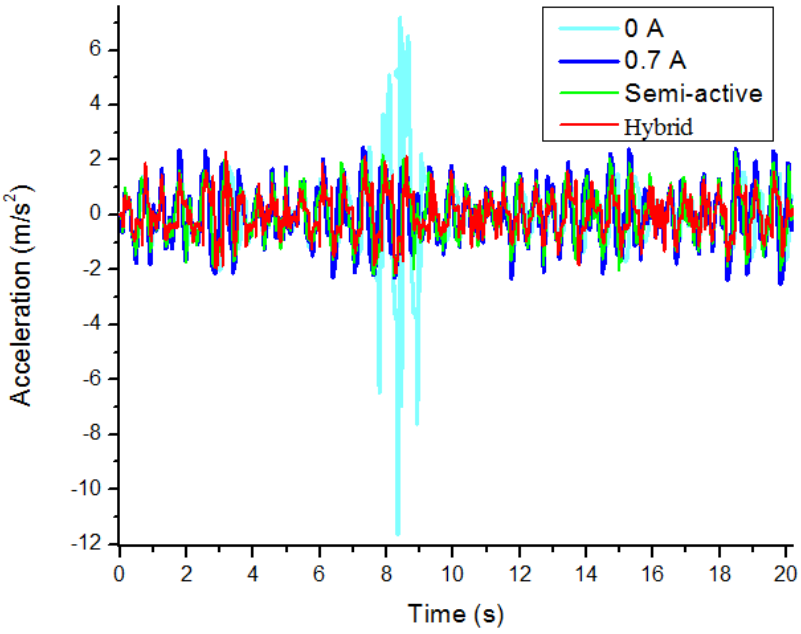

Figure 5-18. Seat acceleration with random vibration.

Table 5-3. RMS acceleration of random vibration (m/s^2)

Power off	Power on	Semi-active	Hybrid
1.3054	1.0195	0.9296	0.6825

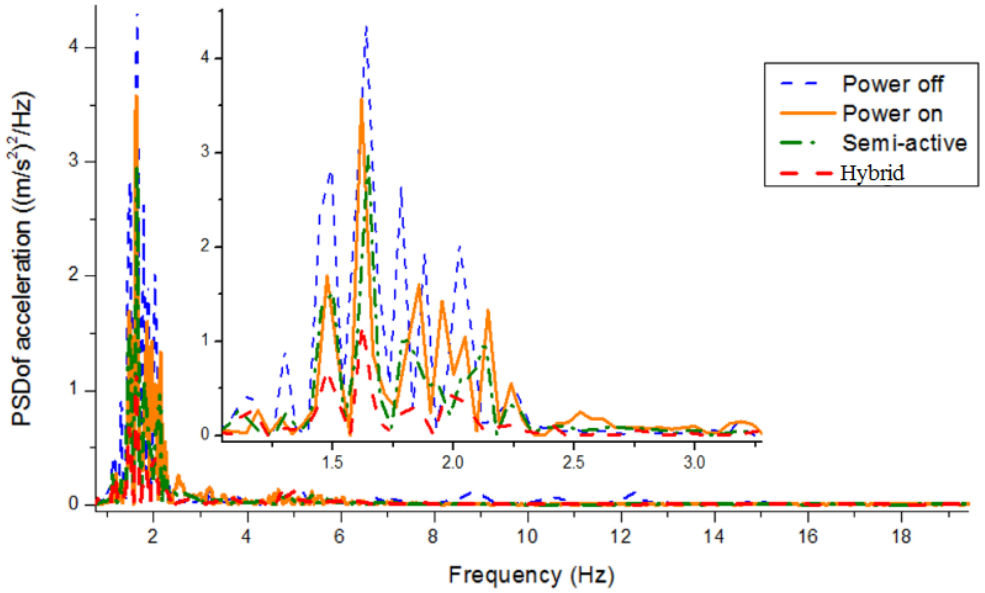

Figure 5-19. PSD of acceleration with random vibration.

5.6 Conclusions

In this chapter, an hybrid active and semi-active seat suspension for heavy duty vehicles has been proposed, built and tested. The proposed control algorithm for the seat suspension prototype applied measureable variables in practical, namely, relative displacement and seat acceleration. The hybrid seat suspension has an active motor and a semi-active MR damper; gearboxes are applied to amplify the actuators torque output. The field, amplitude, and frequency-dependent performance of the seat suspension have been tested with MTS system. The tests results show that the semi-active actuator of the hybrid seat suspension is controllable. The simulation and experiment were implemented and both validated the proposed hybrid seat suspension and controller. In the random vibration experiment, the RMS acceleration of hybrid control seat suspension has 47.7%, 33.1% and 26.5% reductions when compared with power on, power off and semi-active control seat suspension, respectively. The acceleration PSD value further indicates that the hybrid seat suspension has best performance with random vibration. With the proposed seat suspension, the MR damper can suppress resonance vibration with low power consumption, and then a small active force can

further reduce the vibration magnitude; when vibration frequencies are above the resonance frequency, the MR damper is difficult to further improve the ride comfort, then the small active force can work to control the vibration; thus, the proposed seat suspension has much better performance than the semi-active one. When compared with the active seat suspension, the hybrid seat suspension will consume less energy, and because the low power motor is applied, the seat system will be easy to be integrated into the vehicle system. However, the hybrid seat suspension has two sets of actuators; the system is more complicated than the active and semi-active seat suspension. This hybrid seat suspension has a practical value in engineering application.

6 SINGLE-DOF ELECTROMAGNETIC SEAT SUSPENSION

6.1 Introduction

This chapter presents a design of an EMD seat suspension with the capability of continuously varying damping; two implementation methods are proposed to control the damping of the EMD in real time; one applies a variable external resistor, and another one uses a MOSFET switch and a resistor. In the first method, a rotary rheostat is applied to vary the circuit external resistance directly. The external resistance-dependent, frequency-dependent and amplitude-dependent tests have been implemented, respectively; the integrated mathematical model including the seat suspension and the generator can match the result very well. A MOSFET switch module and an external resistor are applied in the second implementation method. A test system is designed to analyze the variable damping characteristic of the EMD. The test result indicates that the damping of the EMD can be controlled by exerting PWM signal with different value of duty cycle on the MOSFET switch. Based on the test result and the kinematic of the seat suspension, the damping variation range of the seat suspension is

derived, The performance of the EMD seat suspensions in terms of vibration control are validated with experiments.

The main contribution of this chapter is that a new kind of semi-active seat suspension is proposed; different from the traditional semi-active seat suspension with a MR damper, the new system requires very small amount of energy; it is easy to manufacture and control.

6.2 Electromagnetic Seat Suspension

The designed variable damping seat suspension (see Figure 6-1) employs the original structure of a commercial passive seat suspension (GARPEN GSSC7); the controllable EMD is installed in the centre of its scissors structure. In this design, no transmission devices (from linear motion to rotary one) are required as most general regenerative vehicle suspension did. A planetary gearbox is applied to amplify the torque output of the EMD (see Figure 6-2); the variable damper of the seat suspension consists of the gearbox and the EMD. Considering that, with the same volume, the AC motor has higher power than DC motor; in this thesis, a 400 W three-phase motor (MSMJ042G1U) is applied for the EMD; the gearbox ratio is selected as 20:1 which has been proven to be appropriate for a seat suspension in the following content.

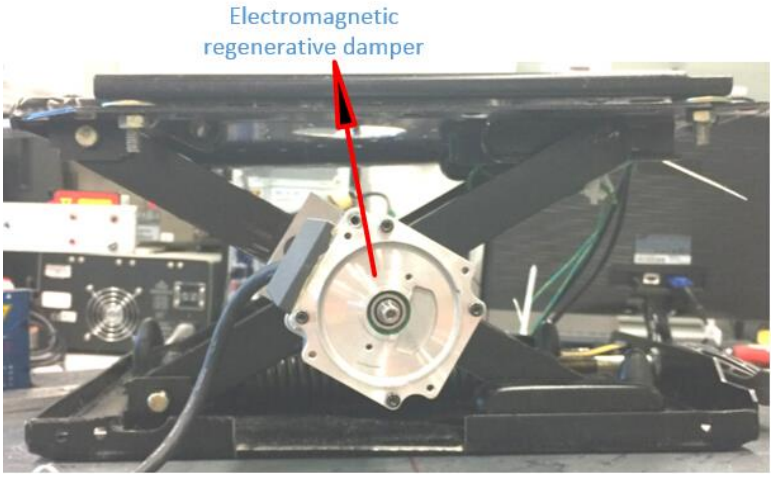

Figure 6-1. Variable damping seat suspension.

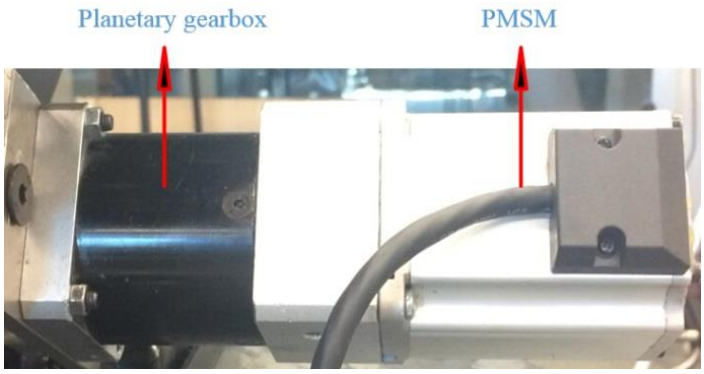

Figure 6-2. Prototype of the variable damper.

6.3 External Resistor Controlled EMD

In this section, a controllable EMD system is proposed with a variable external resistor, and corresponding experiments are implemented to validate the system.

6.3.1 System design

A regenerative seat suspension system schematic diagram is shown in Figure 6-3, where the vibration energy can be stored in a battery by an energy storage circuit. The regenerative shock absorber produces BEM force when it harvests energy from vibration. In this thesis, the BEM force can be controlled for isolating vibration, thus, the regenerative shock absorber can be taken as a semi-active actuator. Generally, a rectifier is applied to transfer the induced AC current to DC current for the easy storage of energy. The principle of this semi-active system is shown in Figure 6-4, where the regenerative shock absorber is working as an electromagnetic generator which has internal resistance and internal inductance. The BEM force can be controlled by varying the external resistance of the circuit in order to control the generated current through the EMD.

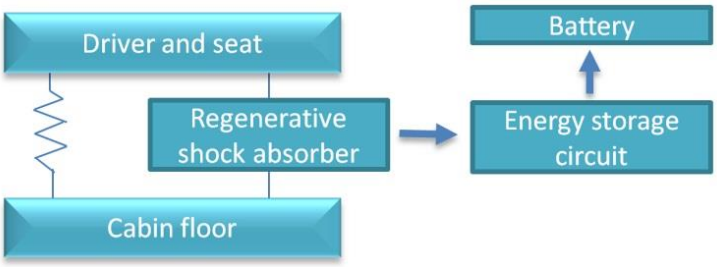

Figure 6-3. Schematic of the regenerative seat suspension system.

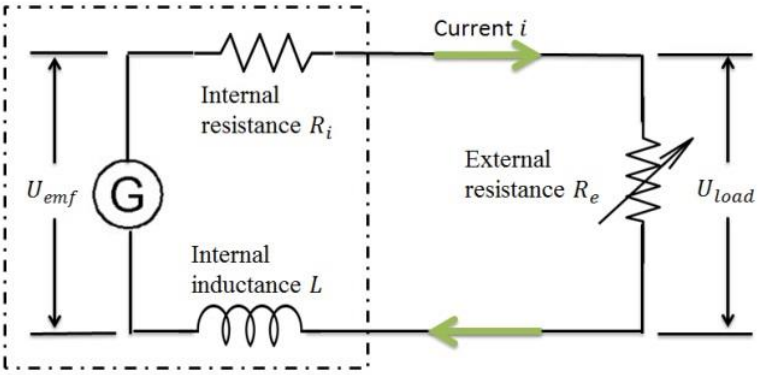

Figure 6-4. Semi-active electromagnetic generator model.

The semi-active control system is built as Figure 6-5. When the seat suspension has relative movement under vibration, the three-phase AC current will be generated and it is converted to DC current by the three-phase rectifier. For easy implementation, a rotary rheostat is applied to vary the circuit external resistance in this thesis, although there are circuits that can change the loop impedance. The resistance of the rotary rheostat can be controlled by a motor which consumes very little power to accurately rotate the rheostat. Comparing with other semi-active seat suspensions such as MR damper seat and ER damper seat, the energy consumption of the proposed seat suspension is much less. Whereas, the energy storage components and circuit have not been included in this system, because this thesis is focusing on investigating the vibration isolation potential of the proposed regenerative seat suspension.

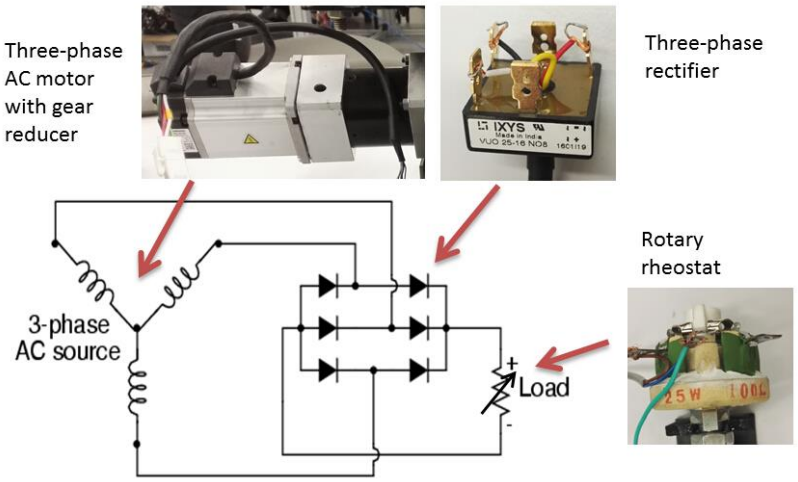

Figure 6-5. Semi-active vibration control system.

6.3.2 System model

The circuit model with three-phase diode bridge rectifier is complicated [122]. Considering that this thesis just aims to emphasise on vibration control, and only low frequency voltages are generated, thus a simplified equivalent model, which is proven effective for describing the system, is applied (see Figure 6-4). The system model can be fully built by combining the kinematics model of the seat suspension (Figure 6-6) and the semi-active electromagnetic generator model. The kinematics model of the seat suspension is defined as:

$$\dot{\theta}(t) = \frac{d}{dt}\left(2\arcsin\left(\frac{H(t)}{L_0}\right)\right) \tag{6-1}$$

$$H(t) = h_0 + h(t) \tag{6-2}$$

$$\omega(t) = r_g \dot{\theta}(t) \tag{6-3}$$

where h_0 is the initial suspension height; $h(t)$ is the suspension relative movement displacement which can be measured in real time; L_0 is the bar length of scissors structure; $\dot{\theta}$ is the rotational rate of scissors structure center; r_g is the gear reducer rate; ω is the rotational rate of the generator.

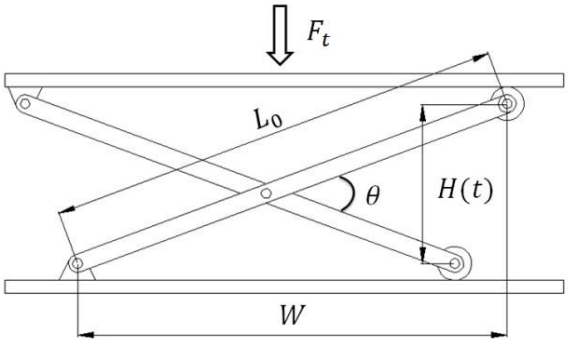

Figure 6-6. Kinematics model of the seat suspension.

The BEM voltage U_{emf} is proportional to rotation speed ω with BEM voltage constant k_e:

$$U_{emf}(t) = k_e\omega(t) \tag{6-4}$$

Based on Kirchhoff's voltage laws, we can get:

$$U_{emf}(t) = L\frac{\mathrm{d}i}{\mathrm{d}t} + i(t)(R_i + R_e) \tag{6-5}$$

where L is the equivalent internal inductance; R_i and R_e are the equivalent internal resistance and variable external resistance, respectively; i is the DC current through external resistance.

The current i in the motor will produce torque:

$$T_i(t) = k_T i(t) \tag{6-6}$$

where k_T is the torque constant.

Considering the inertia of the motor rotor J_m, we have:

$$T_m(t) = T_i(t) + J_m\dot{\omega} \tag{6-7}$$

where T_m is the input mechanical torque on the motor.

The seat suspension upper platform is loaded with force F_t which follows the relationship:

$$-F_t(t) = \frac{2T_m(t)r_g}{\sqrt{L^2 - H(t)^2}} + f_r(t) + k_s h(t) \tag{6-8}$$

where k_s is the seat suspension spring stiffness; the inner friction of the suspension is simply defined as $f_r = f_0 \mathrm{sgn}(\omega)$ where f_0 is the coulomb friction parameters.

6.3.3 System test and parameters identification

The dynamic properties of the regenerative seat suspension were tested by a MTS machine (Load Frame Model: 370.02, MST Systems Corporation), and the voltage of the external resistance was measured with NI myRIO as shown in Figure 6-7. The measured force can be defined as:

$$F = -F_t + f_b \tag{6-9}$$

where f_b is a test bias force.

(a) (b)

Figure 6-7. Model test system. (a) MTS system. (b) NI myRIO.

The external resistance-dependent, frequency-dependent and amplitude-dependent tests were implemented, respectively. Based on the test results, the parameters in the regenerative seat suspension model are identified as Table 6-1.

Table 6-1. Parameters identification.

Internal **resistance** R_{i}	5 Ohm
Voltage constant k_e	0.385 Vs/rad
Torque constant k_T	0.512 Nm/A
Internal inductance L	0.01 H
Rotor inertia J_m	0.26e-4 kg $*$ m^2
Gear reducer ratio r_g	20
Coulomb friction constant f_0	60 N
Length of bar L_0	0.287 m
Initial suspension height h_0	0.01 m
Spring stiffness k_s	4600 N/m
Test bias force f_b	-952.87 N

The external resistance-dependent performance of the seat suspension is shown in Figure 6-8. External resistance-dependent test (amplitude 20 mm, frequency 2 Hz)., when the external resistance was set with different values (0 Ohm, 3 Ohm, 5 Ohm, 10 Ohm and 50 Ohm) at constant amplitude (20 mm) and frequency (2 Hz) sinusoidal load. With the identified parameters, the experimental result (marking as '_exp') matches the simulation result (marking as '_sim') very well. As the area of the enclosed force-displacement loops indicate the system damping, the result shows that the seat suspension damping is decreasing when the external resistance is increased.

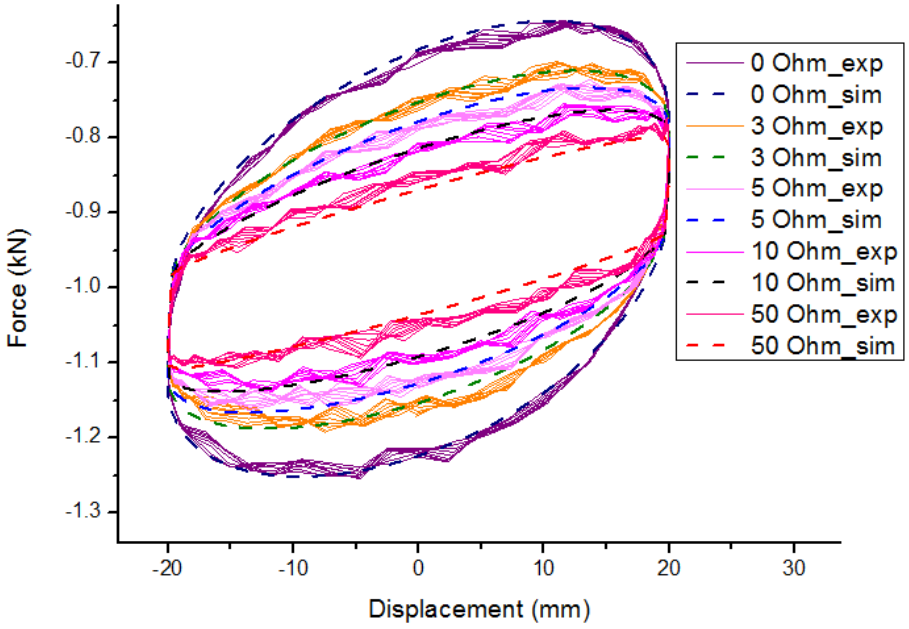

Figure 6-8. External resistance-dependent test (amplitude 20 mm, frequency 2 Hz).

The frequency-dependent and amplitude-dependent test results further verify the accurate of the regenerative seat suspension model (see Figure 6-9and Figure 6-10). When higher frequency sinusoidal movement is loaded with same amplitude and external resistance, the measured force will increase. Similarly, with the same external resistance and same frequency sinusoidal movement, the area of the enclosed force-displacement loop is increasing with the movement amplitude. The results indicate that, with same external resistance, the generated BEM force will increase when the suspension relative velocity is increased.

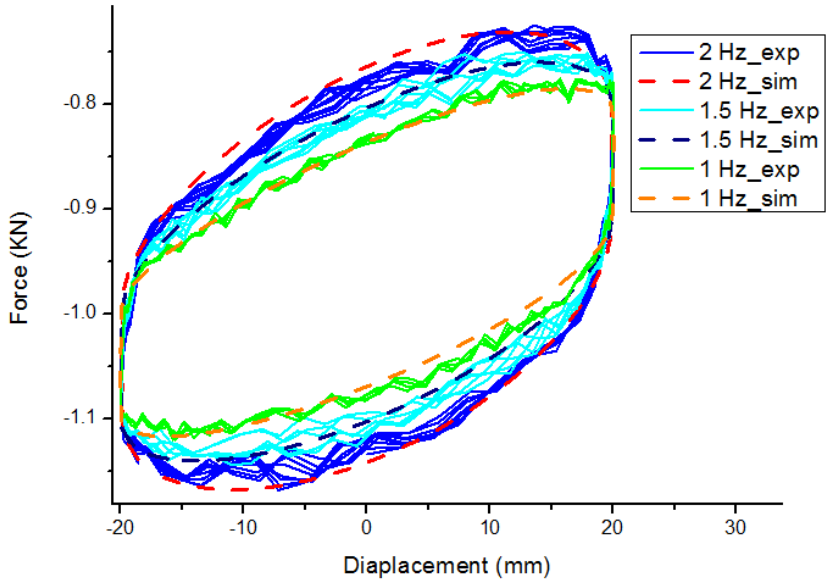

Figure 6-9. Frequency-dependant test (amplitude 20 mm, external resistance 4 Ohm).

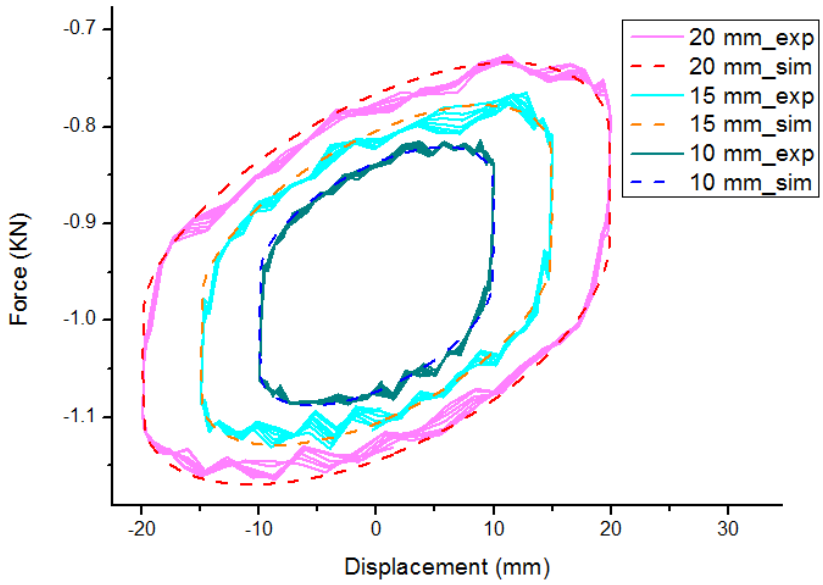

Figure 6-10. Amplitude-dependant test (external resistance 4 Ohm, frequency 2 Hz).

The voltage of the external resistance is defiend as:

$$U_{load}(t) = i(t)R_e \tag{6-10}$$

So, the experiemntaly measured U_{load} can also match the simulation result with the identified parameters, as shown in Figure 6-11. The measured voltage magnitude is increasing with the external resistance value.

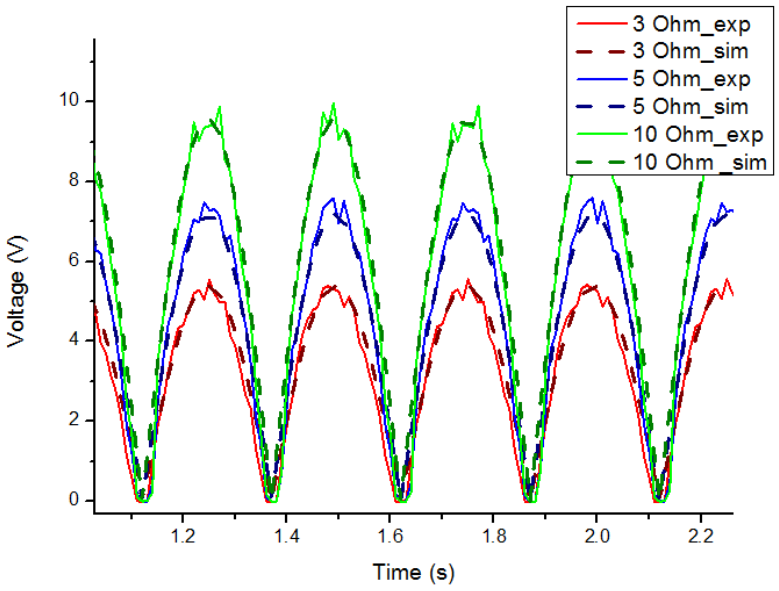

Figure 6-11. Voltage of external resistance (amplitude 20 mm, frequency 2 Hz).

The test and simulation results indicate that the regenerative seat suspension model (6-8) can effectively describe the regenerative seat suspension prototype, and the BEM force of the motor can be controlled by a variable external resistance.

6.3.4 Controller design

6.3.4.1 Model simplification

The fundamental principle of the semi-active control is to vary the suspension damping between 'soft' and 'hard' under different vibration situation. The proposed regenerative seat suspension can vary its BEM force by controlling its external resistance which is designed to vary from 0 Ohm to 50 Ohm; accordingly, the rheostat needs to be rotated from 0 degree to 100 degree. When the external resistance is set as 50 Ohm, the suspension is in the softest state; and when it is set as 0 Ohm, the suspension damping becomes high. For simplifying the controller design, the regenerative seat suspension model is defined as Figure 6-12 where m is the mass loaded on the suspension; k_0 and c_0 are the suspension stiffness and damping with 50 Ohm external resistance, respectively; Δk and Δc are the variable stiffness and damping, respectively; z_s is the seat displacement and z_v is cabin floor displacement.

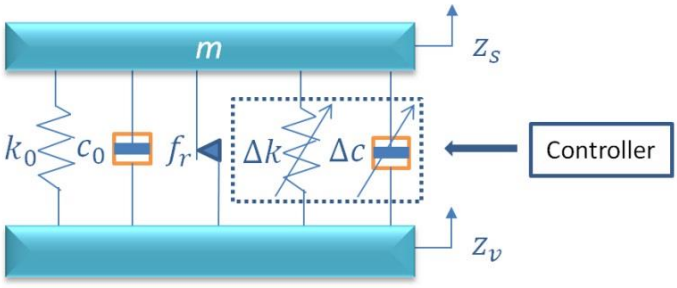

Figure 6-12. Semi-active seat suspension model.

The suspension equivalent stiffness and damping are identified with the external resistance-dependent test result as shown in Figure 6-13 and Figure 6-14. Thus, the relationship between suspension stiffness and damping with external resistance are defined as:

$$k = k_0 + \left(\frac{a_k}{b_k + R_e} + c_k\right) = k_0 + \Delta k \tag{6-11}$$

$$c = c_0 + \left(\frac{a_c}{b_c + R_e} + c_c\right) = c_0 + \Delta c \tag{6-12}$$

where a_k, b_k and c_k are parameters for stiffness fitting; a_c, b_c and c_c are parameters for damping fitting. Table 6-2 shows the identified parameters. The fitting results are shown in Figure 6-13 and Figure 6-14. When the external resistance is bigger than 5 Ohm, the stiffness variation is very small; by this reason, similar to some research, the stiffness variation caused by BEM force is ignored [50]. The damping can be changed from 136.16 Nm/s to 801.57 Nm/s, when the external resistance is varied from 50 Ohm to 0 Ohm.

Table 6-2. Parameters of seat suspension stiffness and damping.

$\boldsymbol{k_0}$	4500		$\boldsymbol{c_0}$	136.16
a_k	3592		a_c	4065
b_k	2.345		b_c	5.292
c_k	-99.94		c_c	-78.73

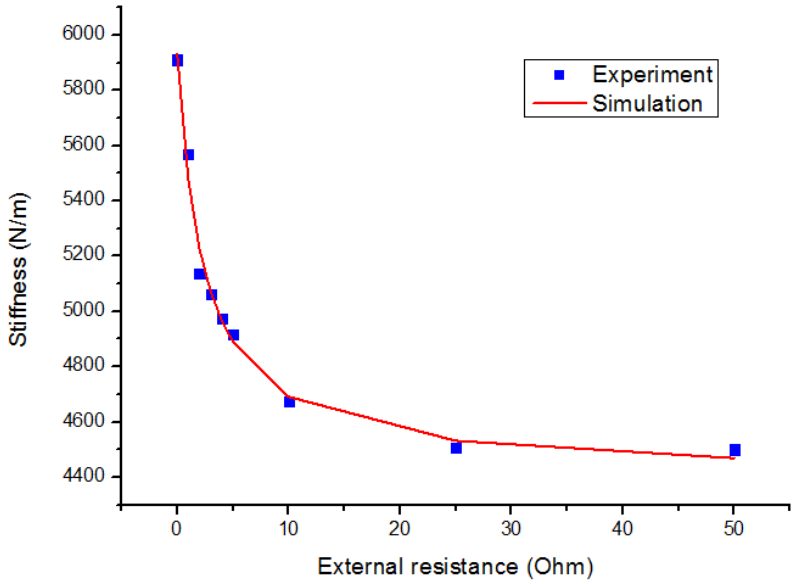

Figure 6-13. Total stiffness coefficients with different external resistance.

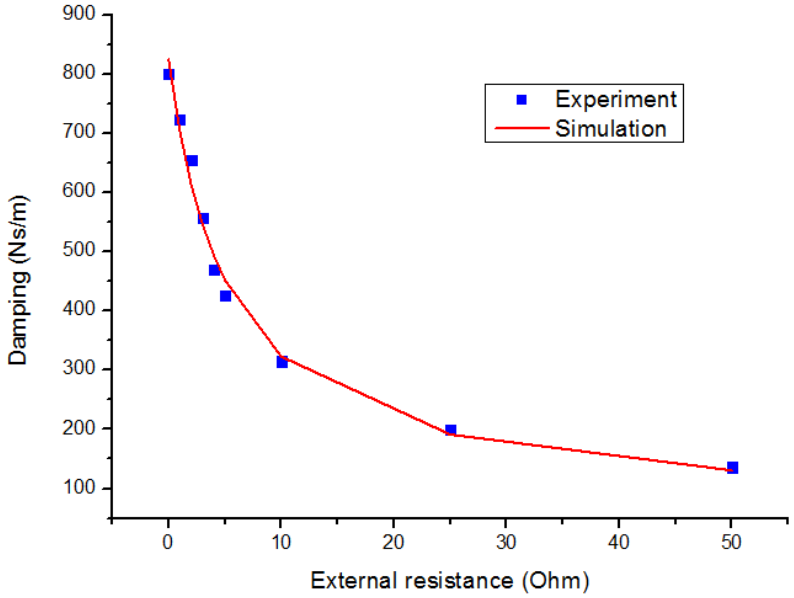

Figure 6-14. Damping coefficients with different external resistance.

The seat suspension model is defined as:

$$m\ddot{z}_s = -k_0(z_s - z_v) - c_0(\dot{z}_s - \dot{z}_v) - F_d + u \tag{6-13}$$

$$F_d = f_r + \Delta u \tag{6-14}$$

where u is force output when the external resistance is controlled; F_d is the total disturbance; Δu is the uncertainty of force output which is caused by the model simplification.

6.3.4.2 Sate feedback H_∞ controller

Many reputable suspension control algorithm has been proposed [3, 68]; in this section, an H_∞ controller is designed for the simplified model. The state variables are chosen as $x_1 = z_s - z_v$, $x_2 = \dot{z}_s$. There are two disturbances, i.e., $d_1 = \dot{z}_v$, $d_2 = F_d$. Thus, the suspension model can be written as state-space form:

$$\dot{\mathbf{X}} = \mathbf{A}\mathbf{X} + \mathbf{B_1}\boldsymbol{\omega} + \mathbf{B_2}u \tag{6-15}$$

where $\mathbf{X} = [x_1\ x_2]^{\mathrm{T}}$, $\mathbf{A} = \begin{bmatrix} 0 & 1 \\ -\frac{k_0}{m} & -\frac{c_0}{m} \end{bmatrix}$, $\mathbf{B_1} = \begin{bmatrix} -1 & 0 \\ \frac{c_0}{m} & -\frac{1}{m} \end{bmatrix}$, $\boldsymbol{\omega} = [d_1\ d_2]^{\mathrm{T}}$, $\mathbf{B_2} = [0\ \frac{1}{m}]^{\mathrm{T}}$.

For the seat suspension design, the seat acceleration should be controlled. At the same time, the seat suspension deflection also needs to be controlled to ensure the driver can easily handle the operational devices because those devices, such as steering wheel and gear shift lever, are always fixed on the vehicle cabin floor. The controlled output is defined as:

$$\mathbf{Z} = \mathbf{C_1}\mathbf{X} + \mathbf{D_{11}}\boldsymbol{\omega} + \mathbf{D_{12}}u \tag{6-16}$$

where $\mathbf{Z} = [z_s - z_v\ \ddot{z}_s]^{\mathrm{T}}$, $\mathbf{C_1} = \begin{bmatrix} \alpha & 0 \\ -\frac{k_0}{m} & -\frac{c_0}{m} \end{bmatrix}$, $\mathbf{D_{11}} = \begin{bmatrix} 0 & 0 \\ \frac{c_0}{m} & -\frac{1}{m} \end{bmatrix}$, $\mathbf{D_{12}} = [0\ \frac{1}{m}]^{\mathrm{T}}$, α is positive weighting constant.

Considering an H_∞ performance criterion under zero initial condition:

$$\int_0^\infty (\mathbf{Z}^{\mathrm{T}}\mathbf{Z} - \gamma^2\boldsymbol{\omega}^{\mathrm{T}}\boldsymbol{\omega})\,\mathrm{d}t < 0 \tag{6-17}$$

where γ is the desired level of disturbance attenuation.

A state feedback control is designed as:

$$u = \mathbf{K}\mathbf{X} \tag{6-18}$$

where $\mathbf{K}$ is the feedback gain to be designed.

Based on Lyapunov theorem, if there exists a matrix $\mathbf{P} = \mathbf{P}^{\mathrm{T}} > 0$, such that the following linear matrix inequality (LMI) is satisfied:

$$\begin{bmatrix} * + \mathbf{P}(\mathbf{A} + \mathbf{B_2}\mathbf{K}) & * & * \\ \mathbf{B_1}^{\boldsymbol{T}}\mathbf{P} & -\gamma^2\mathbf{I} & * \\ \mathbf{C_1} + \mathbf{D_{12}}\mathbf{K} & \mathbf{D_{11}} & -\mathbf{I} \end{bmatrix} < 0 \tag{6-19}$$

then the system (6-15) is stable with H_∞ disturbance attenuation $\gamma > 0$ [113].

Pre- and post-multiplying (6-19) by diag($\mathbf{P^{-1}}, \mathbf{I}, \mathbf{I}$) and its transpose, respectively. Defining $\mathbf{Q} = \mathbf{P^{-1}}$, $\mathbf{W} = \mathbf{KQ}$, following LMI is obtained:

$$\begin{bmatrix} * + (\mathbf{A}\mathbf{Q} + \mathbf{B_2}\mathbf{W}) & * & * \\ \mathbf{B_1}^{\mathbf{T}} & -\gamma^2\mathbf{I} & * \\ \mathbf{C_1}\mathbf{Q} + \mathbf{D_{12}}\mathbf{W} & \mathbf{D_{11}} & -\mathbf{I} \end{bmatrix} < 0 \tag{6-20}$$

By solving (6-20) with MATLAB LMI toolbox, the controller gain $\mathbf{K} = \mathbf{W}\mathbf{Q^{-1}}$ is obtained.

6.3.4.3 Controller implementation

The controller implementation is shown in Figure 6-15 where a desired force is calculated out by the designed controller firstly, and then the desired external resistance is obtained with the simplified model.

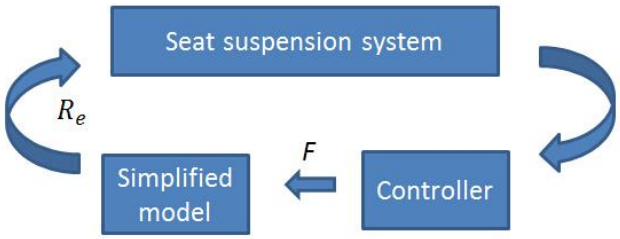

Figure 6-15. Controller implementation.

Because the external resistance can only be varied from 0 Ohm to 50 Ohm, and the BEM force of the seat suspension is generated passively, it cannot implement all the desired force

designed by the H_∞ controller. The desired external resistance R_{ed} can be easily obtained by solving $u = -\left(\frac{a_k}{b_k+R_{ed}} + c_k\right)h(t) - (\frac{a_c}{b_c+R_{ed}} + c_c)\dot{h}(t)$. Because the external resistance should have a positive value, it is easy to get the possible desired external resistance:

$$R_{ed} = \frac{-M+\sqrt{M^2-4LI}}{2L} \tag{6-21}$$

where $L = u + c_k h(t) + c_c \dot{h}(t)$, $M = L(b_k + b_c) + a_k h(t) + a_c \dot{h}(t)$, $I = L b_k b_c + a_k b_c h(t) + a_c b_k \dot{h}(t)$.

It is known that there is a theoretically possibility that $M^2 - 4LI < 0$ when the u in Eq. (6-21) cannot be achieved, then the implementable R_e will apply the previous solution.

When $M^2 - 4LI > 0$ the implementable resistance can be obtained with a saturation function:

$$R_e = \text{sat}(R_{ed}) = \begin{cases} 0 & R_{ed} \le 0 \\ 50 & R_{ed} \ge 50 \\ R_{ed} & 0 < R_{ed} < 50 \end{cases} \tag{6-22}$$

When the R_e is obtained, the rheostat will be rotated to the corresponding angle.

6.3.5 Evaluation

6.3.5.1 Numerical simulations

In this section, the proposed controller is validated with the identified regenerative seat suspension model in numerical simulation. The H_∞ controller gain is designed as $\mathbf{K} = [4600 \quad -600]$. The harmonic excitation test, which was a sweep frequency signal from 1 Hz to 3 Hz in 40 seconds with 30 mm amplitude, was implemented. Figure 6-16 shows the seat absolute displacement comparison. When the external resistance is 50 Ohm, the suspension damping is small; big displacement appears around the resonance frequency. When the external resistance is turned to 0 Ohm, the suspension is ‘hard’; it can successfully suppress the resonance vibration, but it has worse vibration isolation performance than the ‘soft’ one in

high frequency. Obviously, the proposed semi-active H_∞ controller with simplified model has best performance. Because, for the conventional passive seat suspension, the damping has to compromise between the soft one which is comfortable and the hard one which can keep the suspension stable in resonance frequency, this simulation result indicates that the regenerative seat suspension with the proposed controller can improve the ride comfort greatly by combining the advantages of the soft and hard seat suspensions.

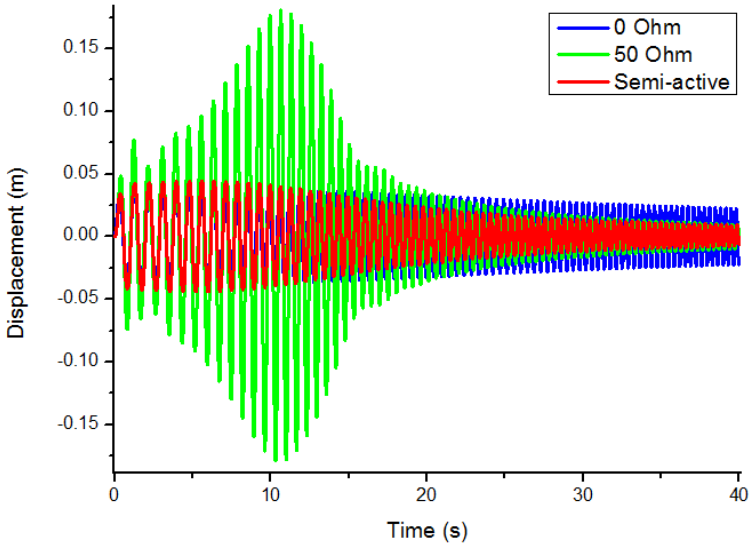

Figure 6-16. Seat absolute displacement.

6.3.5.2 Experimental setup

The experimental system is shown in Figure 6-17. The accelerations of the seat suspension base and top are acquired by two accelerometers (ACXL 203EB). A displacement sensor (Micro Epsilon ILD1302-100) is applied to measure suspension relative displacement. The vibration displacement is also measured by a displacement sensor (Micro Epsilon optoNCDT 1700). Combining the data of two displacement sensors, the seat absolute displacement can be acquired. The proposed controller is implemented on NI CompactRio 9074 which calculates out desired external resistance based on sensors data and then sends command to a motor to control the resistance of a rotary rheostat. The current though external resistance is measured out by a NI module (9227) on NI CompactRio 9074. The voltage of external

resistance is also acquired by the controller. Considering the rotary rate limitation of rheostat, the control frequency is set as 100 Hz.

The regenerative seat suspension is tested with different external resistances. Then the experiment results are compared with the semi-active control seat suspension. For further verifying the proposed semi-active seat suspension system, a well-tuned passive seat suspension (GARPEN GSSC7) is also tested.

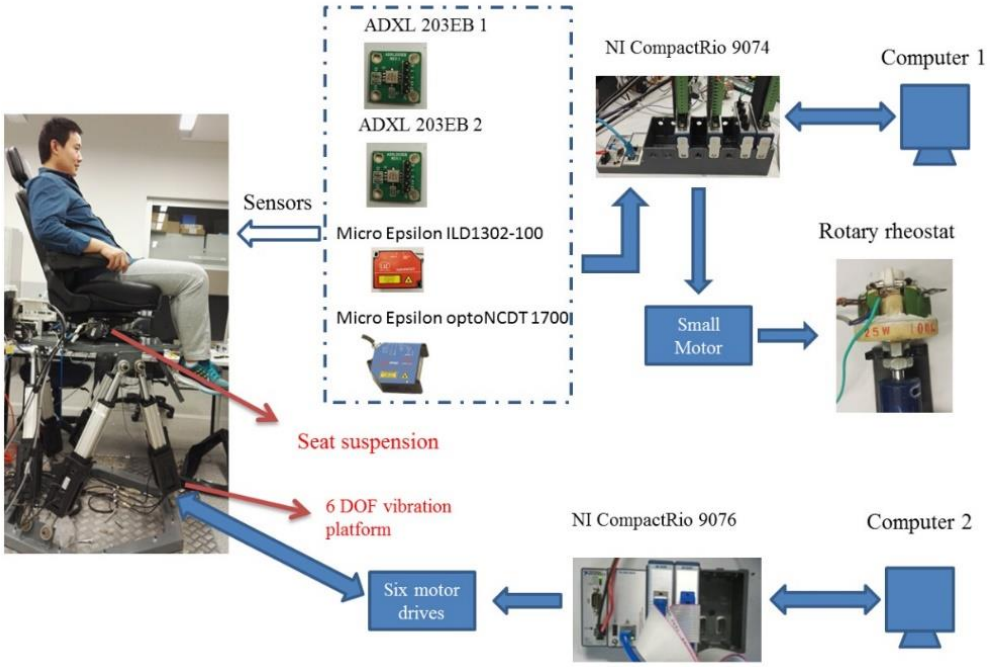

Figure 6-17. Experimental setup.

6.3.5.3 Experimental results

The sinusoidal excitations were applied to the seat suspensions with 80 Kg load for testing their frequency performance. Figure 6-18 shows the seat acceleration with 1.5 Hz vibration. When external resistance is varied from 50 Ohm to 0 Ohm, the suspension damping and stiffness are increasing accordingly; the suspension is becoming stiffer; therefore, the resonance vibration is suppressed. The semi-active control suspension has closely performance as the hardest one (0 Ohm external resistance). Figure 6-19 shows their vibration transmissibility among the tested frequency range. When the vibration is around the

resonance frequency, the softest suspension amplifies the vibration and the suspension is unstable. The semi-active control suspension can successfully suppress the resonance vibration; and its transmissibility value is just a little bigger than the hardest one. When the vibration is around 1.8 Hz, the seat suspensions is turning from amplifying vibration to isolating vibration; the semi-active seat suspension has best performance. In the higher frequencies, the performance of the semi-active control seat is close to the softest one which means the advantage of the soft suspension, namely ride comfort, is kept.

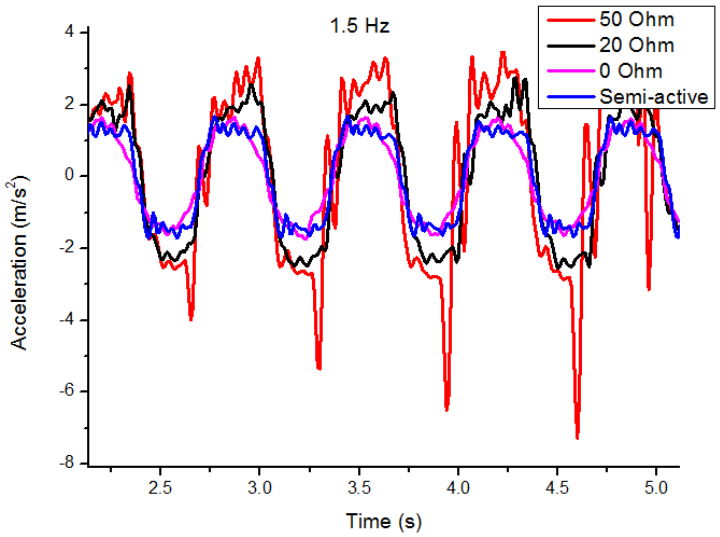

Figure 6-18. Seat acceleration with 1.5 Hz vibration.

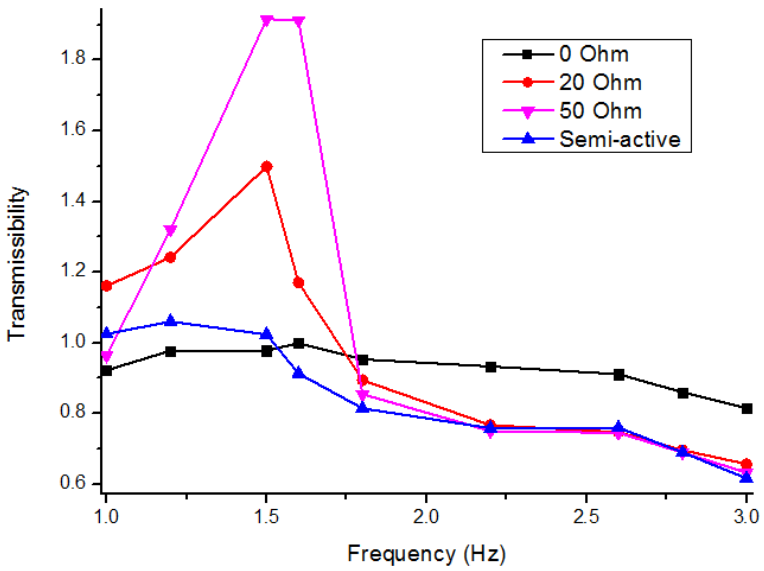

Figure 6-19. Acceleration transmissibility.

The bump road test can indicate the controller's capacity to respond to excitation. Figure 6-20 shows the seat acceleration of the well-tuned conventional passive seat suspension and the proposed semi-active one under bumpy road conditions. The peak acceleration magnitude drops from 1.652 m/s^2 to 1.265 m/s^2; there is a 23.4% reduction.

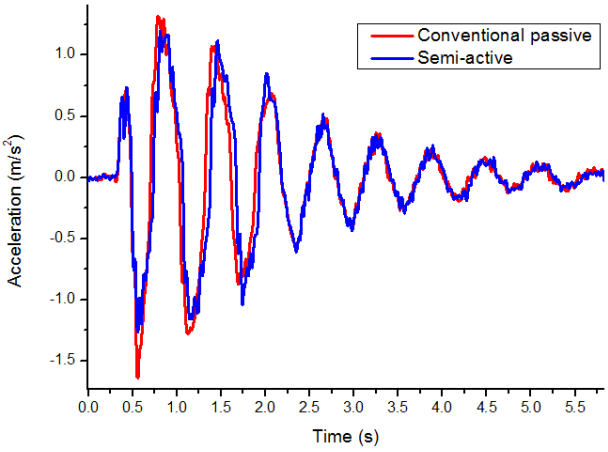

(a)

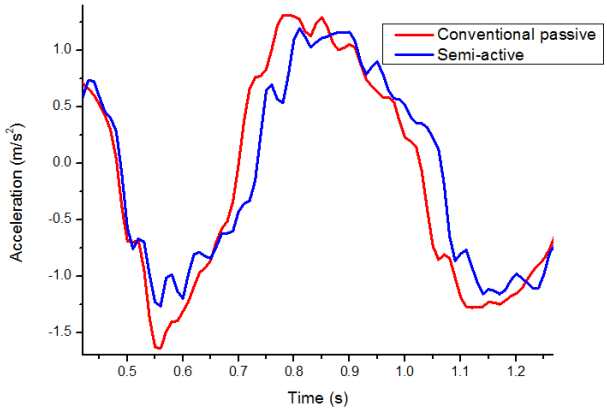

(b)

Figure 6-20. Seat acceleration with bump road. (a) Time domain graph. (b) Zoom in.

The random excitation test is always applied to evaluate the seat suspension performance in time domain. Figure 6-21 shows acceleration comparison of the semi-active control regenerative seat suspension with its soft (50 Ohm) and hard (0 Ohm) states; from Figure

6-21 (b), the controlled seat suspension can suppress the resonance frequency and keep the vibration isolation ability in high frequency. The performance comparison with conventional passive seat suspension is shown in Figure 6-22 where the controlled regenerative seat suspension has better performance in all the test time.

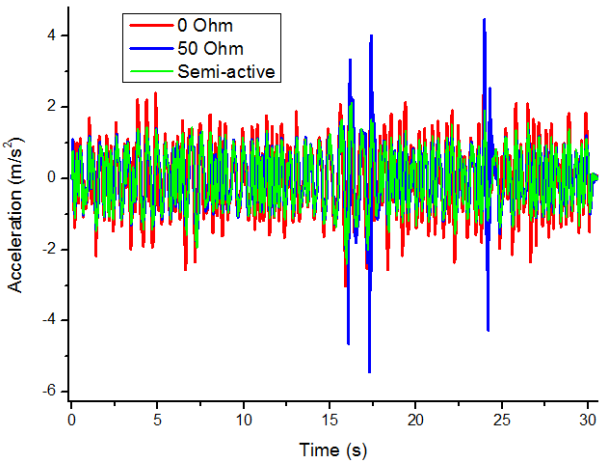

(a)

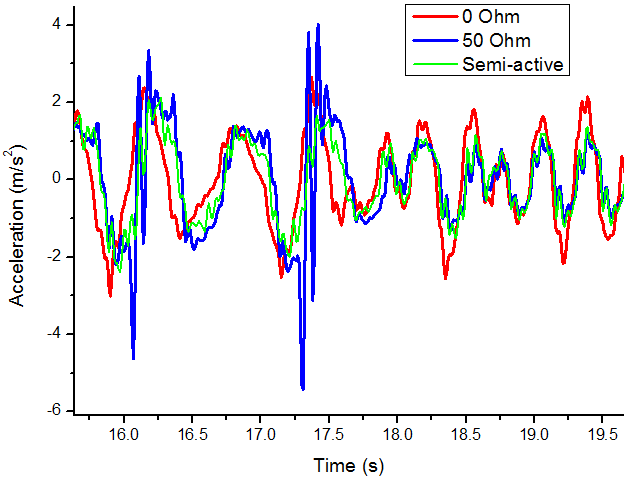

(b)

Figure 6-21. Regenerative seat suspension acceleration under random road. (a) Time domain graph. (b) Zoom in.

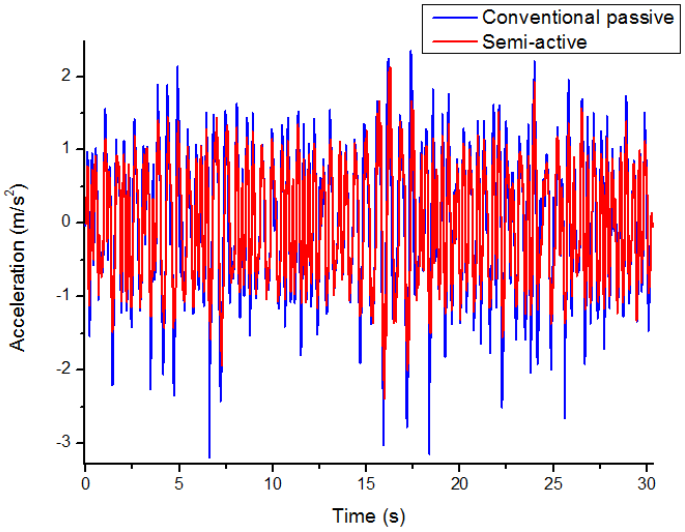

(a)

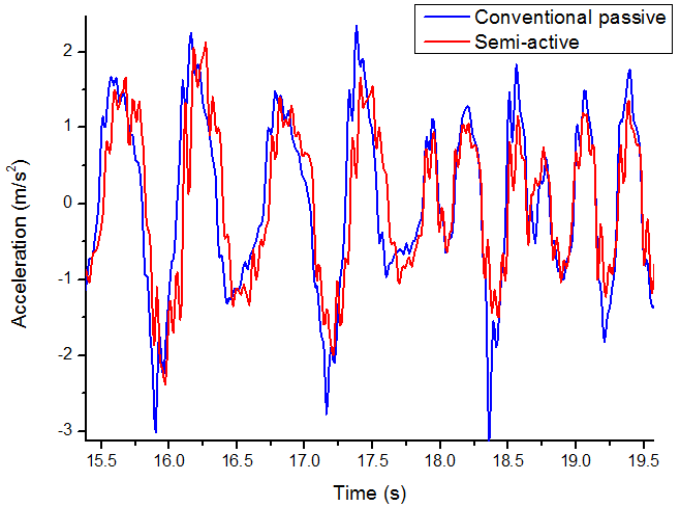

(b)

Figure 6-22. Comparison with conventional seat suspension acceleration under random road. (a) Time domain graph. (b) Zoom in.

Table 6-3 shows the comparison of evaluation parameters for each seat suspensions. The RMS and FW-RMS acceleration of the passive one is between the uncontrolled soft and hard regenerative seat suspension; but its VDV value is smaller than both of them. This proves the passive seat suspension with nonlinear damper is well tuned. The semi-active controlled seat has best performance in all the evaluation parameters. For clearly showing the performance

improvement, Table 6-4 shows the vibration reduction percentage of the semi-active seat suspension comparing with other three. The 22.84% reduction of RW-RMS when comparing with passive seat suspension validates the effectiveness of the proposed semi-active regenerative seat suspension.

Table 6-3. Seat vibration evaluation.

	0 Ohm	50 Ohm	Passive	Semi-active
RMS (m/s^2)	0.9884	0.8496	0.9473	0.7694
FW-RMS (m/s^2)	0.7372	0.6056	0.6922	0.5341
VDV ($m/s^{1.75}$)	2.072	2.43	1.962	1.451
SEAT	0.6594	0.5417	0.6191	0.4777
VDV ratio	0.5351	0.6276	0.5067	0.3747

Table 6-4. Vibration reduction percentage of Semi-active seat suspension.

	0 Ohm	50 Ohm	Passive
RMS (m/s^2)	-22.16%	-9.44%	-18.78%
FW-RMS (m/s^2)	-27.55%	11.81%	-22.84%
VDV ($m/s^{1.75}$)	-29.97%	-40.29%	-26.04%
SEAT	-27.55%	-11.81%	-22.84%
VDV ratio	-29.97%	-40.29%	-26.04%

The current through the variable external resistance is shown in Figure 6-23 where the maximum current is 1.267 A and the RMS current is 0.152 A. The generated power is defined as $P = U_e I_e$ where U_e is the voltage of external resistance and I_e is the current

through it. Figure 6-24 shows the generated power when the suspension is controlled; there is a maximum power of 13.88 W and the RMS power is 1.21 W which shows the energy harvesting potential of the regenerative seat suspension.

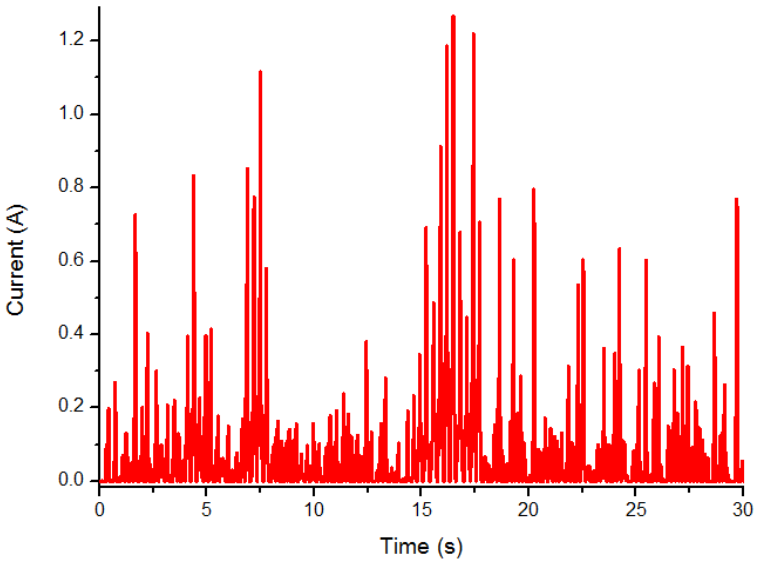

Figure 6-23. Generated current of semi-active control.

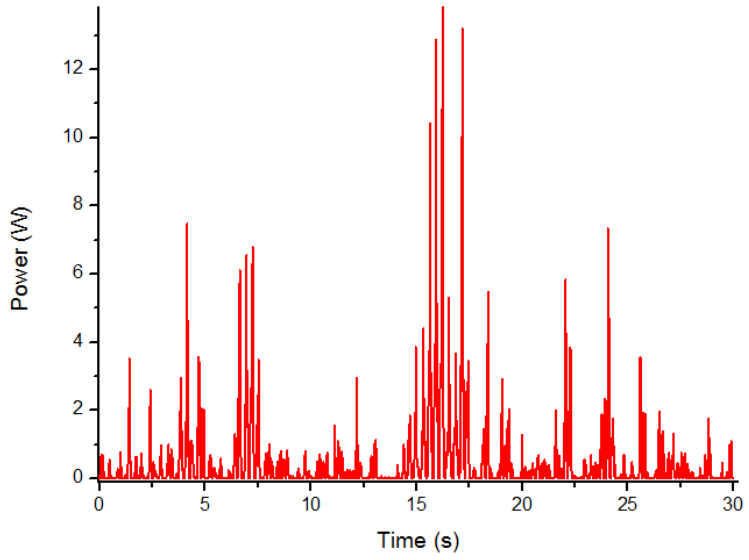

Figure 6-24. Generated power of semi-active control.

6.4 MOSFET Switch Based EMD

In this section, a new method is proposed to control the damping of EMD system. Instead of rotating an external resistor, a MOSFET switch and a constant resistor are applied, thus the system is further simplified.

6.4.1 Damping controllable EMD system

The schematic diagram of the controllable EMD system is shown in Figure 6-25 and its prototype is shown in Figure 6-26. In the system, a 3-phase permanent magnet synchronous motor (PMSM) which can be modelled as three back electromotive force (EMF) voltages (e_a, e_b, e_c), three internal resistors (R_{ia}, R_{ib}, R_{ic}) and three internal inductors (L_{ia}, L_{ib}, L_{ic}) is utilised; a 3-phase rectifier is applied to transfer the generated alternating current (AC) to direct current (DC); the MOSFET switch module is controlled by a 5 V PWM signal; the diode and the capacitance C are applied to regulate and filter the harvestable energy; R_e is an external resistor and it can be replaced by an energy storage circuit. The applied PMSM is a Panasonic motor (MSMJ042G1U). The MOSFET switch module consists of a photocoupler (DPC-817C) and a MOSFET (IRF5305S). Based on the datasheet of the photocoupler, the absolute maximum rating of the input power is 70 mW; it indicates that the proposed system can be controlled with power no more than 70 mW.

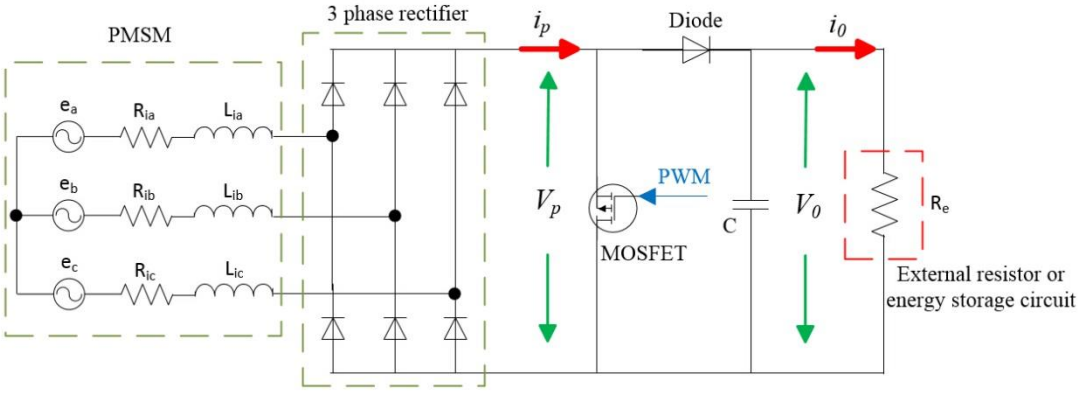

Figure 6-25. Controllable EMD system schematic.

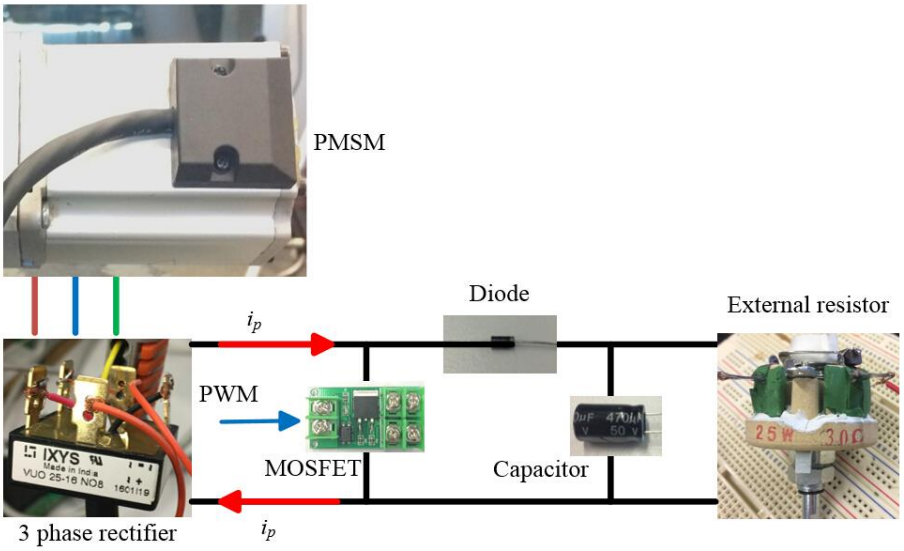

Figure 6-26. Controllable EMD system prototype.

The working principle of the system is intuitive. The damping of the EMD is increasing with the decrease of the external loads [50]. When the input PWM signal is in 5 V state, the MOSFET switch should be on, then the positive and negative terminals of the 3-phase rectifier are shorted, which is equivalent to that a 0 Ω external resistor is applied to the EMD, and in this scenario, the EMD has its biggest damping. On the contrary, when the input PWM signal is in 0 V state, the MOSFET switch is off, then the damping of the EMD is determined by the external resistor R_e. In this chapter, a 30 Ω resistor is used as the external load which determines the smallest damping of the EMD. Thus, the damping of the EMD can be varied between its smallest and biggest values, when the high frequency PWM signal (2000 Hz) is implemented with different duty cycle values.

6.4.2 Variable damping tests

In this section, the proposed controllable EMD system prototype is comprehensively tested and analysed.

6.4.2.1 Test system

The test system is shown in Figure 6-27. A 400 W Panasonic servo motor, which can be accurately controlled by its drive, is used to rotate the EMD; thus, the EMD will make passive rotation. The encoder in the servo motor can be used to record the real rotation angle, and the applied torque of the servo motor can be taken as the torque output of the EMD. An NI CompactRio 9074 is applied to control the system and record data with different modules: NI 9401 is used for controlling the servo motor and MOSFET module; NI 9207 is used for acquiring servo motor's output torque; NI 9227 is used for measuring the currents i_p and i_0; and NI 9239 is applied to measure the voltages V_p and V_0.

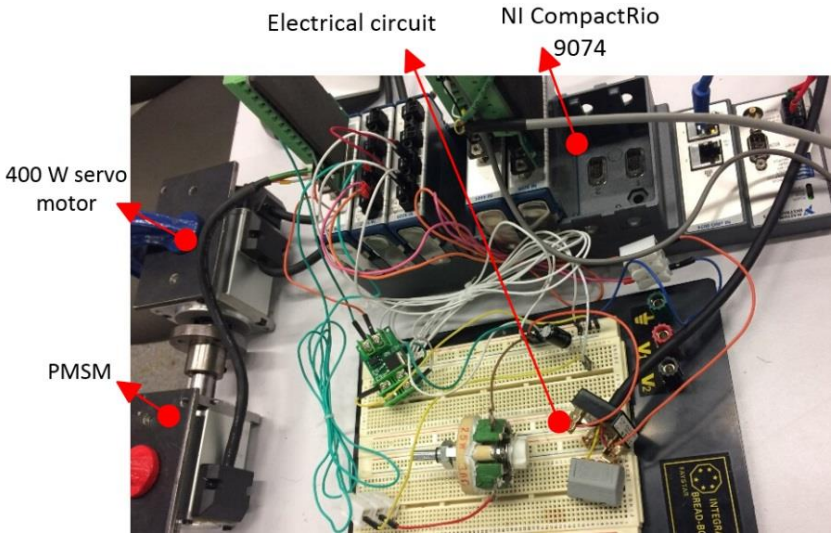

Figure 6-27. Test system for controllable EMD.

6.4.2.2 Sinusoidal rotation test

The sinusoidal rotation test is implemented firstly. The servo motor drives the EMD to rotate with sinusoidal profile (with 2 Hz frequency, 500 degree amplitude). When PWM signal with different duty cycle is exerted on the MOSFET switch, the output torque of the EMD is changed (see Figure 6-28). Moreover, the plot of relationship between rotary rate and torque is shown in Figure 6-29. The result indicates that, the system damping can be controlled by

varying PWM duty cycle; when the PWM duty cycle varies from 0 to 1, the damping is increased.

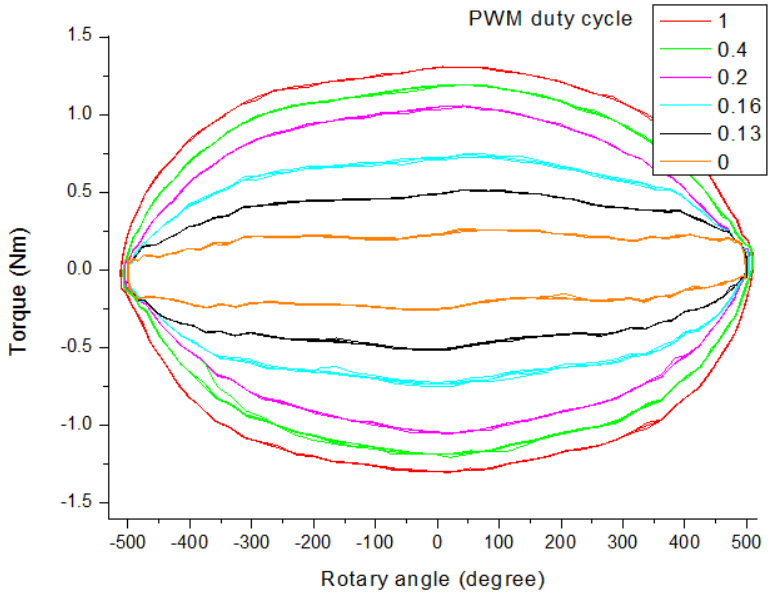

Figure 6-28. Rotary angle-torque.

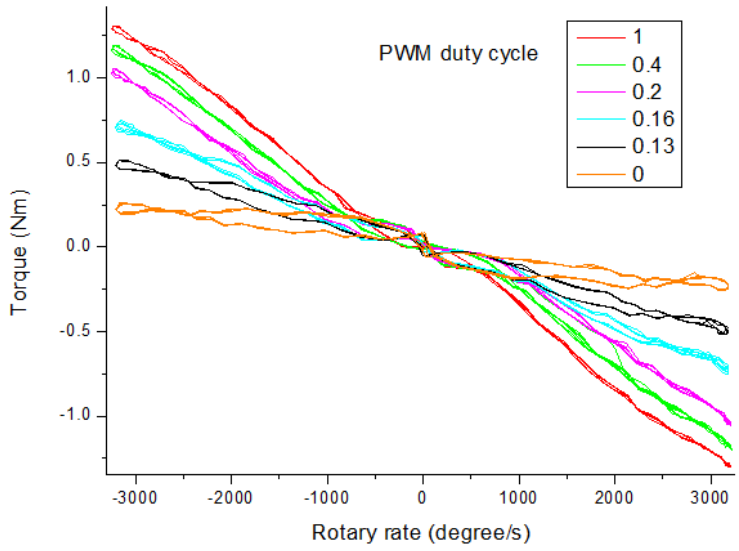

Figure 6-29. Rotary rate-torque.

The current through the external resistor is show in Figure 6-30 where i_0 is decreasing with the increase of PWM duty cycle. Ideally, when the PWM duty cycle is 1, there should be no current through the external resistor. But, it needs a threshold voltage to fully turn the

MOSFET switch on; in other words, although the input PWM duty cycle is equal to 1, the MOSFET switch will not turn on until the voltage between the two output terminals of the 3-phase rectifier higher than a certain value (2 to 4 V based on its datasheet), thus, there exists a low current in the experiment.

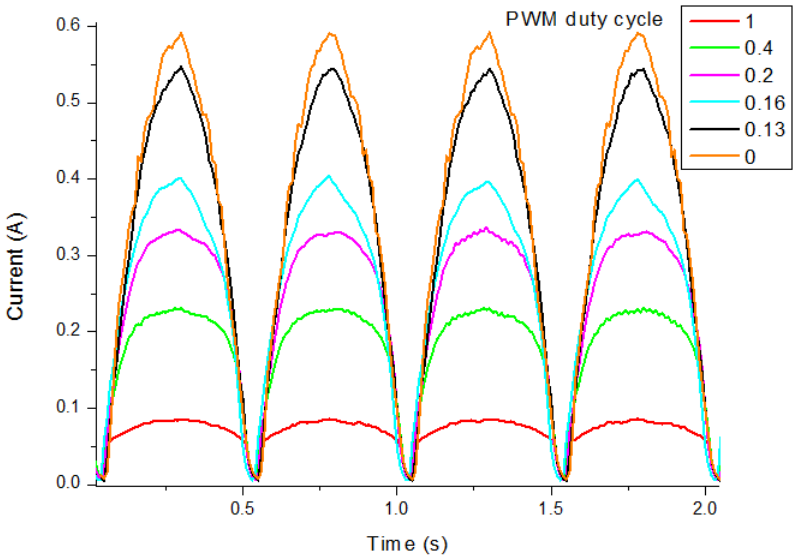

Figure 6-30. Current i_0.

The dissipated energy by the external resistor can be taken as the harvestable energy, thus, the harvestable power is defined as:

$$P_h = {i_0}^2 R_e \tag{6-23}$$

Figure 6-31 shows the harvestable power with different PWM duty cycles. When the MOSFET switch is turn on, the two output terminals of the 3-phase rectifier will be shorted, thus very low power can be harvested by the external resistor.

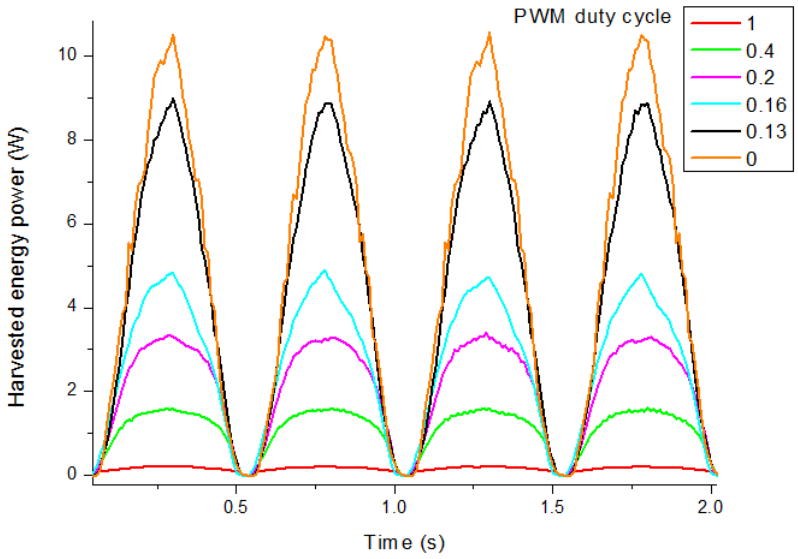

Figure 6-31. Harvestable power.

The input mechanical power can be defined as:

$$P_m = T_d \omega \tag{6-24}$$

where T_d is the test damping torque, and ω is the rotary rate of the EMD. Figure 6-32 shows the peak power comparison of the input mechanical power and harvested electrical power. With the increasing of PWM duty cycle value, the damping of the EMD is also increased, thus more mechanical power is needed to drive the EMD doing sinusoidal rotation. In the meanwhile, less electrical power can be harvested. Figure 6-33 shows the energy harvesting efficiency ($\frac{P_h}{P_m}$); the highest efficiency value is 76%, and when the PWM duty cycle is higher than 0.2, the efficiency will less than 10%.

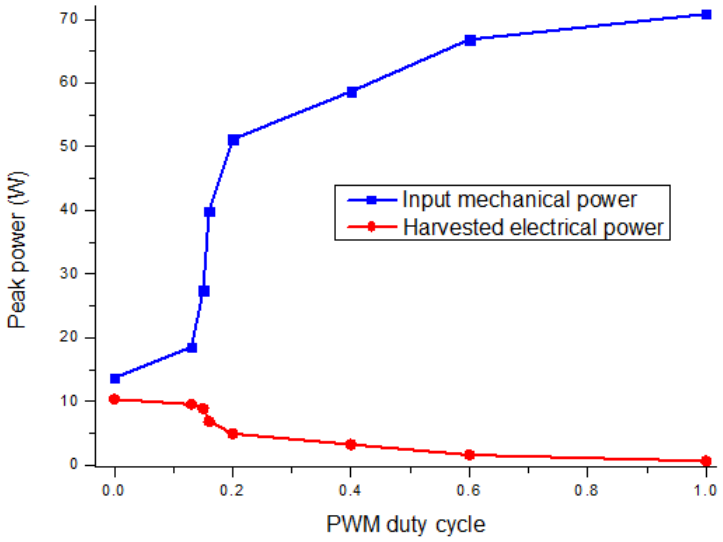

Figure 6-32. Peak power comparison.

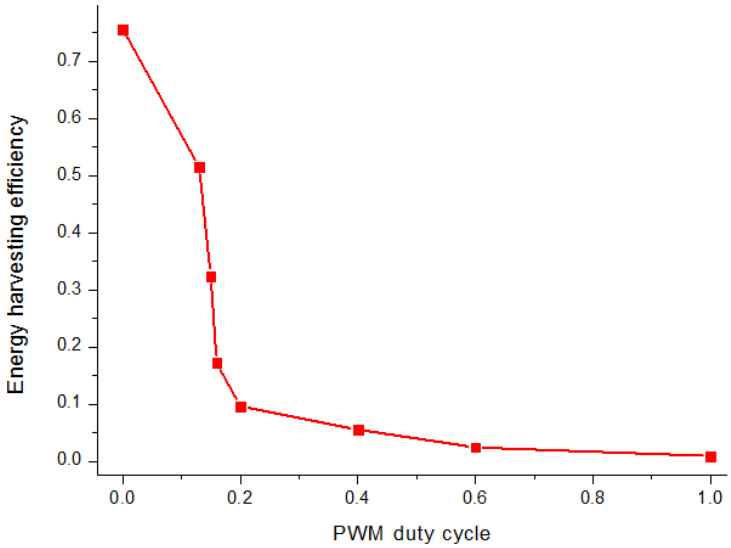

Figure 6-33. Energy harvesting efficiency.

6.4.2.3 Constant rate rotation test

In order to analyse the EMD and control it, another series of tests is implemented. The servo motor drives the EMD to rotate with constant rates (1000 degree/s, 1500 degree/s, 2000 degree/s, 2500 degree/s), and its output torque is recorded with different PWM duty cycles. Figure 6-34 shows that, with same rotary rate, the output torque of EMD is not linear with PWM duty cycle; the change rate of the torque is big when the PWM duty cycle is between 0.1 to 0.2. In Figure 6-35, when the PWM duty cycle is a constant value, the output torque is

almost linear with the EMD rotary rate; in other words, the dampings of the EMD are constant values corresponding to certain PWM duty cycle values. Thus, in the application, the desired damping can be obtained firstly, then the corresponding PWM duty cycle value can be found and applied.

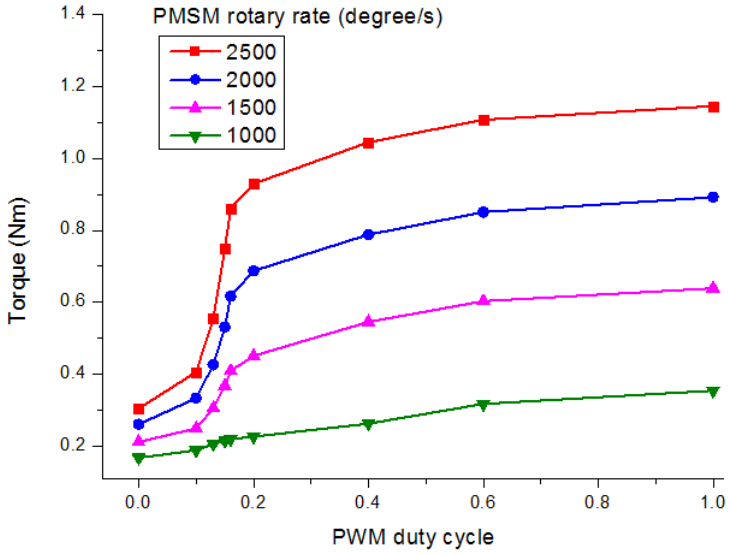

Figure 6-34. Torque output with PWM duty cycle variation.

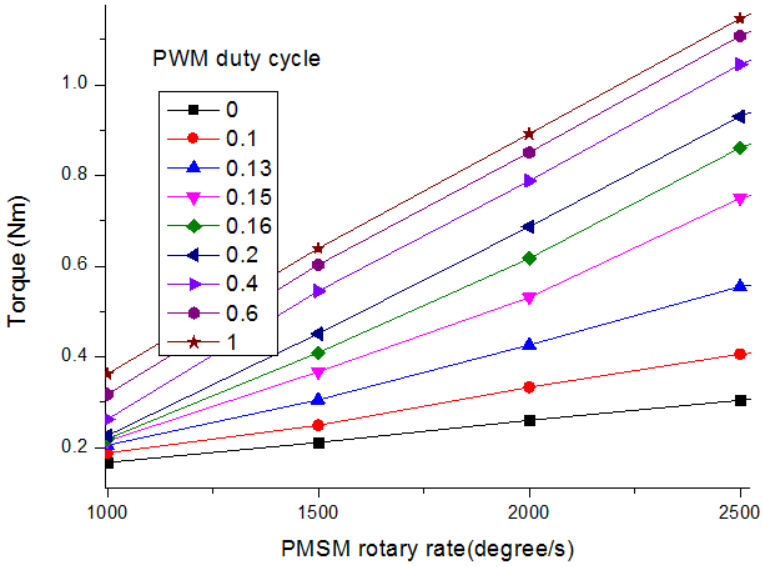

Figure 6-35. Torque output with PMSM rotary rate variation.

6.4.2.4 Variable damping of the seat suspension

The variable damper consists of the gearbox and the EMD, thus, its damping is defined as:

$$c_r = \frac{T_d r_g}{\omega / r_g} = c_{EMD} {r_g}^2 \tag{6-25}$$

where r_g is the ratio of the gearbox; c_{EMD} is the tested damping of the EMD based on the results in Figure 6-35.

The damping of the variable damper and the corresponding PWM duty cycle is shown in Figure 6-36 where four lines are applied to fit it:

$$P_{duty} = (c_{rd} - c_i) * k_i + P_i, \qquad (i = 1, 2, 3, 4) \tag{6-26}$$

where P_{duty} is the derived PWM duty cycle with value between 0 and 1; c_{rd} is the desired damping; c_i, k_i, P_i are parameters of the four lines which are defined in Table 6-5. The parameters selection is also defined in Table 6-5 where when c_{rd} is in different ranges, the corresponding parameters are applied.

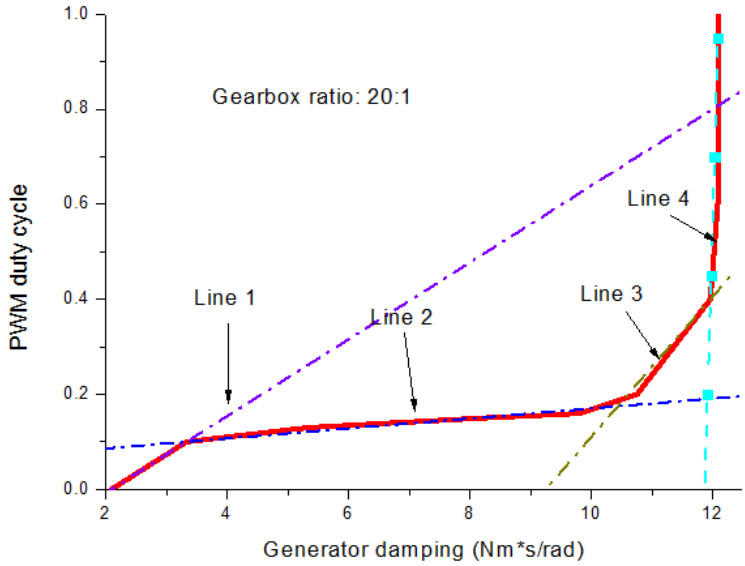

Figure 6-36. Variable damping.

Table 6-5. Parameters of lines.

i	c_i	k_i	P_i

$c_{rd} \leq c_2$	1	2.093	0.0808	0
$c_2 < c_{rd} \leq c_3$	2	3.331	0.0105	0.1
$c_3 < c_{rd} \leq c_4$	3	10.438	0.1476	0.175
$c_4 < c_{rd}$	4	11.963	4.3633	0.4

In addtion, the equivalent vertical damping of the seat suspension should be acquired when the controllabe damper is installed.

The ouput torque of the damper is equivelent to a vertical force. According to the kinematic model of the seat suspension (see Figure 6-37), the equivelent vertical force can be defined as:

$$F = ch(\dot{t}) = \frac{2T}{\sqrt{L^2-(h_0+h(t))^2}} \tag{6-27}$$

where c is the equivalent damping of the seat suspension; $T = c_r\dot{\theta}$ is the torque generated by the damper, and $\dot{\theta}$ is the rotary rate of the variable damper; $L = 0.287$ m is the length of the bar; $h_0 = 0.1$ m is the height of the seat suspension when it is loaded with mass; $h(t)$ is the relative displacement when vibration is exerted on the suspension.

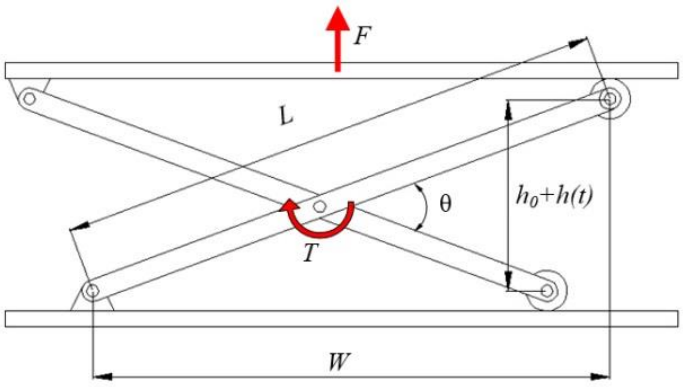

Figure 6-37. Kinematic model of seat suspension.

The rotary angle of the variable damper can be defined based on the measurement of seat suspension's vertical motion:

$$sin(\frac{\theta}{2}) = \frac{h_0+h(t)}{L} \tag{6-28}$$

Thus, the rotary rate and the relative velocity of the seat suspension is:

$$\frac{\dot{\theta}}{2}\, cos\left(\frac{\theta}{2}\right) = \frac{\dot{h(t)}}{L} \tag{6-29}$$

Combining (6-27)-(6-29), the vertical damping of the seat suspension is:

$$c = \frac{4}{cos\left(\text{asin}(\frac{h_0+h(t)}{L})\right)L\sqrt{L^2-(h_0+h(t))^2}} c_r = \gamma c_r \tag{6-30}$$

When $h(t)$ is between -0.01 m to 0.01 m, γ is between 53.8 to 56.9, Thus, by assuming that $\gamma = 55.35$, the damping of the seat suspension can be controlled between 115.68 Ns/m and 669.74 Ns/m; this change range is suitable for seat suspension.

6.4.3 Controller design

In this section, an implementable control method is proposed for the variable damping seat suspension.

The simplified seat suspension model is shown in Figure 6-38 where m is the mass loaded on the suspension; k is the suspension stiffness; c is the controllable damping; f_r is the friction; z_s is the seat displacement and z_v is the cabin floor displacement.

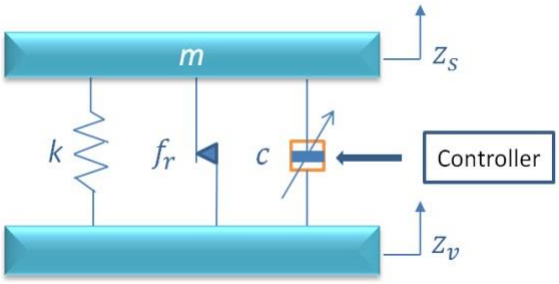

Figure 6-38. Seat suspension model.

The seat suspension model is defined as:

$$m\ddot{z}_s = -k(z_s - z_v) + u + \omega \tag{6-31}$$

$$\omega = \Delta u - f_r \tag{6-32}$$

$$u = -cv_r \tag{6-33}$$

where v_r is the suspension relative velocity; Δu is the uncertainty of the force output; ω is the total disturbance.

For designing a controller, the state variables are chosen as $x_1 = z_s - z_v$, $x_2 = \dot{z}_s$. There are two disturbances, i.e., $d_1 = \dot{z}_v$, $d_2 = \omega$. Thus, the suspension model can be written as a state space form:

$$\dot{\mathrm{X}} = \mathrm{AX} + \mathrm{B}_1\omega + \mathrm{B}_2 u \tag{6-34}$$

where $\mathbf{X} = [x_1\ x_2]^{\mathrm{T}}$, $\mathbf{A} = \begin{bmatrix} 0 & 1 \\ -\frac{k}{m} & 0 \end{bmatrix}$, $\mathbf{B_1} = \begin{bmatrix} -1 & 0 \\ 0 & -\frac{1}{m} \end{bmatrix}$, $\boldsymbol{\omega} = [d_1\ d_2]^{\mathrm{T}}$, $\mathbf{B_2} = [0\ \frac{1}{m}]^{\mathrm{T}}$.

A state feedback H_∞ controller can be designed as:

$$u = \mathrm{KX} \tag{6-35}$$

where **K** is the feedback gain to be designed.

As the H_∞ controller has been applied in many control systems [123], the destailed design procedure of the controller is not presented here for saving space. $\mathbf{K} = [3000\ \ -200]$ is selected in this thesis.

The implementation of the controller can be seen in Figure 6-39. The desired vertical force is obtained from the H_∞ controller firstly. The direction of the damping force is reverse with the suspension relative velocity; it means that when the product of the desired vertical force and the suspension relative velocity is a negative number, a corresponding rotary damping c_{rd} of the controllable damper can be found; or the damper cannot generate a force which can help

to isolate vibration, and at that time, the damper can keep its smallest damping. Then, based on the desired rotary damping, the corresponding PWM duty cycle value can be obtained by (6-26).

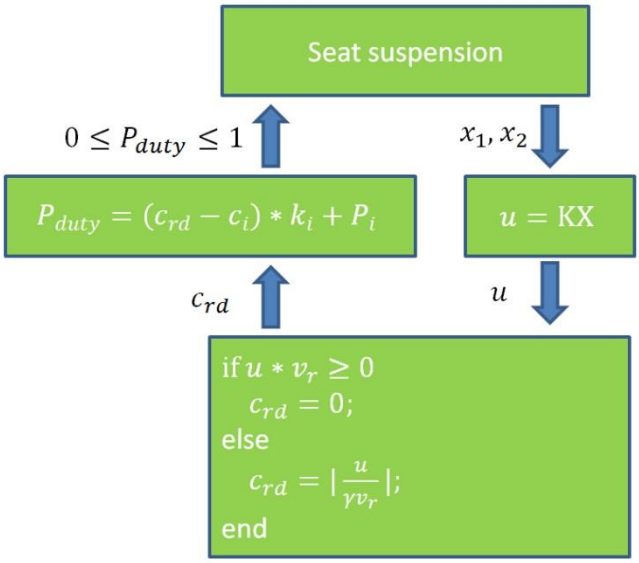

Figure 6-39. Controller implementation.

6.4.4 Evaluation

6.4.4.1 Experimental setup

The experimental setup is shown in Figure 6-40. The relative displacement of the seat suspension is measured by a laser sensor (Micro Epsilon optoNCDT 1700); and another laser sensor is applied to measure the displacement of the top platform of the seat suspension. Two acceleration sensors (ADXL 203EB) are used to obtain the top and base acceleration of the seat suspension. An NI CompactRio 9074 is used to control a MOSFET module based on sensors' feedback.

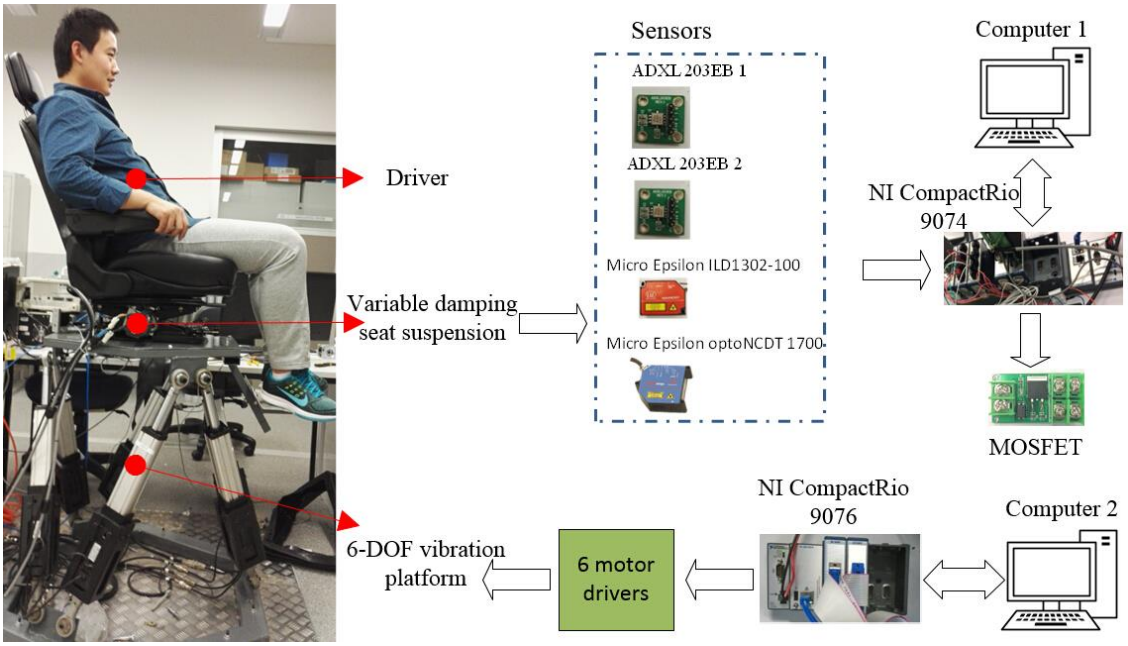

Figure 6-40. Experimental setup.

For evaluating the vibration control performance of the variable damping seat suspension, a well tuned commercial passive seat suspension (GARPEN GSSC7) is also tested; it is the same type of seat suspension that has been modified to the variable damping seat suspension. The proposed seat suspension is tested under two conditions, controlled and uncontrolled.

6.4.4.2 Acceleration transmissibility

The acceleration transmissibility can show the performance of a seat suspension in frequency domain; lower transmissibility value means less acceleration can be transferred to driver from seat base. By exerting different frequencies of vibration on the base of the seat suspension, the RMS accelerations of the seat suspension top and base are caculated; then, the transmissibility of RMS acceleration which is shown in Figure 6-41 can be obtained by using RMS acceleration of the top devided by the one of base. The well tuned passive seat suspension has a nonliner damper of which parameter has been optimised by the manufacturer for heavy duty vehicles; its transmissibility value has a peak around 1.45 Hz, then decreasing with the increase of vibration frequency. The uncontrolled variable damping

seat suspension also has a high resonance peak around 1.45 Hz, and then has loweast transmissibility value compared with other two, because the uncontrolled one has the loweast damping which causes high transmissibility around resonant freuqency. The controlled one can succsessfully supress the resonance vibration; In higher vibration frequency, athough its transmissibility is a little high than the uncontrolled one, it has better performance than the passive seat suspenion within the whole test range.

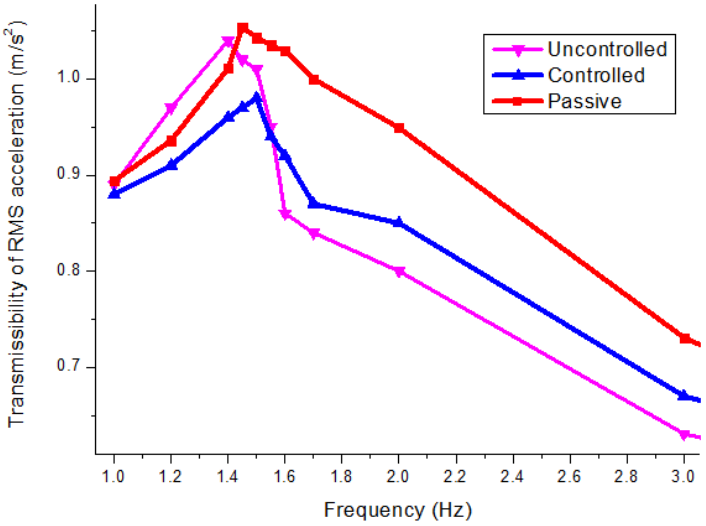

Figure 6-41. Transmissibility of RMS acceleration.

6.4.4.3 Random vibration test

For evaluating its time domain performance, the random excitation test is implemented. Figure 6-42 shows the seat acceleration of the controlled variable damping seat suspension and the passive one in time domain where the performance of the controlled one is obviously better than the passive one. In order to analyse it quantitatively, an international standard ISO 2631-1 [110] is applied to evaluate it.

Figure 6-43. Evaluation parameters. shows the value of the evaluation parameters where, with the controlled variable damping seat suspension, the FW-RMS acceleration and VDV are decreased 19.7% and 25.6%, respectively.

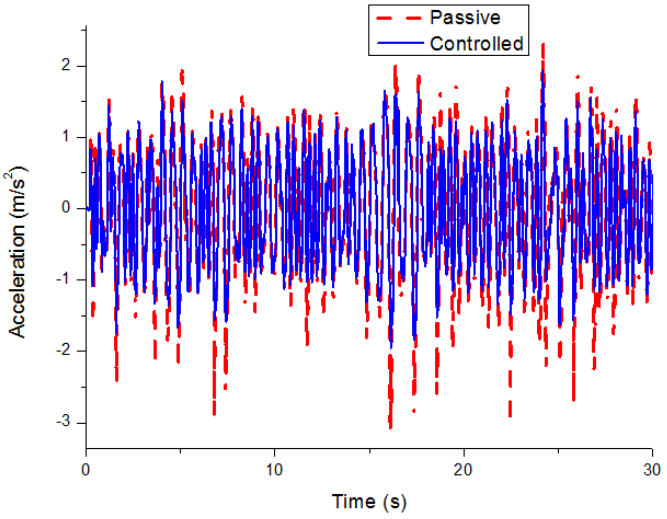

Figure 6-42. Random vibration test.

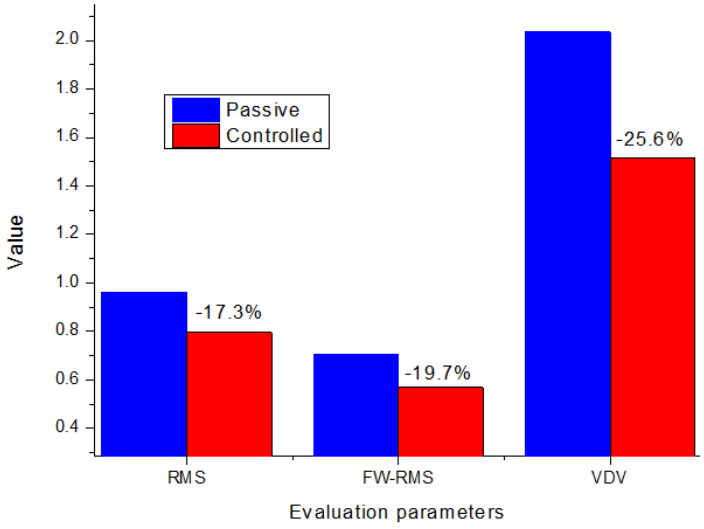

Figure 6-43. Evaluation parameters.

The PWM duty cycle output of the proposed seat suspension system is shown in Figure 6-44 which indicates that, with the proposed control method, the damping of the seat suspension is varying between its maximum and minimum values.

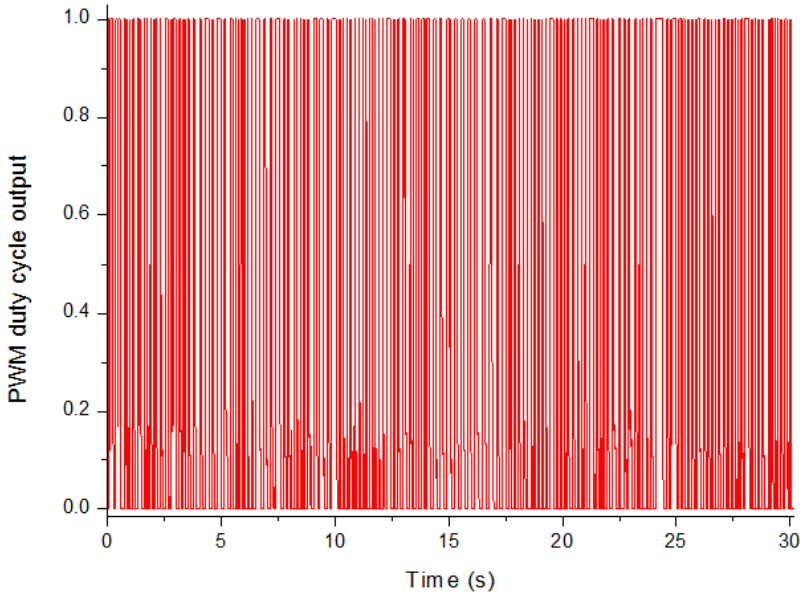

(a)

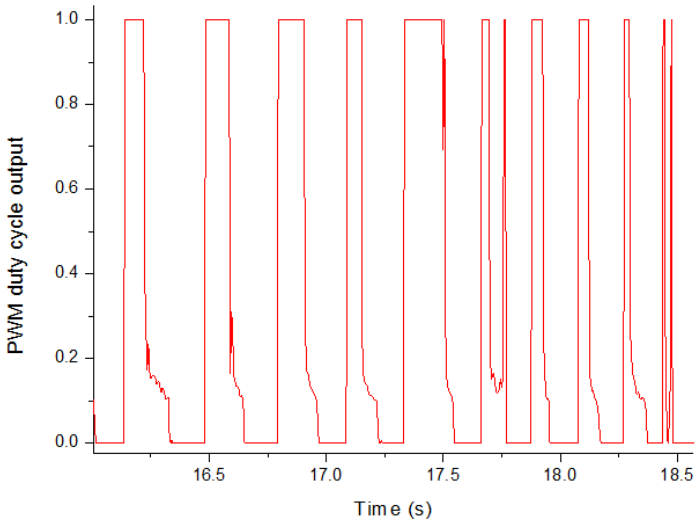

(b)

Figure 6-44. PWM duty cycle output.

The harvestable power is shown in Figure 6-45. The maximum power can reach 12 W, and the RMS power is 1.115 W. The energy harvesting potential of the variable damping seat suspension is much higher than its consumption, which is less than 70 mW. If energy storage devices, such as the battery and supercapacitor, are introduced to the system, the system can work without energy provision from vehicle battery. In addition, the application of this seat

suspension can be extended; when the vehicle is working on roads with different roughness, corresponding damping can be selected, thus, real-time control is not required and fewer sensors are needed.

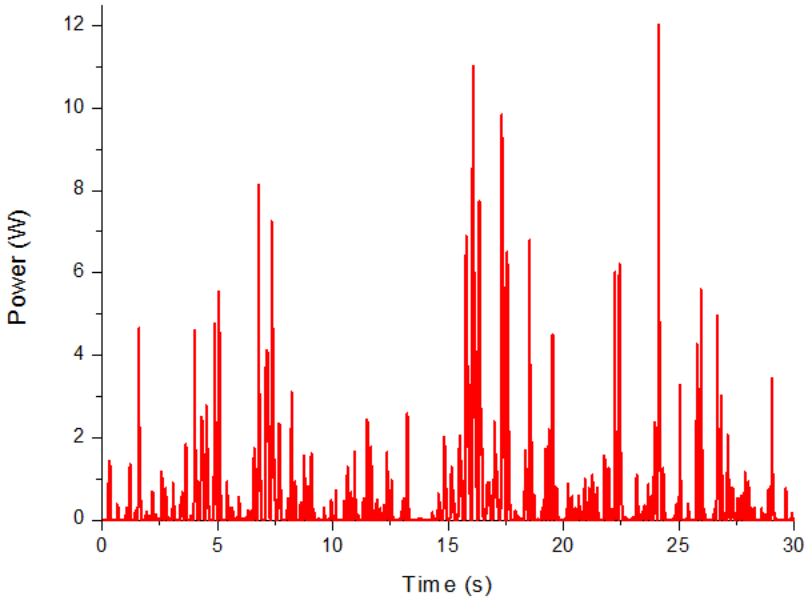

Figure 6-45. Harvestable power.

6.5 Conclusions

In this chapter, an energy regenerative EMD seat suspension has been designed, manufactured and evaluated; two implementation methods have been proposed to vary the damping of the EMD in real time in order to reduce the vibration magnitude of the seat suspension. This damping controllable EMD seat suspension applies a three-phase rotary generator and a gear reducer installed in the seat's scissors structure; the generated damping force (BEM force) can be controlled by a variable external resistance or a MOSFET switch. The basic control concept of the two methods is to control the current through the system circuit by changing the total resistance, thus, the BEM force of the EMD can be controlled. The proposed seat suspension is energy saving when compared with other variable damping seat suspension, such as MR or ER damper seat suspension, and it has regeneration capability.

In the first method, a rotary rheostat has been applied to vary the circuit external resistance directly. The external resistance-dependent, frequency-dependent and amplitude-dependent tests have been implemented, respectively; the integrated mathematical model including the seat suspension and the generator can match the result very well. An experimental phenomenon model has been built for the controller design. A semi-active state feedback H_∞ controller is designed for this seat suspension, and it is validated with simulations and experiments. A well tuned passive seat suspension is applied to evaluate the performance improvement. Based on ISO 2631-1, the FW-RMS acceleration of the semi-active controlled regenerative seat suspension has a 22.84% reduction when compared with conventional passive seat under random vibration. This indicates a great improvement of ride comfort. At the same time, there are 1.21 W of RMS power can be harvested.

A MOSFET switch module and an external resistor have been applied in the second implementation method. A test system has been designed to analyze the variable damping characteristic of the EMD. The test result indicates that the damping of the EMD can be controlled by exerting PWM signal with different value of duty cycle on the MOSFET switch. Based on the test result and the kinematic of the seat suspension, the damping variation range of the seat suspension has been derived, which is from 115.68 Ns/m to 669.74 Ns/m. Then, a control method for vibration isolation has been designed for the seat suspension prototype. The designed seat suspension and its control method have been validated with vibration test on a 6-DOF vibration platform in frequency domain and time domain; a well tuned commercial passive seat suspension has also been tested for comparison. When the variable damping seat suspension is controlled, the FW-RMS acceleration and VDV are decreased 19.7% and 25.6%, respectively, compared with the passive one. At the same time, the harvestable RMS power is 1.115 W which is much higher than energy consumption of the

PWM control signal (less than 70 mW). Thus, this energy saving variable damping seat suspension is promising in the application, especially for the future electrical vehicles.

Both implementation methods can greatly improve the ride comfort with very few energy consumption; the first one has a better performance in terms of vibration control but it needs an additional motor to control the external resistor; the second one is directly controlled by PWM signal, thus, it is more stable and practical.

7 MULTIPLE-DOF ACTIVE SEAT SUSPENSION

7.1 Introduction

In the above three chapters, the single-DOF seat suspensions for reducing vertical vibration have been designed, manufactured and validated. This chapter will present an innovative two-layer multiple-DOF seat suspension for heavy duty vehicles. The seat suspension can reduce the vibration of driver body in five DOFs except the yaw vibration, which has least effect on human, with only three actuators; though the five DOFs cannot be fully controlled by the three actuators, all of their magnitudes can be reduced. Another advantage of a two-layer structure is that, the vertical vibration reduction can be decoupled from reducing the lateral trunk bending and forward flexion of the driver body, according to the fact that the most sensitive frequency contents of the vertical vibration to human are much higher than the frequency content of other four DOFs vibrations. A H_∞ controller is designed for the top layer control based on a simplified and decoupled model. Further, a nonsingular terminal sliding mode controller is designed based on a coupled mode with top and bottom layers suspension. The low cost MEMS sensor mpu9205 is applied in the implementation of the two

controllers. The proposed seat suspension and controllers are validated with simulation and experiments.

7.2 Multiple-DOF Active Seat Suspension Design

In this section, the WBV on heavy duty vehicle drivers is discussed, and then, a multiple-DOF seat suspension with two layers is proposed and manufactured.

7.2.1 Whole body vibration

Generally, the vertical vibration isolation, which is proven to have the biggest vibration magnitude and affect most drivers' comfort in common passenger vehicles, is considered in designing a seat suspension; when operating a heavy duty vehicle, the severe vibration caused by uneven roads and operation of machine tools for digging, dumping, shovelling, and loading will be transferred to the seat, thus the occupant often experiences WBV. The WBV in terms of the body frame x3-y3-z3 are defined as shown in Figure 7-1, where the three translational vibrations are along x3, y3 and z3 axes; the three rotational vibrations, which are also called roll, pitch and yaw motions, are around the three axes.

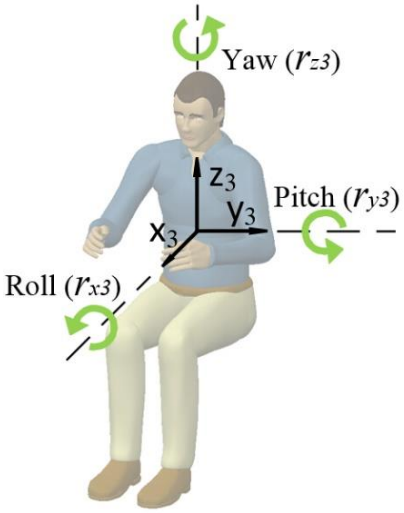

Figure 7-1. WBV of the seated human body.

To evaluate human exposure to WBV in vehicles, ISO 2631-1 is always applied, which has defined methods for the measurement of WBV and provides guidance on the possible effects of vibration on health, comfort, perception and motion sickness. The effect of vibration on the driver's health and ride comfort is dependent on the vibration frequency content. The FW-RMS acceleration and VDV have been defined in Section 4.4.2.

ISO 2631-1 has defined the evaluation way of the WBV's effects on drivers' comfort and perception; the six-DOF vibration from seat surface can be combined as follows:

$$\boldsymbol{a_v} = (\boldsymbol{k_x}^2\boldsymbol{a_{wx}}^2 + \boldsymbol{k_y}^2\boldsymbol{a_{wy}}^2 + \boldsymbol{k_z}^2\boldsymbol{a_{wz}}^2 + \boldsymbol{k_{rx}}^2\boldsymbol{a_{wrx}}^2 + \boldsymbol{k_{ry}}^2\boldsymbol{a_{wry}}^2 + \boldsymbol{k_{rz}}^2\boldsymbol{a_{wrz}}^2)^{\frac{1}{2}} \quad (7\text{-}1)$$

where a_{wx}, a_{wy} and a_{wz} are the FW-RMS accelerations with respect to the x3, y3 and z3 axes, respectively; $a_{wrx,}a_{wry}$ and a_{wrz} are FW-RMS rotational accelerations with respect to the three axes, respectively; $k_x = 1$, $k_y = 1$, $k_z = 1$ $k_{rx} = 0.63\,\mathrm{m/rad}$, $k_{ry} = 0.4\,\mathrm{m/rad}$ and $k_{rz} = 0.2\,\mathrm{m/rad}$ are multiplying factors defined by ISO 2631-1, which indicates that the sensitivities of driver with WBV in six DOFs are different. Among the three rotational accelerations, a_{rz} has the smallest multiplying factor, thus it contributes least to the combined six-DOF vibration a_v which is applied to evaluate human exposure to WBV. Further, based on the frequency-weighting curves for single-DOF vibrations defined in ISO 2631-1, the driver's comfort is affected most seriously by 5 to 8 Hz translational vibration along z3 axis, 1 to 1.25 Hz translational vibration along x3 and y3 axes, and 0.8 Hz rotational vibration around three axes. It is easy to notice that the most sensitive frequencies for human are close in terms of translational vibration along x3 and y3 axes, and the three rotational vibrations; and the sensitive frequencies of translational vibration along z3 axis are much higher than vibrations in other DOFs. Thus, in conclusion, when designing a multiple-DOF seat suspension, the yaw vibration control could not be considered in order to reduce the

complexity of the seat suspension; the translational vibration along z3 axis could be decoupled from other DOFs for vibration control.

7.2.2 Multiple-DOF seat suspension for WBV control

Although the driver is exposed to vibration in six DOFs for heavy duty vehicles, the seat suspension structure will be complicated and the cost and energy consumption will be high if all the vibrations are considered to be reduced. In this section, a novel two-layer multiple-DOF seat suspension with three active actuators is proposed to reduce WBV in five DOFs where the yaw vibration is not included considering the ISO 2631-1 evaluation criteria, the possible complexity of the structure, and the implementation cost.

Figure 7-2 shows the schematic diagram of the proposed two-layer multiple-DOF seat suspension model. The bottom-layer suspension is a single-DOF seat suspension with spring stiffness k_s, friction f_{rt}, actuator output u_b; this suspension can isolate vibration along the z axes of the three coordinate frames. The top-layer suspension has a two-DOF active joint which can rotate around the x2 and y2 axes (Figure 7-2 shows the structure in y2-z2 plane which is the same in x2-z2 plane). In the joint, there are friction torques f_{rrx} and f_{rry}, and actuator output torques u_{rx} and u_{ry}. At the same time, the springs k_t will make the joint have rotary stiffness around x2 and y2 axes. k_c and c_c are the stiffness and damping of the seat cushion, respectively. The coordinate frame 3 is in the center of gravity of the driver body mass. H_b is the distance between coordinate frame 3 and coordinate frame 2; H_s is the distance between coordinate frame 2 and coordinate frame 1.

The cab floor transfers multiple-DOF vibrations to the seat suspension. The proposed seat suspension can isolate those vibrations transferred to driver body in five DOFs except the yaw vibration. The effectiveness of the bottom-layer suspension in translational vibration control along z3 axis has been extensively validated in single-DOF active seat suspension

studies, thus, it is not further explained in this chapter. When a roll vibration (r_{x1}) is exerted on the seat base, a translational vibration along y3 axis and a rotational vibration around x3 axis (r_{x3}) are both generated. Based on ISO 2631-1, the most sensitive frequencies for human are close in terms of translational vibration along y3 axis, and the roll vibration (r_{x3}), thus, the low frequency of roll vibration input will deteriorate driver's comfort seriously in two DOFs. With the proposed multiple-DOF seat suspension, an active torque can be exerted on the x2 axis which can reduce vibration in the two DOFs. The similar situation exists in pitch vibration input.

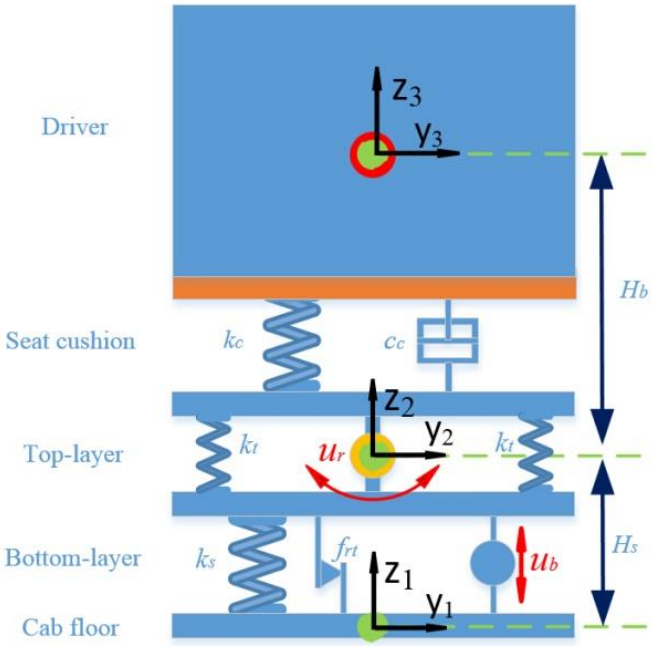

Figure 7-2. Schematic diagram of a two-layer M-DOF seat suspension.

For further illustrating the vibration isolation concept of the proposed seat suspension, a roll vibration excitation (r_{x1}) is taken as an example as shown in Figure 7-3. It is assumed that, in the equilibrium position, the distances of the center of driver body mass (coordinate frame 3) to the cab floor (coordinate frame 1) are equal in both the proposed multiple-DOF seat suspension and a traditional single-DOF one, which does not have a two-DOF rotational joint. It is seen from Figure 7-3 (a) that, when the single-DOF seat is applied, with a roll

vibration angle θ, the driver body will have an equal roll vibration angle θ, and its mass center will have a horizontal translation L_1. By controlling the joint of the multiple-DOF seat suspension, the rotational angle and the translational distance of the driver body can be compensated, respectively.

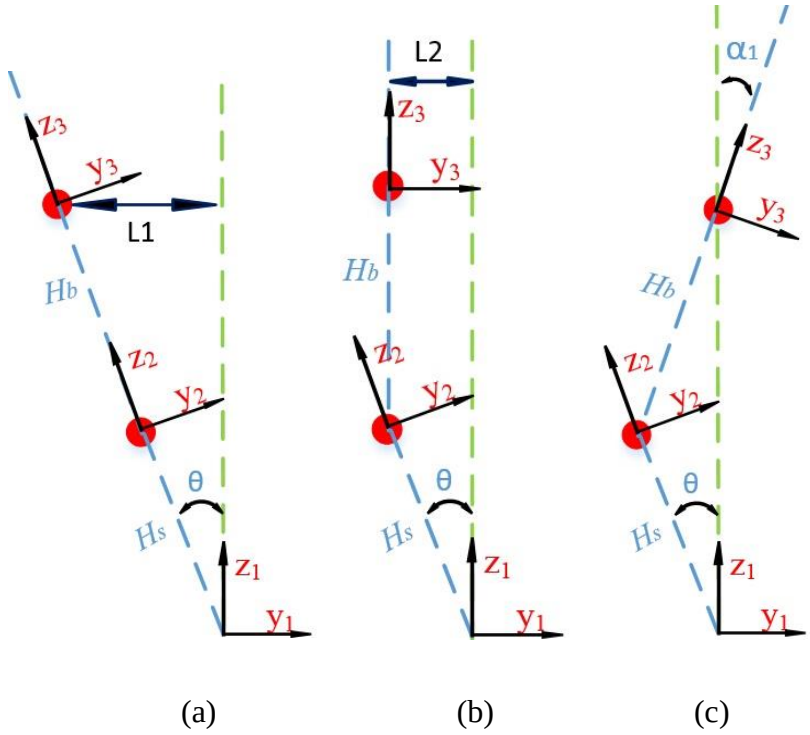

(a) (b) (c)

Figure 7-3. Seat suspension with roll vibration. (a) Single-DOF seat suspension. (b) Multiple-DOF seat suspension with rotational angle compensation. (c) Multiple-DOF seat suspension with translational distance compensation.

Table 7-1 shows the results of the rotational angle compensation and the translational distance compensation compared with the single-DOF seat. By controlling one rotary DOF, two DOFs vibration of driver body can be reduced with both compensation ways because the translational distance and rotational angle are both decreased; thus the driver body is suffered less translational and rotational vibrations than with the single-DOF seat. Combining with the bottom-layer suspension control, the proposed two-layer seat suspension is able to isolate translational vibrations along x3, y3 and z3 axes, and rotational vibrations of roll (r_{x3}) and

pitch (r_{y3}) by controlling three active actuators, that is, the WBV of driver body can be reduced in five DOFs. In addition, the results show the translational vibration along y3 and rotational vibration r_{x3} cannot be simultaneously reduced to zero, which means that the five DOFs vibrations cannot be independently reduced by only three active actuators.

Table 7-1. Driver body movement with Roll vibration.

	Single-DOF seat	Multiple-DOF seat	
		Rotational Angle compensation	Translational distance compensation
Translational distance	$L_1 = \sin\theta(H_b + H_s)$	$L_2 = \sin\theta H_s$	0
Rotational angle	θ	0	$\alpha_1 = -arcsin\frac{sin\theta H_s}{H_b}^*$

*Generally, $H_s < H_b$, thus $|\theta| > |-arcsin\frac{sin\theta H_s}{H_b}|$

7.2.3 Multiple-DOF seat suspension prototype

A multiple-DOF seat suspension prototype has been built based on the concept analysis of the last section, as shown in Figure 7-4. In Chapter 4, a single-DOF active seat suspension with rotary motor has been developed, which is adopted as the bottom-layer suspension of the multiple-DOF seat suspension. The top-layer suspension is mounted on the top of the bottom-layer suspension; its main part is a two-DOF rotary joint as shown in Figure 7-5; the joint consists of a seat mount plate which will be fixed with a seat, and two drive shafts which are used to rotate the seat mount plate; the seat mount plate is assembled with the drive shaft in roll with a bearing and connecting shaft, thus, the drive shaft in pitch can exert a force on lower part of the seat mount plate to make it rotate around y2 axis (the connecting shaft); the drive shaft in roll can rotate the seat mount plate around x2 axis. Therefore, the seat mount plate can rotate around y2 and x2 axes. Figure 7-6 shows the layout of the top-layer

suspension, where there are four springs assembled in the four corners of the bottom-layer suspension providing rotary stiffness. The actuators are composed with rotary motors and planetary gear reducers, where the planetary gear reducers are applied to amplify torque output of the motors to reduce the requirement of motor's rated torque output and also reduce the actuator cost. In this thesis, for the top-layer suspension, Panasonic servo motors (MSMJ042G1U) with 1.3 Nm rated torque output and gear reducers with ratio 40:1 are used, thus, the rated torque output of the actuators can reach 52 Nm.

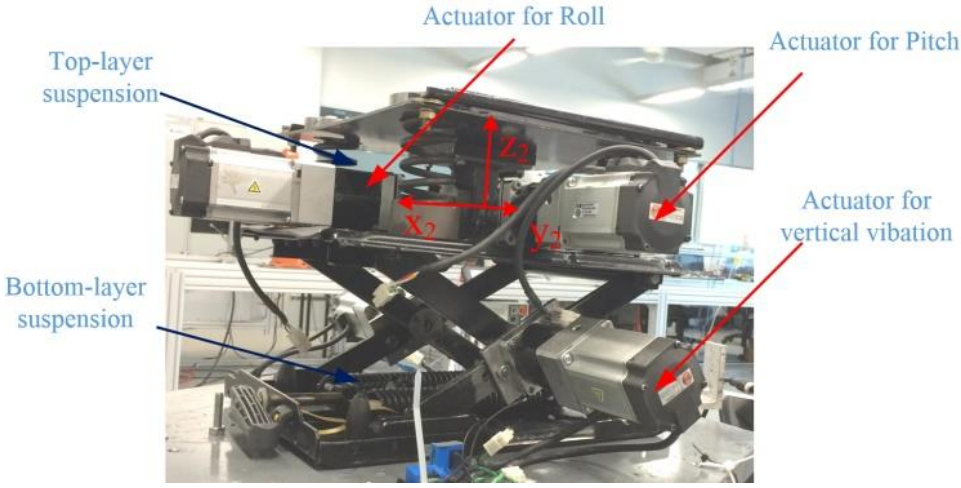

Figure 7-4. M-DOF seat suspension prototype.

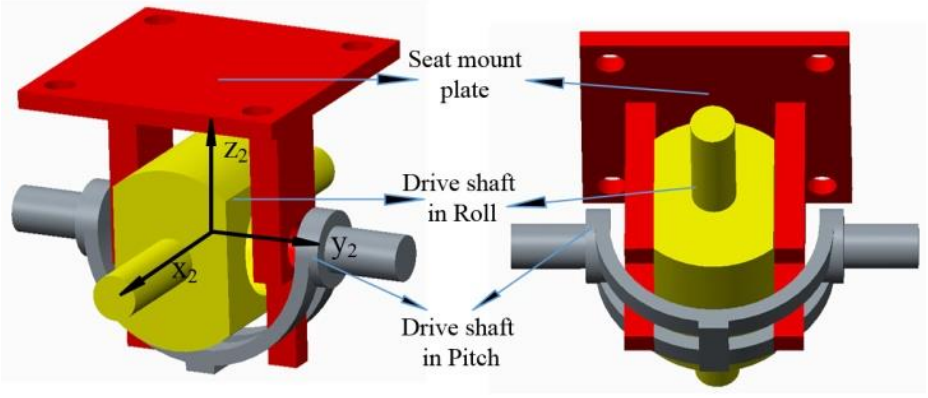

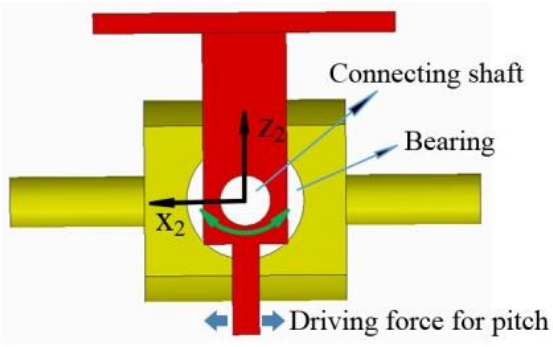

(a)

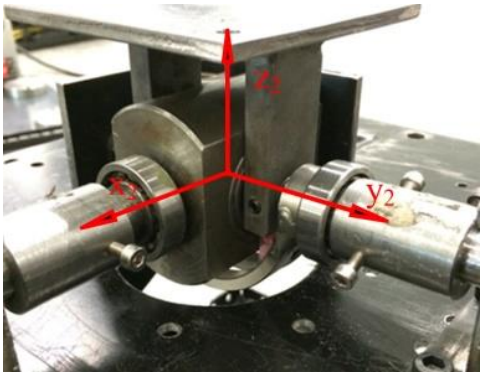

(b)

Figure 7-5. Two-DOF rotary joint. (a) Design. (b) Prototype.

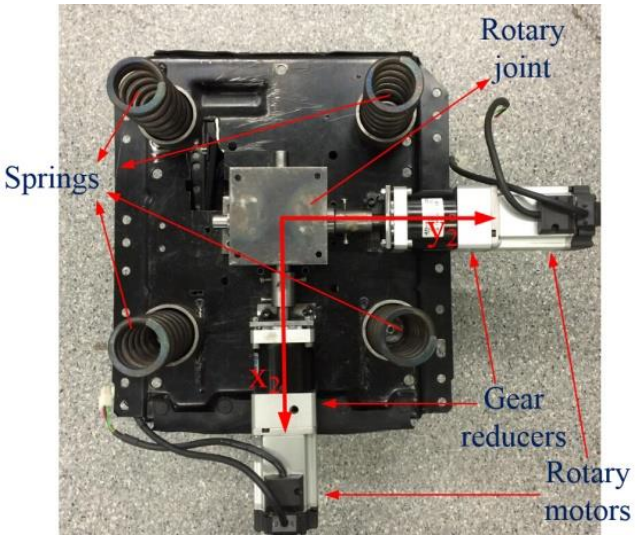

Figure 7-6. Top-layer suspension layout.

7.3 Parameters Identification of Top Layer Suspension

In this section, the top-layer of the multiple-DOF seat suspension prototype is tested. Furthermore, based on the test results, the top-layer suspension's parameters are identified.

7.3.1 Test system

For identifying the parameters of the top-layer suspension, a test system has been built as shown in Figure 7-7, where a CompactRio 9074 is applied to send desired motor motion profile to the motor drive and receive feedback signals. The rotational angle of the motor can be accurately controlled by its drive. The encoder in the motor can feedback the real rotational angle, and the real torque output of the motor can be also sent to CompactRio 9074 by its drive.

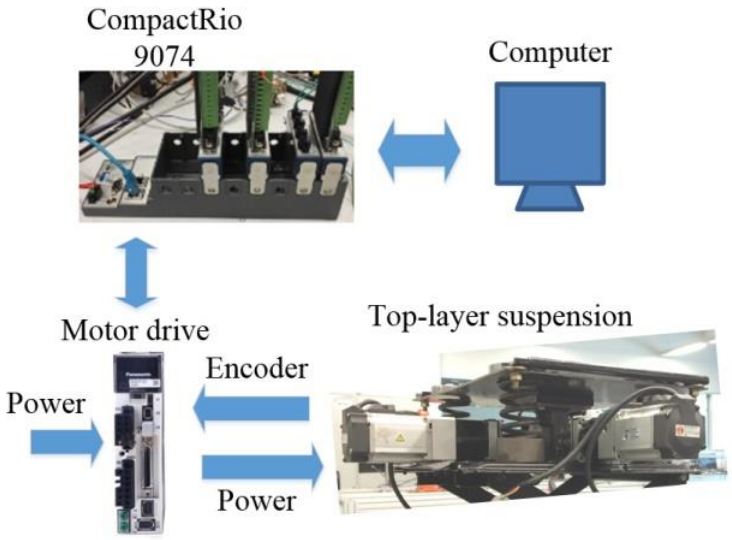

Figure 7-7. Top-layer suspension test system.

7.3.2 Test results and parameters identification

The two-DOF joint is designed to be controlled independently for the two rotational DOFs. The two actuators can drive the seat mount plate, where the seat is fixed, to move according to the designed sinusoidal profile. For roll (r_{x2}) and pitch (r_{y3}) movements, the frequency-

dependent and amplitude-dependent tests were conducted, respectively. The measured torque T of the actuator (amplified by its gear reducer) is defined as:

$$T = k_r(\theta - \theta_{bias}) + f_{rr} \tag{7-2}$$

where k_r is the rotary stiffness determined by the four corner springs that need to be identified in each tested rotary DOF; θ is the real rotary angle obtained from the encoder; θ_{bias} is a small initial bias of the rotary angle caused by the imperfection of the manufactured prototype, which should be zero ideally; f_{rr} is the friction torque generated by gear reducer and the joint. A simplified friction model is applied in this thesis as:

$$f_{rr} = \begin{cases} F_{rr} sign(\dot{\theta}), & |\dot{\theta}| > \delta \\ F_{rr} \frac{\dot{\theta}}{\delta}, & |\dot{\theta}| < \delta \end{cases} \tag{7-3}$$

where $\delta > 0$ is a small rotary velocity boundary for the direction switching of the friction; F_{rr} is the Coulomb friction parameter. It can be seen from (7-2) that the torque output depends on the suspension spring torque and friction torque.

The test results in roll and pitch directions are shown in Figure 7-8 and Figure 7-9, respectively, where the upper platform of the suspension is forced to do sinusoidal rotation with different amplitudes (3 degree and 5 degree) and frequencies (0.1 Hz and 0.5 Hz). When the same amplitude rotations are implemented, the torque outputs of the actuators are nearly overlapped with different frequencies in both DOFs. In each direction, when rotations with different amplitudes are implemented, the slope rates of the torque-rotation angle curves are very close. But when comparing the two directions, the slope rates of the torque-rotation angle curves are different. The results indicate that the rotary stiffness in the two directions is different. The identified model parameters are shown in Table 7-2. Figure 7-10 shows comparison between the simulation result and experimental result in roll direction. Figure 7-11 shows the comparison between the simulation result and experiment in pitch direction.

The comparison results indicate that the identified parameters can be applied to describe the dynamic characteristics of the designed top-layer suspension. It is also seen from Table 7-2 that the rotary stiffness in roll direction is higher than it in pitch direction.

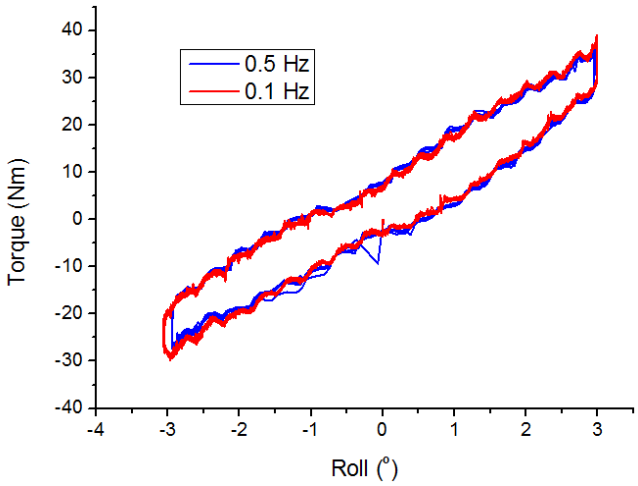

(a)

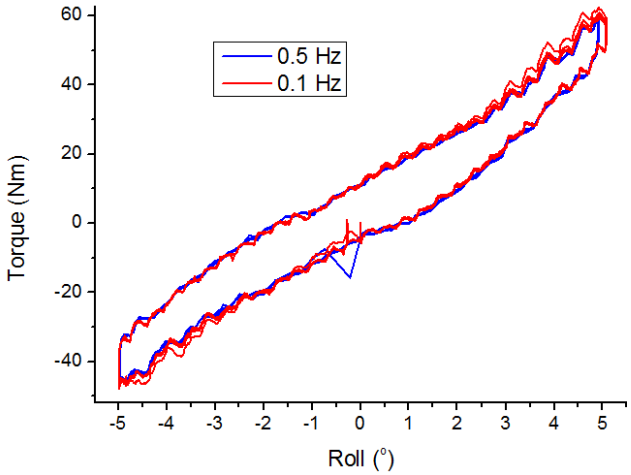

(b)

Figure 7-8. Roll test of the top-layer suspension. (a) with 3 degree amplitude. (b) with 5 degree amplitude.

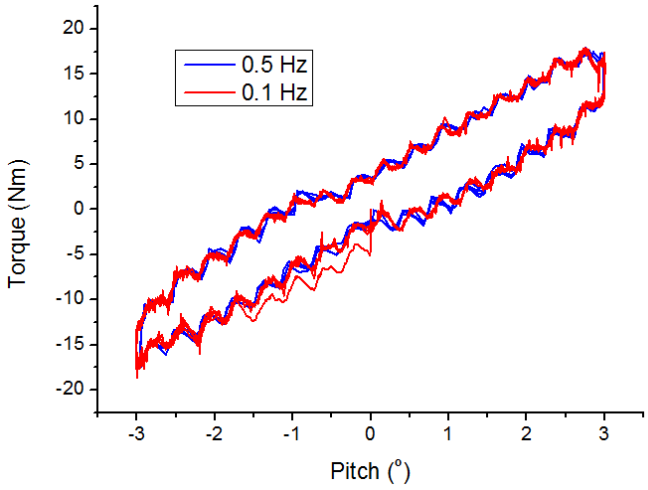

(a)

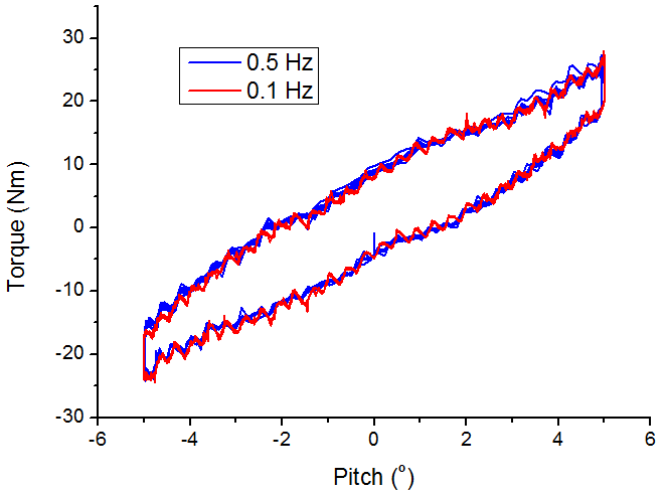

(b)

Figure 7-9. Pitch test of the top-layer suspension. (a) with 3 degree amplitude. (b) with 5 degree amplitude.

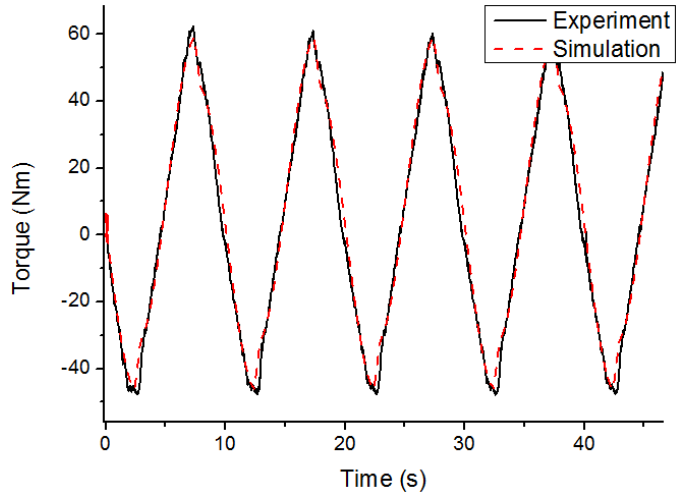

(a)

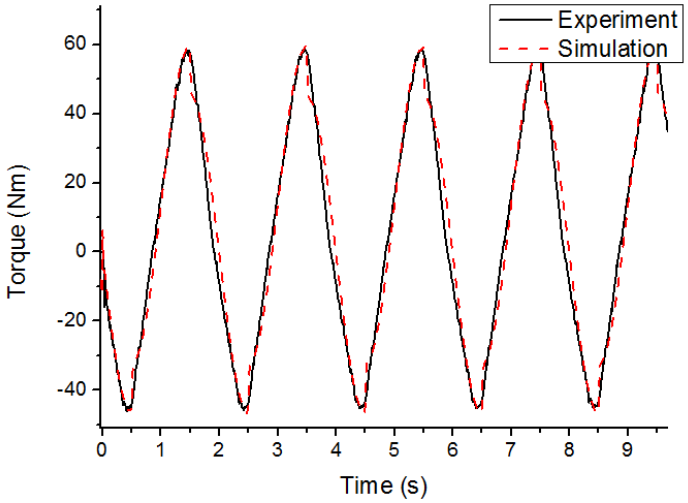

(b)

Figure 7-10. Torque comparison in roll direction. (a) Frequency 0.1 Hz, Amplitude 5°. (b) Frequency 0.5 Hz, Amplitude 5°.

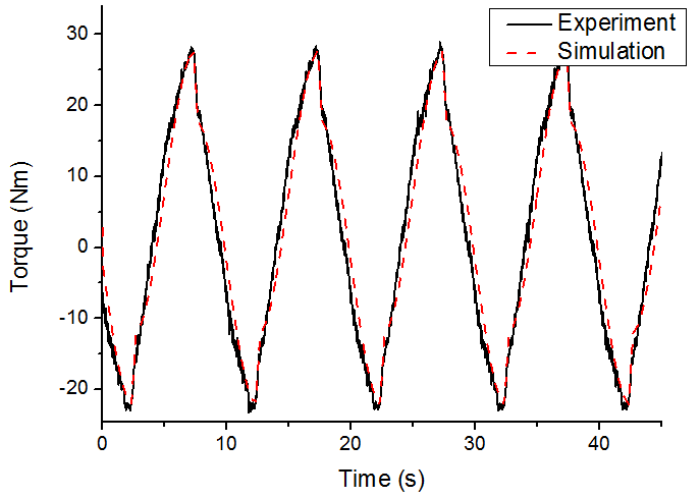

(a)

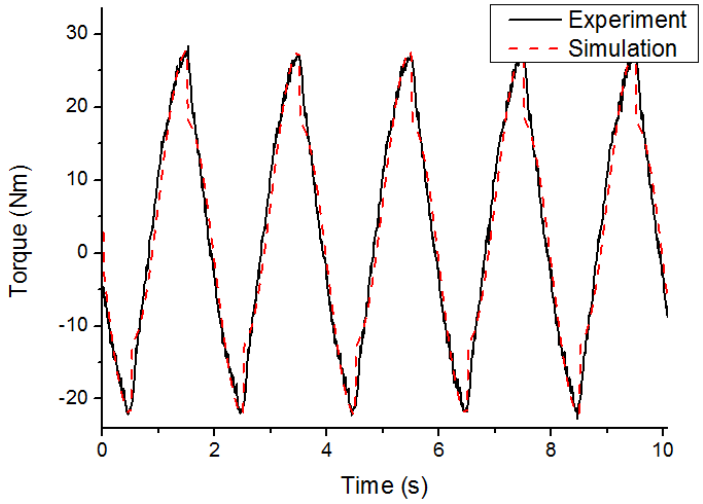

(b)

Figure 7-11. Torque comparison in pitch direction. (a) Frequency 0.1 Hz, Amplitude 5°. (b) Frequency 0.5 Hz, Amplitude 5°.

Table 7-2. Parameters identification.

	Roll	Pitch
k_r	9.2 Nm/degree	4 Nm/degree

F_{rr}	7.3 Nm	5 Nm

7.4 H_∞ Controller with Decoupled model

In this section, a simplified model is built and a H_∞ Controller is applied to control the top-layer.

7.4.1 Decoupled model

Benefiting from the two-layer structure, the control of the three actuators has very few interactions which have been validated in the next section; the two DOFs of the top-layer suspension joint can be controlled independently, thus, their controllers can be separately designed. Moreover, the system analysis of the y-z plane is similar with the x-z plane, thus, only the model of y-z plane is built and simulated in this thesis. For designing the two controllers for the rotary joint, the model of the multiple-DOF seat suspension can be decoupled and simplified with the following assumptions:

Assumption 1: The seat cushion and driver body are assumed to be one rigid body, because the stiffness and damping of the cushion are normally much higher than seat suspension, then the system model is simplified.

Assumption 2: When the system is in the equilibrium position, the z axes of the three coordinate frames are on a line.

Assumption 3: Only roll vibration (r_{x1}) is inputted into the system; the bottom-layer suspension is working in passive way.

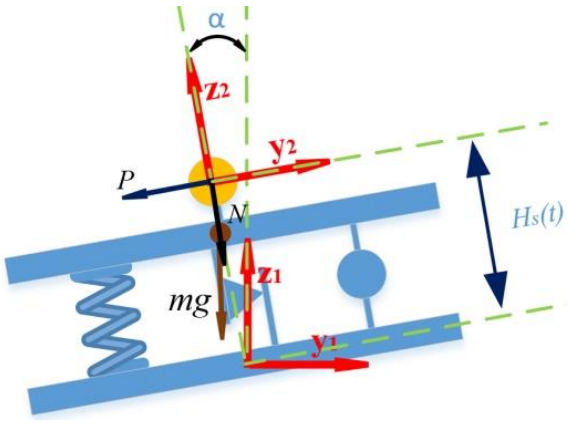

Figure 7-12. Analysis of the bottom-layer.

Figure 7-12 shows the analysis of the bottom-layer where x1-y1-z1 is the fixed reference frame and it is coincident with the center of the seat suspension base; x2-y2-z2 is the frame in the two-DOF joint and fixed with the top of the bottom-layer; $H_s(t)$ (H_s is applied in the following for simplification) is the distance between the two coordinate frames; α is the roll vibration angle; m is the mass of the bottom-layer top; P and N are the reaction forces of the top-layer along y2 and z2 axes, respectively.

H_s is calculated by the bottom-layer's dynamics:

$$m\ddot{H}_s = k_s(l_0 - H_s) - mg\cos\alpha - f_{rt} + u_b - N + m\dot{\alpha}^2 H_s \tag{7-4}$$

which includes spring force, gravity, friction, active force, reaction force and centrifugal force; l_0 is distance between the origins of the two frames when the spring is in free length.

Then, the coordinate of joint (frame 2) in the reference frame 1 is defined as:

$$y_2^1 = -H_s\sin\alpha \tag{7-5}$$

$$z_2^1 = H_s\cos\alpha \tag{7-6}$$

Their acceleration in the refenence frame 1 can be obtained with double derivative:

$$\ddot{y_2^1} = -\left(\ddot{H}_s - H_s\dot{\alpha}^2\right)\sin\alpha + (-2\dot{H}_s\dot{\alpha} - H_s\ddot{\alpha})\cos\alpha \tag{7-7}$$

$$\ddot{z}_2^1 = \left(\ddot{H}_s - H_s\dot{\alpha}^2\right)\cos\alpha + \left(-2\dot{H}_s\dot{\alpha} - H_s\ddot{\alpha}\right)\sin\alpha \tag{7-8}$$

Figure 7-13 shows the analysis of the top-layer where x3-y3-z3 is a frame fixed on the centre of driver body mass; θ is the rotation angle of frame 3 in terms of the reference frame 1; $\theta - \alpha$ is the relative rotation angle of the top-layer.

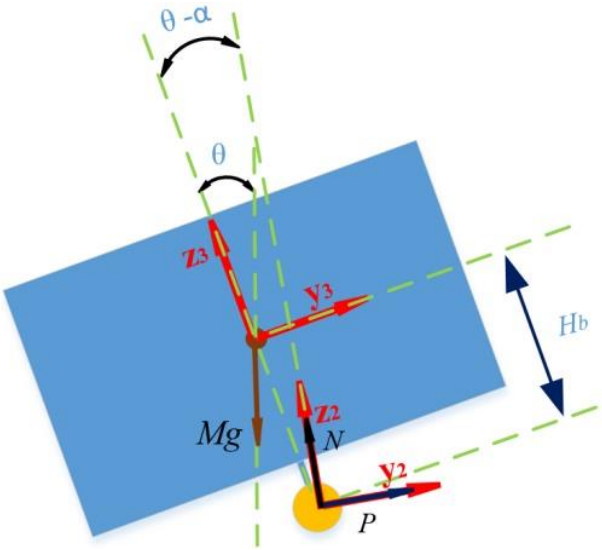

Figure 7-13. Analysis of the top-layer.

The accelerations of driver body along y3 and z3 axes are defined as:

$$\ddot{y}_3^3 = -H_b\ddot{\theta} + \ddot{y}_2^1\cos\theta + \ddot{z}_2^1\sin\theta \tag{7-9}$$

$$\ddot{z}_3^3 = -\dot{\theta}^2 H_b - \ddot{y}_2^1\sin\theta + \ddot{z}_2^1\cos\theta \tag{7-10}$$

The suspension performance can be evaluated by $\ddot{y}_3^3$, $\ddot{z}_3^3$ and $\ddot{\theta}$.

Summing the forces of the top-layer along y3 axis, we can get the following equation:

$$N\sin(\theta - \alpha) + P\cos(\theta - \alpha) - Mg\sin\theta = M\ddot{y}_3^3 \tag{7-11}$$

To get rid of the unknown forces P and N terms in the above equation, sum the moments about the centroid of the driver body:

$$I\ddot{\theta} = [N\sin(\theta - \alpha) + P\cos(\theta - \alpha)]H_b - k_r(\theta - \alpha) - f_{rr} + u_r \tag{7-12}$$

where u_r is the control torque; I is the rotational inertia of the driver body around the x3 axis.

Thus, the decoupled model in y-z plane is:

$$\left(I + MH_b{}^2\right)\ddot{\theta} = -k_r(\theta - \alpha) - f_{rr} + u_r + H_b Mgsin\theta + MH_b\ddot{y}_2^1 cos\theta + MH_b\ddot{z}_2^1 \sin\theta \quad (7\text{-}13)$$

Now, N is still required to be calculated out for obtaining H_s. Therefore, the dynamic of the driver body along z3 axis is derived:

$$N\cos(\theta - \alpha) - P\sin(\theta - \alpha) - Mg\cos\theta - M\dot{\theta}^2 H_b = M\ddot{z}_3^3 \quad (7\text{-}14)$$

Combining with (7-11), thus,

$$N = (M\ddot{z}_3^3 + Mg\cos\theta + M\dot{\theta}^2 H_b)\cos(\theta - \alpha) + (M\ddot{y}_3^3 + Mg\sin\theta)\sin(\theta - \alpha) \quad (7\text{-}15)$$

The analysis of single-DOF seat suspension is shown in Figure 7-14 where H_c is the distance of the frame 1 and frame 3; the whole weight of the seat-body system is the same with the multiple-DOF seat suspension. Similar with the bottom-layer of the multiple-DOF seat, H_c is decided by:

$$(m + M)\ddot{H}_c = k_s(l_0 + H_b - H_c) - (M + m)g\cos\alpha - f_{rt} + u_b + (M + m)\dot{\alpha}^2 H_c \quad (7\text{-}16)$$

The acceleration of driver body along the y3 and z3 axes are derived as:

$$\ddot{y}_3^3 = -2\dot{H}_c\dot{\alpha} - H_c\ddot{\alpha} \quad (7\text{-}17)$$

$$\ddot{z}_3^3 = \ddot{H}_c - H_c\dot{\alpha}^2 \quad (7\text{-}18)$$

The roll acceleration of the driver body is equal to the roll vibration input acceleration $\ddot{\alpha}$.

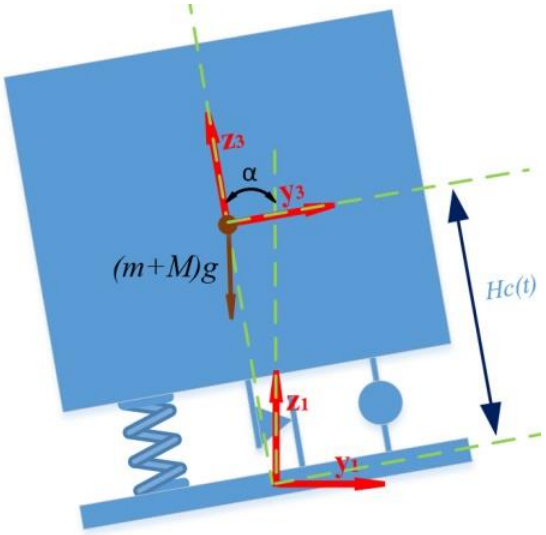

Figure 7-14. Analysis of the single-DOF seat.

7.4.2 Controller design

For the controller design of the rotary joint, the state variables are set as $x_1 = \theta - \alpha$, $x_2 = \dot{\theta}$. The simplification $sin\theta \approx \theta$ is applied for the fourth terms in the right hand of model (7-13), the system model is rewritten as:

$$\dot{x_1} = x_2 + \omega_1 \tag{7-19}$$

$$\dot{x_2} = -\left(\frac{k_r - H_b Mg}{I + MH_b{}^2}\right) x_1 + \frac{u_r}{I + MH_b{}^2} + \omega_2 \tag{7-20}$$

where $\omega_1 = -\dot{\alpha}$, and $\omega_2 = \frac{H_b Mg\alpha + MH_b \ddot{y_U^O} cos\theta - MH_b \ddot{z_U^O} \sin\theta - f_{rr}}{I + MH_b{}^2} + \Delta$, which are both bounded disturbances; Δ is the model uncertainty; u_r is a bounded torque output within -52 Nm to 52 Nm.

For improving the drivers' comfort and keeping the suspension stablity, two controlled outputs are defined as $z_1 = x_1$ and $z_2 = \dot{x_2}$.

Then, the state space equation of the system can be derived as:

$$\dot{\mathbf{X}} = \mathbf{AX} + \mathbf{B_1} u_r + \mathbf{B_2 \omega} \tag{7-21}$$

$$\mathbf{Z} = \mathbf{CX} + \mathbf{D_1}u_r + \mathbf{D_2}\boldsymbol{\omega} \tag{7-22}$$

where $\mathbf{X} = [\, x_1 \; x_2]^{\mathrm{T}}$, $\boldsymbol{\omega} = [\omega_1 \; \omega_2]^{\mathrm{T}}$, $\mathbf{Z} = [z_1 \; z_2]^{\mathrm{T}}$,

$$\mathbf{A} = \begin{bmatrix} 0 & 1 \\ -\left(\frac{k_r - H_b Mg}{I + MH_b{}^2}\right) & 0 \end{bmatrix},\ \mathbf{B_1} = \begin{bmatrix} 0 \\ \frac{1}{I + MH_b{}^2} \end{bmatrix},\ \mathbf{B_2} = \begin{bmatrix} 1 & 0 \\ 0 & 1 \end{bmatrix},$$

$$\mathbf{C} = \begin{bmatrix} 1 & 0 \\ -\left(\frac{k_r - H_b Mg}{I + MH_b{}^2}\right) & 0 \end{bmatrix},\ \mathbf{D_1} = \begin{bmatrix} 0 \\ \frac{1}{I + MH_b{}^2} \end{bmatrix},\ \mathbf{D_2} = \begin{bmatrix} 0 & 0 \\ 0 & 1 \end{bmatrix}.$$

For keeping the system's stability, $k_r > H_b Mg$ should be considered when selecting the spring stiffness.

Thus, a state feedback H_∞ controller is designed as:

$$u_r = \mathbf{KX} \tag{7-23}$$

where **K** is the controller gain to be designed.

As the H_∞ controller has been applied in many control systems [123], the destailed design procedure of the controller, is not presented here for saving space.

7.4.3 Performance validation

In this section, the simulation result with the designed controller is presented. To experimentally validate the effectiveness of the multiple-DOF seat suspension prototype in suppressing vibrations in multiple DOFs, the prototype is tested on a six-DOF vibration platform. The random roll and pitch vibration with random vertical vibration test results are shown and discussed.

7.4.3.1 Simulation

Table III shows the model parameters in the simulation. The friction model (7-3) is also applied for the bottom-layer suspension friction. The controller is designed as $\mathbf{K} =$

$[-900 \quad -350]$. A sweep frequency rotational vibration is applied; its frequency is from 0.3 Hz to 2.5 Hz with duration 50 s; the vibration amplitude is set as 1 ° (about 0.0175 rad).

Table 7-3. Simulation parameters.

H_b	0.4 m
l_0	0.363 m
I	2 kg*m^2
M	70 kg
m	5 kg
g	9.81 m/s^2
k_r	527.4 Nm/rad
k_s	4600 N/m
F_{rr}	7.3 Nm
F_{rt}	80 N

The body's roll (r_{x3}) acceleration is shown in Figure 7-15 where the rotational acceleration is greatly reduced with the multiple-DOF seat. At the same time, the body's acceleration along y3 axis is also controlled, as shown in Figure 7-16. In both seats, body's accelerations along z3 axis are very small, as shown in Figure 7-17, which indicates that, with low frequency rotational vibration, the body's translational vibration along z3 axis has been affected very little. The simulation results indicate that, when only roll vibration (r_{x1}) is applied to the seat suspension, for the single-DOF seat suspension, the rotational accelration will all be transmitted to the human body and a big mangitude translational vibration along y3 axis will

also be introduced. With the proposed multiple-DOF seat suspension, the rotational and translational vibration can be controlled simultaneously.

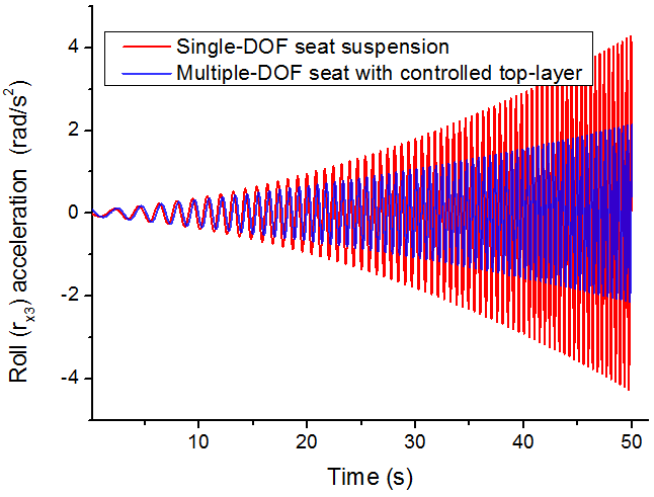

Figure 7-15. Body's rotational acceleration around x axis of reference frame.

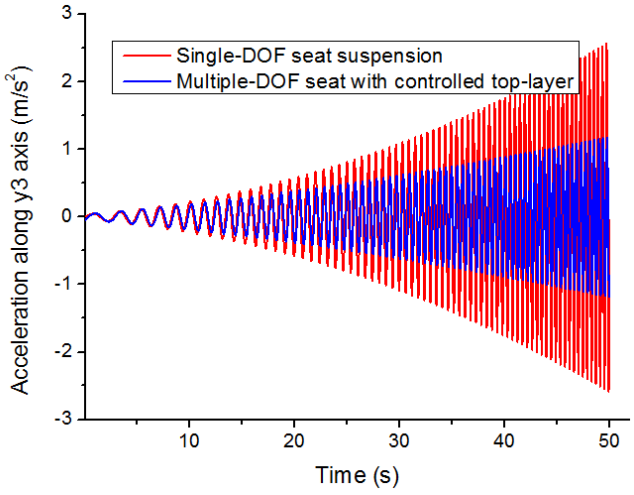

Figure 7-16. Body's translational acceleration in reference frame along y_3 axis.

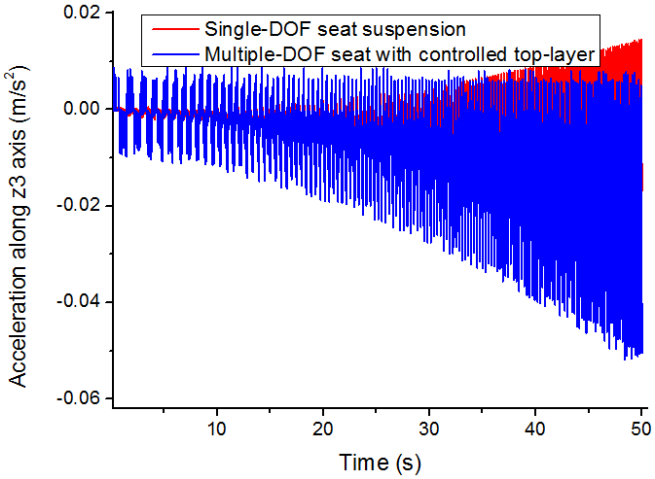

Figure 7-17. Body's translational acceleration in reference frame along z_3 axis.

7.4.3.2 Experimental setup

The experimental setup is shown in Figure 7-18, where the multiple-DOF seat suspension is fixed on the top of the six-DOF vibration platform. A 45 Kg mass is loaded on the seat to simulate the driver body mass. An inertial measurement unit (IMU) sensor (XSENS) is attached on the seat surface to record the multiple DOFs vibration. The location of sensors is shown in Figure 7-19; a MEMS sensor (MPU9250) is attached at the centre of the multiple-DOF seat suspension upper platform to measure the rotational velocities of the seat; an accelerometer (ADXL 203EB) and a laser displacement sensor (optoNCDT 1302) are applied for bottom-layer control. Figure 7-20 shows the whole experiment system, where the multiple-DOF seat suspension is controlled by a CompactRio 9074 which can get the vibration signals of the seat from MPU9250 and the relative rotation angles of the top-layer suspension from encoders of the motor. The designed controller calculates out the desired torques according to the feedback signals and sends to the corresponding drive of the motors on the suspension. Then the actuators will output corresponding torques.

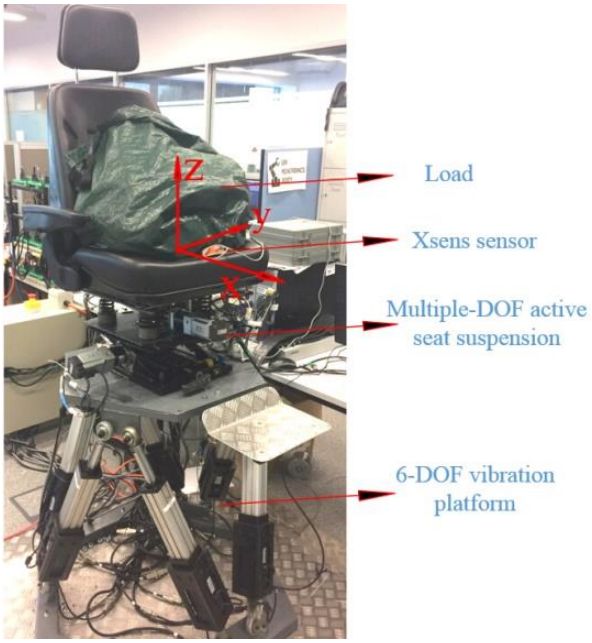

Figure 7-18. Experiment setup.

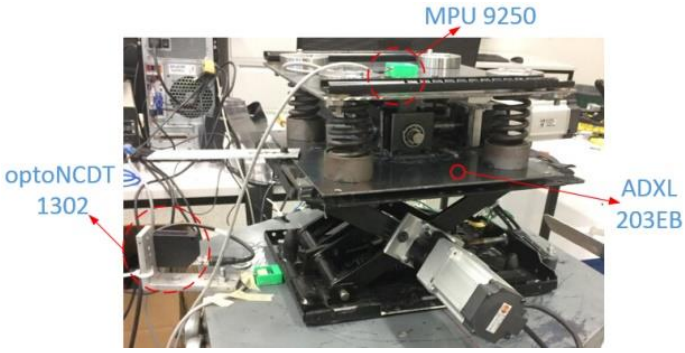

Figure 7-19. Location of sensors.

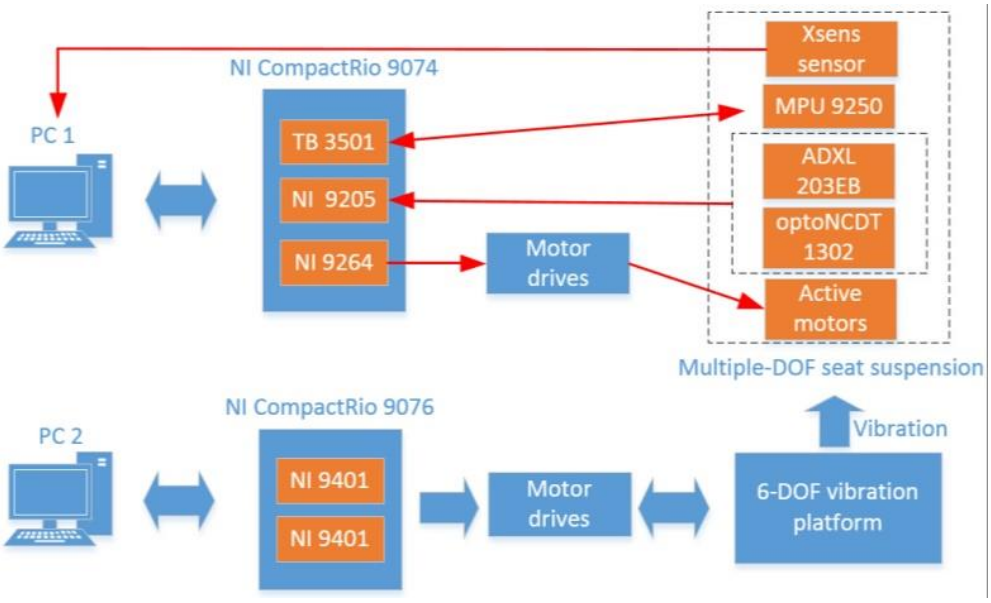

Figure 7-20. Experiment system.

In this chapter, two sets of vibration are applied, the random roll vibration with random vertical vibration and the random pitch vibration with random vertical vibration. The vibration signals recorded by XSENS sensor are used to evaluate the control performance. By trial and error based on simulation result, the controller gains are designed as $\mathbf{K} = [-700 \quad -320]$ and $\mathbf{K} = [-600 \quad -250]$, for the roll and pitch motions, respectively. For validating the effectiveness of the multiple-DOF seat suspension and investigating the interaction between the top-layer and bottom-layer control, three kinds of experiments are implemented with each set of vibration, the bottom-layer and top-layer are both uncontrolled, the bottom-layer is controlled and top-layer is uncontrolled, and the bottom-layer and top-layer are both controlled.

7.4.3.3 Random vibration test

When the six-DOF vibration platform generates a random roll vibration with random vertical vibration, several DOFs vibrations will yield in the seat surface. Figure 7-21 shows the comparison of z axis acceleration of seat surface where when the bottom-layer suspension is controlled, the vibration magnitude is reduced obviously no matter whether the top-layer is

controlled. The y axis acceleration of the seat surface is shown in Figure 7-22 where when the top-layer suspension is controlled, the y axis acceleration is controlled; a similar result exists in Figure 7-23 which shows the estimated roll angle by XSENS sensor. The results indicate that the interaction of the top-layer control and bottom-layer control is very small. Figure 7-24 shows the desired control torque output; because the maximum torque output is 52 Nm, the applied actuator can generate enough torque except a few moments when the roll vibration magnitude is very big.

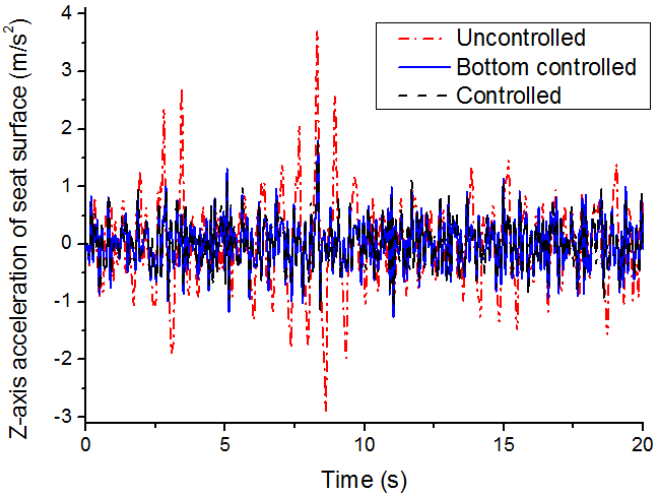

Figure 7-21. z-axis acceleration of seat surface.

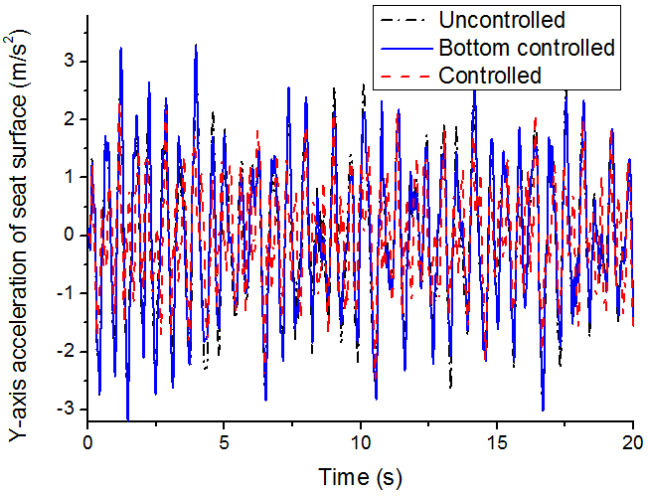

Figure 7-22. y-axis acceleration of seat surface.

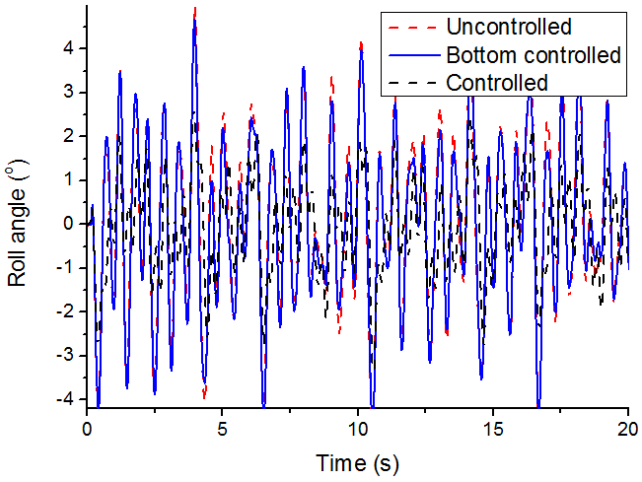

Figure 7-23. Roll angle of seat surface.

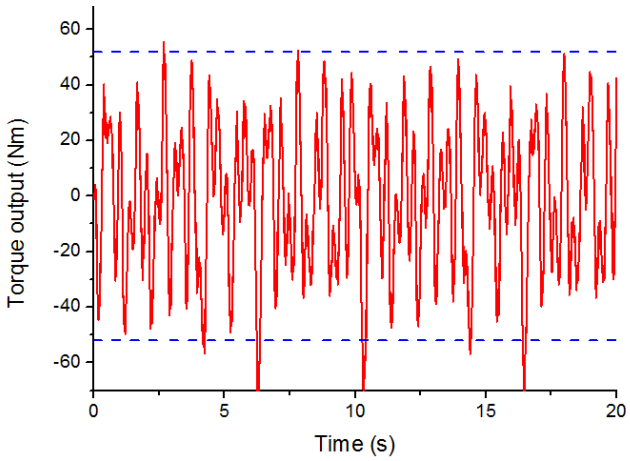

Figure 7-24. The control torque.

Table 7-4 shows the FW-RMS values of the test results, from which it can be seen that when only the bottom-layer is controlled, the z axis FW-RMS acceleration of the seat surface is reduced by 20.4%, but the values of the other two DOFs vibrations caused by the roll vibration are close with the uncontrolled case; when the multiple-DOF seat suspension is fully controlled, the vibration in three DOFs are all controlled; the WBV is reduced by 38.5%.

Table 7-4. FW-RMS acceleration of seat surface with roll and vertical vibration.

	Z axis (m/s^2)	Y axis (m/s^2)	Roll (rad/s^2)	WBV (m/s^2)
Uncontrolled	0.51	1.211	2.081	1.856
Bottom controlled	0.4059	1.192	2.095	1.824
Controlled	0.3973	0.7096	1.271	1.141

Similarly, the pitch and vertical vibration test results are analyzed in Table 7-5. When only the bottom-layer is controlled, though the z axis FW-RMS acceleration is reduced by 23.5%, the WBV control has not been improved; when the multiple-DOF seat suspension is fully controlled, the FW-RMS value of z axis acceleration, y axis acceleration and pitch acceleration are reduced by 25.5%, 32.1% and 40.7%, respectively, and the magnitude of WBV is reduced by 33.8%.

Table 7-5.FW-RMS acceleration of seat surface with pith and vertical vibration.

	Z axis (m/s^2)	Y axis (m/s^2)	Pitch (rad/s^2)	WBV (m/s^2)
Uncontrolled	0.51	1.37	2.31	1.729
Bottom controlled	0.39	1.36	2.53	1.7395
Controlled	0.38	0.93	1.37	1.144

In the experiments, the magnitude of the applied roll and pitch vibration is big in order to fully demonstrate the advantage of the two-layer seat suspension. The test results indicate that by exerting rotational vibration on the base of a seat suspension, a rotational vibration and a translational vibration will be both introduced on the seat surface; the proposed multiple-DOF seat suspension with the top-layer suspension can decrease those vibrations greatly; the interaction of the top-layer and bottom-layer control is small, thus their controller can be designed independently.

7.5 Roll and Vertical Vibration Control with A Nonsingular Terminal Sliding Mode Controller

In the last section, the vertical vibration has not been considered in the model. In this section a more detailed model is built, and a non-singular terminal sliding mode controller is developed based on it.

7.5.1 Roll movement effect on ride comfort and health

Generally, the vertical vibration isolation is considered when designing a seat suspension for conventional road vehicles but for heavy duty vehicles, such as agricultural vehicles and construction vehicles, the severe roll vibration caused by uneven roads under the left and right tires of the vehicle will deteriorate the ride comfort greatly. Figure 7-25 shows a half-car model with chassis and seat suspension, where m_l, m_r, m_v and m_b are masses of the left tire, right tire, vehicle body and driver body, respectively; K and C are corresponding stiffness and damping. The uneven road under the left and right tires will cause vehicle's vertical vibration, and at the same time, the roll vibration of vehicle chassis θ is generated. The vertical vibration and roll vibration will all be transferred to seat suspension. For normal road conditions, the magnitude of θ is small, thus, the roll vibration of driver body α is also small. By only controlling the vertical vibration, the ride comfort will be improved greatly. When the roll vibration magnitude is high, the driver body can be regarded as a mass in the top of an inverted pendulum; thus high magnitude lateral acceleration is caused by the rotary vibration:

$$a_{y4} = \ddot{\alpha} r \tag{7-24}$$

where $\ddot{\alpha}$ is the roll acceleration of driver body; r is the distance from the centre of driver body mass to its unknown rotary centre; a_{y4} is the acceleration along y_4 axis of driver body caused by roll acceleration.

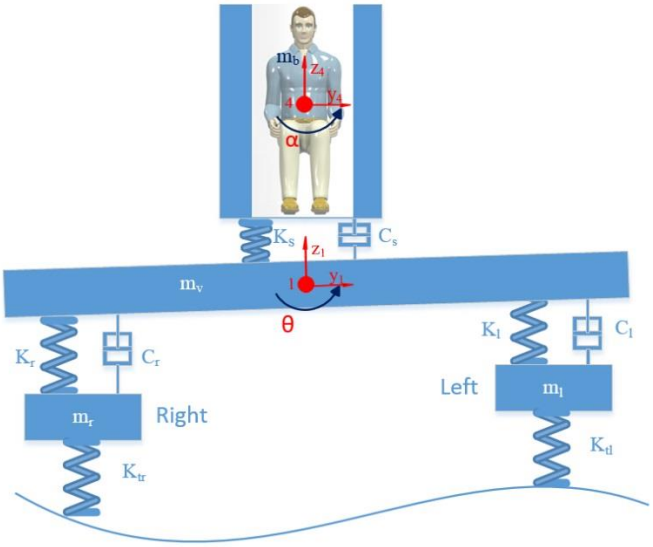

Figure 7-25. Half car model with chassis and seat suspension

The vibration total value of FW-RMS acceleration is calculated as:

$$a_v = (k_x^2 a_{wx}^2 + k_y^2 a_{wy}^2 + k_z^2 a_{wz}^2)^2 \tag{7-25}$$

where a_{wx}, a_{wy} and $a_{wz}$are FW-RMS accelerations with respect to the three orthogonal axes; k_x, k_y and k_z are multiplying factors which are defined in Table 7-6 with respect to health and ride comfort. The value of multiplying factors indicates that, with respect to the effect on ride comfort, the vibrations along three axes have same weightings; but the longitudinal vibration (a_{wx}) and lateral vibration (a_{wy}) have more influence on health than vertical vibration (a_{wz}).

Table 7-6. Multiplying factors for WBV [110]

	Health	Comfort
k_x	1.4	1
k_y	1.4	1
k_z	1	1

Due to the limited space, in this section, only the control of vibrations along z_4 and y_4 axes of the driver body is studied. The vibration along the x_4 axis of the driver's body is much

more complicated considering the existing effects of road slope, seat backrest, and feet on the floor, thus, its control problem will not be discussed in the current work.

7.5.2 System Modelling

The roll acceleration caused lateral vibration and vertical vibration will be studied, thus, a Y-Z plane model of the Multiple-DOF seat suspension is built in this thesis. As shown in Figure 7-26, five coordinate frames are built: frame 0 is the fixed reference; frame 1 is in the base of the seat suspension; frame 2 and frame 3 are in the roll joint U, and fixed at bottom and top-layer, respectively; frame 4 is in the mass centre of the driver's body and seat. Using right hand rule, the x axes of all the frames can be known. There are vibration sources to cause frame 1 to move along z_0 and rotate around x_0, namely, the vertical vibration and roll vibration. m_1 is the total mass of driver and seat; m_2 is the mass between top and bottom-layer; h_b is the distance between frame 4 and frame 2; h_s is the distance between frame 2 and the mass centre of m_2; h_0 is the initial height of frame 2 to frame 1; $h(t)$ is the dynamic displacement of frame 2 referred to frame 1. The bottom layer has stiffness k_s, friction force f_{rt} and active force u_t. In the top-layer, there are rotational stiffness k_r, friction torque f_{rr} and active torque u_r.

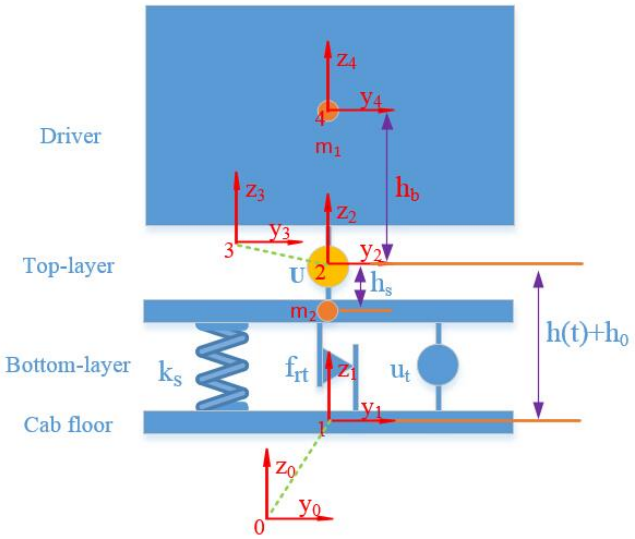

Figure 7-26. Y-Z plane model of Multiple-DOF seat suspension.

The model is further decomposed into two parts as shown in Figure 7-27 where P and N are the interaction forces aligned with the axes of frame 2.

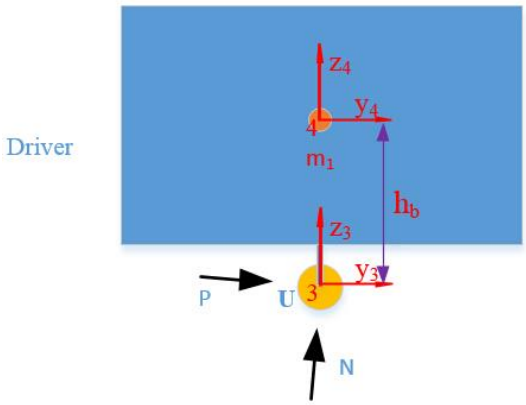

(a)

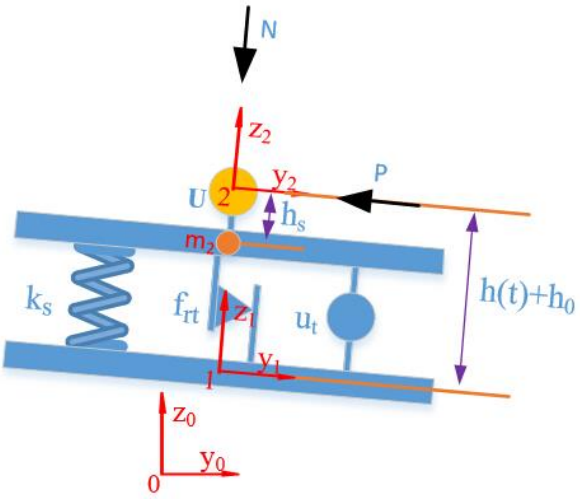

(b)

Figure 7-27. Model decomposition. (a) top-layer. (b) bottom-layer.

For deriving the seat suspension model, the 4×4 homogeneous transformation matrix T and 4×1 homogeneous coordinate are applied [16]:

$$T \triangleq \begin{bmatrix} R & p \\ \mathbf{0} & 1 \end{bmatrix} \tag{7-26}$$

$$q = \begin{bmatrix} p \\ 1 \end{bmatrix} \tag{7-27}$$

where R is the 3×3 rotation matrix; p is a 3×1translation vector.

Thus, the transformation matrices of adjacent frames are defined as:

$$T_0^1 = \begin{bmatrix} 1 & 0 & 0 & 0 \\ 0 & c\theta & -s\theta & 0 \\ 0 & s\theta & c\theta & z_s \\ 0 & 0 & 0 & 1 \end{bmatrix} \tag{7-28}$$

$$T_1^2 = \begin{bmatrix} 1 & 0 & 0 & 0 \\ 0 & 1 & 0 & 0 \\ 0 & 0 & 1 & h + h_0 \\ 0 & 0 & 0 & 1 \end{bmatrix} \tag{7-29}$$

$$T_2^3 = \begin{bmatrix} 1 & 0 & 0 & 0 \\ 0 & c\beta & -s\beta & 0 \\ 0 & s\beta & c\beta & 0 \\ 0 & 0 & 0 & 1 \end{bmatrix} \tag{7-30}$$

$$T_3^4 = \begin{bmatrix} 1 & 0 & 0 & 0 \\ 0 & 1 & 0 & 0 \\ 0 & 0 & 1 & h_b \\ 0 & 0 & 0 & 1 \end{bmatrix} \tag{7-31}$$

where θ is the roll vibration from the cab floor; z_s is the vertical vibration; β is the relative rotary angle of frames 2 and 3. Thus, the roll vibration of the driver body is $\alpha = \theta + \beta$.

Then, the transformation matrices of frames 2, 3 and 4 referred to frame 0 can be derived:

$$T_0^2 = T_0^1 T_1^2 = \begin{bmatrix} 1 & 0 & 0 & 0 \\ 0 & c\theta & -s\theta & -s\theta(h + h_0) \\ 0 & s\theta & c\theta & c\theta(h + h_0) + z_s \\ 0 & 0 & 0 & 1 \end{bmatrix} \tag{7-32}$$

$$T_0^3 = T_0^2 T_2^3 = \begin{bmatrix} 1 & 0 & 0 & 0 \\ 0 & c(\theta + \beta) & -s(\theta + \beta) & -s\theta(h + h_0) \\ 0 & s(\theta + \beta) & c(\theta + \beta) & c\theta(h + h_0) + z_s \\ 0 & 0 & 0 & 1 \end{bmatrix} \tag{7-33}$$

$$T_0^4 = T_0^3 T_3^4 = \begin{bmatrix} 1 & 0 & 0 & 0 \\ 0 & c(\theta+\beta) & -s(\theta+\beta) & -s\theta(h+h_0) - s(\theta+\beta)h_b \\ 0 & s(\theta+\beta) & c(\theta+\beta) & c\theta(h+h_0) + z_s + c(\theta+\beta)h_b \\ 0 & 0 & 0 & 1 \end{bmatrix} \quad (7\text{-}34)$$

The interaction force from upper joint on lower joint in frame 2 is defined as:

$$F_2^a = [0 \quad -P \quad -N]^{\mathrm{T}} \quad (7\text{-}35)$$

Thus, the reaction force on upper joint in frame 3 and frame 4 can be defined as:

$$F_4^{ra} = F_3^{ra} = -R_2^{3^T} F_2^a = -R_3^2 F_2^a = \begin{bmatrix} 0 \\ c\beta P + s\beta N \\ -s\beta P + c\beta N \end{bmatrix} \quad (7\text{-}36)$$

The gravity of m_1 in frame 0 is:

$$G_0^{m1} = [0 \quad 0 \quad -m_1 g]^{\mathrm{T}} \quad (7\text{-}37)$$

Thus the gravity of m_1 in frame 4 is:

$$G_4^{m1} = R_4^0 G_0^{m1} = \begin{bmatrix} 0 \\ -s\alpha m_1 g \\ -c\alpha m_1 g \end{bmatrix} \quad (7\text{-}38)$$

It is easy to obtain the coordinate of m_1 in frame 0:

$$q_0^{m1} = \begin{bmatrix} 0 \\ -s\theta(h+h_0) - s\alpha h_b \\ c\theta(h+h_0) + z_s + c\alpha h_b \\ 1 \end{bmatrix} \quad (7\text{-}39)$$

Its velocity and acceleration can be derived:

$$q_0^{\dot{m}1} = \begin{bmatrix} 0 \\ -\dot{\theta}c\theta(h+h_0) - s\theta\dot{h} - \dot{\alpha}c\alpha h_b \\ -\dot{\theta}s\theta(h+h_0) + c\theta\dot{h} + \dot{z}_s - \dot{\alpha}s\alpha h_b \\ 1 \end{bmatrix} \quad (7\text{-}40)$$

$$q_0^{\ddot{m}1} = \begin{bmatrix} 0 \\ -\ddot{\theta}c\theta(h+h_0) + \dot{\theta}^2 s\theta(h+h_0) - 2\dot{\theta}c\theta\dot{h} - s\theta\ddot{h} - \ddot{\alpha}c\alpha h_b + \dot{\alpha}^2 s\alpha h_b \\ -\ddot{\theta}s\theta(h+h_0) - \dot{\theta}^2 c\theta(h+h_0) - 2\dot{\theta}s\theta\dot{h} + c\theta\ddot{h} + \ddot{z}_s - \ddot{\alpha}s\alpha h_b - \dot{\alpha}^2 c\alpha h_b \\ 1 \end{bmatrix} \quad (7\text{-}41)$$

For formulating the dynamic equation of m_1, its acceleration vector is transferred into frame 4:

$$\ddot{p}_4^{m1} = R_4^0 \ddot{p}_0^{m1} = \begin{bmatrix} 0 \\ -s\beta\left[\dot{\theta}^2(h+h_0) - \ddot{h}\right] - c\beta\left[\ddot{\theta}(h+h_0) + 2\dot{\theta}\dot{h}\right] - \ddot{\alpha}h_b + s\alpha\ddot{z}_s \\ -c\beta[\dot{\theta}^2(h+h_0) - \ddot{h}] + s\beta[\ddot{\theta}(h+h_0) + 2\dot{\theta}\dot{h}] - \dot{\alpha}^2 h_b + c\alpha\ddot{z}_s \end{bmatrix} \quad (7\text{-}42)$$

Then, its dynamic equation is formulated:

$$m_1 \ddot{p}_4^{m1} = F_4^{ra} + G_4^{m1} \quad (7\text{-}43)$$

We can get two equations:

$$m_1\left\{-s\beta\left[\dot{\theta}^2(h+h_0) - \ddot{h}\right] - c\beta\left[\ddot{\theta}(h+h_0) + 2\dot{\theta}\dot{h}\right] - \ddot{\alpha}h_b + s\alpha\ddot{z}_s\right\} = c\beta P + s\beta N - s\alpha m_1 g \quad (7\text{-}44)$$

$$m_1\left\{-c\beta\left[\dot{\theta}^2(h+h_0) - \ddot{h}\right] + s\beta\left[\ddot{\theta}(h+h_0) + 2\dot{\theta}\dot{h}\right] - \dot{\alpha}^2 h_b + c\alpha\ddot{z}_s\right\} = -s\beta P + c\beta N - c\alpha m_1 g \quad (7\text{-}45)$$

The interaction force *N* is calculated for after derivation:

$$N = m_1[-\dot{\theta}^2(h+h_0) + \ddot{h} - \dot{\alpha}^2 h_b c\beta - \ddot{\alpha}h_b s\beta + c\theta\ddot{z}_s + c\theta g] \quad (7\text{-}46)$$

The rotational inertial of m_1 around x_4 axis is I_{m1}. Summing the moments about the centroid of the driver body, a dynamic equation is obtained:

$$I_{m1}\ddot{\alpha} = -k_r\beta - f_{rr} + u_r + (c\beta P + s\beta N)h_b \quad (7\text{-}47)$$

where the simplified friction model is applied $f_{rr} = F_{rr}sgn(\dot{\beta})$, F_{rr} is the Coulomb friction coefficient.

Combing equations (7-44) and (7-47):

$$(I_{m1} + m_1 {h_b}^2)\ddot{\alpha} = -k_r\beta - F_{rr}sgn(\dot{\beta}) + u_r - m_1\{s\beta[\dot{\theta}^2(h+h_0) - \ddot{h}] + c\beta[\ddot{\theta}(h+h_0) + 2\dot{\theta}\dot{h}] - s\alpha\ddot{z}_s - s\alpha g\}h_b \quad (7\text{-}48)$$

Because the coordinate of m_2 in frame 2 is:

$$q_2^{m2} = [0 \quad 0 \quad -h_s \quad 1]^{\mathrm{T}} \tag{7-49}$$

its coordinate in frame 0 can be defined as:

$$q_0^{m2} = T_0^2 q_2^{m2} = [0 \quad -s\theta(h + h_0 - h_s) \quad c\theta(h + h_0 - h_s) + z_s \quad 1]^{\mathrm{T}} \tag{7-50}$$

Its velocity and acceleration can be derived:

$$\dot{q_0^{m2}} = \begin{bmatrix} 0 \\ -\dot{\theta}c\theta(h + h_0 - h_s) - s\theta\dot{h} \\ -\dot{\theta}s\theta(h + h_0 - h_s) + c\theta\dot{h} + \dot{z_s} \\ 1 \end{bmatrix} \tag{7-51}$$

$$\ddot{q_0^{m2}} = \begin{bmatrix} 0 \\ \dot{\theta}^2 s\theta(h + h_0 - h_s) - \ddot{\theta}c\theta(h + h_0 - h_s) - \dot{\theta}c\theta\dot{h} - \dot{\theta}c\theta\dot{h} - s\theta\ddot{h} \\ -\dot{\theta}^2 c\theta(h + h_0 - h_s) - \ddot{\theta}s\theta(h + h_0 - h_s) - \dot{\theta}s\theta\dot{h} - \dot{\theta}s\theta\dot{h} + c\theta\ddot{h} + \ddot{z_s} \\ 1 \end{bmatrix} \tag{7-52}$$

For formulating the dynamic equation of m_2, its acceleration vector is transferred into frame 2:

$$\ddot{p_2^{m2}} = R_2^0 \ddot{p_0^{m2}} = \begin{bmatrix} 0 \\ -\ddot{\theta}(h + h_0 - h_s) - 2\dot{\theta}\dot{h} + s\theta\ddot{z_s} \\ -\dot{\theta}^2(h + h_0 - h_s) + \ddot{h} + c\theta\ddot{z_s} \end{bmatrix} \tag{7-53}$$

In the initial condition, the spring in the bottom-layer is compressed to support the gravity of m_1 and m_2. Thus, the preload force of spring is:

$$f_p = (m_1 + m_2)g \tag{7-54}$$

The gravity of m_2 in frame 0 is:

$$G_0^{m2} = [0 \quad 0 \quad -m_2 g]^{\mathrm{T}} \tag{7-55}$$

The gravity of m_2 in frame 2 is:

$$G_2^{m2} = R_2^0 G_0^{m2} = \begin{bmatrix} 0 \\ -s\theta m_2 g \\ -c\theta m_2 g \end{bmatrix} \tag{7-56}$$

Because the active actuator of the bottom layer can only control the suspension's dynamic along the z_2 axis, the dynamic equation of m_2 along the z_2 axis is built:

$$m_2 \ddot{p}_{2\,(z2)}^{m2} = -k_s h - F_{rt} sgn(\dot{h}) + u_t + f_p + G_{2\,(z2)}^{m2} - N \quad (7\text{-}57)$$

It can be rearranged as:

$$(m_2 + m_1)\ddot{h} = -k_s h - F_{rt} sgn(\dot{h}) + u_t - m_1\left[-\dot{\theta}^2(h + h_0) - \dot{\alpha}^2 h_b c\beta - \ddot{\alpha} h_b s\beta + c\theta \ddot{z}_s + c\theta g - g\right] - m_2[-\dot{\theta}^2(h + h_0 - h_s) + c\theta \ddot{z}_s - g + c\theta g] \quad (7\text{-}58)$$

The dynamic of the multiple-DOF seat suspension is determined by equations (7-48) and (7-58).

7.5.3 Controller design

The roll movement and vertical vibration are controlled independently in this research. This control strategy requires the controllers to be robust enough to overcome disturbance from the system coupling.

In terms of the practical implementation, the feedback variables of the controller should be measurable in application. The acceleration of m_2 and the dynamic displacement h, which can be easily obtained, are applied to control the bottom-layer. The roll angles of the Multiple-DOF seat suspension base and top are used for controlling the top-layer. The roll angle cannot be measured directly, but it can be accurately estimated by MEMS (microelectromechanical systems) IMU (inertial measurement unit) sensors. The IMU sensor consists of an accelerometer to measure three axes accelerations and a gyroscope to measure three axes rotational rates.

7.5.3.1 Roll vibration controller

Because the roll angle of the top seat suspension can be estimated, if we know a desired roll angle which can decrease the lateral acceleration, the tracking control can be applied and

there are many methods to do this. The decision as to the desired roll angle can follow two rules, least lateral displacement and least roll angle, as shown in Figure 7-28. The first rule causes the centre of driver mass to have the least lateral displacement, thus, the desired angle is defined as:

$$\alpha_1 = -\text{asin}(\frac{h+h_0}{h_b}\sin(\theta)) \tag{7-59}$$

The second rule reduces the roll movement of the driver's body, thus the desired angle is $\alpha_2 = 0$.

Combining these two rules, the desired roll angle of the driver body is designed as:

$$\alpha_d = \varepsilon\alpha_1 \tag{7-60}$$

where $\varepsilon \in [0 \quad 1]$ is a weighting parameter.

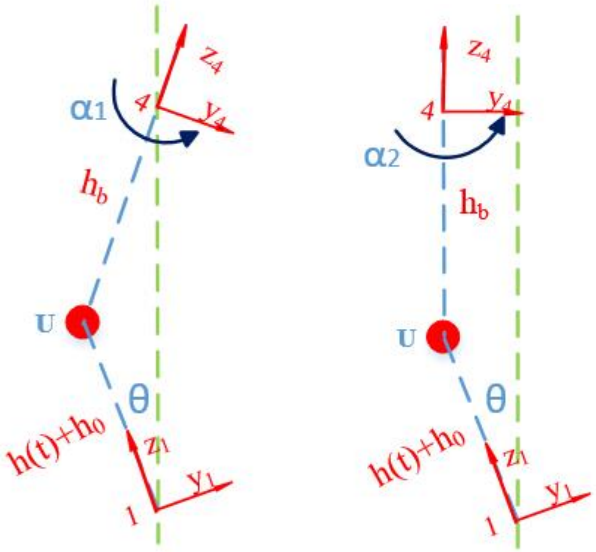

(a) (b)

Figure 7-28. Desired roll angle of driver body. (a) Least lateral displacement. (b) Least roll angle.

The dynamics of the roll movement are shown in equation (7-48) which is nonlinear and is coupling with the vertical vibration. The nonsingular terminal sliding mode controller is selected to track the desired roll movement. The roll movement dynamic is rearranged as:

$$\left(I_{m1} + m_1 {h_b}^2\right)\ddot{\alpha} = -k_r(\alpha - \theta) + u_r + \omega_1 \tag{7-61}$$

$$\omega_1 = -F_{rr} sgn\left(\dot{\alpha} - \dot{\theta}\right) - m_1\left\{s\beta\left[\dot{\theta}^2(h + h_0) - \ddot{h}\right] + c\beta\left[\ddot{\theta}(h + h_0) + 2\dot{\theta}\dot{h}\right] - s\alpha\ddot{z}_s - s\alpha g\right\}h_b \tag{7-62}$$

where ω_1 is assumed to have a bound as ξ_1.

The tracking error and its derivative value is:

$$e = \alpha_d - \alpha,\ \dot{e} = \dot{\alpha_d} - \dot{\alpha} \tag{7-63}$$

The nonsingular sliding variable is selected as:

$$s = e + \frac{1}{\beta}\dot{e}^{p/q} \tag{7-64}$$

where $\beta > 0,\ p, q\ (p > q)$ are positive odd integers, $1 < \frac{p}{q} < 2$.

Generally, the nonlinear terminal sliding mode controller is designed as:

$$u_r = k_r(\alpha - \theta) + \eta \mathrm{sgn}(s) + (I_{m1} + m_1 {h_b}^2)(\ \ddot{\alpha_d} + \beta\frac{q}{p}\dot{e}^{2-p/q}) \tag{7-65}$$

where $\eta > \xi_1 > 0$.

With this controller, theoretically, the sliding mode variable will converge to zero quickly without singular problem [57]. In practical implementation, it will have difficulties. The sliding variable s and the desired roll acceleration $\ddot{\alpha_d}$ are all derived from the roll vibration source θ which is estimated from the IMU sensor. The estimation error and measurement noise already exist in the value of θ. It is well known that the derivative of a measurement value will amplify its error and noise; double derivative will severely deteriorate its accuracy.

Thus, high magnitude of noise may exist in $\ddot{\alpha}_d$. In addition, $\ddot{\alpha}_1$ is bounded and $\ddot{\alpha}_2 = 0$, so $\ddot{\alpha}_d(I_{m1} + m_1{h_b}^2)$ should have a bound ξ_2. The roll movement controller is designed as:

$$u_r = k_r(\alpha - \theta) + \eta \text{sgn}(s) + (I_{m1} + m_1{h_b}^2)\beta \frac{q}{p}\dot{e}^{2-p/q} \tag{7-66}$$

where $\eta > \xi_1 + \xi_2 > 0$.

For further decreasing the chattering of the controller, the sign function is implemented as a hyperbolic function:

$$\text{sgn}(s) \approx \tanh(\varepsilon s) \tag{7-67}$$

where $\varepsilon > 0$ is applied to avoid the dramatically change when s is around 0.

Analysis of stability shows

$$\begin{aligned}
\dot{s} &= \dot{e} + \frac{1}{\beta}\frac{p}{q}\dot{e}^{p/q-1}(\ddot{\alpha}_d - \ddot{\alpha}) \\
&= \dot{e} + \frac{1}{\beta}\frac{p}{q}\dot{e}^{p/q-1}\left(\ddot{\alpha}_d - \frac{1}{I_{m1}+m_1{h_b}^2}(-k_r(\alpha-\theta) + u_r + \omega_1)\right) \\
&= \frac{1}{\beta}\frac{p}{q}\dot{e}^{p/q-1}\left(\ddot{\alpha}_d - \frac{1}{I_{m1}+m_1{h_b}^2}(\eta sgn(s) + \omega_1)\right) \\
&= \Psi\left(-\eta sgn(s) - \omega_1 + \ddot{\alpha}_d(I_{m1} + m_1{h_b}^2)\right)
\end{aligned} \tag{7-68}$$

where $\Psi = \frac{1}{I_{m1}+m_1{h_b}^2}\frac{1}{\beta}\frac{p}{q}\dot{e}^{p/q-1}$.

Because $1 < \frac{p}{q} < 2$, $0 < \frac{p}{q} - 1 < 1$. When $\dot{e} \neq 0$,

$$\dot{e}^{p/q-1} > 0 \tag{7-69}$$

$$\dot{s}s = \Psi\left(-\eta|s| - \omega_1 s + \ddot{\alpha}_d(I_{m1} + m_1{h_b}^2)s\right) < \Psi(-\eta|s| + (\xi_1 + \xi_2)s) < 0 \tag{7-70}$$

thus, the Lyapunov condition is satisfied.

When $\dot{e} = 0$, from equations (7-61) and (7-66), we get:

$$\left(I_{m1} + m_1 {h_b}^2\right)\ddot{\alpha} = \eta \mathrm{sgn}(\alpha_d - \alpha) + \omega_1 \tag{7-71}$$

When $\alpha_d > \alpha$, $\ddot{\alpha} > 0$; when $\alpha_d < \alpha$, $\ddot{\alpha} < 0$; when $\alpha_d = \alpha$, $s = 0$ can be obtained in a finite time.

7.5.3.2 Vertical vibration controller

The controller developed in Chapter 4 is proven to be robust with friction disturbance. This controller applies the acceleration and the relative displacement of the vertical seat suspension as feedback signals. In practice, the roll angle of the cab floor is limited in a small range in order to keep the stability of the vehicle, thus the relative rotary angle of the roll joint is also bounded within a certain range. We assume that $c\beta = c\theta = 1$, $s\beta = 0$, model (7-58) can be simplified as:

$$(m_2 + m_1)(\ddot{h} + \ddot{z}_s) = -k_s h - F_{rt} sgn(\dot{h}) + u_t - m_1\left[-\dot{\theta}^2(h + h_0) - \dot{\alpha}^2 h_b\right] - m_2[-\dot{\theta}^2(h + h_0 - h_s)] \tag{7-72}$$

This model is similar to a single-DOF vertical active seat suspension except the centripetal forces. Those centripetal forces can be taken as disturbances with friction together. Then the model is further simplified as:

$$M a_z = -k_s h + u_t + \omega_2 \tag{7-73}$$

$$\omega_2 = -F_{rt} sgn(\dot{h}) - m_1\left[-\dot{\theta}^2(h + h_0) - \dot{\alpha}^2 h_b\right] - m_2[-\dot{\theta}^2(h + h_0 - h_s)] \tag{7-74}$$

where $M = m_2 + m_1$, $a_z = \ddot{h} + \ddot{z}_s$. Assume that a_z is the vertically measured acceleration of the plate between top and bottom-layer.

Now, we can control it with the same method as for a single-DOF vertical active seat suspension as shown in Figure 7-29. The state variables are chosen as $x_1 = h, x_2 = \dot{h}$. The measurement variables are $y_1 = a_z$, $y_2 = x_1$, $y_3 = x_2$. The control variable is $z = \varphi a_z$; φ is a weighting parameter.

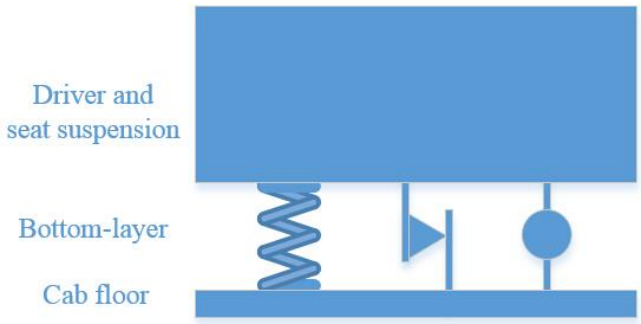

Figure 7-29. Simplified vertical vibration mode

The disturbance observer can be designed as:

$$\dot{\widehat{\omega_2}} = L(y_1 - \frac{1}{M}(-k_s h + u_t + \widehat{\omega_2})) \tag{7-75}$$

where $L > 0$ is observer gain, $\widehat{\omega_2}$ is the observed disturbance.

Then the observed disturbance is compensated into a H_∞ controller:

$$u_t = KX - \widehat{\omega_2} \tag{7-76}$$

where $X = [x_1\ x_2]^T$, $K = [k_1\ k_2]$ is a controller gain vector.

7.5.4 Performance evaluation

7.5.4.1 Simulation

For comparison, a conventional single-DOF passive seat suspension with same dimension is applied in the simulation. Unlike the active seat suspension, the passive seat suspension has a damper c_s instead of friction to dissipate vibration energy. Based on the kinematic model, the acceleration of the driver body in its own frame is:

$$\ddot{p_4^{m1}} = \begin{bmatrix} 0 \\ -[\ddot{\theta}(h + h_0 + h_b) + 2\dot{\theta}\dot{h}] + s\theta\ddot{z_s} \\ -[\dot{\theta}^2(h + h_0 + h_b) - \ddot{h}] + c\theta\ddot{z_s} \end{bmatrix} \tag{7-77}$$

Because the passive seat suspension does not have a DOF in roll direction, the roll acceleration of the vehicle body will totally be transferred to driver body. Thus, $\ddot{\alpha} = \ddot{\theta}$.

The dynamic of the seat suspension can be defined as:

$$(m_2 + m_1)\ddot{h} = -k_s h - c_s \dot{h} + u_t - m_1\left[-\dot{\theta}^2(h + h_0 + h_b) + c\theta \ddot{z}_s + c\theta g - g\right] - m_2[-\dot{\theta}^2(h + h_0 - h_s) + c\theta \ddot{z}_s - g + c\theta g] \quad (7\text{-}78)$$

The parameters of the Multiple-DOF active seat suspension and the single-DOF passive seat suspension are listed in Table 7-7. The designed controller parameters are listed in

Table 7-8.

Table 7-7. Model parameters

$\boldsymbol{m_1}$	80 Kg	$\boldsymbol{h_b}$	0.3 m
m_2	8 Kg	F_{rr}	8 Nm
k_s	5000 N/m	F_{rt}	80 N
h_0	0.2 m	k_r	700 Nm/rad
h_s	0.05 m	I_{m1}	2 kg*m^2
c_s	2000 Ns/m		

Table 7-8. Controller parameters

$\boldsymbol{\varepsilon}$	0.5	$\boldsymbol{k_1}$	4500
p	5	k_2	-200
q	3	L	3500
β	10	η	20

In the simulation, a random vertical vibration and a random roll vibration are exerted on the Multiple-DOF active seat suspension models (7-48) and (7-58) and the single-DOF passive seat suspension model (7-78), simultaneously.

The roll acceleration (Figure 7-30), roll velocity (Figure 7-31), vertical acceleration (Figure 7-32) and lateral acceleration (Figure 7-33) of the driver's body with Multiple-DOF active seat suspension and single-DOF passive seat suspension are presented. Their RMS values are

shown in Table 7-9 which indicates that the vertical and lateral accelerations can be controlled simultaneously with the proposed Multiple-DOF seat suspension and control method.

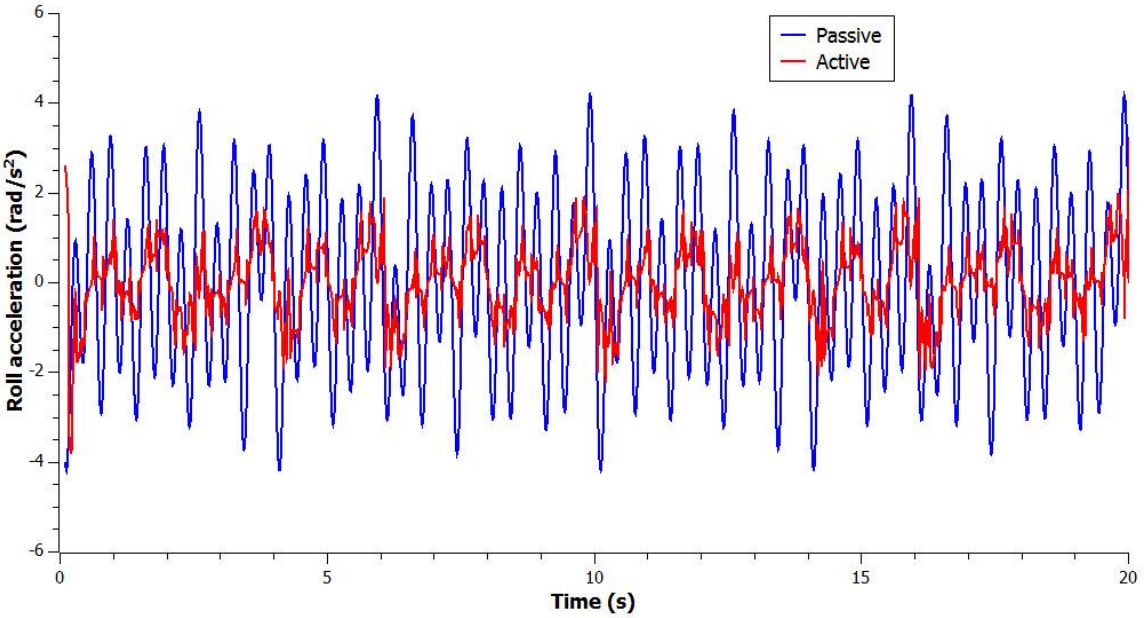

Figure 7-30. Roll acceleration

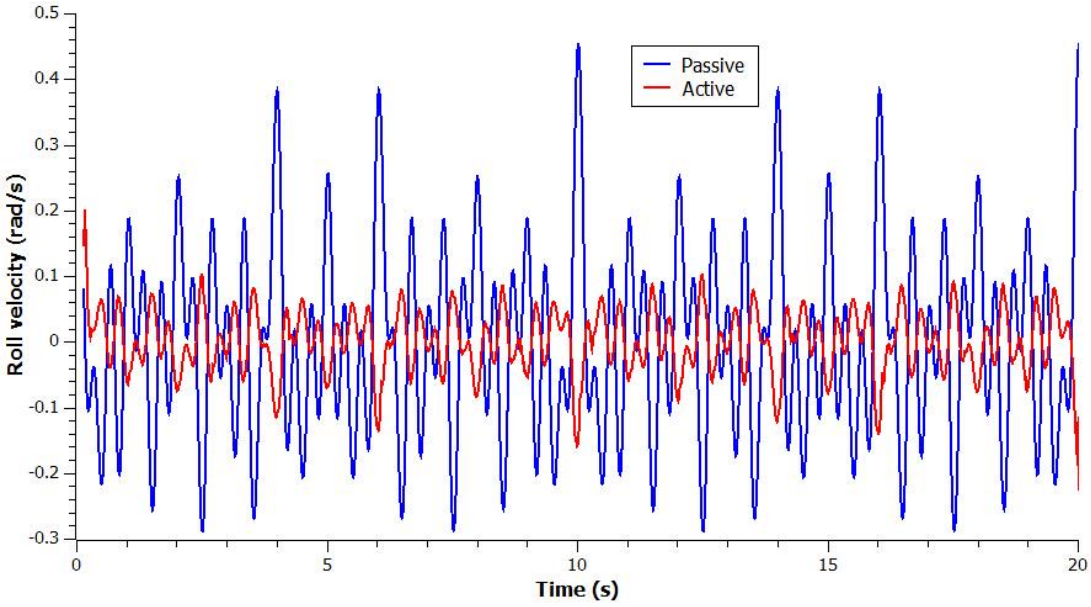

Figure 7-31. Roll velocity

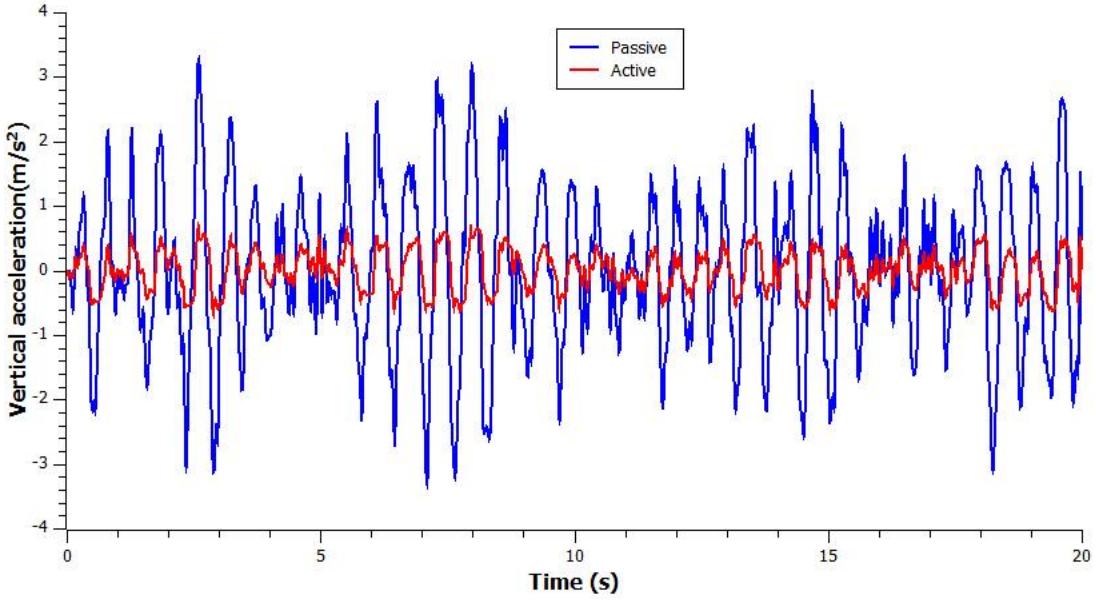

Figure 7-32. Vertical acceleration

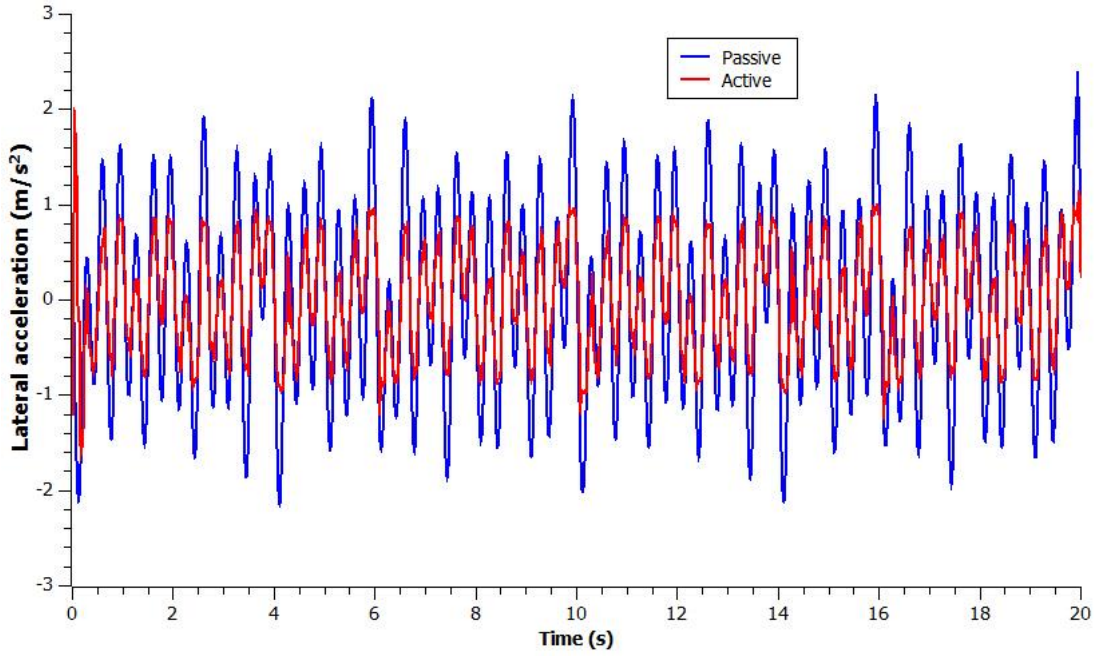

Figure 7-33. Lateral acceleration

Table 7-9. Simulation result

RMS value	Passive	Active	Reduction (%)
Roll acceleration $\ddot{\alpha}$	1.972 rad/s^2	0.8197 rad/s^2	58.4
Roll velocity $\dot{\alpha}$	0.1429 rad/s	0.0468 rad/s	67.2
Vertical acceleration	1.26 m/s^2	0.3137 m/s^2	75.1
Lateral acceleration	0.99 m/s^2	0.563 m/s^2	43.1

7.5.4.2 Experiments

The proposed controller is implemented on the multiple-DOF active seat suspension prototype in the lab. The experimental setup is shown in Figure 7-34 where the multiple-DOF active seat suspension and a conventional passive seat suspension are fixed on a 6-DOF vibration platform and the same load is applied in the comparison experiments. The schematic diagram of the whole system is shown in Figure 7-35. The Multiple-DOF active seat suspension is controlled by an NI CompactRio 9074 with three modules, namely TB 3501, NI 9205 and NI 9264; and a computer is applied to set the controller parameters and record experimental data. With a Serial Peripheral Interface (SPI) bus, the TB 3501 module can read the data of MPU 9250. The analog input module NI 9205 can get the feedback from an acceleration sensor ADXL 203EB and a displacement sensor optoNCDT 1302. Based on the feedback, the desired active force and torque are calculated and the corresponding commands are sent to their motor drives. The 6 DOFs vibration of the seat surface is measured by a XSENS sensor which is one of the best performing MEMS based sensor on the market. Figure 7-36 shows the location of sensors where the optoNCDT 1302 is used to measure the relative displacement of the bottom layer; the ADXL 203EB is placed under the plate between top and bottom layers; two MPU 9250s are set on the top and base of the Multiple-DOF seat suspension, respectively.

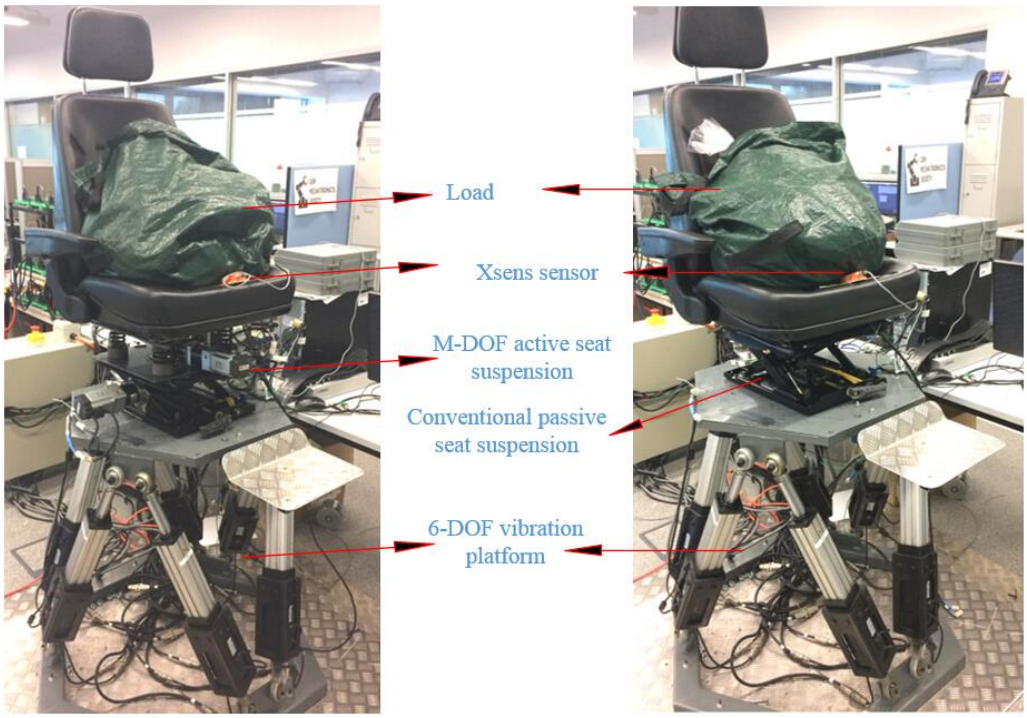

Figure 7-34. Experimental setup

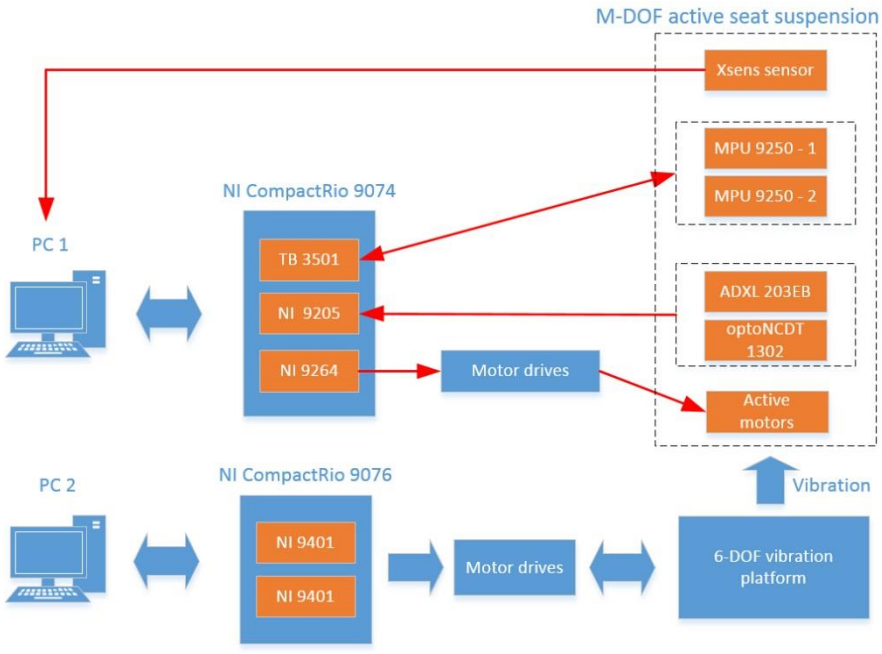

Figure 7-35. Schematic diagram of experimental setup

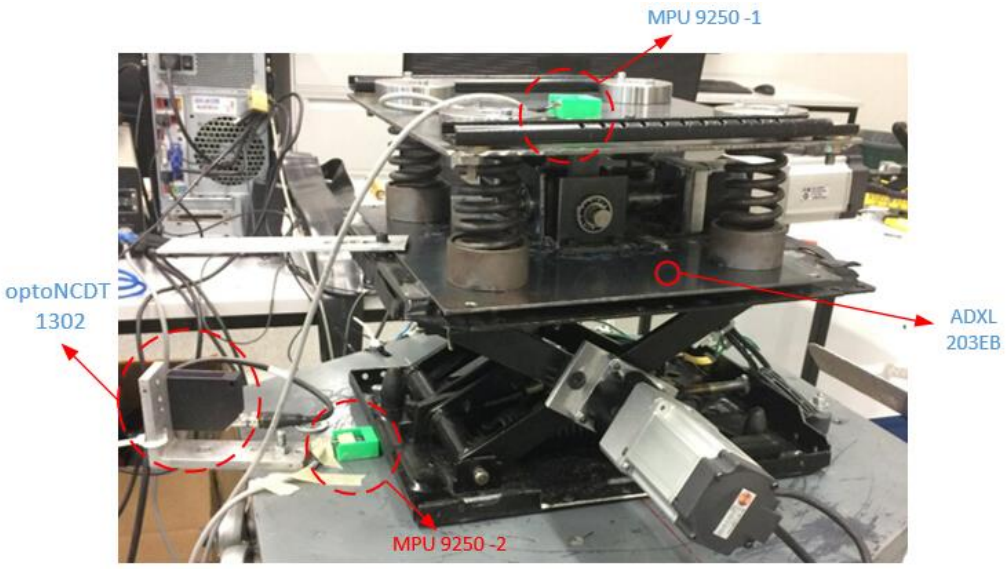

Figure 7-36. Location of sensors

MPU 9250 is a low cost IMU which contains a 3-axis gyroscope, a 3-axis accelerometer and a 3-axis digital compass. In this research, the accelerometer and gyroscope data are applied to estimate the roll angle. First, the calibration techniques in [50] have been implemented to deal with the sensor errors like bias, scale factor and nonorthogonality. Then, with the calibrated data, the rotary angles of the seat suspension's base and top platform are estimated based on an orientation filter [124].

In the experiment, the random vertical vibration and random roll vibration are generated by the 6-DOF vibration platform, simultaneously. The XSENS sensor can obtain the vibration information of both seat surfaces which include the 3-axis rotary velocities, 3-axis acclerations and estimated 3-axis rotary angles; all the measured data are referred to the fixed reference coordinate. Figure 7-37 shows the tested roll velocity of the multiple-DOF acitve and single-DOF passive seat surfaces; the RMS value of the passive seat is 0.289 rad/s, and the active one is 0.126 rad/s; there is a 56.4% reduction. The roll velocity can indicate the roll vibration magnitude of the seat surface. In Figures 7-38 and 7-39, the vertical and lateral accelerations are presented. For evaluating the improvement of the multiple-DOF seat

suspension in health and ride comfort, the FW-RMS and VDV are calculated based on ISO 2631. Table 7-10 shows the comparision of the vibrations in both seat surfaces. The reduction of the FW-RMS vertical acceleration is 32.1% which is very close to the result of our previous study for signle-DOF vertical vibration isolation. This indicates the applied H_∞ controller with disturbance compensation is also effective under multiple-DOF vibration conditions. The FW-RMS lateral acceleration has a 49.4% reduction which implies great improvement in ride comfort. By assuming that there is no longitudinal acceleration (a_{wx}), in Table 7-11, the vibration total value of FW-RMS acceleration is calculated with the suggested weighting multiplying factors for health and comfort. The results indicate that with the multiple-DOF active seat suspension there is a 42.3% improvement in driver health, and a 40.9% improvement in ride comfort.

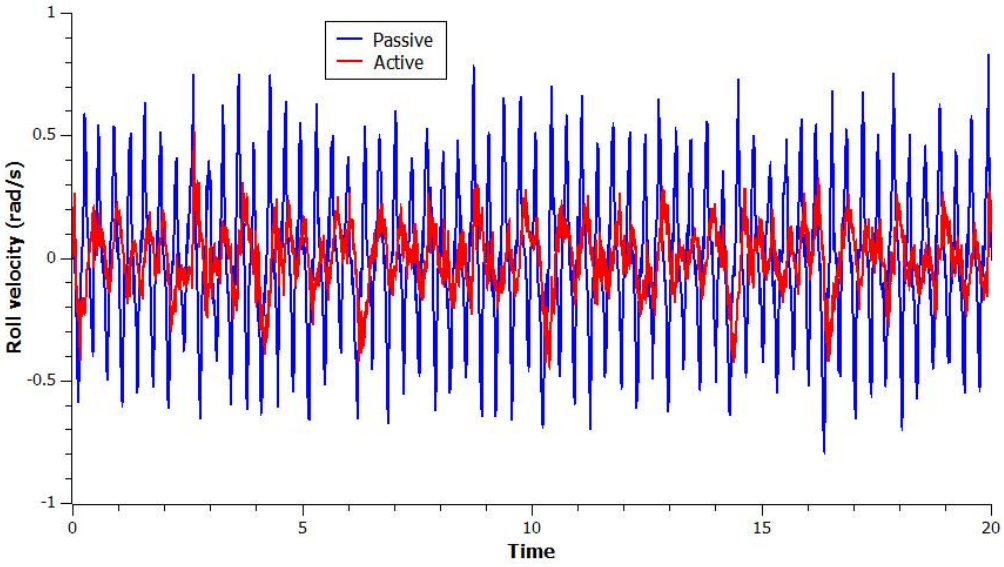

Figure 7-37. Roll velocity of seat surface

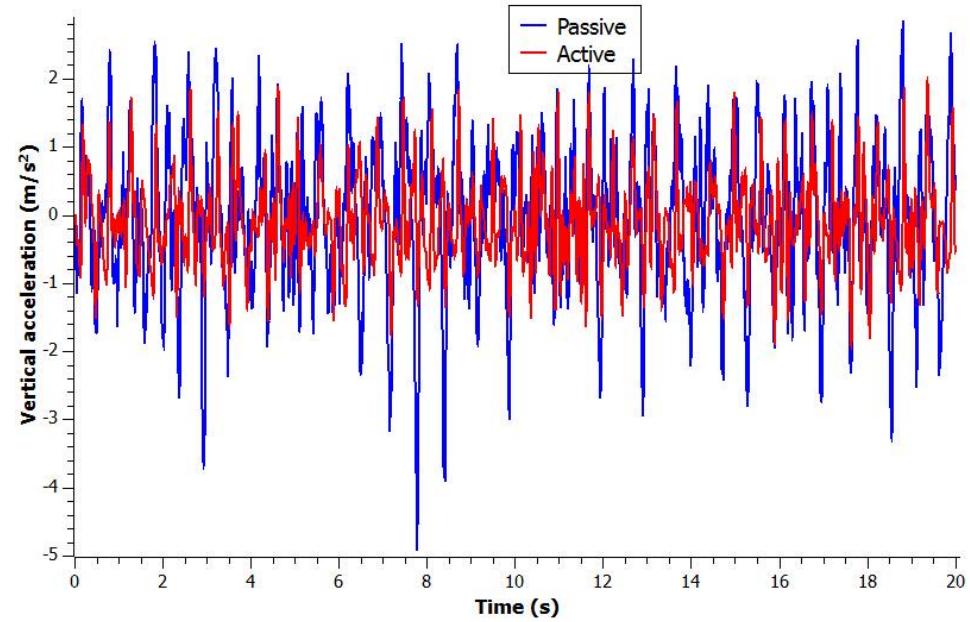

Figure 7-38. Vertical acceleration of seat surface

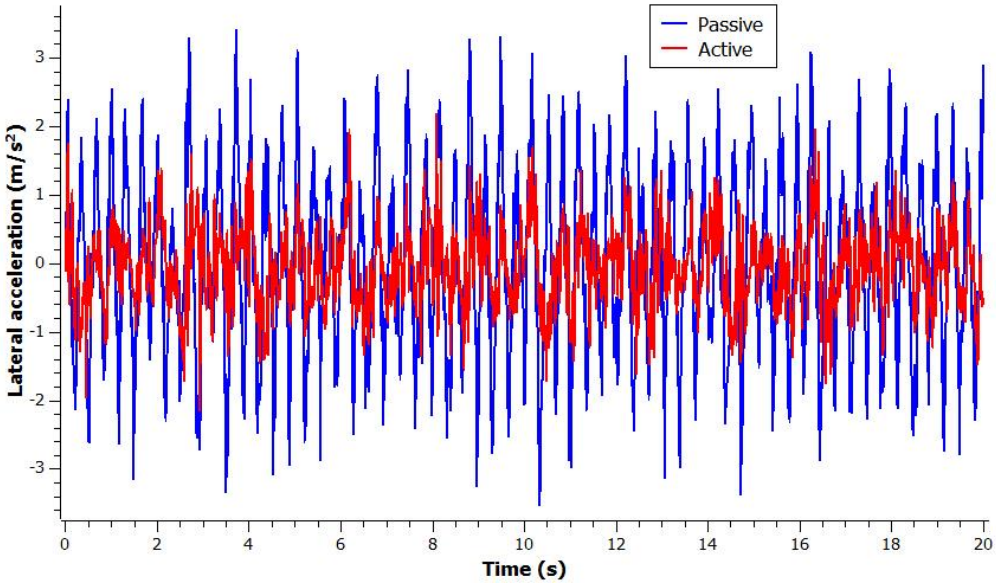

Figure 7-39. Lateral acceleration of seat surface

Table 7-10. Seat surface vibration comparison

		Passive	Active	Reduction (%)
Vertical acceleration	RMS (m/s^2)	1.113	0.647	41.9
	FW-RMS (m/s^2)	0.895	0.608	32.1
	VDV ($m/s^{1.75}$)	2.601	1.748	32.8
Lateral acceleration	RMS (m/s^2)	1.298	0.579	55.4
	FW-RMS (m/s^2)	0.928	0.47	49.4
	VDV ($m/s^{1.75}$)	2.392	1.144	52.2

Table 7-11. Vibration total value of FW-RMS acceleration

	Passive (m/s^2)	Active (m/s^2)	Reduction (%)
Health	2.131	1.037	51.3
Comfort	1.710	0.868	49.2

7.6 Conclusions

In this chapter, an innovative two-layer multiple-DOF seat suspension for heavy duty vehicles has been designed and manufactured. Because the yaw vibration has the least effect on the ride comfort, the proposed seat suspension is designed to reduce the other five DOFs of WBV in order to decrease system complexity. An active two DOFs rotary joint is applied in the top-layer suspension for controlling the lateral trunk bending and forward flexion of the driver body; the translational vibration along x3 and y3 axes of the body frame and body's roll and pitch vibrations can be all reduced, though the four DOFs vibration cannot be fully controlled by a two DOFs joint,. The bottom-layer suspension is applied to control the acceleration along z3 axis of the body frame. Thus, the proposed seat suspension is capable to reduce WBV in five DOFs. Another advantage of the two-layer seat suspension is that the

sensitive frequency content of human to the four DOFs vibration controlled by the top-layer is around 1 Hz, while the sensitive frequency content of human body to vibration controlled by the bottom-layer is between 5-8 Hz; this kind of decoupling will benefit the controller design. The seat suspension structure is concise and it just increases a little volume compared with the single-DOF seat suspension. The top-layer suspension parameters have been identified based on testing results. A H_∞ controller has been designed for the top layer control based on a simplified and decoupled model. Further, a nonsingular terminal sliding mode controller has been designed based on a coupled mode with top and bottom layers suspension. The low cost MEMS sensor mpu9205 has been applied in the implementation of the two controllers. The proposed seat suspension and controllers have been validated with simulation and experiments. With the H_∞ controller, when the multiple-DOF vibration is exerted, the seat suspension with only bottom-layer controlled can reduce the vertical vibration, but the WBV cannot be controlled effectively; when the fully controlled two-layer seat suspension is applied, the WBV can be reduced by 38.5% and 33.8% with the two sets of vibration applied in this thesis, respectively. The performance of the nonsingular terminal sliding mode controller has been compared with a well-tuned single-DOF passive seat suspension; the roll vibration and lateral vibration of the seat surface can be greatly reduced by controlling the roll movement of the top layer. Based on ISO 2631, FW-RMS accelerations of seat surface have 32.1% and 49.4% reduction in vertical and lateral direction, respectively. The vibration total value of FW-RMS acceleration of seat surface has 51.3% and 49.2% reduction for evaluating its influence on health and ride comfort, respectively. The nonlinear terminal sliding model controller has a better performance than the H_∞ one, which is partly caused by that the estimated rotary angle is applied for the feedback. This multiple-DOF seat suspension will improve the driver's work condition and is practical in application.

8 CONCLUSIONS AND FUTURE WORK

8.1 Introduction

This chapter will present the conclusions of the whole thesis; at the same time, the recommendations for the future work are discussed.

8.2 Single-DOF seat suspension design and control

The single-DOF seat suspension for reducing the vertical vibration has been widely studied; in this thesis, three kinds of single-DOF seat suspensions have been proposed and manufactured, and the corresponding controllers have been designed and validated.

The proposed single-DOF active seat suspension applied a rotary actuator as actuator, and the scissors structure of a conventional passive seat suspension has been applied to transmits the rotary motion to the vertical motion, thus, no additional transmission mechanism is required; this kind of concise structure is easy to manufacture, and generally, the rotary actuator has a lower price and is easier to be maintained than the linear actuators. In this seat suspension, the friction has a significant effect on the dynamics; three controllers have been designed by considering estimation and compensation of the friction force. The three designed controllers

all applied the measurable variable in the practical application as feedback. Comprehensive experiments have been implemented to validate the designed seat suspension and controllers.

For fulfilling the performance gap of the active seat suspension and the semi-active MR seat suspension, an hybrid seat suspension has been designed and its prototype has been manufactured. The seat suspension has a structure the same with the above active seat suspension; a rotary MR damper and an active rotary actuator with small maximum torque output have been mounted on two sides of the scissors structure of a conventional passive seat suspension. The field, amplitude, and frequency-dependent performance of the seat suspension have been tested with MTS system. The tests results show that the semi-active actuator of the hybrid seat suspension is controllable. In this seat prototype, an active actuator with a low maximum force output (70 N), which is insufficient for an active seat suspension to control the resonance vibration, is applied together with a semi-active MR damper. The MR damper can suppress the high vibration energy in resonance frequency, and then a small active force can further reduce the vibration magnitude. The simulation and experiments have validated the effectiveness of the seat suspension; the performance of a MR seat suspension can be greatly improved with less power consumed than an active seat suspension.

An energy regenerative EMD seat suspension has been designed, manufactured and evaluated; the generated damping force (BEM force) can be controlled, thus the semi-active vibration control for the seat suspension can be achieved. Two implementation methods have been proposed to vary the damping of the EMD in real time. The basic concept of system is to control the current of the circuit by changing the total resistance; then the BEM force can be controlled. The proposed seat suspension is an energy saving one when compared with other variable damping seat suspension, such as MR or ER damper seat suspension, and it has regeneration capability. In the first method, a rotary rheostat has been applied to vary the circuit external resistance. The external resistance-dependent, frequency-dependent and

amplitude-dependent tests have been implemented, respectively; the integrated mathematical model including the seat suspension and the generator can match the result very well. In the second method, a MOSFET switch module and an external resistor have been applied. A test system has been designed to analyze the variable damping characteristic of the EMD. The test result indicates that the damping of the EMD can be controlled by exerting PWM signal with different value of duty cycle on the MOSFET switch. The performance of the semi-active seat suspension with the two kinds of implementation methods has been verified with experiments; the experimental results show that the semi-active EMD seat suspension can greatly improve the ride comfort and consumes low energy which can be ignored when considering its energy regenerative capability.

8.3 Multiple-DOF seat suspension

In this thesis, a two-layer multiple-DOF seat suspension has been designed, manufactured and tested. The operators of heavy duty vehicles are exposed in severe WBV which includes vibration in 6 DOFs due to its special working requirements. However, most of the existing seat suspensions are designed in order to control the vertical vibration. The proposed seat suspension is composed of a bottom-layer suspension for vertical vibration control and a top-layer suspension with two independently controlled rotational DOFs. The proposed seat suspension can reduce the vibration of driver body in five DOFs except the yaw vibration, which has least effect on human, with only three actuators; though the five DOFs cannot be fully reduced by the three actuators, all of their magnitudes can be reduced. Another advantage of a two-layer structure is that, the vertical vibration reduction can be decoupled from reducing the lateral trunk bending and forward flexion of the driver body, according to the fact that the most sensitive frequency contents of the vertical vibration to human are much higher than the frequency content of other four DOFs vibrations.

For developing the controllers for the top-layer suspension, its rotational stiffness and frictions of the two rotary DOFs are identified with test firstly. A H_∞ controller has been designed for the top layer control based on a simplified and decoupled model; the controller applied the relative rotary angle of the top-layer suspension which is measured by an encoder on the rotary motor and the absolute rotary velocity of the seat which can be obtained from an IMU sensor as the feedback. Further, a nonsingular terminal sliding mode controller has been designed based on a coupled mode with top and bottom layers suspension; the estimated rotary angles of the seat from the IMU sensor have been applied in the controller. The experiments have validated the effectiveness of the seat suspension and controller.

8.4 Experiment setups for seat suspension study

The experiment setups, including the vibration platform and the test system for parameters identification, are significant in the study of seat suspension. .

A 6-DOF vibration platform has been built for the seat suspension development. This platform consists of 6 electrical cylinders with their servo drives, an upper platform for assembling seat suspension and the base fixed on the ground. According to the desired 6 DOFs motion of the upper platform, the corresponding motion of each cylinder can be calculated by the inverse kinematic model. The test results have illustrated that the 6-DOF vibration platform can accurately generate desired multiple-DOF vibration for seat suspension analysis.

In the thesis, the MTS system, which can exert desired vertical movement on the tested item and record the displacement and the responding force, has been applied to identify the parameters of the single-DOF seat suspensions; a similar system for testing the rotary movement has also been built. A rotary actuator is controlled by its drive in order to accurately rotate as the desired profile; the rotary angle and torque can be recorded. With the

rotary testing system, the tests for the rotary EMD system has been comprehensively implemented in order to verify its capability of varying damping; the stiffness and friction parameters of the top-layer of the multiple-DOF seat suspension has been identified.

8.5 Recommendation for the Future work

8.5.1 Improving the active vibration control performance in high frequency

Within the experiments of active vibration control, the low frequency vibration is mainly concerned, and the high frequency content of vibration is always introduced by the measurement noise and the high dynamics of the controller. Though the high frequency vibration will not affect ride comfort much, which has been proven in the thesis, for further improving the performance of an active seat suspension, the controller which can suppress high frequency and low frequency vibration can be developed in the future.

8.5.2 Improving the controllable EMD system

The effectiveness of the EMD system controlled by a MOSFET switch has been validated in this thesis, however, there are more works need to be done in order to improve its performance in practical application. The integrated model including the electrical circuit and the dynamics and kinematics of the seat suspension should be built for controller design; the semi-active controller should only apply the measurable variables as feedback; the comprehensive system including the energy harvesting circuit can be developed in the future.

8.5.3 Nonlinear multiple-DOF seat suspension

In the thesis, a two-layer structure is proposed for seat suspension, where the top layer can be regarded as a nonlinear inverted pendulum system. For improving the top layer convergence, the nonlinear stiffness structure can be designed; a small stiffness is required around the equilibrium position for a good high frequency vibration isolation performance; a big stiffness is wanted when the driver body is far away from the equilibrium point, which

always happened when the system is in resonance, then a low active force is required to control the vibration.

9 REFERENCES

1. Paddan, G. and M. Griffin, *Evaluation of whole-body vibration in vehicles.* Journal of sound and vibration, 2002. **253**(1): p. 195-213.
2. Mabbott, N., G. Foster, and B. McPhee, *Heavy vehicle seat vibration and driver fatigue*. Report No: CR 203. 2001.
3. Mandapuram, S., et al., *Energy absorption of seated body exposed to single and three-axis whole body vibration.* Journal of Low Frequency Noise, Vibration and Active Control, 2015. **34**(1): p. 21-38.
4. Yao, G., et al., *MR damper and its application for semi-active control of vehicle suspension system.* Mechatronics, 2002. **12**(7): p. 963-973.
5. Li, W., et al., *Testing and steady state modeling of a linear MR damper under sinusoidal loading.* Smart Materials and Structures, 2000. **9**(1): p. 95.
6. Kwok, N., et al., *Bouc–Wen model parameter identification for a MR fluid damper using computationally efficient GA.* ISA transactions, 2007. **46**(2): p. 167-179.
7. Tang, X., et al., *Takagi–Sugeno Fuzzy Control for Semi-Active Vehicle Suspension With a Magnetorheological Damper and Experimental Validation.* IEEE/ASME Transactions on Mechatronics, 2017. **22**(1): p. 291-300.
8. Frechin, M., S. Arino, and J. Fontaine, *ACTISEAT: active vehicle seat for acceleration compensation.* Proceedings of the Institution of Mechanical Engineers, Part D: Journal of Automobile Engineering, 2004. **218**(9): p. 925-933.
9. Paddan, G. and M. Griffin, *Effect of seating on exposures to whole-body vibration in vehicles.* Journal of Sound and Vibration, 2002. **253**(1): p. 215-241.
10. Kumar, S., *Vibration in operating heavy haul trucks in overburden mining.* Applied Ergonomics, 2004. **35**(6): p. 509-520.
11. Dewangan, K.N., et al., *Vertical and fore-aft seat-to-head transmissibility response to vertical whole body vibration: Gender and anthropometric effects.* Journal of Low Frequency Noise, Vibration and Active Control, 2013. **32**(1-2): p. 11-40.

12. Jack, R., et al., *Six-degree-of-freedom whole-body vibration exposure levels during routine skidder operations.* Ergonomics, 2010. **53**(5): p. 696-715.

13. Cation, S., et al., *Six degree of freedom whole-body vibration during forestry skidder operations.* International Journal of Industrial Ergonomics, 2008. **38**(9): p. 739-757.

14. Coyte, J.L., et al., *Seated whole-body vibration analysis, technologies, and modeling: A survey.* IEEE Transactions on Systems, Man, and Cybernetics: Systems, 2016. **46**(6): p. 725-739.

15. Conrad, L.F., et al., *Quantification of 6-degree-of-freedom chassis whole-body vibration in mobile heavy vehicles used in the steel making industry.* Journal of Low Frequency Noise, Vibration and Active Control, 2012. **31**(2): p. 85-104.

16. Salmoni, A.W., et al., *Case studies in whole-body vibration assessment in the transportation industry–Challenges in the field.* International Journal of Industrial Ergonomics, 2008. **38**(9): p. 783-791.

17. Choi, S.-B., M.-H. Nam, and B.-K. Lee, *Vibration control of a MR seat damper for commercial vehicles.* Journal of Intelligent Material Systems and Structures, 2000. **11**(12): p. 936-944.

18. Stewart, D., *A platform with six degrees of freedom.* Proceedings of the institution of mechanical engineers, 1965. **180**(1): p. 371-386.

19. Inner, B. and S. Kucuk, *A novel kinematic design, analysis and simulation tool for general Stewart platforms.* Simulation, 2013. **89**(7): p. 876-897.

20. Meng, Q., et al., *Dynamic modeling of a 6-degree-of-freedom Stewart platform driven by a permanent magnet synchronous motor.* Journal of Zhejiang University-Science C, 2010. **11**(10): p. 751-761.

21. Dasgupta, B. and T. Mruthyunjaya, *The Stewart platform manipulator: a review.* Mechanism and machine theory, 2000. **35**(1): p. 15-40.

22. Shao, Z.-F., et al., *A Fuzzy PID Approach for the Vibration Control of the FSPM.* International Journal of Advanced Robotic Systems, 2013. **10**(1): p. 59.

23. Dickey, J.P., T.R. Eger, and M.L. Oliver, *A systematic approach to simulating field-based occupational whole-body vibration exposure in the lab using a 6df robot.* Work, 2010. **35**(1): p. 15-26.

24. Conrad, L.F., et al., *Selecting seats for steel industry mobile machines based on seat effective amplitude transmissibility and comfort.* Work, 2014. **47**(1): p. 123-136.

25. Wan, Y. and J.M. Schimmels, *Improved vibration isolating seat suspension designs based on position-dependent nonlinear stiffness and damping characteristics.* Journal of dynamic systems, measurement, and control, 2003. **125**(3): p. 330-338.

26. Le, T.D. and K.K. Ahn, *A vibration isolation system in low frequency excitation region using negative stiffness structure for vehicle seat.* Journal of Sound and Vibration, 2011. **330**(26): p. 6311-6335.

27. Liu, Y., H. Matsuhisa, and H. Utsuno, *Semi-active vibration isolation system with variable stiffness and damping control.* Journal of sound and vibration, 2008. **313**(1): p. 16-28.

28. Pan, G.Y. and F.Q. Fan. *Research on semi-active suspension system with variable stiffness and damping*. in *Applied Mechanics and Materials*. 2012. Trans Tech Publ.

29. Gavin, H.P. and N.S. Doke. *Resonance suppression through variable stiffness and damping mechanisms*. in *1999 Symposium on Smart Structures and Materials*. 1999. International Society for Optics and Photonics.

30. Walsh, K.K., et al. *Development and testing of a newly proposed continuously variable stiffness/damping device for vibration control*. in *SPIE Smart Structures and Materials+ Nondestructive Evaluation and Health Monitoring*. 2012. International Society for Optics and Photonics.

31. Fulin, Z., et al., *Theoretical and experimental research on a new system of semi-active structural control with variable stiffness and damping.* Earthquake Engineering and Engineering Vibration, 2002. **1**(1).

32. Sun, S., et al., *A compact variable stiffness and damping shock absorber for vehicle suspension.* IEEE/ASME Transactions on Mechatronics, 2015. **20**(5): p. 2621-2629.

33. Li, W., X. Zhang, and H. Du, *Development and simulation evaluation of a magnetorheological elastomer isolator for seat vibration control.* Journal of Intelligent Material Systems and Structures, 2012. **23**(9): p. 1041-1048.

34. Choi, S., et al., *A semi-active suspension using ER fluids for a commercial vehicle seat.* Journal of Intelligent Material Systems and Structures, 1998. **9**(8): p. 601-606.

35. Hiemenz, G.J., W. Hu, and N.M. Wereley, *Semi-active magnetorheological helicopter crew seat suspension for vibration isolation.* Journal of Aircraft, 2008. **45**(3): p. 945-953.

36. Du, H., W. Li, and N. Zhang, *Semi-active variable stiffness vibration control of vehicle seat suspension using an MR elastomer isolator.* Smart materials and structures, 2011. **20**(10): p. 105003.

37. Sun, S., et al., *Horizontal vibration reduction of a seat suspension using negative changing stiffness magnetorheological elastomer isolators.* International Journal of Vehicle Design, 2015. **68**(1-3): p. 104-118.

38. Sun, S., et al., *A seat suspension with a rotary magnetorheological damper for heavy duty vehicles.* Smart Materials and Structures, 2016. **25**(10): p. 105032.

39. Shin, D.K., S.-M. Choi, and S.-B. Choi, *An adaptive fuzzy sliding mode control of magneto-rheological seat suspension with human body model.* Journal of Intelligent Material Systems and Structures, 2016. **27**(7): p. 925-934.

40. Gan, Z., A.J. Hillis, and J. Darling, *Adaptive control of an active seat for occupant vibration reduction.* Journal of Sound and Vibration, 2015. **349**: p. 39-55.

41. Maciejewski, I., L. Meyer, and T. Krzyzynski, *The vibration damping effectiveness of an active seat suspension system and its robustness to varying mass loading.* Journal of Sound and Vibration, 2010. **329**(19): p. 3898-3914.

42. Kawana, M. and T. Shimogo, *Active suspension of truck seat.* Shock and vibration, 1998. **5**(1): p. 35-41.

43. Ahn, K.K., *Active pneumatic vibration isolation system using negative stiffness structures for a vehicle seat.* Journal of Sound and Vibration, 2014. **333**(5): p. 1245-1268.

44. Perisse, J. and L. Jezequel, *An original feedback control with a reversible electromechanical actuator used as an active isolation system for a seat suspension. Part I: theoretical study.* Vehicle System Dynamics, 2000. **34**(5): p. 305-331.

45. Perisse, J. and L. Jezequel, *An original feedback control with a reversible electromechanical actuator used as an active isolation system for a seat suspension. Part II: experimental study.* Vehicle System Dynamics, 2000. **34**(6): p. 381-399.

46. Khoshnoud, F., et al., *Energy harvesting from suspension systems using regenerative force actuators.* International Journal of Vehicle Noise and Vibration, 2013. **9**(3-4): p. 294-311.

47. Wang, R., R. Ding, and L. Chen, *Application of hybrid electromagnetic suspension in vibration energy regeneration and active control.* Journal of Vibration and Control, 2016: p. 1077546316637726.

48. Zuo, L. and P.-S. Zhang, *Energy harvesting, ride comfort, and road handling of regenerative vehicle suspensions.* Journal of Vibration and Acoustics, 2013. **135**(1): p. 011002.

49. Pires, L., et al., *Design trade-offs for energy regeneration and control in vehicle suspensions.* International Journal of Control, 2013. **86**(11): p. 2022-2034.

50. Li, Z., et al., *Electromagnetic energy-harvesting shock absorbers: design, modeling, and road tests.* IEEE Transactions on Vehicular Technology, 2013. **62**(3): p. 1065-1074.

51. Zhang, Z., et al., *A high-efficiency energy regenerative shock absorber using supercapacitors for renewable energy applications in range extended electric vehicle.* Applied Energy, 2016. **178**: p. 177-188.

52. Zuo, L., et al., *Design and characterization of an electromagnetic energy harvester for vehicle suspensions.* Smart Materials and Structures, 2010. **19**(4): p. 045003.

53. Zhu, S., W.-a. Shen, and Y.-l. Xu, *Linear electromagnetic devices for vibration damping and energy harvesting: Modeling and testing.* Engineering Structures, 2012. **34**: p. 198-212.

54. Tang, X., T. Lin, and L. Zuo, *Design and optimization of a tubular linear electromagnetic vibration energy harvester.* IEEE/ASME Transactions on Mechatronics, 2014. **19**(2): p. 615-622.

55. Gupta, A., et al., *Design of electromagnetic shock absorbers.* International Journal of Mechanics and Materials in Design, 2006. **3**(3): p. 285-291.

56. Silva, J.F., *Sliding-mode control of boost-type unity-power-factor PWM rectifiers.* IEEE transactions on industrial electronics, 1999. **46**(3): p. 594-603.

57. Zhang, Y., et al., *Electro-hydraulic damper for energy harvesting suspension: Modeling, prototyping and experimental validation.* Applied Energy, 2017. **199**: p. 1-12.

58. Jin-qiu, Z., et al. *A review on energy-regenerative suspension systems for vehicles*. in *Proceedings of the World Congress on Engineering*. 2013.

59. Shi, D., et al., *Design and experiment study of a semi-active energy-regenerative suspension system.* Smart Materials and Structures, 2014. **24**(1): p. 015001.

60. Sapiński, B., *Energy-harvesting linear MR damper: prototyping and testing.* Smart Materials and Structures, 2014. **23**(3): p. 035021.

61. Choi, S., M. Seong, and K. Kim, *Vibration control of an electrorheological fluid-based suspension system with an energy regenerative mechanism.* Proceedings of the

Institution of Mechanical Engineers, Part D: Journal of Automobile Engineering, 2009. **223**(4): p. 459-469.

62. Sapiński, B., *Experimental study of a self-powered and sensing MR-damper-based vibration control system.* Smart Materials and Structures, 2011. **20**(10): p. 105007.
63. Ryba, D., *Semi-active damping with an electromagnetic force generator.* Vehicle System Dynamics, 1993. **22**(2): p. 79-95.
64. Arana, C., S.A. Evangelou, and D. Dini, *Series active variable geometry suspension for road vehicles.* IEEE/ASME Transactions on Mechatronics, 2015. **20**(1): p. 361-372.
65. Arana, C., S.A. Evangelou, and D. Dini, *Series Active Variable Geometry Suspension application to chassis attitude control.* IEEE/ASME Transactions on Mechatronics, 2016. **21**(1): p. 518-530.
66. Arana, C., S.A. Evangelou, and D. Dini, *Series Active Variable Geometry Suspension application to comfort enhancement.* Control Engineering Practice, 2017. **59**: p. 111-126.
67. Geng, Z.J. and L.S. Haynes, *Six degree-of-freedom active vibration control using the Stewart platforms.* Control Systems Technology, IEEE Transactions on, 1994. **2**(1): p. 45-53.
68. Haynes, L.S., Z.J. Geng, and J.P. Teter. *New Terfenol-D actuator design with applications to multiple DOF active vibration control*. in *1993 North American Conference on Smart Structures and Materials*. 1993. International Society for Optics and Photonics.
69. Spanos, J., Z. Rahman, and G. Blackwood. *A soft 6-axis active vibration isolator*. in *American Control Conference, Proceedings of the 1995*. 1995. IEEE.
70. Rahman, Z.H., J.T. Spanos, and R.A. Laskin. *Multiaxis vibration isolation, suppression, and steering system for space observational applications*. in *Astronomical Telescopes & Instrumentation*. 1998. International Society for Optics and Photonics.
71. Zhang, T., et al., *Giant magnetostrictive actuators for active vibration control.* Smart materials and structures, 2004. **13**(3): p. 473.
72. Hauge, G. and M. Campbell, *Sensors and control of a space-based six-axis vibration isolation system.* Journal of sound and vibration, 2004. **269**(3): p. 913-931.
73. Preumont, A., et al., *A six-axis single-stage active vibration isolator based on Stewart platform.* Journal of sound and vibration, 2007. **300**(3): p. 644-661.
74. Chi, W., et al., *Design and experimental study of a VCM-based Stewart parallel mechanism used for active vibration isolation.* Energies, 2015. **8**(8): p. 8001-8019.
75. Cui, L., et al. *Six degree-of-freedom hydraulic Hexapod platform for large-amplitude vibration isolation*. in *Control, Automation and Systems (ICCAS), 2011 11th International Conference on*. 2011. IEEE.
76. Zhu, T., et al. *The development of a 6 degree of freedom quasi-zero stiffness maglev vibration isolator with adaptive-passive load support*. in *15th International Conference on Mechatronics Technology. URL: http://hdl. handle. net/2440/72548*. 2011.

77. Koutsky, L.J. and C.T. Brodersen, *Active suspension system for vehicle seats*. 2000, Google Patents.

78. Klooster, S.J., *Vibration Suppression and Safety Seat Motion Design of a Hyper-Active Seat*. 2004, Georgia Institute of Technology.

79. Zhao, Y., W. Sun, and H. Gao, *Robust control synthesis for seat suspension systems with actuator saturation and time-varying input delay.* Journal of Sound and Vibration, 2010. **329**(21): p. 4335-4353.

80. Rubio-Massegu, J., et al., *Brief Paper-Static output-feedback controller design for vehicle suspensions: an effective two-step computational approach.* IET Control Theory & Applications, 2014. **8**(15): p. 1566-1574.

81. Wang, R., et al., *Optimization and finite-frequency H∞ control of active suspensions in in-wheel motor driven electric ground vehicles.* Journal of the Franklin Institute, 2015. **352**(2): p. 468-484.

82. Wang, R., et al., *Robust fault-tolerant H∞ control of active suspension systems with finite-frequency constraint.* Mechanical Systems and Signal Processing, 2015. **62**: p. 341-355.

83. Li, H., X. Jing, and H.R. Karimi, *Output-feedback-based control for vehicle suspension systems with control delay.* IEEE Transactions on Industrial Electronics, 2014. **61**(1): p. 436-446.

84. Arana, C., S.A. Evangelou, and D. Dini, *Quarter-Car Experimental Study for Series Active Variable Geometry Suspension.* IEEE Transactions on Control Systems Technology, 2017.

85. Türkay, S. and H. Akçay, *Aspects of achievable performance for quarter-car active suspensions.* Journal of Sound and Vibration, 2008. **311**(1): p. 440-460.

86. He, Y. and J. McPhee, *Multidisciplinary design optimization of mechatronic vehicles with active suspensions.* Journal of Sound and Vibration, 2005. **283**(1): p. 217-241.

87. Li, H., et al., *Adaptive sliding-mode control for nonlinear active suspension vehicle systems using T–S fuzzy approach.* IEEE Transactions on Industrial Electronics, 2013. **60**(8): p. 3328-3338.

88. Nguyen, S.D., Q.H. Nguyen, and S.-B. Choi, *Hybrid clustering based fuzzy structure for vibration control–Part 1: A novel algorithm for building neuro-fuzzy system.* Mechanical Systems and Signal Processing, 2015. **50**: p. 510-525.

89. Nguyen, S.D., Q.H. Nguyen, and S.-B. Choi, *A hybrid clustering based fuzzy structure for vibration control–Part 2: An application to semi-active vehicle seat-suspension system.* Mechanical Systems and Signal Processing, 2015. **56**: p. 288-301.

90. Du, H., et al., *Direct voltage control of magnetorheological damper for vehicle suspensions.* Smart Materials and Structures, 2013. **22**(10): p. 105016.

91. Maciejewski, I., *Control system design of active seat suspensions.* Journal of Sound and Vibration, 2012. **331**(6): p. 1291-1309.

92. Bououden, S., M. Chadli, and H.R. Karimi, *A robust predictive control design for nonlinear active suspension systems.* Asian Journal of Control, 2016. **18**(1): p. 122-132.

93. Deshpande, V.S., P. Shendge, and S. Phadke, *Dual objective active suspension system based on a novel nonlinear disturbance compensator.* Vehicle System Dynamics, 2016. **54**(9): p. 1269-1290.

94. Yang, J., S. Li, and X. Yu, *Sliding-mode control for systems with mismatched uncertainties via a disturbance observer.* Industrial Electronics, IEEE Transactions on, 2013. **60**(1): p. 160-169.

95. Ginoya, D., P. Shendge, and S. Phadke, *Sliding mode control for mismatched uncertain systems using an extended disturbance observer.* Industrial Electronics, IEEE Transactions on, 2014. **61**(4): p. 1983-1992.

96. Kim, K.-S., K.-H. Rew, and S. Kim, *Disturbance observer for estimating higher order disturbances in time series expansion.* Automatic Control, IEEE Transactions on, 2010. **55**(8): p. 1905-1911.

97. Pan, H., X. Jing, and W. Sun, *Robust finite-time tracking control for nonlinear suspension systems via disturbance compensation.* Mechanical Systems and Signal Processing, 2017. **88**: p. 49-61.

98. Vafamand, N., M.H. Asemani, and A. Khayatiyan, *A robust L 1 controller design for continuous-time TS systems with persistent bounded disturbance and actuator saturation.* Engineering Applications of Artificial Intelligence, 2016. **56**: p. 212-221.

99. Nguyen, A., A. Dequidt, and M. Dambrine, *Anti-windup based dynamic output feedback controller design with performance consideration for constrained Takagi–Sugeno systems.* Engineering Applications of Artificial Intelligence, 2015. **40**: p. 76-83.

100. Kothare, M.V., et al., *A unified framework for the study of anti-windup designs.* Automatica, 1994. **30**(12): p. 1869-1883.

101. Tarbouriech, S. and M. Turner, *Anti-windup design: an overview of some recent advances and open problems.* IET control theory & applications, 2009. **3**(1): p. 1-19.

102. Mulder, E.F., P.Y. Tiwari, and M.V. Kothare, *Simultaneous linear and anti-windup controller synthesis using multiobjective convex optimization.* Automatica, 2009. **45**(3): p. 805-811.

103. Rath, J.J., et al., *Output Feedback Active Suspension Control With Higher Order Terminal Sliding Mode.* IEEE Transactions on Industrial Electronics, 2016. **PP**(99): p. 1-1.

104. Choi, S.-B. and Y.-M. Han, *Vibration control of electrorheological seat suspension with human-body model using sliding mode control.* Journal of Sound and Vibration, 2007. **303**(1): p. 391-404.

105. Ginoya, D., P. Shendge, and S. Phadke, *Sliding mode control for mismatched uncertain systems using an extended disturbance observer.* IEEE Transactions on Industrial Electronics, 2014. **4**(61): p. 1983-1992.

106. Yang, J., S. Li, and X. Yu, *Sliding-mode control for systems with mismatched uncertainties via a disturbance observer.* IEEE Transactions on Industrial Electronics, 2013. **60**(1): p. 160-169.

107. Zhihong, M. and X.H. Yu. *Terminal sliding mode control of MIMO linear systems*. in *Decision and Control, 1996., Proceedings of the 35th IEEE Conference on*. 1996. IEEE.

108. Feng, Y., X. Yu, and Z. Man, *Non-singular terminal sliding mode control of rigid manipulators.* Automatica, 2002. **38**(12): p. 2159-2167.

109. Choi, S.-B. and W.-K. Kim, *Vibration control of a semi-active suspension featuring electrorheological fluid dampers.* Journal of Sound and vibration, 2000. **234**(3): p. 537-546.

110. ISO, *Mechanical Vibration and Shock – Evaluation of Human Exposure to Whole-body Vibration – Part 1: General Requirements.* ISO 2631–1, 1997.

111. Li, H., et al., *Reliable fuzzy control for active suspension systems with actuator delay and fault.* IEEE Transactions on Fuzzy Systems, 2012. **20**(2): p. 342-357.

112. Du, H. and N. Zhang, *Fuzzy control for nonlinear uncertain electrohydraulic active suspensions with input constraint.* IEEE Transactions on Fuzzy Systems, 2009. **17**(2): p. 343-356.

113. Lo, J.-C. and M.-L. Lin, *Observer-based robust H∞ control for fuzzy systems using two-step procedure.* IEEE Transactions on Fuzzy Systems, 2004. **12**(3): p. 350-359.

114. Ruderman, M. and T. Bertram, *Two-state dynamic friction model with elasto-plasticity.* Mechanical Systems and Signal Processing, 2013. **39**(1): p. 316-332.

115. Braghin, F., et al., *Design of an active seat suspension for agricultural vehicles*, in *Structural Dynamics, Volume 3*. 2011, Springer. p. 1365-1374.

116. Peng, C., J. Fang, and X. Xu, *Mismatched disturbance rejection control for voltage-controlled active magnetic bearing via state-space disturbance observer.* IEEE Transactions on Power Electronics, 2015. **30**(5): p. 2753-2762.

117. Yang, J., W.-H. Chen, and S. Li, *Non-linear disturbance observer-based robust control for systems with mismatched disturbances/uncertainties.* IET control theory & applications, 2011. **5**(18): p. 2053-2062.

118. Chen, W.-H., et al., *A nonlinear disturbance observer for robotic manipulators.* IEEE Transactions on industrial Electronics, 2000. **47**(4): p. 932-938.

119. Lien, C.-H., et al., *Robust reliable H∞ control for uncertain nonlinear systems via LMI approach.* Applied Mathematics and Computation, 2008. **198**(1): p. 453-462.

120. Euston, M., et al. *A complementary filter for attitude estimation of a fixed-wing UAV*. in *2008 IEEE/RSJ International Conference on Intelligent Robots and Systems*. 2008. IEEE.

121. Yang, J., et al., *Experimental study and modeling of a novel magnetorheological elastomer isolator.* Smart Materials and Structures, 2013. **22**(11): p. 117001.

122. Lian, K., B.K. Perkins, and P. Lehn, *Harmonic analysis of a three-phase diode bridge rectifier based on sampled-data model.* IEEE Transactions on power delivery, 2008. **23**(2): p. 1088-1096.

123. Du, H., J. Lam, and K.Y. Sze, *Non-fragile output feedback H∞ vehicle suspension control using genetic algorithm.* Engineering Applications of Artificial Intelligence, 2003. **16**(7): p. 667-680.

124. Madgwick, S., *An efficient orientation filter for inertial and inertial/magnetic sensor arrays.* Report x-io and University of Bristol (UK), 2010. **25**.